Study of Nuclear Reaction and Nuclear decay modes using Relativistic Mean-field Theory

Thesis submitted in partial fulfillment
for the award of Degree

Doctor of Philosophy

by

AJEET SINGH

RAJIV GANDHI INSTITUTE OF PETROLEUM TECHNOLOGY
JAIS, INDIA – 229304

Enrolment No. PP18-001 2022

CERTIFICATE

It is certified that the work contained in the thesis titled **"Study of Nuclear Reaction and Nuclear decay modes using Relativistic Mean-field theory"** by **"Ajeet Singh"** has been carried out under my supervision and that this work has not been submitted elsewhere for a degree.

It is further certified that the student has fulfilled all the requirements of Comprehensive, Candidacy and SOTA/Open seminar.

Prof. Amritanshu Shukla
(Supervisor)

Prof. Atul Sharma
(Co-Supervisor)

DECLARATION BY THE CANDIDATE

I, **"Ajeet Singh"**, certify that the work embodied in this thesis is my own bona-fide work and carried out by me under the supervision of **"Prof. Amritanshu Shukla"** and **"Prof. Atul Sharma"** from *July 2018* to *November 2022* at the **Department of Sciences and Humanities**, Rajiv Gandhi Institute of Petroleum Technology, Jais. The matter embodied in this thesis has not been submitted for the award of any other degree. I declare that I have faithfully acknowledged and given credits to the research workers wherever their works have been cited in my work in this thesis. I further declare that I have not willfully copied any other's work, paragraphs, text, data, results, etc., reported in journals, books, magazines, reports dissertations, thesis, etc., or available at websites and have not included them in this thesis and have not cited as my own work.

Date:

Place:

Ajeet Singh

CERTIFICATE BY THE SUPERVISOR(S)

It is certified that the above statement made by the student is correct to the best of our knowledge.

Prof. Amritanshu Shukla
(Supervisor)

Prof. Atul Sharma
(Co-Supervisor)

Prof. A.K. Choubey
(Head of the Department
Sciences and Humanities)

CERTIFICATE

It is certified that the work contained in the thesis titled **"Study of Nuclear Reaction and Nuclear decay modes using Relativistic Mean-field theory"** by Mr. **"Ajeet Singh"** has been carried out under my supervision. It is also certified that he fulfilled the mandatory requirement of TWO quality publications arose out of his thesis work.

It is further certified that the two publications (copies enclosed) of the aforesaid Mr. **Ajeet Singh** have been published in the Journals indexed by

(a) SCI
(b) SCI Extended
(c) SCOPUS
(d) *Non-index journal (Only in special cases)
(*Please enclosed DPGC resolution in this regard)

Prof. Amritanshu Shukla
(Supervisor)

Prof. Atul Sharma
(Co-Supervisor)

Dr. Anirban Mukherjee
(DPGC, Convener)

COPYRIGHT TRANSFER CERTIFICATE

Title of the Thesis : Study of Nuclear Reaction and Nuclear decay modes using Relativistic Mean-field theory
Name of the Student : Ajeet Singh

Copyright Transfer

The undersigned hereby assigns to the Rajiv Gandhi Institute of Petroleum Technology, Jais all rights under copyright that may exist in and for the above thesis submitted for the award of the **DOCTOR OF PHILOSOPHY**.

Date:

Place: **Ajeet Singh**

Note: However, the author may reproduce or authorize others to reproduce material extracted verbatim from the thesis or derivative of the thesis for author's personal use provided that the source and the Institute's copyright notice are indicated.

Acknowledgements

First and foremost, I want to express my sincere gratitude to my supervisor **Prof. Amritanshu Shukla** *and co-supervisor* **Prof. Atul Sharma** *for their continuous support, invaluable guidance, and perceptive suggestions during the course of my Ph.D. They have been my tremendous mentor and taught me everything they know. Each and every discussion throughout this journey of our work has been very fruitful. I am deeply grateful to them for encouraging my research work and for allowing me to grow as a research scholar. I express my heartful thanks to our collaborator, Dr. M.K. Gaidarov (Institute of Nuclear Research and Nuclear Energy, Bulgarian Academy of Sciences), for his valuable and priceless support during the completion of my thesis work.*

I express my heartfelt gratitude to the Director of RGIPT, Prof. A.S.K. Sinha, for generously providing me with the essential institute resources and facilities required to conduct my research work.

I would like to thank the Head, Department of Sciences and Humanities, Prof. A.K. Choubey, Prof. Satish Sinha (RPEC member), and Dr. Saurabh Mishra (Dean), for their valuable suggestions and helpful assistance during the different stages of my research work. I am also grateful to all faculty of the Sciences and Humanities department for their help and cooperation throughout my research journey.

Special thanks go to the Director of the Inter-University Accelerator Centre (IUAC), New Delhi, for providing all the facilities and hospitality during my Ph.D. coursework.

I would like to thank my labmates, Dr. Karunesh Kant, Dr. Awanish Kumar Bajpeyi, Dr. Abhishek Anand, Dr. Akhilesh Kumar Yadav, Saurabh Pandey, Renna Shakir, and my friends Shadab, Pooja, Shivam, Rani, Athar, for their unwavering support throughout this journey. Their constant presence and encouragement have made this journey truly wonderful.

Last but not the least, I would like to thank my parents and my family for their moral support and encouragement at every stage of my academic and personal life. I am especially grateful to my brothers Arun, Ambreesh, and Prem for their love, support, and best wishes. They are all my constant source of power and their faith in me has propelled me to overcome all the hurdles swiftly. Finally, I gratefully acknowledge to Council of Scientific and Industrial Research (CSIR), Govt. of India, New Delhi for providing financial support under file no.: 09/1088(0005)/2018-EMR-I.

Ajeet Singh

Dedicated To

My Beloved Parents

Contents

Notations and Abbreviations

ψ	spinor wave function describing nucleons
g_σ	coupling constant for σ-mesons
g_ω	coupling constant for ω-mesons
g_ρ	coupling constant for ρ-mesons
A_μ	the photon-field
τ	Pauli matrices
E_{cm}	center-of-mass energy
R_P	interaction radius of projectile (P)
R_T	interaction radius of target (T)
λ	radioactive decay rate
P	Gamow penetrability factor

List of Figures

List of Tables

Preface

In the entire nuclear landscape, only about 300 stable nuclei exist on the stability line, and the rest other undergo radioactive decay through various modes including alpha decay, beta decay, gamma decay, double beta decay, and so on. In this thesis, we have theoretically investigated the nuclear reaction dynamics of light and medium mass nuclei and decay modes using the Relativistic mean field model. For decay modes, we have studied cluster decay half-lives and two proton decay of several potential radioactive nuclides, which lie on either side of the beta stability line of the nuclear landscape. These studies are quite significant to understand the basic building blocks of nuclear structure.

In Chapter-1 of the thesis, we have presented an introduction of the subject with a brief literature review. Subsequently, we have presented the motivation to take up the present work.

In Chapter-2, a brief description of the nuclear models employed in the thesis work for the calculation of ground-state properties has been presented. We have used the Relativistic Hartree Bogoliubov model with density-dependent meson exchange (DD-ME2), density-dependent point coupling (DD-PC1) parameter sets, and a non-linear NL3* parameter set, in the Relativistic Mean-field (RMF) model. The details of the Glauber model and its description for calculating nuclear reaction cross-section along with the process of using the nuclear densities from this RMF formalism have also been described. A detailed description of the effective liquid drop (ELDM) model, as well as other empirical formulas such as Universal Decay Law (UDL), Tavares-Medeiros (TM), Viola-Seaborg (VS), and Horoi formula, has been given for the sake of completeness in the discussion.

In Chapter-3, we have presented a systematic study of the nuclear reactions of various light and medium mass nuclei (He, Li, Be, B, C, Ca, Ni, Zr, and Sn isotopes) on ^{12}C and proton targets mainly at high energies using Glauber model and a comparison of the results with available experimental data is made. The microscopic nuclear densities needed for these calculations have been obtained using relativistic Hartree-Bogoliubov formalism.

In addition, other ground-state bulk properties are also calculated and compared with the available experimental data. It has been observed that the results obtained using the relativistic framework with the density-dependent meson exchange (DD-ME2) parameter set are in better agreement with the experimental data than with the density-dependent point coupling (DD-PC1) results. Also, it is observed that the total reaction cross-section increases with the increase of the projectile mass and compares well with the experimental data.

In Chapter-4, we have presented our results for the half-lives of alpha-like clusters (^{8}Be, ^{12}C, ^{16}O, ^{20}Ne, and ^{24}Mg) decay in the trans-tin region for ($^{106-116}$Xe, $^{108-120}$Ba, $^{114-126}$Ce, and $^{118-128}$Nd) and in transition metal region ($^{156-166}$Hf, $^{158-172}$W, $^{160-174}$Os, $^{166-180}$Pt, and $^{170-182}$Hg). These half-lives have been calculated using the shape parametrization model of cluster decay in conjunction with the axially deformed relativistic mean-field (RMF) model with the NL3* parameter set. These results have also been compared with the half-lives computed using the latest empirical relations, namely Universal Decay Law (UDL) and the Scaling Law was given by Horoi *et al.*. It has been observed that in the trans-tin region the minimum cluster decay half-lives are found at nearly doubly magic or doubly magic daughter ^{100}Sn nucleus ($N_d = 50$, N_d is the neutron number of the daughter nucleus) and in transition metal region at $N_d = 82$, which is a magic number.

In Chapter-5, we have presented the structural properties, alpha and clusters decay half-lives (for ^{8}Be, ^{12}C, ^{16}O, ^{20}Ne, and ^{24}Mg decay) in the Th, U, and Pu isotopes using the well-known Relativistic Mean-Field (RMF) theory with NL3* parameter set. We have calculated the binding energy per nucleon, RMS radii, two-neutron separation energies (S_{2n}), and other ground-state observables to test the reliability of our calculations. The results are in good agreement with the finite-range droplet model (FRDM) and experimental data available. The half-live calculations are also carried out by using the latest empirical relations, namely Universal Decay Law (UDL), Tavares- Medeiros (TM), Viola-Seaborg (VS), and the Scaling Law given by Horoi et al., and their comparisons with the effective liquid drop model (ELDM) results are found to be in good agreement. In the plots for $log_{10}T_{1/2}$ versus the neutron number of the daughter in the corresponding decay, the half-life is found to be the minimum for the decay leading to nearly doubly magic or doubly magic daughter ^{208}Pb nucleus ($N_d = 126$, N_d is the neutron number of the daughter nucleus).

In Chapter-6, we have presented our study for two proton emitters and results for ground-state properties, i.e., the binding energy per nucleon and two-proton separation energy of Fe, Ni, Zn, Ge, Kr and Zr isotopes by using the relativistic mean-field (RMF) approach with force parameter NL3* results are in excellent agreement with the available experimental data. We have performed systematic studies of the two-proton ($2p$) radioactivity, the two-proton decay energy (Q_{2p}) using the RMF (NL3*) approach, the finite-range droplet model (FRDM), and the Weizsacker-Skyrme-4 (WS4). Then, the effective liquid drop model (ELDM) is applied to find out the two-proton decay half-lives using three kinds of evaluated Q_{2p} values. The two-proton decay half-lives calculations are also carried out by using empirical formulas, namely Liu and Sreeja, and their comparisons with ELDM results are found to be in agreement. Also, we predict the half-lives of possible nuclei of the two-proton radioactivity in the range $30 \leq Z \leq 40$ with released energy $Q_{2p} > 0$, for the planned/upcoming experiments.

In Chapter-7, the summary and conclusion of the thesis work along with the future scope of the present study have been presented.

Chapter 1

Introduction

Before the understanding of the nucleus and nuclear interaction, the structure of the atom itself has been a mystery of nature. It started with Thomson's plum pudding model, which described the atom as a positive charge sphere with electrons embedded into it to balance the total positive charge. The negative charge of the electron was postulated to be similar to "plums" in a "pudding". Ernest Rutherford further described the atomic nucleus in 1911 [1] after performing his famous gold foil experiment, i.e. a gold foil was bombarded with α particles. Based on the experimental results, Rutherford proposed that a major part of the mass of an atom and all of its positive charge were concentrated in a small central core, called the nucleus. The internal composition of an atomic nucleus came to be known in 1932 after the discovery of a neutron by Chadwick [2]. In an atom, the nucleus consists of protons and neutrons. In an atomic nucleus, protons (positively charged particles) and neutrons (neutral particles) are held together by a strong nuclear force. Yukawa later proposed the meson theory of nuclear force in 1935 [3]. According to this theory, nucleons interact with each other via the exchange of mesons.

A large number of theoretical and experimental studies have been performed since then to understand nuclear interaction and predict the endpoints of the neutron-rich and proton-rich sides of the nuclear landscape. The nuclear landscape is basically the periodic table of nuclear physics. It is the arrangement of all possible nuclei according to their unique combinations of protons and neutrons. In figure 1.1, the neutron number (N) is plotted on the x-axis, and the y-axis represents the proton number (Z). Only a few nuclei (approximately 300) occur naturally on Earth, which are represented by block square dots in figure 1.1. The black squares represent stable nuclei that define the value of stability.

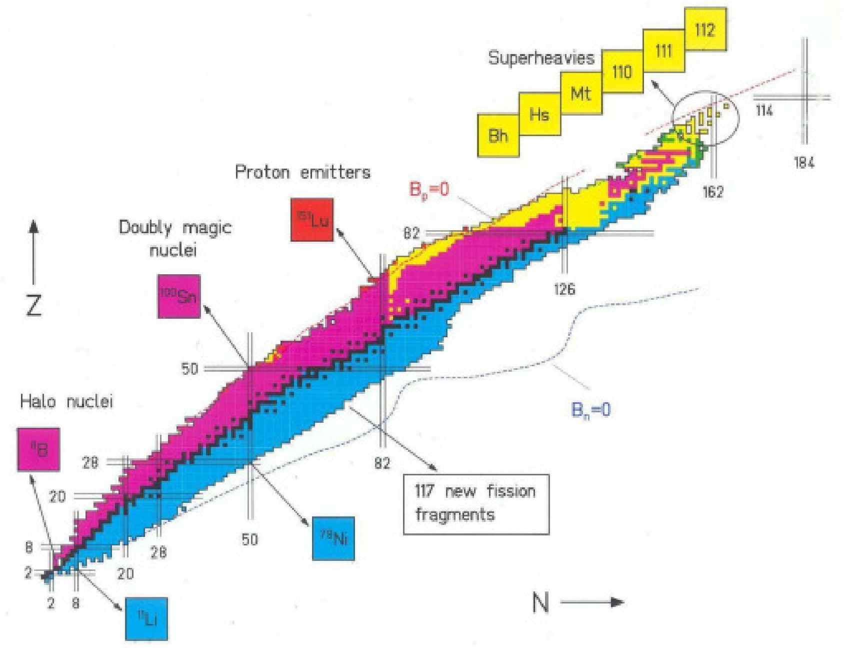

Figure 1.1: Nuclear landscape of stable, experimentally synthesized, and theoretically predicted nuclei.

These nuclei have an almost infinitely long life-time and are known as stable nuclei. The stable nuclei lie on the β-stability line and the unstable nuclei lie above and below the line of stability in the nuclear landscape. In a stable atom, there is enough binding energy to permanently hold the nucleus together. However, in unstable nuclei, the strong nuclear force does not generate enough binding energy to maintain the nucleus together permanently.

To study the entire system in the N-Z plane, we require knowledge of nuclear interaction and nuclei on the stability line and away from the stability line. Currently, different theoretical models suggest more than 6000 bound nuclei exist in the nuclear chart. However, approximately 2000 nuclei have been observed experimentally. With the existence of the other isotopes, which are far from the β-stability line, many experimental and theoretical research groups are working on this aspect. After 1980, the construction of a new generation of radioactive beam facilities in several laboratories around the whole world developed a new approach to studying isotopes in both the proton and neutron drip-line regions. Many theoretical studies [4, 5, 6, 7, 8, 9, 10, 11] and experimental efforts at various laboratories in RIKEN-Japan [12], JINR-Dubna [13, 14], and GANIL-France [15] have led to important results in the concerned field of research.

There are a very small number of nuclei that show proton-rich characteristics, as shown in figure 1.1 above the β-stability line (shown with pink color). Burbidge *et al.* [16], and A.G.W. Cameron [17] showed that the majority of the naturally occurring nuclides beyond the element iron can be made in two different kinds of neutron-capture processes, the slow neutron capture process (s-process) and rapid neutron-capture process (r-process). Generally, the formation of proton-rich nuclei occurs by gradually adding protons to the nuclei (p, γ) or by removing neutrons from nuclei (γ, n). The proton-rich region is bounded by the proton drip line, represented by a dashed red. Neutron-rich nuclei are produced through the r-process or s-process. The r-process is responsible for the formation of approximately half of the atomic nuclei above the iron element. The slow neutron capture process (s-process) occurs with the emission of gamma radiation (n, γ) which takes place at relatively low temperature (T$\sim$1-3$\times 10^8$K) and relatively low neutron densities (10^6 cm^{-3}). Below the β-stability line, the region is neutron-rich (shown in blue) and is limited by the neutron drip line, indicated by a dashed blue line. The neutron drip line is reached when the binding energy for the last neutron, B_n, becomes zero. Similarly, at the drip lines, the binding energy of the last proton, B_p, is zero. The proton drip line is reached quite fast because Coulomb repulsion is a hindrance to the formation of proton-rich nuclei. The nucleus after which no more protons or neutrons can be added is known as the drip line nucleus. These nuclei have very short half-lives and extremely low separation energies for one or two protons.
Some nuclei exhibit very high stability with their proton number Z or neutron number N corresponding to certain values known as magic numbers. These magic numbers are Z=2, 8, 20, 28, 50, 82, and neutron numbers N = 2, 8, 20, 28, 50, 82, and 126. At these magic numbers, a shell closure occurs. These nuclei assume spherical shapes and very stable nuclear configurations. In figure 1.1, the magic numbers are indicated by horizontal and vertical bars. Doubly magic nuclei have higher stability, with a closed shell of both protons and neutrons. Elements greater than Uranium (Z=92) are not usually found in nature and are considered as a super-heavy region. These elements can be synthesized in laboratories, but they have very short half-lives, meaning they decay rapidly. In super-heavy nuclei, a large number of protons are present, and repel each other due to their positive charges. This repulsion makes these nuclei more radioactive and less stable. Super-heavy nuclei are located in the faraway corner of figure 1.1.

In this thesis, we have studied the nuclear reaction dynamics of various nuclei using the relativistic mean-field model, along with some other exotic phenomenon. In the following section, we have given a brief introduction to these topics.

1.1 Nuclear Reaction

This approach to determining the structure of the nucleus is through a nuclear reaction. A nuclear reaction is a process in which the nucleons in the incident particle (projectile) interact with the nucleons of the target nucleus, where energy plays a crucial role. A large amount of energy is required to overcome the electromagnetic repulsion between the protons, known as the Coulomb barrier. If the energy is below this Coulomb barrier, the nuclei will bounce off each other. When an interaction occurs between the projectile and target nucleus, there are two possibilities: either the beam particle scatters elastically, leaving the target nucleus in its ground state or the target nucleus becomes internally excited and subsequently decays by emitting nucleons. A nuclear reaction is characterized by identifying the incident particle, target nucleus, and reaction products. The incoming particle can produce different types of reactions depending on its energy. In 1919, the first nuclear reaction was observed by Rutherford using alpha particles detected at nitrogen ^{14}N+$\alpha \rightarrow$ ^{17}O+p. A nuclear reaction can release protons, electrons, as well as gamma rays.
Common notation of nuclear reaction: a + A = b + B
where a is the projectile, A is the target, and b and B are the reaction products.

Table 1.1: Types of Nuclear Reactions and Observation about Nuclei and Nuclear Energy.

Reaction	**Observation**
Nucleon-Nucleon Scattering	Fundamental Nuclear Force
Elastic Scattering	Nuclear Size and Interaction Potential
Inelastic Scattering	Energy Level Location and Quantum Numbers
Transfer and Knockout Reactions	Details of the Shell Model
Fusion Reactions	Astrophysical Processes
Fission Reactions	Properties of Liquid-drop Model
Compound Nucleus Formation	Statistical Properties of the Nucleus
Multifragmentation	Phases of Nuclear Matter, Collective Model
Pion Reactions	Investigation of the nuclear Glue
Electron Scattering	Quark Structure of Nuclei

Distinct reactions were studied by measuring the kinetic energies and incident angles of the reaction products. The reaction cross section is one of the most important quantities of interest for a specific set of kinematics variables. The cross-section describes the probability of a projectile hitting a target nucleus. Different types of cross-sections are total reaction cross-section (σ_r), differential scattering cross-section ($\frac{d\sigma}{d\Omega}$), nuclear removal cross-section (σ_{1N}), etc. σ_r is one of the very fundamental quantities characterizing nuclear reaction. It has been calculated both theoretically and experimentally. Cross-sections depend on a variety of reaction variables. Theoretically, there are two different types of formalism for investigating the reaction cross-section. The first one is known as the low energy Bass model [18], which is based on an interaction potential. The interaction radius is determined by fitting the experimental data in this model. However, the second kind of theoretical approach is based on the high-energy microscopic Glauber model [19] which considers the individual nucleon-nucleon interaction. The reaction cross-section provides information about the probability of a specific reaction occurring, allowing us to understand the size and distribution of the nuclei. The estimation of reaction cross-section is very important for an overall understanding of the reaction mechanism and associated dynamical behavior. On the basis of projectile energy range, the nuclear reaction is classified as Low-energy reactions ($E_{lab} \leq$30MeV/nucleon), Intermediate energy reactions (E_{lab}=30-1000MeV/nucleon), and High-energy reactions (E_{lab} >1GeV/nucleon). In the low-energy range, where the nuclear system has incident energy E$\leq$30 MeV/nucleon. At this energy the strong absorption effect dominates, and a microscopic description of the process is so difficult to observe. The nuclear reaction requires an energetic projectile beam coming from an accelerator to be incident on the target. Depending on the conditions of the nuclear reaction, different kinds of reactions can occur.

When a projectile strikes the target nucleus it forms an intermediate nucleus called the compound nucleus. The compound nucleus is unstable and decays life-time of the order of 10^{-17}-10^{-15} sec. The compound nucleus disintegrated by emitting a particle-like a proton, neutron, α-particle, and γ-particle, etc. to form a product nucleus.

In a non-compound nuclear reaction, the life-time of the interaction is very small, on the order of 10^{-22} sec, compared to the life-time of the formation of a compound nucleus. In addition to compound nucleus processes, there are other non-compound nucleus decay processes, such as direct reaction, Quasi-fission (QF), Deep-inelastic collisions (DIC), and pre-equilibrium fission [20], etc.

The nuclear reaction in which the projectile does not combine with the target nucleus as a whole and interacts only with the surface is called a direct nuclear reaction. This reaction is completed without the formation of a compound nucleus, and the reaction occurs on the surface of nucleons. The projectile may lose one or more nucleons in direct reactions. The incident particle and the target nucleus have a life-time of the order of 10^{-22} sec and interaction potential depth in MeV. Several processes like inelastic or elastic nuclear reactions, stripping or pick-up reactions give direct reactions. A brief overview of stripping and pick-up reactions is given below.

A stripping reaction is a process in which some part of the incident projectile nucleus interacts with the target nucleus, while the remaining portion continues with an almost similar momentum in the original direction. This reaction was first described by Stuart Thomas Butler [21] in 1950. Stripping reactions of various types, e.g., (d, p), (d, n), (t, p), (t, d) and (α, p), are known to occur at large particle energies with numerous different nuclei. Deuteron stripping reactions have been used to study nuclear reactions and the structure of Cu^{63}(d, p)Cu^{64}.

A pickup reaction is a reaction in which one or more nucleons are transferred from the target nucleus to the projectile nuclei without changing the structure of the remaining nucleons. Reactions of this type include (p, α), (p, t), (p, ^{3}He), (d, t) and (d, ^{3}He). An example of the pick-up reaction is O^{16}(p, d)O^{15}.

In the intermediate energy range of the nuclear system, nucleus-nucleus interaction are dominated by free nucleus-nucleus collision, which suggests that the surface transparency effect increases with the increase of the energy over this region. When the energy of the projectile exceeds 30 MeV/nucleon, the system is considered to be in an extremely excited state. As the projectile energy increases further, reaching up to 200 MeV/nucleon, the multi-fragmentation process starts taking place during a collision, which makes the nuclear system in a boiling state. In the energy of an incident projectile is within the range of 100 MeV/nucleon to a few GeV/nucleon, the system is in a highly excited state and emits various particles through a multi-fragmentation phenomenon.

1.1.1 Nuclear Scattering

Nuclear scattering and nuclear reactions are utilized to estimate the properties of nuclei. When two particles, the projectile and the target, collide without exchanging masses or changing their nature, the interaction is referred to as nuclear scattering. This type of interaction is considered a fundamental nuclear reaction. During nuclear scattering, the projectile and target do not exchange any particles with each other, ensuring that momentum and energy remain unchanged. Nuclear scattering can be classified as elastic or inelastic scattering.

Elastic scattering occurs when the linear momentum and total kinetic energy of the system are conserved throughout the collision, the nucleus to return to its ground state. The study of elastic scattering on both stable and exotic nuclei provides valuable information on nuclear potentials and nuclear matter densities. Matter of interest, the p-p scattering on both stable and neutron-rich nuclei at high energies was successfully investigated by G. D. Alkhazov *et al.* [22]

Inelastic scattering is a fundamental scattering process in which the linear momentum of the system is conserved after the collision, but the kinetic energy of the system does not remain conserved. The probability of the scattering depends on the energy of the incident particle. In inelastic scattering, some of the energy of the incident particle is lost or increased. During inelastic scattering, the incident particle interacts with the target nucleus, leading to the formation of a compound nucleus. The compound nucleus then emits a particle of lower kinetic energy, causing the original nucleus to be left in an excited state. The nucleus will emit this excess energy in the form of γ-emissions to reach its ground state.

The theoretical and experimental study of cluster radioactivity has been discussed in detail, in the section below.

1.2 Cluster Radioactivity

The studies of radioactive decay have contributed immensely to the understanding of nuclear structure. In 1896, Henri Becquerel discovered radioactivity, and later, Curie's in 1898 were confirmed the discovery. Radioactivity, or nuclear decay, refers to the process by which an unstable atomic nucleus losses energy by emitting radiation. The first observation of the atomic nucleus was obtained by studying radioactivity at the beginning of the twentieth century. Early experiments on radioactivity revealed the existence of three modes of radioactive decay: alpha-decay, beta-decay, and gamma-decay. In 1940 [23], another type of radioactive decay was discovered, where unstable nuclei of heavier elements spontaneously split into two nearly equal nuclei, known as spontaneous fission. Furthermore, in 1980, Sandulescu, Poenaru, and Greiner [24, 25] theoretically proposed yet another type of radioactive decay called cluster radioactivity. The phenomenon of Cluster radioactivity (CR) is the spontaneous emission of fragments heavier than alpha particles and lighter than the lightest fission fragments. In this decay process, a parent nucleus (A, Z) (with A as the mass number and Z as the atomic number) breaks into two segments: the associated daughter (A_1, Z_1) and the emitted cluster (A_2, Z_2) (where A

$= A_1+A_2$; Z=Z_1 +Z_2; with A_i, Z_i (i=1,2) as the mass number and the atomic number of the daughter nuclei and emitted cluster, respectively). The term cluster radioactivity was wrought in the same way that proton decay from nuclei was defined as proton radioactivity, alpha particle decay from nuclei was defined as alpha radioactivity. In the same way, cluster decay from nuclei has been defined as cluster radioactivity.

In figure 1.2, a chart of cluster emitters has been given by associating to each emitter

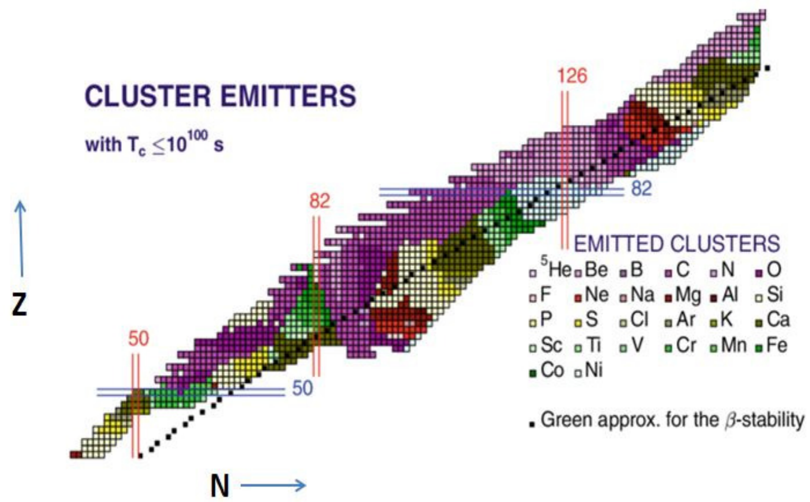

Figure 1.2: Chart of cluster emitters with half-lives up to 10^{100}s [26].

only the most probable emitted cluster. Three islands for cluster radioactivity have been identified: one above ^{100}Sn (N = 50), another above N = 82, and the main island with daughter nuclei in the vicinity of ^{208}Pb (N = 126). These islands are determined by selecting measurable half-lives shorter than 10^{32}s and branching ratios relative to α-decay b $\geq 10^{-17}$.

1.2.1 A brief overview of earlier theoretical studies of cluster radioactivity

Poenaru *et al* [27] have predicted that all stable nuclei lighter than lead with atomic number (Z)>40 were in a meta stable state relative to spontaneous cluster decay, using an analytical super asymmetric fission model. These authors reported half-lives in the range of 10^{40}-10^{50}s for nuclei Z>62. Poenaru *et al* concluded that parent nuclei with Z>60 were expected to decay via clusters such as ^{12}C, ^{16}O, ^{30,32}Si, ^{48,50}Ca, and ^{68}Ni, with half-lives $T_{1/2}$ > 10^{40}s, resulting in the formation of daughter nuclei with Z=50-58 and

N=78-82.

Poenaru *et al.* [28] have calculated partial half-lives for the most probable cluster decay modes from nuclei with Z=52-122, using the analytical super asymmetric fission model (ASAFM) while considering the odd-even effect. The authors specifically selected nuclei for which the partial lifetime for cluster emission is $T_{1/2} < 10^{30}$s and the branching ratio relative to alpha decay b $> 10^{-18}$.

Poenaru, Greiner, and Gherghescu [29] have predicted a new region of proton-rich parent nuclei emitting by spontaneous cluster emission by using the ASAFM model. They calculated the half-lives and branching ratios for the decay of ^{12}C, ^{16}O, and ^{28}Si, as well as a few other cluster decays from nuclei with proton numbers in the range Z=56-64 and neutron numbers N=58-72. Their finding led them to conclude that cluster decay from isotopes of these proton-rich parent nuclei results in the formation of the doubly magic daughter nucleus, ^{100}Sn.

Gupta *et al.* [30] have calculated the possible exotic cluster decay modes of some stable nuclei in the region 50$<$ Z $<$82, utilizing a preformed cluster model (PCM). They have shown that some deformed nuclei in the neighborhood of spherical magic shell at Z=50 and 82 and the deformed stable shell at N=108 are very unstable against various heavy cluster decay modes. The authors reported predicted half-life results for the decays of $^{120}_{56}$Ba via ^{12}C and ^{16}O, and the decay of $^{186}_{80}$Hg via ^{8}Be, to be $T_{1/2} \sim 10^{22}$, 10^{26} and 10^{28} s, respectively.

In 1994, Satish *et al.* [31] have calculated cluster emissions of $^{112-120}$Ba nuclei using the PCM model. The ^{4}He, and ^{12}C emission from ^{112}Ba was found to be the most probable decay and with a half-life time $T_{1/2} \sim 10^{4}$ s. They predicted the lowest half-life value for the decay of ^{112}Ba via ^{12}C, highlighting the significance of the doubly magic ^{100}Sn daughter nucleus in the trans-tin region.

In 1995, Poenaru *et al.* [32] conducted a study on the influence of nuclear masses, radii and interaction potentials on the ^{12}C decay of the ^{114}Ba isotope. They demonstrated that the decay of ^{114}Ba via ^{12}C results in the formation of doubly magic daughter nuclei, specifically ^{100}Sn or its neighbouring isotopes.

Satish *et al* [33], in 1996, investigated cluster decays from neutron-rich ^{146}Ba, ^{152}Ce, ^{156}Nd, ^{160}Sm and ^{164}Gd by using the PCM model. They analyzed the shell effect in binding energies and the corresponding relative preformation probabilities, which indicated that the selected nuclei were stable against ^{4}He and ^{10}Be decay. Furthermore, for non-alpha-like metastable decays with (Q>0), they observed that the minimum half-life values were obtained for decays resulting in the formation of the doubly magic ^{132}Sn nucleus as the daughter nucleus.

In 1997, Bonetti *et al* [34] have investigated the hindrance factors associated with the radioactive decay of ^{233}U via the emission of ^{4}He, ^{24}Ne and ^{28}Mg nuclei using the one-level R-matrix model. They found that by appropriately considering the internal wave function structure, a good agreement with the experimental for the decay via ^{4}He emission was achieved. The authors also made predictions for cluster decays involving ^{28}Mg, and ^{24}Ne, and observed a small experimental branching ratio between these two cluster decays.

In 2000, Santhosh *et al.* [35] have conducted a study on the half-lives of ^{12}C decay from Ba isotopes by considering the potential energy barrier as the sum of the Coulomb and proximity potential (CPPM). They calculated a half-life value of 6.020×10^3 s for the ^{12}C decay of ^{112}Ba, while the experimental value was found to be 5.620×10^3 s. The authors also determined that the emission of ^{12}C from ^{112}Ba was the most probable decay mode.

Santhosh *et al.* [36] have conducted a study where they predicted the logarithmic half-lives for ^{4}He, ^{8}Be, ^{12}C, ^{20}Ne, ^{24}Mg, and ^{32}S decay from various isotopes of the Nd parent using the CPPM model. They found that the predicted half-life for ^{16}O and ^{20}Ne emissions from ^{120}Nd isotopes had the lowest values ($T_{1/2} \approx 10^{10}$s). The authors emphasized the significance of the doubly magic ^{100}Sn daughter nucleus in the trans-tin region based on these conclusions. Additionally, Santhosh *et al.* have compared their predicted half-life values for different cluster decay modes with those values reported by Shanmugam *et al.* [37] using their CYEM model, Poenaru *et al.* [28] based on their ASAFM model, and Satish *et al.* [38] based on their PCM model.

In 2009, Sushil Kumar [39] have conducted a study on the decay of $^{118-132,140-170}$Ce nuclei. The investigation focused on the closed shell associated with the daughter nucleus Sn. The author reported that the half-lives of cluster decay were at a minimum when the neutron number of the daughter nucleus, N_d, was at 50 or 82 (corresponding to closed shell configuration). For the Oxygen cluster decay from the $^{118-132,140-170}$Ce isotopes, the minima of the decay half-life were observed at the magic numbers N_d=50 and 82. The study concluded that the minimum half-lives for cluster decay modes leading to ^{100}Sn and ^{132}Sn indicates the high stability of these nuclei against such cluster decay modes.

In 2010, Mehta *et al.* [40] have conducted a study on the magic numbers in neutron-rich nuclei using the relativistic mean field (RMF) model. The authors utilized the axially deformed RMF model with the NL3 parameter set. The focus of their investigation was on the calculation of magic numbers at proton/neutron numbers N=Z=28 and N=32 and 40 near the neutron drip line in Calcium (Ca) and Nickel (Ni) isotopes. The study revealed that the magicity at N = 28, 40 and 50 was re-established by the RMF study with NL3 parameter, indicating the persistence of these magic numbers in neutron-rich nuclei.

In their study, G. Shiva *et al.* [41] have focused on investigating the logarithmic half-lives of various neutron-rich parent nuclei ($56 \leq Z \leq 64$) undergoing decay through alpha-like and non-alpha-like clusters in the trans-tin region. The authors employed the CPPM model to calculate the half-lives and compared them with the results obtained using the UNIV and UDL formulas. They also compared their findings with the half-lives calculated by Kumar *et al.* [33] using the PCM model, Santhosh *et al.* [42] using the CPPM model, Sheng *et al.* [43] using Effective liquid drop model (ELDM), and Kumar [44] using the PCM model. The authors reported that there was a similar trend among these studies. They highlighted the neutron-proton asymmetry in the parent and daughter nuclei as a potential factor contributing to higher half-life values in the case of decay leading to ^{132}Sn. The authors concluded that their findings emphasized the significance of the doubly magic daughter nuclei ^{132}Sn in cluster radioactivity and confirmed the existence of nuclear shell structure.

In their study, Santhosh *et al* [45] focused on investigating the role of neutron magicity in cluster radioactivity. They employed the CPPM model to examine the cluster decay half-lives of ^{15}N from $^{206-230}$Ac, ^{23}F from $^{212-238}$Pa, ^{25}Ne from $^{217-240}$U and ^{29}Mg from $^{217-239}$U. The obtained results were compared with values obtained from the UNIV, UDL, and Scalling law of Horoi. The study revealed the significance of the doubly magic daughter nucleus ^{208}Pb in cluster radioactivity. Furthermore, it was evident that the role of neutron shell closure was more crucial than proton shell closure in this phenomenon.

In their study conducted in 2012, Bao *et al.* [46] focused on investigating the half-lives of C, O, Ne, Mg and Si decay from parent nuclei in the trans-lead region. They employed the generalized liquid-drop model (GLDM) to treat the cluster decay process as a highly asymmetric spontaneous fission. The half-lives of cluster decay modes were evaluated using the WKB barrier-penetration probability, taking into account various factors such as the nuclear proximity energy, mass asymmetry, accurate nuclear radius, phenomenological pairing correction, and microscopic shell corrections. They have concluded that the cluster decay half-lives appear to be a minimum for the decay leading to the doubly magic daughter nuclei $^{208}_{82}$Pb. Indeed the maximum binding energy of one fragment leads to a maximum Q-value for the cluster decay. They have mentioned that calculated results match well with the experimental data.

In 2013, Santhosh *et al.* [47] have calculated the stability of isotopes $^{248-254}$Cf against alpha and cluster decay using the CPPM model. These authors have found that these nuclei are stable against light cluster emission but unstable against heavy cluster emissions ($A_2 \geq 40$). They mentioned that heavy cluster emissions from these nuclei result in the formation of the doubly magic ^{208}Pb daughter nucleus or a neighbouring one. The authors concluded that, in most cluster decays, the half-lives decrease with the inclusion of quadrupole deformation (β_2) because it reduces the width and height of the barrier. Additionally, the inclusion of hexadecapole deformation has no influence on half-life time.

Ismail *et al.* [48] have investigated decay half-lives and preformation probabilities for a set of 304 cluster emitters in the range $87 \leq Z \leq 96$ and a set of 390 α-emitters in the range $52 \leq Z \leq 120$ by using Wentzel-Kramers-Brillouin (WKB) approximation. The authors checked the validity of this approach against CPPM by comparing logarithmic half-lives and barrier penetration probabilities. They concluded that the low values of the cluster decay half-lives at $N = 126$ reveal the role of neutron magicity. They mentioned that their results are found to be in good agreement with CPPM calculations and with the available experimental data.

Deepthy *et al.* [49] have investigated the ^{4}He, ^{12}C, ^{16}O, ^{20}Ne and ^{24}Mg decays from proton-rich platinum isotopes within the framework of the effective liquid drop model. The authors have concluded that ^{4}He decay from ^{166}Pt isotopes is the most probable decay mode. Additionally, ^{12}C decay from ^{166}Pt is the most probable decay mode in Pt isotopes, since it has the minimum logarithmic half-life. The authors have predicted the shell closure effect for ^{16}O, ^{20}Ne, and ^{24}Mg decays at N_d=82, which is a magic number.

In 2020, Yonghao *et al.* [50] have investigated the possibility of cluster radioactivity (CR) in the neutron-deficient nuclei of the trans-tin region. They utilized the ELDM, GLDM, and several analytical formulas for the analysis. The authors found that the presence of a Q-value shell effect (shell closure) at N_d=50 (^{100}Sn) has an influences on the half-lives. They also mentioned that the daughter nuclei with N_d=50 exhibit the minimum cluster decay half-lives. Additionally, they reported that the half-lives of α-like cluster decay leading to isotopes with N_d=50 are easier to measure compared to non α-like decays.

In 2022, Joshua *et al.* [51] have evaluated cluster decay half-lives for even-even isotopes $^{112-122}$Ba in both ground and intrinsic excited states along the proton drip line. They calculated the decay half-lives using the performed-cluster decay model (PCM) and determined the penetration probability from the interaction potential using the Wentzel-Kramers-Brillouin (WKB) approximation. The authors reported that the minimum decay half-lives for cluster decay of ^{12}C from $^{112-122}$Ba isotopes were obtained for decays leading to daughter nuclei ^{100}Sn. Furthermore, they found that the inclusion of excitation does not dominate or rule out the role of magicity. The authors concluded that the calculated decay half-lives for both the relativistic R3Y NN potential and M3Y potential are in reasonable good agreement with the experimental lower limit of ^{114}Ba.

1.2.2 A Brief Overview of the Experimental Investigation of Cluster Radioactivity

The cluster decay was first observed experimentally via the spontaneous emission of ^{14}C from the decay of ^{223}Ra by Rose and Jones [52] in 1984 at Oxford University by using a solid state counter telescope. The branching ratio for ^{14}C decay relative to alpha decay from ^{223}Ra is $(8.5 \pm 2.5)\times10^{-10}$, corresponding to a reduced width (preformation probability) smaller by a factor of $\sim 10^5$ to 10^6. This means that $(8.5 \pm 2.5)\times10^{-10}$ carbon nuclei are emitted for one alpha particle. Aleksandrov *et al* [53] have confirmed the observation of spontaneous emission of ^{14}C decay from ^{223}Ra parent isotopes. In this decay branching ratio $(7.6 \pm 3.0)\times10^{-10}$ for ^{14}C decay relative to alpha decay. They utilized a ΔE-E detection system to investigate the emitted ^{14}C from the source. subsequently, the discovery was further corroborated by S. Gales *et al* [54] and Price *et al* [55].

Table 1.2: Experimental results of Cluster Radioactivity.

Parent nuclei	**Emitted cluster**	**Daughter nuclei**	**Q-value (MeV)**	**Log $T_{1/2}^{Expt.}$ (s)**	**Branching ratio**	**Reference**
^{114}Ba	^{12}C	^{102}Sn	18.3 - 20.5	>3.63	$< 10^{-4}$	[56]
^{114}Ba	^{12}C	^{102}Sn	18.3 - 20.5	>4.10	3.4×10^{-5}	[57]
^{221}Fr	^{14}C	^{207}Tl	31.28	14.52	$(8.14 \pm 1.14)10^{-13}$	[58]
^{221}Ra	^{14}C	^{207}Pb	32.39	13.39	$(1.15 \pm 0.91)10^{-12}$	[58]
^{222}Ra	^{14}C	^{208}Pb	33.05	11.01	$(3.7 \pm 0.6)10^{-10}$	[55]
^{222}Ra	^{14}C	^{208}Pb	33.05	11.09	$(3.1 \pm 1.0)10^{-10}$	[59]

(Continued on next page)

Table 1.2 – continued from previous page

Parent nuclei	**Emitted cluster**	**Daughter nuclei**	**Q-value (MeV)**	**Log $T_{1/2}^{Expt.}$ (s)**	**Branching ratio**	**Reference**
^{222}Ra	^{14}C	^{208}Pb	33.05	11.22	$(2.3 \pm 0.3)10^{-10}$	[60]
^{223}Ra	^{14}C	^{209}Pb	31.85	15.06	$(8.5 \pm 2.5)10^{-10}$	[52]
^{223}Ra	^{14}C	^{209}Pb	31.85	15.25	$(5.5 \pm 2.0)10^{-10}$	[54]
^{223}Ra	^{14}C	^{209}Pb	31.85	15.11	$(7.6 \pm 3.0)10^{-10}$	[53]
^{223}Ra	^{14}C	^{209}Pb	31.87	15.20	$(6.1 \pm 1.0)10^{-10}$	[55]
^{223}Ra	^{14}C	^{209}Pb	31.85	15.32	$(4.7 \pm 1.3)10^{-10}$	[61]
^{223}Ra	^{14}C	^{209}Pb	31.85	15.19	$(6.4 \pm 0.4)10^{-10}$	[60]
^{223}Ra	^{14}C	^{209}Pb	31.85	15.14	$(7.0 \pm 0.4)10^{-10}$	[62]
^{223}Ra	^{14}C	^{209}Pb	31.85	15.04	$(8.9 \pm 0.4)10^{-10}$	[63, 64]
^{224}Ra	^{14}C	^{210}Pb	30.54	15.86	$(4.3 \pm 1.2)10^{-11}$	[55]
^{224}Ra	^{14}C	^{210}Pb	30.54	15.68	$(6.5 \pm 1.0)10^{-11}$	[62]
^{225}Ac	^{14}C	^{211}Bi	30.48	17.16	$(6.0 \pm 1.3)10^{-12}$	[65]
^{226}Ra	^{14}C	^{212}Pb	28.21	21.19	$(3.2 \pm 1.6)10^{-11}$	[59]
^{226}Ra	^{14}C	^{212}Pb	28.21	21.24	$(2.9 \pm 1.0)10^{-11}$	[66]
^{226}Ra	^{14}C	^{212}Pb	28.21	21.34	$(2.3 \pm 0.8)10^{-11}$	[67]
^{228}Th	^{20}O	^{208}Pb	44.72	20.72	$(1.13 \pm 0.22)10^{-13}$	[68]
^{231}Pa	^{23}F	^{208}Pb	51.84	26.02	$(9.97^{+22.9}_{-8.28})10^{-15}$	[69]
^{230}U	^{22}Ne	^{208}Pb	61.59	>18.20	$(4.8 \pm 2.0)10^{-14}$	[70, 71]
^{230}U	^{22}Ne	^{208}Pb	61.58	20.14	$(1.3 \pm 0.8)10^{-14}$	[72]
^{230}Th	^{24}Ne	^{206}Hg	57.78	24.61	$(5.6 \pm 1.0)10^{-13}$	[73]
^{232}Th	^{24,26}Ne	^{208,206}Hg	55.62,55.97	>29.20	$< 2.82 \times 10^{-12}$	[74]
^{231}Pa	^{24}Ne	^{207}Tl	60.42	23.23	6×10^{-12}	[75]
^{231}Pa	^{24}Ne	^{207}Tl	60.42	22.88	$(1.34 \pm 0.17)10^{-11}$	[69]
^{232}U	^{24}Ne	^{208}Pb	62.31	21.08	$(2.0 \pm 0.5)10^{-12}$	[76]
^{232}U	^{24}Ne	^{208}Pb	62.31	20.42	$(8.68 \pm 0.93)10^{-12}$	[77]
^{232}U	^{24}Ne	^{208}Pb	62.31	20.40	$(9.16 \pm 1.10)10^{-12}$	[78]
^{233}U	^{24,25}Ne	^{209,208}Pb	60.50,60.75	24.83	$(7.5 \pm 2.5)10^{-13}$	[73]
^{233}U	^{24,25}Ne	^{209,208}Pb	60.50,60.75	24.84	$(7.2 \pm 0.9)10^{-13}$	[79]
^{234}U	^{24,26}Ne	^{210,208}Pb	58.84,59.47	25.92	$(9.06 \pm 6.60)10^{-14}$	[78, 80]
^{234}U	^{24,26}Ne	^{210,208}Pb	58.84,59.47	25.88	$(9.90 \pm 9.90)10^{-14}$	[78, 81]
^{235}U	^{24,25}Ne	^{211,210}Pb	57.36,57.83	27.42	$(8.06 \pm 4.32)10^{-12}$	[78, 81]
^{236}U	^{24,26}Ne	^{212,210}Pb	55.96,56.75	>25.90	$< 9.2 \times 10^{-12}$	[81]
^{232}U	^{28}Mg	^{204}Hg	74.32	>22.26	$< 1.18 \times 10^{-13}$	[77]

(Continued on next page)

Table 1.2 – continued from previous page

Parent nuclei	**Emitted cluster**	**Daughter nuclei**	**Q-value (MeV)**	**Log $T_{1/2}^{Expt.}$ (s)**	**Branching ratio**	**Reference**
^{233}U	^{28}Mg	^{205}Hg	74.24	>27.59	2.0×10^{-13}	[79]
^{234}U	^{28}Mg	^{206}Hg	74.13	27.54	$(2.3^{+0.8}_{-0.6})10^{-13}$	[81]
^{234}U	^{28}Mg	^{206}Hg	74.13	25.14	$(1.38 \pm 0.25)10^{-13}$	[80]
^{235}U	^{28,29}Mg	^{207,206}Hg	72.20,72.61	>28.09	$< 1.8 \times 10^{-12}$	[81]
^{236}U	^{28,30}Mg	^{208,206}Hg	71.69,72.51	27.58	2.0×10^{-14}	[82]
^{237}Np	^{30}Mg	^{207}Tl	75.02	>26.93	$< 8.0 \pm 10^{-14}$	[73]
^{237}Np	^{30}Mg	^{207}Tl	75.02	>27.97	$< 1.8 \times 10^{-14}$	[83]
^{236}Pu	^{28}Mg	^{208}Pb	79.67	21.67	2.0×10^{-14}	[84]
^{236}Pu	^{28}Mg	^{208}Pb	79.67	21.52	$(2.7 \pm 0.7)10^{-14}$	[85]
^{238}Pu	^{28,30}Mg	^{210,208}Pb	75.93,77.03	25.70	$(5.62 \pm 3.97)10^{-17}$	[86]
^{238}Pu	^{32}Si	^{206}Hg	91.21	25.27	$(1.38 \pm 0.50)10^{-16}$	[86]
^{240}Pu	^{34}Si	^{206}Hg	90.95	>25.52	$< 6 \times 10^{-15}$	[87]
^{241}Am	^{34}Si	^{207}Tl	93.84	>22.71	$< 2.6 \times 10^{-13}$	[88]
^{241}Am	^{34}Si	^{207}Tl	93.84	>24.41	$< 5.4 \times 10^{-15}$	[73]
^{241}Am	^{34}Si	^{207}Tl	93.84	>25.26	$< 7.4 \times 10^{-16}$	[78]
^{242}Cm	^{34}Si	^{208}Pb	96.53	23.15	$< 1.0 \times 10^{-16}$	[89]

The experimental observation of clusters, such as ^{14}C, ^{20}O, ^{24}Ne, ^{28}Mg, and ^{32}Si, decaying into daughter nuclei in trans-lead region, either the doubly magic ^{208}Pb or its neighbors, has been documented [52, 90, 91]. Furthermore, predictions indicate the existence of another cluster radioactivity (CR) island in the trans-tin region, where clusters decay into the daughter nuclei close to the doubly magic nucleus ^{100}Sn [92]. The detection of heavier clusters, such as ^{24}Ne from ^{231}Pa, ^{233}U and ^{230}Th, were detected by Sandulescu *et al* [73, 79, 93, 94] in Dubna. Bonetti *et al* [71] experimentally investigated the spontaneous emission of neon clusters (^{22}Ne and ^{24}Ne) from ^{230}U isotopes using glass track detectors. Various experimental groups worldwide have reported the observation of ^{14}C decay in ^{221}Fr, $^{221-224,226}$Ra and ^{225}Ac; ^{20}O decay in ^{228}Th; ^{23}F decay in ^{231}Pa; ^{24}Ne decay in ^{230,232}Th, ^{231}Pa and $^{232-236}$U; ^{28}Mg decay in $^{232-236}$U, ^{237}Np, and ^{236,238}Pu; ^{30}Mg decay in ^{238}Pu; ^{32}Si decay in ^{238}Pu, and ^{34}Si decay of ^{238,240}Pu, ^{241}Am, and ^{242}Cm. These findings are compiled in Table 1.2.

1.3 Theoretical models

1.3.1 Relativistic mean field model

The self-consistent mean field (SCMF) model has indeed been successful in describing many nuclear properties across the nuclear chart from proton to neutron drip-line. In 1970s, a significant improvement was made by introducing the relativistic concept into the mean-field model, based on earlier ideas of Teller and Duerr [95, 96]. Walecka [97, 98] and Brockmann [99, 100] performed actual calculations and laid the foundation of the relativistic approach in nuclear physics. This model is based on the relativistic mean field approximation and provides a microscopically consistent, and relatively simple treatment of the nuclear many-body problem via adjustment of the model parameters, coupling constants, and effective mass to the global properties of the nuclei on the stability line. Notably, this model does not require further parameter fitting for nuclei located away from the stability line. One of the advantages of the relativistic mean field model is its ability to describe the properties of the entire nuclear chart, ranging from light nuclei to super-heavy nuclei. The nucleonic and mesonic degrees of freedom are clearly included from the beginning in the relativistic framework. The Relativistic Mean Field Model (RMF) can reproduce the densities and binding energies for finite nuclear matter and also yield spin-orbit interaction automatically in nuclei. Although the ground state properties of nuclei with the non-relativistic density-dependent Hartree-Fock (DDHF) calculations using Skyrme forces are comparable to RMF model, the RMF results are found to have a slight edge over DDHF. The detailed formalism of the relativistic mean-field model is discussed in Chapter 2 of this thesis work.

1.3.2 The Cluster Radioactivity

Before the experimental conformation of cluster radioactivity (CR) by Rose and Jones in 1984, it was first theoretically predicted in 1980 by Sandulescu, Poenaru, and Greiner based on Quantum Mechanical Fragmentation Theory (QMFT). In the early 1970s, Gupta, Scheild, Sandulescu and Greiner [101, 102, 103] investigated the cold reaction (fusion or fission) valley for trans-actinides. Sandulescu *et al.* employed two limiting approaches to predict this new decay mode. The first approach involves super-asymmetric fission, which is a dynamical mass fragmentation process. The second approach is strongly asymmetric two-body fragmentation, similar to α-decay, where the heavy cluster is emitted through

a barrier.
The phenomenon of cluster radioactivity has been explained by making use of many theoretical models and approaches. In general, there exist two types of approaches for predicting new decay modes. In the first kind of approach, the clusters made of several nucleons are performed in the parent nucleus before it penetrates the nuclear interaction barrier [104, 105, 106]. The exponential dependence of the calculated tunneling probability thus calculated leads to a modified Geiger-Nutall law of cluster radioactivity of the particular cluster emission, relating half-lives for CR to the Q value of the reaction. These approaches are commonly referred to as the Preformed cluster model. The parent nucleus is assumed to be deformed continuously and reaches the saddle or scission shape to undergo cluster radioactivity [36, 94, 107]. In This approach, Gamow's idea of quantum mechanical barrier penetration is still used, but without worrying whether the cluster is performed within the parent nucleus or not. Here, the parent nucleus is assumed to undergo continuous dynamical changes from an initial one-nucleus system to final separated multi-nucleus systems as it penetrates the nuclear potential barrier and reaches the saddle configuration, where both the masses and charges of the fission fragments remain fixed. These approaches are generally known as Unified Fission Models (UFM) [108]. In this approach, the effective liquid drop model (ELDM) is chosen as a fission-like model. A detailed discussion of the ELDM model is presented in Chapter 2.

1.4 Motivation to take up the present work

The primary aim of reliable theoretical models in nuclear physics is to explain the available experimental results and estimate the properties of the atomic nuclei throughout the nuclear chart. But, all the experimental observations of nuclear reaction and nuclear decay modes available in the literature could not be explained accurately by a single theoretical model. So, there is still a large scope for further progress both from the theoretical as well as experimental study. The present work is primarily motivated by theoretical study.

The calculated results reported were based on several theoretical models and many empirical formulas proposed earlier. However, there is still a large scope for investigating new decay modes of various parent nuclei in different regions which are experimentally practicable. Moreover, the selection of the most favorable decay modes from an isotope of a parent nucleus is of paramount importance in the experimental analysis of cluster radioactivity phenomena.

In this thesis, we have used the RHB model to calculate bulk properties such as binding energy, charge radius, and the total reaction cross section with light and medium mass nuclei as a projectile on ^{12}C and proton as targets at different energies using the Glauber model. We studied the significance of the doubly magic daughter nucleus ^{100}Sn (N_d= 50) and the role of shell effects in trans-tin cluster radioactivity. The logarithm of half-lives was calculated for various clusters decay modes, including ^{8}Be, ^{12}C, ^{16}O, ^{20}Ne, and ^{24}Mg, originating from various isotopes of trans-tin and transition metal regions. These half-lives were calculated using the ELDM model, UDL, and Horoi formula for cluster radioactive decay. The Geiger-Nuttal plots for different cluster emissions were studied. Additionally, the significance of the doubly magic daughter nucleus ^{208}Pb (N_d= 126) and nuclear shell effects in Th, U, and Pu isotopes were investigated. We examine the structural properties of these isotopes using the relativistic mean field formalism with NL3* force parameters. The α-decay and cluster decay half-lives of the considered isotopes were systematically calculated, utilizing the Q-values obtained from the RMF (NL3*) formalism. Furthermore, We predicted the half-lives of possible nuclei undergoing two-proton radioactivity within the range of $30 \leq Z \leq 40$, as determined by the RMF (NL3*) model.

1.5 Plan of the thesis

The thesis is organized as follows:

In Chapter 2, mathematical details of the model employed, including the Relativistic Hartree Bogoliubov model with density-dependent meson exchange (DD-ME2), density-dependent point coupling (DD-PC1) parameter sets, the non-linear NL3* parameter set in the Relativistic Mean-field (RMF) model, and the Glauber model, are given. A detailed description of the effective liquid drop (ELDM) model, as well as other empirical formulas such as Universal Decay Law (UDL), Tavares-Medeiros (TM), Viola-Seaborg (VS), and Horoi formula, for calculating alpha decay, cluster decay and proton radioactivity, has also been presented in brief.

In Chapter 3, we present the results related to the nuclear reaction studies of He, Li, Be, B, C, Ca, Ni, Zr, and Sn isotopes on ^{12}C and proton targets. First of all, calculate microscopic nuclear densities for these isotopes with relativistic Hartree-Bogoliubov (RHB) formalism. Further, other ground-state bulk properties are also calculated and compared with the available experimental data. A detailed study of reaction cross-sections and differential elastic scattering cross-sections at various incident energies are presented. We found that the total nuclear reaction cross-section increased as a function of the mass number for both the target and projectile nuclei. The elastic scattering angular distributions are calculated for various systems at different energies. It has been observed that the results obtained using the relativistic framework with the DD-ME2 parameter set are in better agreement with the experimental data in comparison with the results obtained with the DD-PC1 parameter set.

In Chapter 4, we studied the cluster radioactivity in the trans-tin region for ($^{106-116}$Xe, $^{108-120}$Ba, $^{114-126}$Ce, and $^{118-128}$Nd) and in transition metal region for ($^{156-166}$Hf, $^{158-172}$W, $^{160-174}$Os, $^{166-180}$Pt, and $^{170-182}$Hg) nuclei. These half-lives have been calculated using the shape parametrization model of cluster decay in conjunction with the axially deformed relativistic mean-field (RMF) model with the NL3* parameter set. It has been observed that in the trans-tin region, the minimum cluster decay half-lives are found at nearly doubly magic or doubly magic daughter ^{100}Sn nucleus ($N_d = 50$, N_d is the neutron number of the daughter nucleus) and in transition metal region at $N_d = 82$, which is a magic number.

In Chapter 5, we have examined the binding energy per nucleon, RMS radii, and two-neutron separation energies (S_{2n}) for the Th, U, and Pu isotopes using the relativistic mean field (RMF) model with NL3* force parameter set. The most stable isotopes are found to be at N $\sim$ 126 (^{216}Th, ^{218}U, and ^{220}Pu) in Th, U, and Pu isotopes, respectively. Also, the alpha and cluster decay half-lives are carried out by the ELDM model and compared with the results obtained by the latest empirical relations, namely Universal Decay Law (UDL), Tavares- Medeiros (TM), Viola-Seaborg (VS), and the Scaling Law given by Horoi et al., are found to be in good agreement. Our study reveals the role of nearly doubly magic or doubly magic daughter ^{208}Pb nucleus ($N_d = 126$, N_d is the neutron number of the daughter nucleus) in cluster decay processes.

In Chapter 6, we have performed calculations to study the ground-state properties, i.e., binding energy per nucleon and two-proton separation energy of Fe, Ni, Zn, Ge, Kr, and Zr isotopes by using the relativistic mean-field (RMF) approach with force parameter NL3*. The obtained results are in excellent agreement with the available experimental data. We have also performed systematic studies of the two-proton ($2p$) radioactivity, the two-proton decay energy (Q_{2p}) using the RMF (NL3*) approach, the finite-range droplet model (FRDM), and the Weizsacker-Skyrme-4 (WS4). Then, the effective liquid drop model (ELDM) is applied to find out the two-proton decay half-lives using three kinds of evaluated Q_{2p} values. The two-proton decay half-lives calculations are also carried out by using empirical formulas, namely Liu and Sreeja, and their comparisons with ELDM results are found to be in agreement. Also, we predict the half-lives of possible nuclei of the two-proton radioactivity in the range $30 \leq Z \leq 40$ with released energy $Q_{2p} > 0$ obtained by RMF (NL3*) model. The estimated results reveal a clear linear connection between the logarithmic two-proton decay half-lives $log_{10}T_{1/2}$ and Coulomb parameters $[(\mathrm{Z}_d^{0.8} + l^{0.25})\ \mathrm{Q}_{2p}^{-1/2}]$.

In Chapter 7, the summary of the thesis work and the future outlook of the thesis have been presented.

Chapter 2

Mathematical Formalism

2.1 Introduction

Many theoretical models have been constructed to find out the structure of nuclear systems throughout the nuclear chart. Among them, the relativistic mean field (RMF) model has been quite successful and has been used to investigate bulk properties, including the density distribution of the nucleus, over the last few decades. In this model, the many-body system is converted into a one-body problem, and pairing correlations are incorporated to achieve an acceptable level of accuracy. The RMF model was developed within the framework of quantum hadrodynamics (QHD). The pairing correlation is taken care of using the Bardeen-Cooper-Schrieffer (BCS) approach.

The Glauber approach is used to study the total reaction cross-section for reactions between projectile and target nuclei. At intermediate energies, the reaction cross-section reflects the geometrical size of the nucleus. The projectile nucleus is supposed to be a core nucleus plus one valence nucleon (core + one nucleon) system. We have to fit the core and target densities in terms of a combination of Gaussians. This model is a microscopic reaction theory of high-energy collision based on the eikonal approximation and the bare nucleon-nucleon interaction.

Cluster radioactivity can be studied using two main approaches; performed Cluster Model and the fission-based approach. The ELDM (fission based) is a successful model for studying two-proton radioactivity, α-decay, and cluster radioactivity. In this model, the nucleus is assumed to be deformed continuously and reach the saddle or scission configuration to undergo cluster radioactivity. By using different combinations of the inertia coefficients and mass transfer descriptions, the experimental half-lives of these decay modes, such as alpha and cluster decay, could be reproduced well. A large number of empirical formulas with various coefficients for half-live calculations are discussed in this chapter. In the present thesis, these theoretical models have been taken and used to analyze the nuclear system. This chapter presents a detailed discussion of the relativistic mean field model along with the Glauber theory, and an effective liquid drop model for half-lives calculation is provided below.

2.2 Relativistic mean field model

The Relativistic Mean Field (RMF) model has been successfully applied to study the structural properties of nuclei throughout the nuclear chart [98, 109, 110, 111]. In 1951, the relativistic field model was first introduced by Schiff [112]. In this theory, he had incorporated non-linear and linear self-interaction in the classical neutral scalar meson field. In 1955, Johnson and Teller made significant modifications to the Schiff theory by introducing the linear interaction of the scalar field, which explained several empirical characteristics of nuclear structure [95]. Rozsnayi in 1961 performed the relativistic Hartree calculations of finite nuclear structure. The complete form of the RMF model was introduced in 1974 by Walecka [97, 98], incorporated σ, ω, and ρ mesons to describe the finite and infinite systems. In the last few decades, the RMF model has been successfully applied to study the properties of both infinite nuclear matter and finite nuclei. The ground state properties such as binding energy, matter radii, charge radii, density profile, etc. have been calculated by the relativistic mean-field theory, and excellent agreement has been found with experimental results. The relativistic mean-field (RMF) theory has the advantage that, with proper relativistic kinematics and with the mesons and their properties already known or fixed from the properties of a few finite nuclei, it gives better results for various ground-state properties. These include the binding energy, root mean square radii, and the quadrupole deformation, not only of spherical nuclei but also of deformed nuclei lying close to the β-stability line, as well as for the nuclei lying away from the β-stability line [10, 109, 113, 114].

The starting point of the Relativistic Mean Field (RMF) model is the effective Lagrangian containing the nucleonic and mesonic degrees of freedom. This model is a phenomenological model of the nuclear many-body problem, which is based on some primary aspects: (1) Nucleons are considered as point-like particles, (2) The rule of Relativity and causality are strongly taken into account, (3) The theory is fully lorentz invariant, (4) The particles move independently in mean fields which originate from nucleon-nucleon interactions. Under these conditions, the nucleons are treated as Dirac spinors ψ. The effective point-like particles are called mesons Φ_j, where j stands for σ, ω, ρ and photon fields. The π-meson is not taken into the relativistic mean field (Hartree) model because of its pseudo-scalar nature [110]. The details of the RMF model can be found in Refs.[111, 115]. The basic ingredient of the RMF model is the relativistic Lagrangian density functional for a nucleon-meson many-body system which is given as [10, 116, 117, 118, 119, 120]

$$\begin{aligned}\mathcal{L} = \overline{\psi_i}(i\gamma^\mu\partial_\mu - M)\psi_i + \frac{1}{2}\partial^\mu\sigma\partial_\mu\sigma - \frac{1}{2}m_\sigma^2\sigma^2 - \frac{1}{3}g_2\sigma^3 - \frac{1}{4}g_3\sigma^4 - g_\sigma\overline{\psi_i}\psi_i\sigma \\ -\frac{1}{4}\Omega^{\mu\nu}\Omega_{\mu\nu} + \frac{1}{2}m_\omega^2 V^\mu V_\mu + \frac{1}{4}c_3(V_\mu V^\mu)^2 - g_w\overline{\psi_i}\gamma^\mu\psi_i V_\mu - \frac{1}{4}\overrightarrow{B}^{\mu\nu}.\overrightarrow{B}_{\mu\nu} \\ +\frac{1}{2}m_\rho^2\overrightarrow{R}^\mu.\overrightarrow{R}_\mu - g_\rho\overline{\psi_i}\gamma^\mu\overrightarrow{\tau}\psi_i.\overrightarrow{R}^\mu - \frac{1}{4}F^{\mu\nu}F_{\mu\nu} - e\overline{\psi_i}\gamma^\mu\frac{(1-\tau_{3i})}{2}\psi_i A_\mu. \end{aligned} \quad (2.2.1)$$

Here σ, V_μ and $\overrightarrow{R}_\mu$ are the fields for isoscalar-scalar σ-meson, isoscalar-vector ω-meson, and isovector-vector ρ-meson, respectively. A^μ is the electromagnetic field. The ψ_i are the Dirac spinors for the nucleons whose third component of isospin is denoted by τ_{3i}. Here g_σ, g_ω, g_ρ and $e^2/4\pi = 1/137$ are the coupling constants for σ, ω, ρ mesons, and photons, respectively. g_2, g_3, and c_3 are the parameters for the nonlinear terms of σ and ω mesons. M is the mass of the nucleon and m_σ, m_ω and m_ρ are the masses of the σ, ω and ρ meson, respectively. $\Omega^{\mu\nu}$, $\overrightarrow{B}^{\mu\nu}$ and $F^{\mu\nu}$ are the field tensors for the V^μ, $\overrightarrow{R}^\mu$ and the photon fields A^μ, respectively [109, 114]:

$$\Omega^{\mu\nu} = \partial^\mu V^\nu - \partial^\nu V^\mu \quad (2.2.2)$$

$$\overrightarrow{B}^{\mu\nu} = \partial^\mu \overrightarrow{R}^\nu - \partial^\nu \overrightarrow{R}^\mu \quad (2.2.3)$$

$$F^{\mu\nu} = \partial^\mu A^\nu - \partial^\nu A^\mu \quad (2.2.4)$$

From the above relativistic Lagrangian, we get the Dirac equation for the nucleons and the Klein-Gordon type equations for mesons and photons. These obtained equations are solved by expanding the upper and lower components of the Dirac spinors (ψ) and the boson fields in an axially deformed harmonic oscillator basis with an initial deformation β_0. The total energy of the system is given by

$$E_{total} = E_{part} + E_\sigma + E_\omega + E_\rho + E_c + E_{pair} + E_{c.m.}, \quad (2.2.5)$$

where E_{part} is the sum of the single-particle energies of the nucleons and E_σ, E_ω, E_ρ, E_c, E_{pair}, $E_{c.m.}$ are the contributions of the meson fields, the Coulomb field, pairing energy and the center-of-mass energy, respectively, are given below.

$$\begin{aligned}
E_{part} &= \sum_{i=1}^{A} v_i^2 \int d^3r\psi_i^\dagger\{-i\overrightarrow{\alpha}.\overrightarrow{\nabla} + \beta M^* + V\}\psi_i \\
&= \sum_{i}^{A} v_i^2\varepsilon_i \\
E_\sigma &= \int d^3r\{\frac{1}{2}(\nabla\sigma)^2 + U\sigma\} \\
E_\omega &= -\int d^3r\frac{1}{2}\{(\nabla V_0)^2) + m_\omega^2 V_0^2 \\
E_\rho &= -\int d^3r\frac{1}{2}\{(\nabla \rho_0)^2) + m_\rho^2 \rho_0^2 \\
E_c &= -\int d^3r\frac{1}{2}(\nabla A_0)^2) \\
E_{c.m.} &= -\frac{3}{4}\hbar\omega_0 = -\frac{3}{4}41A^{-1/3}, \\
E_{pair} &= -G(\sum_{i=1}^{A} u_i v_i)^2.
\end{aligned}$$

The quadrupole deformation parameter β_2 is extracted from the calculated quadrupole moments of neutrons and protons through the following relation

$$Q = Q_n + Q_p = \sqrt{\frac{16\pi}{5}}\left(\frac{3}{4\pi}AR^2\beta_2\right), \tag{2.2.6}$$

where $R = 1.2A^{1/3}$. The charge radius is calculated using the following formula:

$$r_c = \sqrt{r_p^2 + 0.64}, \tag{2.2.7}$$

The factor 0.64 in Eq 2.2.7 accounts for the finite size effects of the proton.
The proton radius (r_p), neutron radius (r_n) and matter radius (r_m) are given as [10]

$$< r_p^2 >= \frac{1}{Z}\int \rho_p(r)r_p^2 d\tau_p, \tag{2.2.8}$$

$$< r_n^2 >= \frac{1}{Z}\int \rho_n(r)r_n^2 d\tau_n, \tag{2.2.9}$$

$$< r_m^2 >= \frac{1}{A}\int \rho(r)r^2 d\tau, \tag{2.2.10}$$

This model predicts good results in terms of binding energy, root mean square radius, and quadrupole deformation parameter, not only for stable nuclei but also for nuclei throughout the periodic table. This relativistic mean-field model, especially with the NL3 effective interaction (or with a slightly improved version, i.e., NL3* effective interaction), has provided an excellent description of many nuclear reactions and structural studies of spherical and deformed nuclei. The well-known NL3* parameter sets are presented in Table 2.1 [121]. This parameter set not only reproduces the properties of stable nuclei but also predicts those away from the valley of β-stability.

Table 2.1: The parameter sets of NL3* in the Lagrangian, masses in MeV, while g_2 is in fm^{-1}.

M = 939.00	m_ω = 782.60	m_ρ = 763.00	m_σ = 502.5742
g_σ = 10.0944	$g_\omega(\rho_{(sat)})$ = 12.8065	g_ρ = 4.5748	g_2 = -10.8093
g_3 = -30.1486	-	-	-

2.2.1 Pairing calculation in RMF formalism

In medium and heavy nuclei, pairing correlations play a very vital role in calculating the nuclear properties. The constant gap BCS model is valid for nuclei not too far from the valley of β-stability line. The BCS model may fail for light neutron-rich nuclei (which is not the case in this study; the nuclei selected here are not light neutron-rich nuclei), and the RMF value with BCS treatment should be credible. The pairing energy expression is given as

$$E_{pair} = -G\left[\sum_{i>0} u_i v_i\right]^2 \tag{2.2.11}$$

with G the pairing force constant, v_i^2 and $u_i^2 = 1 - v_i^2$ are the occupation probabilities [122, 123, 124, 125].

The variational procedure with respect to the occupation numbers v_i^2, gives the BCS equation

$$2\varepsilon_i u_i v_i - \Delta(u_i^2 - v_i^2) = 0 \tag{2.2.12}$$

and the gap Δ is defined as

$$\Delta = G\sum_{i>0} u_i v_i. \tag{2.2.13}$$

This is the BCS equation for pairing energy. The densities are contained within the occupation number

$$n_i = v_i^2 = \frac{1}{2}\left[1 - \frac{\varepsilon_i - \lambda}{\sqrt{(\varepsilon_i - \lambda)^2 + \Delta^2}}\right]. \tag{2.2.14}$$

The pairing energy is determined as

$$E_{pair} = -\Delta \sum_{i>0} u_i v_i. \tag{2.2.15}$$

The pairing energy E_{pair} depends on the occupation probabilities u_i and v_i. We use the constant gaps for proton and neutron, as given in [125, 126, 127]:

$$\Delta_p(MeV) = RB_s e^{sI-tI^2}/Z^{1/3} \tag{2.2.16}$$

and

$$\Delta_n(MeV) = RB_s e^{-sI-tI^2}/A^{1/3} \tag{2.2.17}$$

with R= 5.72 MeV, s=0.118, t=8.12, $B_s = 1$ and $I = (N-Z)/(N+Z)$. This type of prescription for pairing effects, both RMF and Skyrme-based approaches have already been used by us and many other authors [117]. For this pairing approach, it has been shown [117, 128] that the results for binding energies and quadrupole deformations are almost identical to the predictions of the relativistic Hartree-Bogoliubov (RHB) approach.

2.3 Relativistic Hartree-Bogoliubov model

The Density functional theory (DFT) is a successful method for understanding nuclear many-body dynamics. The Covariant density functional theory (CDFT) is based on energy density functionals (EDF) and has been highly successful in investigating various nuclear structure phenomena across the entire nuclear chart. The relativistic Hartree-Bogoliubov (RHB) model [129] is based on the density-dependent effective interactions. Density-dependent meson exchange [130] and point coupling interactions [131] are used for the analysis of nuclear structural phenomena. The key difference between these two models lies in the treatment of the interaction range, the meson, and the density dependence. These models are briefly discussed in the following subsections.

2.3.1 Meson-Exchange model

In the DD-ME2 model, the nucleus is described as a system of Dirac nucleons. These nucleons interact via the exchange of mesons with finite masses which leads to finite range interactions [121, 130, 132]. The isoscalar-scalar σ meson, the isoscalar-vector ω meson, and the isovector-vector ρ meson constitute the minimum set of meson fields for a quantitative description of nuclei. The Lagrangian density for the meson exchange model [98, 109, 133] can be written as:

$$\mathcal{L} = \mathcal{L}_N + \mathcal{L}_M + \mathcal{L}_{int}. \tag{2.3.18}$$

The Lagrangian density corresponding to free nucleon is denoted by $\mathcal{L}_N$ and takes

$$\mathcal{L}_N = \overline{\psi}[i\gamma_\mu\partial^\mu - m]\psi, \tag{2.3.19}$$

Where, m and ψ corresponds to bare nucleon mass and Dirac spinor respectively. The Lagrangian density for free mesons ($\mathcal{L}_M$) and electromagnetic fields ($\mathcal{L}_A$) are given as:

$$\mathcal{L}_\sigma = \frac{1}{2}(\partial_\mu\sigma\partial^\mu\sigma - m_\sigma^2\sigma^2), \tag{2.3.20}$$

$$\mathcal{L}_\omega = -\frac{1}{2}(\Omega_{\mu\nu}\Omega^{\mu\nu} - m_\omega^2\omega_\mu\omega^\mu), \tag{2.3.21}$$

$$\mathcal{L}_\rho = -\frac{1}{4}\overrightarrow{R}_{\mu\nu}.\overrightarrow{R}^{\mu\nu} + \frac{1}{2}m_\rho^2\overrightarrow{\rho_\mu}.\overrightarrow{\rho}^\mu, \tag{2.3.22}$$

$$\mathcal{L}_A = -\frac{1}{4}F_{\mu\nu}F^{\mu\nu}, \tag{2.3.23}$$

$\mathcal{L}_{int}$ is the interaction lagrangian between nucleons and mesons, given as:

$$\mathcal{L}_{int} = -g_\sigma\overrightarrow{\psi}\rho\psi - g_\omega\overrightarrow{\psi}\gamma_\mu\omega^\mu\psi - g_\rho\overrightarrow{\psi}\gamma_\mu\overrightarrow{\tau}\overrightarrow{\rho}^\mu\psi - e\overline{\psi}\gamma^\mu\psi A_\mu, \tag{2.3.24}$$

The Lagrangian density for DD-ME2 interaction is the sum of the Lagrangian density for free nucleon, Lagrangian density for the free mesons and electromagnetic fields and is expressed as

$$\begin{aligned}\mathcal{L} = \overline{\psi}[\gamma(\iota\partial - g_\omega\omega - g_\rho\overrightarrow{\rho}\overrightarrow{\tau} - eA) - m - g_\sigma\sigma]\psi + \frac{1}{2}(\eth\sigma)^2 - \frac{1}{2}m_\sigma^2\sigma^2 \\ -\frac{1}{4}\Omega_{\mu\nu}\Omega^{\mu\nu} + \frac{1}{2}m_\omega^2\omega^2 - \frac{1}{4}\overrightarrow{R}_{\mu\nu}.\overrightarrow{R}^{\mu\nu} + \frac{1}{2}m_\rho^2\overrightarrow{\rho}_\mu.\overrightarrow{\rho}^\mu - \frac{1}{4}F_{\mu\nu}F^{\mu\nu},\end{aligned} \tag{2.3.25}$$

where ψ is the Dirac spinor and m denotes the bare nucleon mass. m_σ, m_ω, and m_ρ are the masses of σ, ω and ρ mesons, respectively. g_σ, g_ω, and g_ρ and $\frac{e^2}{4\pi} = \frac{1}{137}$ are the coupling constants for the σ, ω and ρ mesons and photons, respectively. The $\overrightarrow{\tau}$ denotes the Pauli isospin matrices. $\Omega^{\mu\nu}$, $R^{\mu\nu}$, and $F^{\mu\nu}$ as field tensors of the vector field ω, ρ, and photon can be written:

$$\Omega^{\mu\nu} = \partial^\mu\omega^\nu - \partial^\nu\omega^\mu, \tag{2.3.26}$$

$$\overrightarrow{R}^{\mu\nu} = \partial^\mu\overrightarrow{\rho}^\nu - \partial^\nu\overrightarrow{\rho}^\mu, \tag{2.3.27}$$

$$F^{\mu\nu} = \partial^\mu A^\nu - \partial^\nu A^\mu. \tag{2.3.28}$$

We obtain the total energy by integrating the Hamiltonian density [110] over the r-space which depends on the Dirac spinors $\psi, \overline{\psi}$ and the meson fields $\sigma, \omega^\mu, \overrightarrow{\rho}^\mu, A^\mu$:

$$E_{RMF}[\psi, \overline{\psi}, \sigma, \omega^\mu, \overrightarrow{\rho}^\mu, A^\mu] = \int d^3 r H(r). \tag{2.3.29}$$

The coupling of σ-meson and ω-meson to the nucleon field [132, 133, 134] in the phenomenological approach is given by

$$g_i(\rho) = g_i(\rho_{sat}) f_i(x) \quad \text{for} \quad i = \sigma, \omega, \tag{2.3.30}$$

where

$$f_i(x) = a_i \frac{1 + b_i(x + d_i)^2}{1 + c_i(x + d_i)^2} \tag{2.3.31}$$

is a function of $x = \rho/\rho_{sat}$, and ρ_{sat} denotes the baryon density at saturation in symmetric nuclear matter. The eight real parameters in (Eq. 2.3.30) are not independent, but constrained as follows:

$$f_i(1) = 1, \quad f_\sigma^{"}(1) = f_\omega^{"}(1), \quad and \quad f_i^{"}(0) = 0 \tag{2.3.32}$$

These five constraints reduced the number of independent parameters to three. The three additional parameters in the isoscalar channel are $g_\sigma(\rho_{sat})$, $g_\omega(\rho_{sat})$, and m_σ , which is the mass of the phenomenological σ-meson. The asymmetric nuclear matter calculations [135] within the Dirac-Brueckner approach suggested the functional form of the density dependence of ρ-meson couplings as

$$g_\rho(\rho) = g_\rho(\rho_{sat}) e^{-a_\rho(x-1)}. \tag{2.3.33}$$

The isovector channel is parameterized by $g_\rho(\rho_{sat})$ and a_ρ. The eight independent parameters (seven coupling parameters and the mass of the σ meson) have been adjusted to reproduce the properties of symmetric and asymmetric nuclear matter and to ground-state properties of spherical nuclei. The DD-ME2 parameter set used in this study is presented in Table 2.2.

Table 2.2: The parameter sets of DD-ME2.

M=939.00	m$_\omega$=783.00	m$_\rho$=763.00	m$_\sigma$=550.124
g$_\sigma$($\rho_{(sat)}$)=10.5396	g$_\omega$($\rho_{(sat)}$)=13.0189	g$_\rho$($\rho_{(sat)}$)=3.6836	a$_p$=0.5647
a$_\sigma$=1.3881	a$_\omega$=1.3892	b$_\sigma$=1.0943	b$_\omega$=0.9240
c$_\sigma$=1.7057	c$_\omega$=1.4620	d$_\sigma$=0.4421	d$_\omega$=0.4775

2.3.2 Point-Coupling model

The point-coupling model represents an alternative formulation of the self-consistent RMF framework. The four Fermionic vertices with corresponding fields are given below which are used in the present study.
(1) The isoscalar-scalar $(\overline{\psi}\psi)^2$ correspond to σ-field
(2) The isoscalar-vector $(\overline{\psi}\gamma_\mu\psi)(\overline{\psi}\gamma^\mu\psi)$ correspond to ω-field
(3) The isovector-vector $(\overline{\psi}\overrightarrow{\tau}\gamma_\mu\psi)(\overline{\psi}\overrightarrow{\tau}\gamma^\mu\psi)$ correspond to ρ-field
(4) $\partial_\nu(....)\partial^\nu(....)$ are corresponding fields gradient couplings.
The effective Lagrangian for the density-dependent point coupling model that includes the isoscalar-scalar, isoscalar-vector, and isovector-vector four-fermion interactions are given by [131]

$$\begin{aligned}\mathcal{L} = \overline{\psi}(i\gamma.\partial - m)\psi - \frac{1}{2}\alpha_S(\widehat{\rho})(\overline{\psi}\psi)(\overline{\psi}\psi) - \frac{1}{2}\alpha_V(\widehat{\rho})(\overline{\psi}\gamma^\mu\psi)(\overline{\psi}\gamma_\mu\psi)\\ -\frac{1}{2}\alpha_{TV}(\rho)(\overline{\psi}\overrightarrow{\tau}\gamma^\mu\psi)(\overline{\psi}\overrightarrow{\tau}\gamma_\mu\psi) + \frac{1}{2}\delta_S(\partial_\nu\overline{\psi}\psi)(\partial^\nu\overline{\psi}\psi)\\ -e\overline{\psi}\gamma.A\frac{(1-\tau_3)}{2}\psi.\end{aligned} \tag{2.3.34}$$

It contains the Lagrangian density for free nucleons, point-coupling interaction terms, and the coupling of the proton to the electromagnetic field. Ten density-dependent constant parameters in this model are listed in Table 2.3, which controls the strength and density dependence of the interaction Lagrangian. The derivative terms in Eq. 2.3.34 account for the leading effects of finite range interactions that are crucial for a quantitative description of the nuclear properties. The total energy-density functional of RMF for the point-coupling model can be written as

$$E_{RMF}[\psi,\overline{\psi},A_\mu] = \int d^3r H(r), \tag{2.3.35}$$

where the Hamiltonian density $H(r)$ can be obtained from the Lagrangian density.
The functional form of the couplings is given by

$$\alpha_i(\rho) = a_i + (b_i + c_i x)e^{-d_i x}, \quad (i \equiv S, V, TV), \tag{2.3.36}$$

with $x = \rho/\rho_{sat}$, where ρ_{sat} denotes the nucleon density at saturation in symmetric nuclear matter.

2.3.3 RHB theory with a Pairing interaction

Pairing correlations are important to consider for a quantitative description of open-shell nuclei. The RHB model represents a relativistic extension of the conventional

Table 2.3: The parameter sets of DD-PC1.

M=939.00			
$a_s(fm^2)$=-10.04616	$b_s(fm^2)$=-9.15042	$c_s(fm^2)$=-6.42729	d_s=1.37235
$a_v(fm^2)$=5.91946	$b_v(fm^2)$=8.86370	d_v=0.65835	$b_{TV}(fm^2)$=1.83595
d_{TV}=0.64025	$\delta_s(fm^4)$=-0.8149		

Hartree-Bogoliubov framework in which mean-field and pairing correlations are treated self-consistently [110]. The RHB model gives a unified description of particle-hole (ph) and particle-particle (pp) correlations on a mean-field level by using the average self-consistent mean-field potential that encloses the long-range ph correlations and a pairing field potential which sums up the pp correlations. The density matrix in the presence of pairing is generalized to two densities, the normal density $\widehat{\rho}$, and pairing tensor $\widehat{k}$. The RHB energy-density functional can be written as

$$E_{RHB}[\widehat{\rho},\widehat{k}] = E_{RMF}[\widehat{\rho}] + E_{pair}[\widehat{k}]. \tag{2.3.37}$$

The pairing part of the RHB functional is given by

$$E_{pair}[\widehat{k}] = \frac{1}{4}\sum_{n_1 n_1'}\sum_{n_2 n_2'} k^*_{n_1 n_1'}\langle n_1 n_1'|V^{PP}|n_2 n_2'\rangle k_{n_2 n_2'}, \tag{2.3.38}$$

where $\langle n_1 n_1'|V^{PP}|n_2 n_2'\rangle k_{n_2 n_2'}$ are the matrix elements of the two-body pairing interaction and indices n_1, n_1', n_2 and n_2' denote quantum numbers that specify the Dirac indices of the spinor. The pairing interaction is taken in the form

$$V^{PP}(r_1, r_2, r_1', r_2') = -G\delta(R - R')P(r)P(r'), \tag{2.3.39}$$

where $R = \frac{1}{\sqrt{2}}(r_1 + r_2)$ and $r = \frac{1}{\sqrt{2}}(r_1 - r_2)$ represent the center of mass and the relative coordinates, and the form factor $P(r)$ is the Fourier transform of $p(k)$:

$$P(r) = \frac{1}{(4\pi a^2)^{3/2}} e^{-r^2/2a^2}. \tag{2.3.40}$$

The pairing force has a finite range and, because of the factor $\delta(R - R')$, it preserves the translational invariance. Finally, the pairing energy in the nuclear ground state is given by [136]

$$E_{pair} = -G\sum_N P_N^* P_N. \tag{2.3.41}$$

2.4 Reaction cross-section using Glauber model

The Glauber model has been applied to describe heavy ion collision at high energies. This model provides a quantitative consideration of the geometrical configuration of the nuclei when they collide. The basic assumption of the Glauber model is a minimal mean free path, which results in the projectile moving along a straight path along the collision direction and gives the nucleus-nucleus interaction in terms of interaction between the constituent nucleons and nuclear density distributions. One of the most important physical quantities characterizing nuclear reactions is the total reaction cross-section. The Glauber model can be studied using two types of approaches: the first one is known as the Optical limit approach, and the second type is the Monte Carlo eikonal approach. These approaches of the Glauber model are based on standard models that estimate the nucleus-nucleus interaction in terms of nucleon-nucleon interaction for a given density distribution of projectile and target nuclear system. Further details of the Glauber model are provided in the subsections discussed below.

2.4.1 Total reaction cross-section

The well-known Glauber model has been established to reproduce the experimental data at high energies. However, it fails to reasonably describe collisions induced at relatively low energies. In such case, the Glauber model is modified to take care of finite range effects in the profile function and Coulomb-modified trajectories. The details for calculating reaction cross-sections using the Glauber approach have been given by R.J. Glauber [137]. The standard Glauber form for the total reaction cross-section at high energies is expressed [19, 138, 139] as:

$$\sigma_R = 2\pi \int_0^{\infty} \overrightarrow{b}[1 - T(\overrightarrow{b})]d\overrightarrow{b}, \tag{2.4.42}$$

where $T(\overrightarrow{b})$ is the transparency function at the impact parameter $\overrightarrow{b}$. The function $T(\overrightarrow{b})$ is calculated in the overlap region between the projectile and the target, assuming that the interaction is formed from a single nucleon-nucleon (NN) collision. It is given by [116]:

$$T(\overrightarrow{b}) = exp\left[-\sum_{i,j} \overline{\sigma}_{i,j} \int \overline{\rho}_{pi}(\overrightarrow{s})\overline{\rho}_{tj}(|\overrightarrow{b} - \overrightarrow{s}|)d\overrightarrow{s}\right]. \tag{2.4.43}$$

Here the summation is over the nucleons i and j, where i belongs to the projectile and j belongs to the target nuclei. The subscripts p and t refer to the projectile and the target, respectively. $\overline{\sigma}_{i,j}$ is the experimental nucleon-nucleon reaction cross-section which depends on the energy.

This Glauber model agrees well with the experimental data at high energies but fails to accurately describe collisions induced at relatively low energies. This disagreement arises due to the presence of the Coulomb repulsive potential, whose effects are evident in the low-energy range. At low energies, the Coulomb effect violates the characteristic Glauber assumption that the projectile moves in a straight path along the collision direction and gives the nucleus-nucleus interaction. Various attempts have been made to include the Coulomb effect in the Glauber model. The most successful model is based on the WKB approximation for the phase shifts. The impact parameter $\overrightarrow{b}$ replaces in the transparency function $T(\overrightarrow{b})$ by the distance $\overrightarrow{b_c}$ of the closest approach of the deviated projectile trajectory due to the Coulomb effect. The argument of $T(b)$ in Eq. 2.4.43 is $(|\overrightarrow{b}-\overrightarrow{s}|)$, which stands for the impact parameter between the ith and jth nucleons. The Glauber model is designed for high-energy approximation. However, it was found to work fairly well, for both the nucleus-nucleus reaction cross-sections and the differential elastic scattering cross-sections, over a broad energy range [140, 141]. Thus, for the finite range approximation, the transparency function is given by [142, 143]

$$T(b) = exp\left[-\int_{p,t}\sum_{i,j}[\Gamma_{ij}(\overrightarrow{b}-\overrightarrow{s}+\overrightarrow{t})]\overline{\rho}_{pi}(\overrightarrow{t})\overline{\rho}_{tj}(\overrightarrow{s})d\overrightarrow{s}d\overrightarrow{t}\right], \tag{2.4.44}$$

where the summation indices i and j run over neutron and proton for both target and projectile. Here the profile function Γ_{NN} for optical limit approximation is defined as

$$\Gamma_{NN} = \Gamma_{ij}(b_{eff}) = \frac{1-i\alpha_{NN}}{2\pi\beta_{NN}^2}\overline{\sigma}_{NN}exp(-\frac{b_{eff}^2}{2\beta_{NN}^2}) \tag{2.4.45}$$

for the finite range and

$$\Gamma_{NN} = \Gamma_{ij}(b_{eff}) = \frac{1-i\alpha_{NN}}{2}\sigma_{NN}\delta(b) \tag{2.4.46}$$

for the zero range with $b_{eff}=|\overrightarrow{b}-\overrightarrow{s}+\overrightarrow{t}|$, $\overrightarrow{b}$ is the impact parameter in which $\overrightarrow{s}$ and $\overrightarrow{t}$ are the dummy variables for integration over the z-integrated target and projectile densities.

To calculate the total reaction cross-section for unstable nuclei, some phenomenological parameters are required to estimate the NN cross-section. Here $\overline{\sigma}_{NN}$ is the total reaction cross-section of nucleon-nucleon collisions, α_{NN} is the ratio of the real to the imaginary part of the forward nucleon-nucleon scattering amplitude, and β_{NN} is the slope parameter. The slope parameter determines the fall of the angular distribution of the nucleon-nucleon scattering. These parameters are usually dependent upon the proton-proton, neutron-neutron and proton-neutron interactions. The nucleon-nucleon cross-section ($\overline{\sigma}_{NN}$) is estimated by the expression [144, 145, 146]

$$\overline{\sigma}_{NN} = \frac{N_p N_t \sigma_{nn} + Z_p Z_t \sigma_{pp} + N_p Z_t \sigma_{np} + N_t Z_p \sigma_{np}}{A_p A_t}, \tag{2.4.47}$$

where $A_p, A_t, Z_p, Z_t, N_p, N_t$ are the mass number, charge number and neutron number of the projectile and the target, respectively. The value of the range parameter β_{NN} as a function of projectile energy E is given by [147, 148]

$$\beta_{NN} = 0.99exp[\frac{-E}{106.679}] + 0.089 \tag{2.4.48}$$

2.4.2 Elastic scattering differential cross-section

One of the advantages of the Glauber theory is that the same input which is used in the reaction cross-section calculation is readily applicable for the calculation of the differential cross-section of elastic scattering. The diffraction pattern in the differential cross-section is expected to depend mainly on the diffuseness of the nuclear surface. Brief details of the mathematical formalism for calculating differential scattering cross-section are presented here. The nucleus-nucleus elastic scattering amplitude is written as

$$F(\overrightarrow{q}) = \frac{iK}{2\pi} \int db e^{i\overrightarrow{q}.\overrightarrow{b}} (1 - e^{i\chi(\overrightarrow{b})}). \tag{2.4.49}$$

At low energies, this model is modified to include a finite range effects in the profile function and Coulomb-modified trajectories. $F(\overrightarrow{q})$ and $F_{\rm coul}(\overrightarrow{q})$ are the elastic and Coulomb (elastic) scattering amplitudes, respectively. The elastic scattering amplitude $F(q)$ is written as

$$F(\overrightarrow{q}) = e^{i\chi_s} \left\{ F_{\rm coul}(\overrightarrow{q}) + \frac{iK}{2\pi} \int db e^{-i\overrightarrow{q}.\overrightarrow{b} + 2i\eta \ln(Kb)} T(\overrightarrow{b}) \right\} \tag{2.4.50}$$

with the Coulomb elastic scattering amplitude $F_{coul}(\overrightarrow{q})$ given as

$$F_{\rm coul}(\overrightarrow{q}) = \frac{-2\eta K}{q^2} exp\left[-2i\eta ln(\frac{q}{2K}) + 2i \arg\Gamma(1 + i\eta) \right], \tag{2.4.51}$$

where K is the momentum of the projectile and q is the momentum transferred from the projectile to the target. Here $\eta = \frac{Z_p Z_t e^2}{\hbar\nu}$ is the Sommerfeld parameter, ν is the incident velocity, and $\chi_s = -2\eta \ln(2Ka)$ with a being the screening radius. The elastic scattering differential cross-section does not depend on the screening radius a [19, 123]. The elastic differential cross-section is given by

$$\frac{d\sigma}{d\Omega} = |F(\overrightarrow{q})|^2 \tag{2.4.52}$$

and the ratio of the angular elastic to the Rutherford elastic differential cross-section is given as

$$\frac{d\sigma}{d\sigma_r} = \frac{(d\sigma/d\Omega)}{(d\sigma/d\Omega)_r} = \frac{|F(\overrightarrow{q})|^2}{|F_{\text{coul}}(\overrightarrow{q})|^2}. \tag{2.4.53}$$

2.5 Reaction cross-section using empirical formula

A large number of empirical formulas (models) with different parameters for total reaction cross-section calculations have been introduced by several researchers [149, 150, 151, 152, 153, 154, 155, 156, 157, 158, 159, 160, 161]. These models are developed considering the black sphere model with different modifications added from time to time to reproduce the experimental data. The available empirical formula has been compiled in Table 2.4. In the thesis work, we have also calculated the total reaction cross-section using the empirical formula given by Sihver *et al.* [153, 154, 156] which is discussed below. The model is dependent on the interaction radius R and Coulomb barrier B using a strong absorption model [156]:

$$\sigma_R = \pi R^2 \left[1 - \frac{B}{E_{cm}}\right], \tag{2.5.54}$$

where R is the interaction radius, E_{cm} is the center-of-mass energy of the collision and B is the Coulomb barrier of the projectile-target system:

$$\begin{aligned} B_{Shen} &= \frac{1.44 Z_P Z_T e^2}{R_P + R_T + 3.2} - \frac{R_P R_T}{R_P + R_T}, \\ R_i &= 1.12 A_i^{\frac{1}{3}} - 0.94 A_i^{-\frac{1}{3}}, \quad i = P, T, \end{aligned} \tag{2.5.55}$$

where Z_P, Z_T, A_P, A_T, R_P, and R_T are the atomic numbers, mass numbers, and interaction radius of projectile (P) and the target (T), respectively. The interaction radius R is given by

$$\begin{aligned} R_{Shen} = 1.1 \Bigg(& A_P^{\frac{1}{3}} + A_T^{\frac{1}{3}} + 1.85 \frac{A_P^{\frac{1}{3}} A_T^{\frac{1}{3}}}{A_P^{\frac{1}{3}} + A_T^{\frac{1}{3}}} - C(E) \Bigg) \\ & + \frac{5(A_T - 2Z_T)Z_P}{A_P A_T} + 0.176 E_{cm}^{-\frac{1}{3}} \frac{A_P^{\frac{1}{3}} A_T^{\frac{1}{3}}}{A_P^{\frac{1}{3}} + A_T^{\frac{1}{3}}}. \end{aligned} \tag{2.5.56}$$

The energy-dependent transparency coefficient $C(E)$ is

$$C(E) = 1.91 - 16.0e^{-0.7274E^{0.3493}}cos(0.0849E^{0.5904}), \tag{2.5.57}$$

where the projectile kinetic energy E is in MeV/nucleon. The calculated reaction cross-section using the Shen formula shows good agreement with the experimental data in the high-energy regions.

Table 2.4: List of empirical formulae for reaction cross-section calculations.

interation	Models	Relation/Value	Reference
Nucleus-Nucleus	Bradt-Peters	$\sigma_R = \pi r_0^2(A_P^{\frac{1}{3}}+A_T^{\frac{1}{3}} - \delta)^2$	[149]
	Kox	$\sigma_R = \pi r_0^2(A_P^{\frac{1}{3}} + A_T^{\frac{1}{3}} - \delta)^2(1 - \frac{B_C}{E_{cm}})$	[150]
	Kox	$\sigma_R = \pi r_0^2(A_P^{\frac{1}{3}} + A_T^{\frac{1}{3}} - a\frac{A_P^{\frac{1}{3}}A_T^{\frac{1}{3}}}{A_P^{\frac{1}{3}}+A_T^{\frac{1}{3}}} - C)^2(1 - \frac{B_C}{E_{cm}})$	[151]
	Kox	$\sigma_R = \pi R_{int}^2(1\text{-}\frac{B_C}{E_{cm}})$	[152, 153]
	Townsend	$\sigma_R = \pi R_{int}^2(1\text{-}\frac{B_c}{E_{cm}})$, $R_{int} = R_{vol} + R_{surf}$	[155]
	Shen	$\sigma_R = 10\pi R_{int}^2(1\text{-}\frac{B}{E_{cm}})$	[153, 154]
	Sihver	$\sigma_R = \pi r_0^2[A_P^{\frac{1}{3}}+A_T^{\frac{1}{3}} - b_0(A_P^{\frac{-1}{3}}+A_T^{\frac{-1}{3}})]^2$	[153, 158]
	Tripathi	$\sigma_R = \pi r_0^2(A_P^{\frac{1}{3}}+A_T^{\frac{1}{3}} +\delta_E)^2(1 - R_c\frac{B}{E_{cm}})X_m$	[153, 157]
	Kei Iida	$\sigma_R = \pi[(a_{P0} + \Delta ap)f_P^{\frac{1}{2}} + (a_{T0} + \Delta a_T)f_T^{\frac{1}{2}}]^2$	[159]
	Sihver	$\sigma_R = \pi R^2(1\text{-}\frac{B}{E_{cm}})$	[153, 156]
Proton-Nucleus	Sihver	$\sigma_R = \pi r_0^2[1 + A_T^{\frac{1}{3}} - b_0[1 + A^{\frac{-1}{3}}]]^2$	[158]
	Tripathi	$\sigma_R = \pi r_0^2(A_P^{\frac{1}{3}}+A_T^{\frac{1}{3}} +\delta_E)^2(1 - \frac{B}{E_{cm}})$	[161]
	Axen	$\sigma_R = f_1(log_{10}E_{kin}, A).f_2(log_{10}E_{kin}, A).\sigma_R^0)$	[160]
	Kei Iida	$\sigma_R = \pi a_0^2[1 + (\frac{\rho_0 a_0}{Dn_{c0}} - \frac{a_0}{L_0}\frac{dL}{da}\|_0)^{-1}\frac{\Delta\bar{\sigma}_{pN}}{\bar{\sigma}_{pN0}}]^2$	[159]

For the proton as the target, we have calculated the total reaction cross-section using the empirical formula given by Wellisch and Axen [160] in terms of the mass number of the target A and b_0 is the overlap or transparency parameter (see, for details, Ref. [160]):

$$\sigma_R^0 = f_{corr}\pi r_0^2 lnN[1 + A^{1/3} - b_0(1 - A^{-1/3})], \tag{2.5.58}$$

$$b_0 = 2.247 - 0.915(1 + A^{-1/3}), \quad and \quad r_0 = 1.36fm, \tag{2.5.59}$$

where N is the number of neutrons in the target.

$$f_{corr} = \frac{1 + 0.15e^{-E_{kin}}}{1 + 0.0007A}, \tag{2.5.60}$$

$$\sigma_R(Axen) = f_1(log_{10}E_{kin}, A).f_2(log_{10}E_{kin}, A).\sigma_R^0. \tag{2.5.61}$$

The two functions can be written as

$$f_1(x, y) = \frac{1}{1 + e^{-P_1(y)(x+P_2(y))}} \tag{2.5.62}$$

and

$$f_2(x, y) = 1 + P_3(y)\left(1 - \frac{1}{1 + e^{-P_4(y)(x+P_5(y))}}\right), \tag{2.5.63}$$

where x is the $log_{10}E_{kin}$ in units of MeV and y is the target atomic number.

$$P_1(y) = \left(8 - \frac{8}{y} - 0.008y\right), \tag{2.5.64}$$

$$P_2(y) = 18.72 - \frac{42.2}{y} - 0.0224y, \tag{2.5.65}$$

$$P_3(y) = 0.8 + \frac{18}{y} - 0.002y, \tag{2.5.66}$$

$$P_4(y) = 5.6 - 0.01y, \tag{2.5.67}$$

$$P_5(y) = 10.96\left(1 + \frac{1}{y}\right). \tag{2.5.68}$$

2.6 Effective liquid drop model for cluster decay and two-proton radioactivity

In the present thesis work, the Effective liquid drop model is chosen as fission-like, given by M. Gonclaves *et al.* [162, 163, 164]. In this model, the parent nucleus is supposed to be deformed continuously and reach the saddle or scission shape to undergo cluster radioactivity. Gamow's idea of quantum mechanical barrier penetration is still used, but

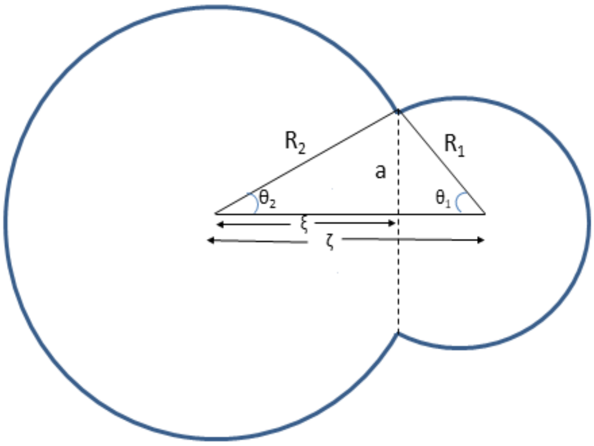

Figure 2.1: Shape parametrization of nuclear deformation.

without worrying about the cluster being or not being performed in the parent nucleus. Here the parent nucleus is assumed to undergo continuous dynamical changes from the initial one-nucleus system to the final separated multi-nucleus systems, as it penetrates the nuclear potential barrier and attains the saddle configuration, where both the masses and charges of the fission fragments are fixed. To describe the molecular stage of the system, the geometrical configuration of the deformed system is approximated by two intersecting spheres of different radii. Four independent coordinates are necessary to explain the configuration in shape parametrization (R_1, R_2, ζ, and ξ), as illustrated in Fig. 2.1. The radii of the emitted cluster and heavier daughter nucleus are R_1 and R_2, respectively. ζ denotes the distance between their geometric center and the distance between the plane of intersection and the geometrical center of the daughter nucleus is represented by ξ. The four-dimensional problem is reduced to one-dimensional by using three constraint relations in the model. The first one,

$$2(R_1^3 + R_2^3) + 3[R_1^2(\zeta - \xi) + R_2^2\xi] - [(\zeta - \xi)^3 + \xi^3] = 4R_p^3, \tag{2.6.69}$$

where R_p is the radius of parent nuclei. The second is the geometrical constraint

$$R_1^2 - R_2^2 - (\zeta - \xi)^2 + \xi^2 = 0 \tag{2.6.70}$$

The last constraint is connected with the flux of mass through the plain of the intersection of the two spheroids. The radius of a lighter fragment is constant,

$$R_1 - \overline{R}_1 = 0, \tag{2.6.71}$$

where $\overline{R}_1$ is the radius of the light fragment. Now, the four-dimensional problem is reduced to one-dimensional.

In ELDM the effective one-dimensional potential energy can be calculated using the relation

$$V = V_C + V_s + V_l. \tag{2.6.72}$$

Here V_C, V_s and V_l are the Coulomb, surface and centrifugal potentials, respectively. The Coulomb potential (V_C) which was developed by Gaudin [165] is given by

$$V_C = \frac{8}{9}\pi a^5 \varepsilon(x_1, x_2)\rho_c, \tag{2.6.73}$$

where ρ_c is the initial charge density, a is the sharp neck radius and $\varepsilon(x_1, x_2)$ denotes the function of angular variables x_1 and x_2,

$$x_1 = \pi - \theta_1, \tag{2.6.74}$$

$$x_2 = \theta_2 - \pi. \tag{2.6.75}$$

which are defined in terms of the angle θ_1 and θ_2 given in Fig. 2.1.

The effective surface potential V_s can be calculated by

$$V_s = 4\pi(R_p^2 - R_1^2 - R_2^2)\sigma_{(eff)}, \tag{2.6.76}$$

where $\sigma_{(eff)}$ denotes the effective surface tension and R_p denotes the radius of the parent nucleus.

The centrifugal potential is calculated as

$$V_l = \frac{\hbar^2}{2\overline{\mu}}\frac{l(l+1)}{\zeta^2}, \tag{2.6.77}$$

where $\overline{\mu} = (M_1 M_2 / M_1 + M_2)$ is the reduced mass.

We have used the Shi and Swiatecki [166] hindrance for even-even parent nuclei and, P is the Gamow penetrability factor for one dimension barrier used in shape parameterization of the dinuclear system calculated by equation

$$P = exp\left[\frac{-2}{\hbar}\int_{\zeta_0}^{\zeta_c}\sqrt{2\mu[V(\zeta) - Q]}d\zeta\right]. \tag{2.6.78}$$

The limits of integration in Eq. 2.6.78 ζ_0 and ζ_c are the inner and outer turning points on the barrier evaluated by the constraint used to reduce the one-dimensional problems by introducing $\zeta_0 = R_p - \overline{R_1}$ and $\zeta_c = Z_1 Z_2 e^2/Q$. μ is the inertia coefficient. In the μ estimation, two inertial approximations (Werner-Wheeler's inertial approximation (WW) and Effective inertial approximation (Eff.)) and two different modes (Varying Mass Asymmetry Shape (VMAS) and Constant Mass Asymmetry Shape (CMAS)) are used to describe the dynamical evolution of the separating dinuclear system. So, for μ there are four types of combinations, which are μ_{WW}^{VMAS}, μ_{Eff}^{VMAS}, μ_{WW}^{CMAS} and, μ_{Eff}^{CMAS}, respectively. Here, the radius of the parent nuclei is R_p, and the Q value of the reaction is calculated by mass excess data through RMF (NL3* parameter set) calculations.
The half-life for the cluster decay is given as

$$T_{1/2} = \left(\frac{ln2}{\lambda}\right), \tag{2.6.79}$$

where λ is the radioactive decay rate given by

$$\lambda = \nu P. \tag{2.6.80}$$

In Eq. (2.6.80) $\nu = (\frac{2E_\nu}{h})$ is the parameter for assault frequency of the barrier. The empirical zero point vibration energy E_ν is given by [94]

$$E_\nu = Q[0.056 + 0.039exp[(4 - A_2)/2.5]], \quad \text{for} \quad A_2 \geq 4. \tag{2.6.81}$$

The assault frequency was determined using Eq. (2.6.81) for each parent nuclei and emitted cluster combination and was used in Eq. (2.6.80) to determine the half-life values.

2.7 Cluster decay Half-lives using empirical formula

Empirical formulas (models), such as the KPS [167], Royer formula [168], UNIV formula [169], BKAG formula [170], Ni-Ren-Dong-Xu (NRDX) formula [171], VSS formula [172], UDL formula [50, 173, 174], Horoi formula [50, 175, 176], Viola-Seaborg-Sobiczewski (VS) formula [177, 178, 179], and TM formula [180] are commonly used to calculate and predict the alpha and cluster decay half-lives. In the present thesis, we have also calculated the half-lives using empirical formula UDL given by C. Qi *et al.* [50, 173, 174], Viola-Seaborg formula (VS) [177, 178, 179], the Scaling law of Horoi given by Horoi *et al.* [50, 175, 176] and TM formula [180] which is discussed below.

2.7.1 The Viola-Seaborg formula (VS)

Viola and Seaborg [177, 178] introduced the Viola-Seaborg semi-empirical formula with different parameters, which is written as

$$log_{10}T_{1/2}(VS) = (aZ_P + b)Q_\alpha^{-1/2} + (cZ_P + d) + h_{log}, \tag{2.7.82}$$

where Z_P is the atomic number of the parent nucleus. The four parameters a, b, c, and d are fitting parameters whose values are 1.66175, -8.5166, -0.20228, and -33.9069, respectively. Here we have chosen the hindrances factor as, $h_{log} = 0$ for Z = even, N = even; $h_{log} = 0.722$ for Z = odd, N = even; $h_{log} = 1.066$ for Z = even, N = odd; $h_{log} = 1.114$ for Z, N = odd.

2.7.2 The Universal Decay Law (UDL)

The Universal Decay Law (UDL) for alpha and cluster decay was introduced by C. Qi *et al.* [50, 173, 174] starting from the R-matrix theory [181]. The UDL formula holds for the monopole radioactive decay of all clusters [173]. The model is dependent on the mass, charge numbers of the daughter and emitted clusters, and the Q value. The UDL formula is given by the expression

$$log_{10}T_{1/2}(UDL) = aZ_eZ_d\sqrt{\frac{\mu}{Q}} + b\sqrt{\mu Z_eZ_d(A_e^{1/3} + A_d^{1/3})} + c, \tag{2.7.83}$$

$$log_{10}T_{1/2}(UDL) = a\chi' + b\rho' + c. \tag{2.7.84}$$

The factors χ' and ρ' are defined as,

$$\chi' = \frac{\hbar}{e^2\sqrt{2m}}\chi = Z_eZ_d\sqrt{\frac{\mu}{Q}},$$
$$\rho' = \frac{\hbar}{\sqrt{2mR_0e^2}}(\rho\chi)^{\frac{1}{2}} = \sqrt{\mu Z_eZ_d(A_e^{1/3} + A_d^{1/3})},$$

where $\mu = A_eA_d/(A_e + A_d)$ is the reduced mass and A_e, A_d are the mass numbers of the daughter and emitted cluster, respectively. The three coefficient sets of Eq. (2.7.84) are a = 0.3949, b = -0.3693, and c = -23.7615. The term $b\rho' + c$ includes the effects that induce the clusterization in the parent nucleus.

2.7.3 Scaling law of Horoi *et al.*

We have calculated the half-life of alpha and cluster decays using the empirical formula given by M. Horoi *et al.* [50, 175, 176] in terms of reduced mass μ, and the constants a,

b, c, and d are the coefficients set (see, for details, Refs. [50, 175, 176]):

$$log_{10}T_{1/2}(Horoi) = (a\mu^{0.416} + b)[(Z_e Z_d)^{(0.613)}/\sqrt{Q} - 7] + (c\mu^{0.416} + d), \qquad (2.7.85)$$

where $T_{1/2}$ is the cluster decay half-life and Z_d and Z_e represent the atomic number of the daughter and emitted nucleus. The four coefficient sets are a = 9.1, b = -10.2, c = 7.39, and d = -23.2.

2.7.4 TM formula

The cluster decay half-life is evaluated using the empirical formula given by Tavares *et al.* [180] in terms of the proton numbers of the product (daughter and cluster) nuclei and the calculated Q-value of the two-body disintegration system as

$$log_{10}T_{1/2}(TM) = (aZ_C + b)(Z_d/Q)^{1/2} + (cZ_C + d). \qquad (2.7.86)$$

Here Z_C and Z_d are the atomic numbers of the emitted cluster and daughter nucleus. The four parameters a, b, c, and d are 12.8717, -5.1222, -4.6496, and -73.3326, respectively.

2.8 Two-proton decay Half-lives using empirical formula

The two empirical formulas (models), such as Liu [182] and Sreeja [183] formulas, are used to estimate and predict the two-proton radioactivity half-lives that were lately proposed by extending the empirical models for one proton radioactivity half-lives founded on the Geiger-Nuttall law [182, 183]. In the present thesis, we have also estimated the two-proton radioactivity half-lives using the empirical formula given by Liu and Sreeja which is discussed below.

2.8.1 Liu formula

The two-proton decay half-lives are evaluated within the empirical formula introduced by Liu *et al.* [182] in terms of the daughter nuclei atomic number and the calculated Q_{2p}-value of the two-body disintegration system as

$$log_{10}T_{1/2} = a(Z_d^{0.8} + l^b)Q_{2p}^{-1/2} + c. \qquad (2.8.87)$$

Here, the adjustable parameters $a = 2.032$, $b = 0.25$, and $c = -26.832$, are obtained by fitting the experimental value and the estimated results based on the ELDM. Here the fitting parameter b reveals the effect of the angular momentum l on the two-proton decay half-lives.

2.8.2 Sreeja formula

Sreeja and Balasubramaniam [183] introduced Sreeja's formula, with different parameters which are given as

$$log_{10}T_{1/2} = (al + b)\xi + cl + d. \tag{2.8.88}$$

where $\xi = Z_d^{0.8} Q_{2p}^{-1/2}$, with Z_d being the atomic number of the daughter nucleus. The four parameters a, b, c, and d are fitting parameters whose values are obtained by fitting the two proton decay half-lives estimated by the ELDM. These four fitting parameters a, b, c, and d come out to be 0.1578, 1.9474, -1.8795, and -24.847, respectively.

Chapter 3

A combined Glauber model plus Relativistic Hartree-Bogoliubov theory analysis of nuclear reactions for light and medium mass nuclei[1]

3.1 Introduction

Recently, the radioactive ion beam (RIB) facilities and advanced detection technologies have become a standard tool to study nuclear structure and reaction properties of nuclei lying at the drip line (far away from the β stability line). The quantities measured in various nuclear reactions include the total reaction cross-sections, elastic scattering differential cross-sections, nucleon removal cross-sections, nuclear and Coulomb breakup cross-sections, and momentum distributions of fragments in breakup processes on nuclear targets. These observables have been used to study the nuclear structure of unstable nuclei in detail, particularly the halo structure near the drip lines [116, 184, 185, 186]. From another side, it has been found quite useful to understand the role of nuclear interaction, especially at proton/neutron drip line, as these reaction characteristics exhibit many interesting nuclear structural features, such as one/two neutron halo, skin effect, deformations, bubbleness, and magicity/emergence of new shell gaps [187, 188]. The measurement of the total reaction and differential cross-sections are particularly useful

[1]The results discussed in this chapter have been published in *Pramana - J. Phys.* 96, 8 (2022).

for these unstable nuclei as the effects produced by weekly bound neutron/proton nuclei are quite different from the nuclear core. For stable nuclei, electron and proton elastic scattering data provide the charge and matter density distributions, while for unstable nuclei, not only electron elastic scattering experiments are yet to be performed, but also proton scattering data obtained from RIBs colliding with a proton target [189, 190] are scarce. Hence, the deduction of the rms matter radius of unstable nuclei is mainly performed through measurements of reaction cross-section only.

The measurement of reaction cross-sections and matter radii of ^{6,8}He, ^{11}Li, and ^{11,14}Be [189, 190, 191] has shown anomalously large values compared to that of the neighboring nuclei. Also, very recently, the measured interaction cross-sections of very neutron-rich carbon isotopes have ^{22}C deduced to be two-neutron halo nucleus (the ^{21}C nucleus is unstable) [192, 193, 194]. The momentum distribution and the one-neutron removal cross-section have also shown that ^{22}C is a halo nucleus and $N = 16$ is considered to be a new magic number in neutron-rich nuclei [195]. The observation of such nuclear halo and other novel features are closely connected with the evolution of the shell structure in He, Li, Be, B, and C isotopes. These investigations have stimulated several theoretical studies in the past [196, 197], yet it needs further refinement to reduce the theoretical uncertainty and to constrain the theoretical approaches. These are the arguments that motivate us to study the nuclear reaction cross-sections of such nuclei consistently with nuclear structure details. For these calculations, realistic nuclear density is required, which can be obtained from a certain number of nuclear models. Hence, it is very important to choose a suitable set of density/wave functions before employing them for further calculations. We have used the relativistic Hartree-Bogoliubov (RHB) model for calculating the ground-state properties of nuclei considered in the present chapter. Cross-section studies have been performed using the Glauber model which can account for the breakup effect of the weakly bound nucleus [198, 199]. The Glauber model has been successfully applied to study high-energy nucleus-nucleus reaction cross-section data. The model is based on the eikonal approximation which exhibits complex behavior as compared to nucleon-nucleon interaction [5, 7]. The main input to obtain the reaction cross-sections through the Glauber model is the structural information of the nuclei involved, which is provided through the density profile. The Glauber model predicts the values of the total reaction cross-sections at higher energies much closer to the experimental data. In our previous studies, we have shown that the density obtained from the relativistic mean field can be used effectively for reaction studies [129, 200, 201].

In this chapter, we have calculated the nuclear reaction properties of even-even $^{4-8}$He,

$^{6-10}$Li, $^{10-14}$Be, $^{8-16}$B, $^{10-22}$C, ^{40}Ca, ^{58}Ni, ^{90}Zr, and ^{120}Sn nuclei extending from the proton to the neutron drip line. The evaluation of the credibility of the nuclear densities used as inputs for reaction studies has been performed by comparing the nuclear ground-state properties, i.e. the binding energies and charge radii, with the corresponding experimental values. The ground-state properties of the considered nuclei are calculated using the relativistic Hartree-Bogoliubov model with density-dependent meson exchange (DD-ME2) and point coupling (DD-PC1) interactions and with separable pairing interaction. The nuclear reaction cross-section for light nuclei, such as He, Li, Be, B, and C isotopes, as the projectile on the ^{12}C target are calculated using the Glauber model, with densities obtained from RHB formalism. We have also calculated the reaction cross-section in medium mass nuclei, namely Ca, Ni, Zr, and Sn isotopes, on the proton target. The elastic scattering differential cross-sections are also analyzed for various projectile energies. They give different types of diffraction patterns that depend on the diffuseness of the nuclear surface.

3.2 Results and Discussion

This section presents our calculated results of binding energies, charge radius (r_{ch}), and nuclear density for isotopes of He, Li, Be, B, C, Ca, Ni, Zr, and Sn using the relativistic Hartree-Bogoliubov theoretical model with DD-ME2 (meson-exchange coupling) and DD-PC1 (point coupling) parameter sets. The calculated results are compared with experimental data.

3.2.1 Binding energies, nuclear radii, and density profiles

The calculated binding energies for the considered nuclei along with the experimental values taken from ref. [202] are presented in Table 3.1. It can be seen from Table 3.1 that the calculated binding energies from the RHB formalism are in good agreement with available experimental data [202, 203]. In comparison, the DD-PC1 values of the binding energies are slightly higher than the DD-ME2 values and overestimate the experimental data. For the results given in Table 3.1, the square-weighted mean square error with respect to the experimental data is 0.0010 and 0.0011 for DD-ME2 and DD-PC1 parameter sets, respectively. The binding energy of a nucleus indicates nuclear stability, as well as protons and neutrons decay energies. These results give the confidence to use DD-ME2 and DD-PC1 densities in the calculation of reaction dynamics.

The charge radius (r_{ch}) is obtained from the point proton rms radius through the relation

Table 3.1: The calculated values of binding energy (in MeV) and charge radius (r_{ch} in fm) for the projectile and target nuclei using RHB (DD-ME2 and DD-PC1) formalism and comparison with experimental data [202, 203].

Nucleus	Binding energy			Charge radius (r_{ch})		
	DD-ME2	DD-PC1	Expt.	DD-ME2	DD-PC1	Expt.
^{4}He	27.818	26.902	28.292	2.140	2.177	1.676
^{6}He	28.979	29.321	29.270	2.118	2.131	2.068
^{8}He	29.626	31.514	31.41	2.124	2.126	1.929
^{6}Li	32.470	32.385	31.994	2.431	2.408	2.539
^{8}Li	42.155	43.042	41.277	2.336	2.331	2.29
^{10}Li	47.669	49.765	45.316	2.342	2.337	-
^{10}Be	61.444	62.191	64.970	2.394	2.420	2.36
^{12}Be	68.916	71.096	68.649	2.461	2.461	-
^{14}Be	66.628	68.185	69.916	2.489	2.488	-
^{8}B	37.865	38.744	37.737	2.725	2.666	-
^{10}B	63.382	64.039	64.751	2.523	2.532	2.428
^{12}B	81.517	82.641	79.575	2.496	2.516	-
^{14}B	87.826	89.425	85.423	2.535	2.545	-
^{16}B	88.076	90.012	88.144	2.566	2.569	-
^{10}C	55.923	56.860	60.321	2.669	2.661	-
^{12}C	87.317	87.517	92.160	2.507	2.552	2.47
^{14}C	104.921	105.766	105.280	2.556	2.585	2.56
^{16}C	108.544	109.970	110.752	2.585	2.607	-
^{18}C	111.792	113.945	115.280	2.612	2.628	-
^{20}C	114.573	117.580	119.18	2.636	2.649	-
^{22}C	116.652	120.562	120.736	2.653	2.663	-
^{40}Ca	342.778	344.791	342.120	3.475	3.457	3.476
^{58}Ni	501.634	501.916	506.459	3.752	3.775	3.774
^{90}Zr	783.195	785.273	783.898	4.268	4.267	4.272
^{120}Sn	1019.399	1020.894	1020.539	4.645	4.645	4.652

given below [10]:

$$r_c = \sqrt{r_p^2 + 0.64}\,, \tag{3.2.1}$$

where the proton radius is considered to be 0.8 fm. In Table 3.1, we have presented the calculated values of charge radius using RHB (DD-ME2 and DD-PC1) formalism along with the experimental data, wherever available [204]. It is found that the calculated values of the charge radius agree well with the experimental ones. For instance, the obtained values of r_{ch} for ^{12}C with DD-ME2 and DD-PC1 are 2.507 and 2.552 fm, respectively, and they compare well with the measured value of 2.47 fm. As can be seen, the calculated values of charge radii are slightly higher for DD-PC1 than for the DD-ME2 parameter set. For the results given in Table 3.1, the square-weighted mean square errors with respect to the experimental data are 0.0036 and 0.0043 for DD-ME2 and DD-PC1 parameter sets, respectively. Since the charge radius is obtained from the density profile, our RHB results for charge radii match well with the experimental results. We have used these densities to find coefficients c_i and ranges a_i for reaction cross-section calculations.

To check the reliability of the calculated total nuclear densities, we have compared the

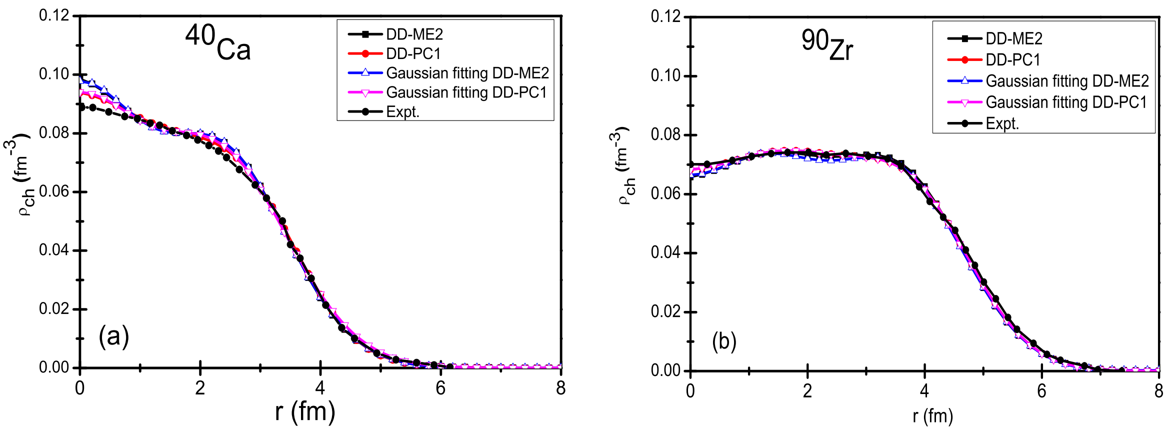

Figure 3.1: Comparison of charge densities ρ_{ch} obtained from RHB (DD-ME2 and DD-PC1) calculations for ^{40}Ca (shown in 1(a)) and ^{90}Zr (shown in 1(b)). Experimental data [205, 206] are also given for comparison.

calculated charge densities with the available experimental data (for ^{40}Ca and ^{90}Zr), as shown in Fig 3.1. Fig 3.1 represents the densities of ^{40}Ca and ^{90}Zr as a function of radial distance r. In Fig 3.1(a), the nuclear charge densities with and without Gaussian fitting are illustrated. It is clear from Fig 3.1(a) that the densities calculated with DD-ME2 and

DD-PC1 compare well with the experimental data [205, 206] and are almost similar except for a small difference at the center. In the nucleus, the nucleon density distribution in the central region reaches a maximum and starts decreasing towards the surface. Similarly, we have calculated the densities for ^{90}Zr using DD-ME2 and DD-PC1 parameters and plotted in Fig 3.1(b). In case of ^{40}Ca, the densities obtained using both DD-PC1 and DD-ME2 both overestimate slightly the experimental density at the center, whereas in the case of ^{90}Zr, the results show almost one-to-one match with the experimental charge density. We have observed that RHB nuclear densities and nuclear densities fitted by a sum of Gaussian functions are quite similar. However, to calculate the nuclear reaction cross-section, we require a sum of Gaussian for the total nuclear densities, and hence the coefficient for the same (a_i, c_i) are given in Table 3.2 for both DD-ME2 and DD-PC1 parameter sets.

The nuclear densities obtained from the RHB calculations are fitted to a sum of Gaussian functions, with suitable coefficients c_i and ranges a_i chosen for the respective nuclei which are expressed as

$$\rho(r) = \sum_{i=1}^{N} c_i exp[-a_i r^2] \tag{3.2.2}$$

Then, the Glauber model is used to calculate the total reaction cross-section for both the stable and unstable nuclei considered in the present study.

3.2.2 Total reaction cross-section

One of the main inputs for calculating of reaction cross-section from the Glauber model is the densities of the projectile and the target. We calculate the total nuclear reaction cross-sections for even-even light mass nuclei (as a projectile) on ^{12}C target using the well-known Glauber model for incident energy 30-1100 MeV/nucleon and compared with the experimental data [184, 207, 208, 209].

Fig 3.2 shows the variation of the total reaction cross-section for ^{12}C projectile on ^{12}C target with experimental data [199, 208, 209]. It can be seen from Fig 3.2 that the DD-ME2 results match well for all E, particularly at higher values. At low energies, the Coulomb effect breaks the characteristic Glauber assumption that the projectile moves in a straight path along the collision direction and gives the nucleus-nucleus interaction. The theoretically calculated total reaction cross-section using the Shen formula is also given in Fig 3.2 for comparison. At high projectile energy σ_r is almost constant but in the low energy region σ_r decreases with energy. The results obtained with DD-ME2 and DD-PC1

Table 3.2: The Gaussian coefficients c_1, c_2 (in fm^{-3}), and ranges a_1, a_2 (in fm^{-2}) for the projectile and the target nuclei using RHB (DD-ME2 and DD-PC1) densities.

Nucleus	DD-ME2				DD-PC1			
	c_1	a_1	c_2	a_2	c_1	a_1	c_2	a_2
^{4}He	-1.21074	0.430376	1.40447	0.430362	-1.18094	0.518707	1.33754	0.493431
^{6}He	-1.21274	0.338221	1.40269	0.338139	-1.22195	0.406079	1.38382	0.387125
^{8}He	-1.21473	0.277103	1.40067	0.277053	-0.0344762	0.668599	0.198228	0.266596
^{6}Li	-1.21111	0.331916	1.40443	0.331834	-1.22467	0.418282	1.38844	0.3959
^{8}Li	-0.954186	0.317045	1.15509	0.216906	-1.22505	0.382127	1.39652	0.355307
^{10}Li	-0.0280104	0.746477	0.215441	0.24405	-1.22875	0.345937	1.39616	0.317875
^{10}Be	-0.715954	0.399514	0.932236	0.35115	-2.55755	0.364366	2.74063	0.346752
^{12}Be	-0.144797	0.524765	0.322591	0.255807	-2.95383	0.32823	3.12016	0.312574
^{14}Be	-0.029346	0.884583	0.225294	0.206446	-0.34928	0.338282	0.518984	0.248758
^{8}B	-0.90949	0.280753	1.10632	0.278896	-1.22359	0.377247	1.39324	0.351645
^{10}B	-0.115597	0.560674	0.328971	0.295178	-2.7156	0.365758	2.89883	0.348638
^{12}B	-0.238443	0.500846	0.436427	0.289529	-1.42745	0.353198	1.60728	0.317607
^{14}B	-0.155061	0.53503	0.342766	0.243962	-1.45564	0.322088	1.62735	0.289066
^{16}B	-0.0727572	0.625991	0.267665	0.203858	-2.74612	0.282948	2.91882	0.267825
^{10}C	-0.0714023	0.630206	0.282435	0.279806	-2.42795	0.360827	2.60865	0.342949
^{12}C	-0.252934	0.559829	0.477824	0.312322	-3.57555	0.358487	3.7741	0.342315
^{14}C	-1.11983	0.397884	1.30388	0.328356	-1.78721	0.339177	1.96548	0.306
^{16}C	-0.220029	0.494813	0.40971	0.242021	-4.06649	0.29889	4.24279	0.28573
^{18}C	-0.148886	0.502663	0.342854	0.210082	-1.65748	0.282132	1.83413	0.254483
^{20}C	-0.128874	0.470349	0.324278	0.191071	-1.59376	0.259582	1.7731	0.234468
^{22}C	-0.145042	0.407697	0.340242	0.182128	-1.45633	0.240223	1.64281	0.216755
^{40}Ca	-2.20954	0.182730	2.50586	0.168420	-2.19931	0.172717	2.4568	0.159720
^{58}Ni	-3.01691	0.15353	3.26215	0.1424370	-2.98792	0.149701	3.19114	0.138475
^{90}Zr	-3.39482	0.131204	3.50470	0.121798	-3.30983	0.123187	3.41661	0.114503
^{120}Sn	-3.50362	0.115378	3.67986	0.1044921	-3.49871	0.110147	3.57124	0.099754

densities are in good agreement with the experimental data. Also, we have presented the values of the reaction cross-section obtained from the RMF approach using non-linear terms (NL3) parametrization [123] in Fig 3.2. As one can see in this figure, the results of the reaction cross-section with RHB (DD-ME2) densities appear slightly better than the ones obtained with RMF (NL3) model.

In Fig 3.3, we present the total reaction cross-sections for $^{4-8}$He, $^{6-10}$Li, $^{10-14}$Be, and $^{8-16}$B nuclei on ^{12}C performing calculations with DD-ME2 and DD-PC1 at fixed E=790

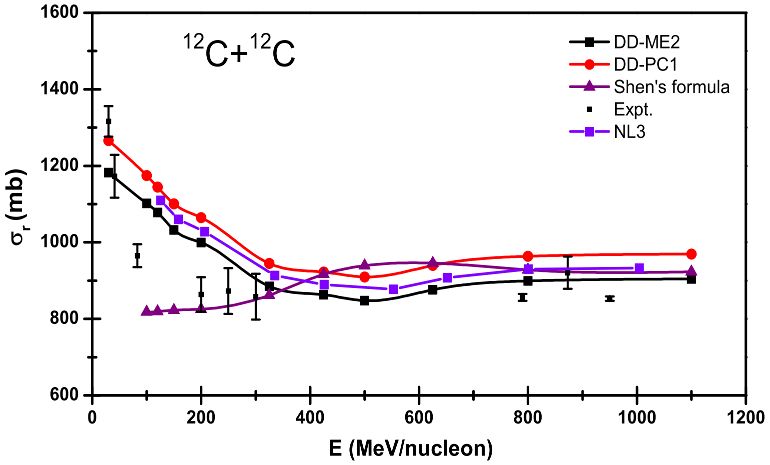

Figure 3.2: The total nuclear reaction cross-sections σ_r for ^{12}C+^{12}C system at different incident energies. The results obtained from DD-ME2, DD-PC1 densities, RMF (NL3) value [123] and Shen formula are compared with the available experimental data [208, 209].

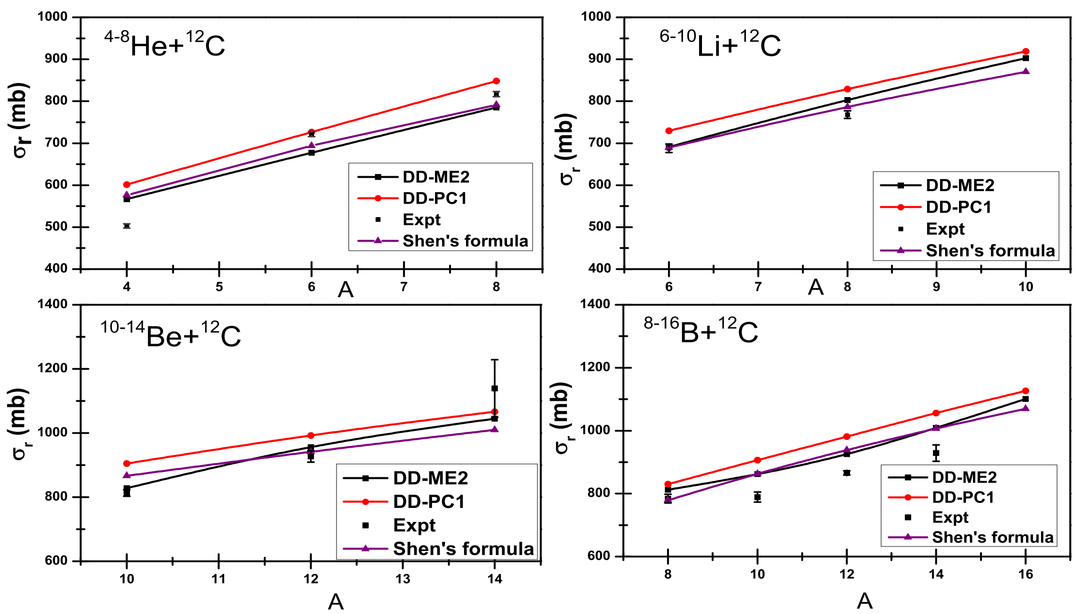

Figure 3.3: The comparison of total reaction cross-sections at 790 MeV/nucleon for various projectiles (He, Li, Be, and B isotopes) on ^{12}C target. Experimental data [208, 209, 199] are also given for comparison.

MeV/nucleon and make a comparison with experimental data [199, 208, 209]. In addition, we also calculate the total reaction cross-section using the Shen formula. A similar trend is observed for all calculations on different projectiles. Also, the total reaction cross-sections obtained from the DD-ME2 densities agree well with the experimental data.

Fig 3.4 shows the variation of total reaction cross-section for ^{10,14,16,18,20,22}C on ^{12}C target

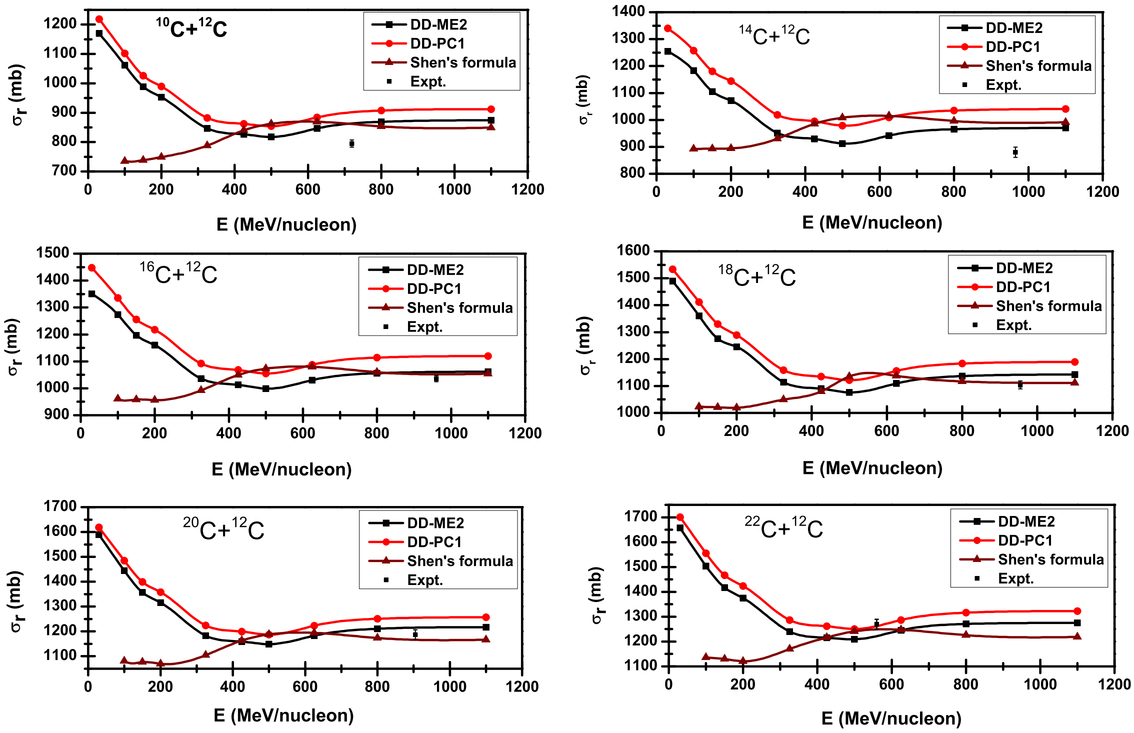

Figure 3.4: Energy dependence of the total nuclear reaction cross-sections σ_r for ^{10,14,16,18,20,22}C as projectiles on ^{12}C target. The results obtained from DD-ME2 and DD-PC1 densities and the Shen formula are compared with the available experimental data [187, 208, 209].

as a function of the projectile energy in the energy range of 30-1100 MeV/nucleon and experimental results are also given for comparison [199, 208, 209, 210]. The total reaction cross-section is higher at lower incident E (30-200 MeV/nucleon) and starts decreasing with the increase of E (400 MeV/nucleon). A small increment in σ_r appears at about 500-800 MeV/nucleon and after that it is constant. The calculated results using the Shen formula at high energy are also constant. We have seen that the total reaction cross-section σ_r also increases with the increase of the projectile mass. For example, the total reaction cross-section for ^{16}C is higher than the σ_r for ^{14}C with fixed ^{12}C target. This increase in σ_r may be related to the geometrical area πR^2. The sharp decrease in σ_r with increasing projectile energy up to 400 MeV/nucleon at which point π production causes the total cross-section to rise [211]. This remarkable dip in the total reaction cross-section can be attributed to the behaviour of the scattering phase shift.

The total reaction cross-section for an unstable+unstable projectile-target system is one of the main challenges in experimental nuclear physics. Such measurements give a better understanding of some of the cosmological phenomena such as supernovae, X-ray bursts, and in the r-process nucleosynthesis. In recent years, considerable efforts are underway at various laboratories to look for RIB+RIB cross-sections. To study the total reaction cross-section for the RIB+RIB system, we select ^{8}Li+^{8}Li, ^{14}Be+^{14}Be, and ^{8}B+^{8}B systems and the results are presented in Fig 3.5. In the figure, the variation of the total reaction cross-section using the densities from DD-ME2 and DD-PC1 parameter sets with various incident energies is shown. We found that the value of σ_r with DD-ME2 is a little bit higher than with the DD-PC1.

The total reaction cross-sections for medium mass nuclei of ^{40}Ca, ^{58}Ni, ^{90}Zr, and ^{120}Sn

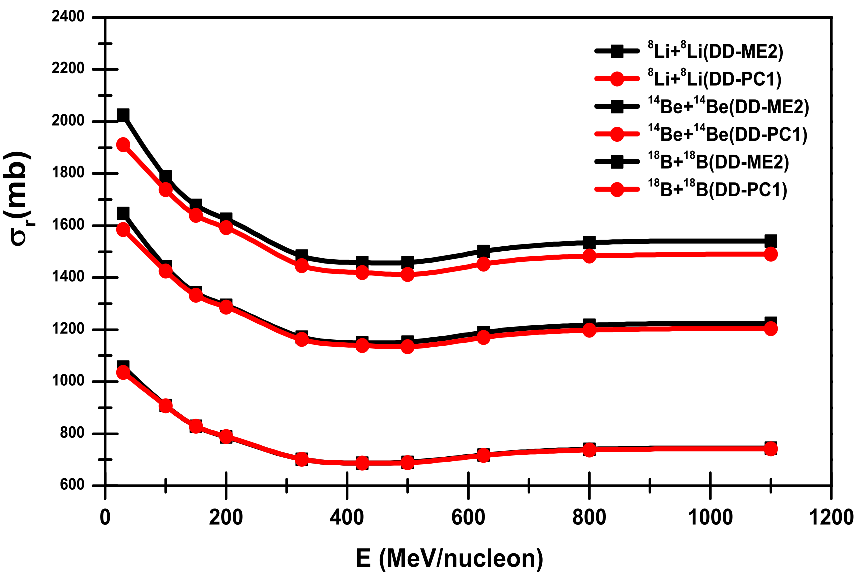

Figure 3.5: The total reaction cross-sections for ^{8}Li+^{8}Li, ^{14}Be+^{14}Be and ^{18}B+^{18}B systems using RHB densities with different energies.

as projectiles on proton target are shown in Fig 3.6. The experimental data are also given for comparison [212]. It is clear from Fig 3.6 that the calculated value of the total reaction cross-section is higher at small incident energy and starts decreasing up to 400 MeV/nucleon. σ_r increases in the range of 800 MeV/nucleon and after that, it remains constant. We also calculate the total reaction cross-section using the Axen formula and compare it with experimental data [212, 213, 214]. A similar trend is observed for all calculations on different projectiles. The total reaction cross-sections obtained

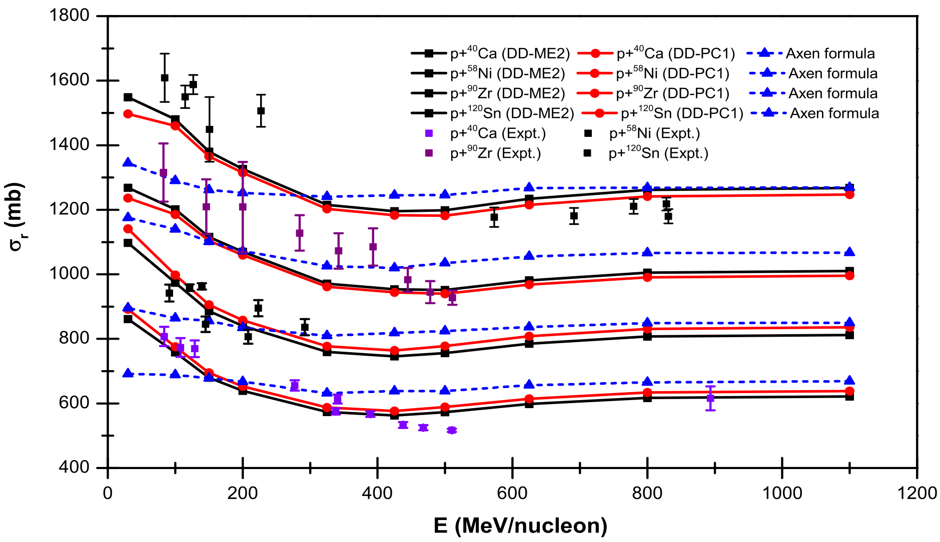

Figure 3.6: The comparison of total reaction cross-sections at different incident energies for ^{40}Ca, ^{58}Ni, ^{90}Zr, and ^{120}Sn as projectiles on proton target. Experimental data [212, 213, 214] are also given for comparison.

from the DD-PC1 densities are slightly higher than the ones obtained from the DD-ME2 densities. Also, the total reaction cross-section obtained from the DD-ME2 density agrees well with the experimental values. In low-energy regions, the experimental cross-section overestimates the theoretically obtained cross-sections.

3.2.3 Differential elastic scattering cross-section

We present numerical results for the elastic scattering differential cross-sections [eq. (2.4.53)] and compare them with the available experimental results to study how precisely our estimates for the nuclear size lie within the Glauber theory. We start with the calculation of the differential cross-section for ^{12}C+^{12}C system at incident energies 30 and 85 MeV/nucleon incident energies as presented in Fig 3.7. The comparison between our theoretical calculations and experimental data shows that calculated values agree well with the experimental data [123, 207], which suggests that the parameters of the NN scattering amplitude are well determined. At low angle region, both differential scattering cross-sections (DD-ME2 and DD-PC1) are similar to each other and show oscillatory structure, while at higher angle region, the cross-sections deviate slightly from the experimental data, but the nature of the curve is similar. In general, the results obtained

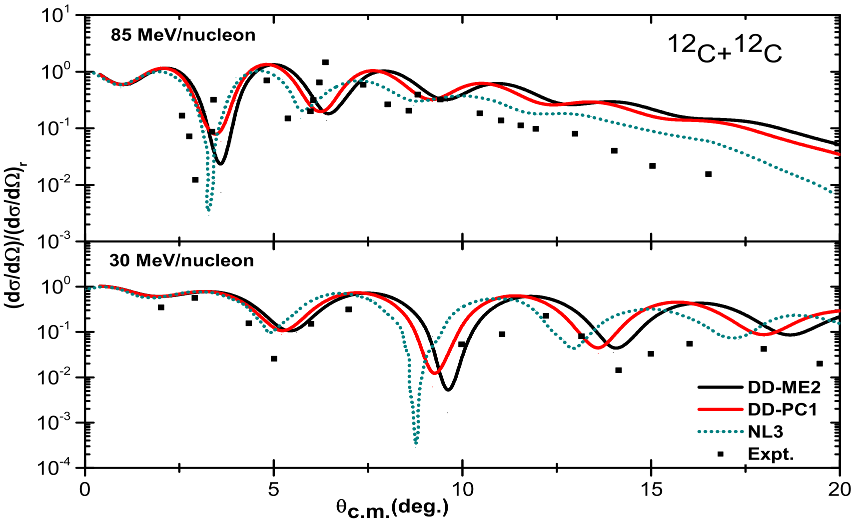

Figure 3.7: Comparison of elastic scattering differential cross-sections for $^{12}C+^{12}C$ system at 30 and 85 MeV/nucleon energies with experimental data. The experimental data are taken from reference [123, 207].

from DD-ME2 and DD-PC1 are similar and give excellent agreement in overall energy ranges. At high scattering angles, the calculated values of elastic scattering differential cross-sections overestimate the experimental data for $^{12}C+^{12}C$ system. Fig 3.7 also shows the comparison of results obtained in the present work with the results using the RMF (NL3) model [123] for $^{12}C+^{12}C$ system at 30 and 85 MeV/nucleon incident energies. The calculated values in the present work are slightly underestimated whereas the results obtained using RMF (NL3) are slightly overestimated at low-angle regions. At large angles, both approaches show a similar trend in comparison to the experimental data but fail to have a one-to-one correspondence with experimental results.

Fig 3.8 shows the differential cross-section for $^{6}He+^{12}C$ at 38.3 and 41.6 MeV/nucleon incident energies using RHB (DD-ME2 and DD-PC1) densities along with the experimental data [215, 216]. From Fig 3.8 we conclude that the RHB densities produce remarkable agreement of differential elastic cross-section with the experimental data. The role of realistic density for the two-neutron halo nucleus ^{6}He is confirmed in ref. [217], where the same experimental data have been analyzed using microscopic optical potentials obtained by a double-folding procedure and high-energy approximation. In this approach, the mi-

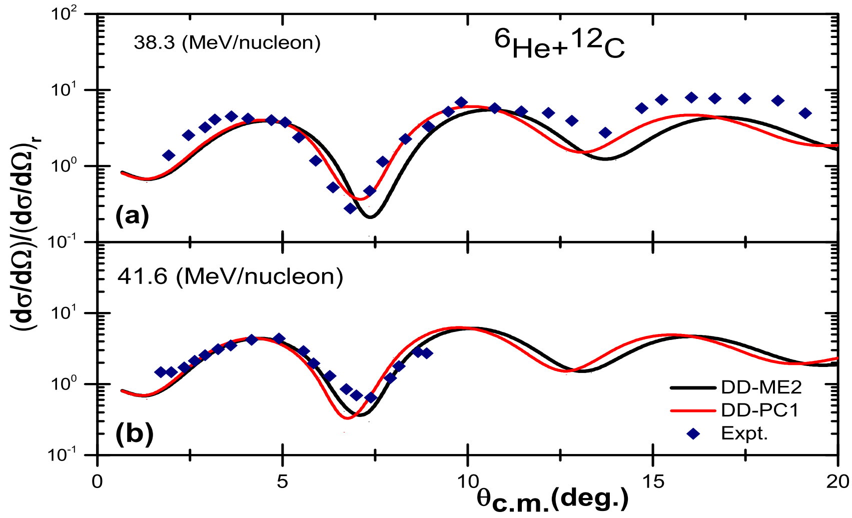

Figure 3.8: Elastic scattering differential cross-section for ^{6}He projectile on ^{12}C target: (a) at an incident energy of 38.3 MeV/nucleon; (b) at an incident energy of 41.6 MeV/nucleon. The experimental data are taken from reference [215, 216].

croscopic densities of protons and neutrons in ^{6}He were calculated within the large-scale shell model. In general, it is seen from Fig 3.8 that the experimental data are higher than differential elastic scattering cross-sections for RHB densities at high scattering angles.

Figure 3.9 presents our calculated value of the differential cross-section for the ^{14}Be+^{12}C

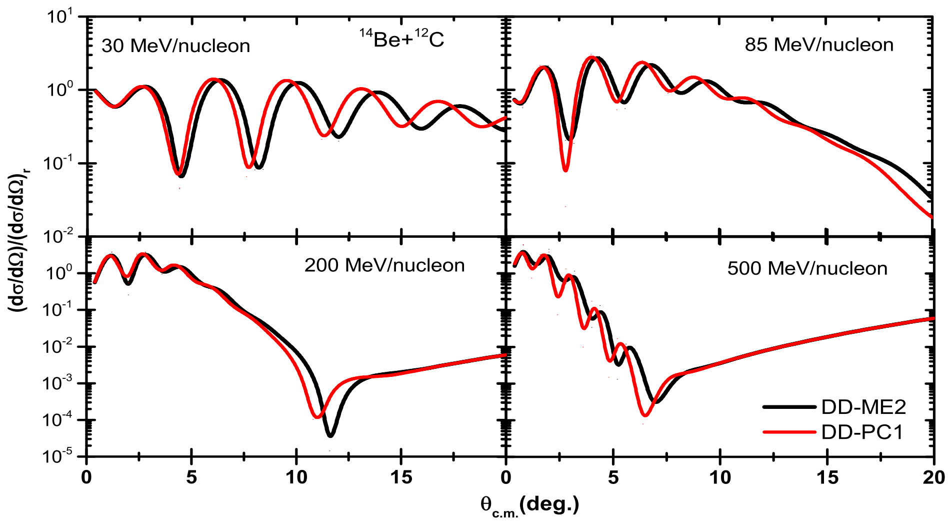

Figure 3.9: Elastic scattering differential cross-sections for ^{14}Be projectile on ^{12}C target at different energies as a function of scattering angle using the RHB (DD-ME2 and DD-PC1) formalism.

system at energies of 30, 85, 200, and 500 MeV/nucleon energies, respectively, using the DD-ME2 and DD-PC1 densities. From Fig 3.9 we can see that the calculated results for RHB (DD-ME2 and DD-PC1) formalism using the Glauber model are almost identical and show large variation with incident projectile energy. The DD-ME2 and DD-PC1 calculations produce a small difference up to the first minimum. The oscillatory structure of the elastic scattering differential cross-section at a low scattering angle increases with the increase of incident projectile energy. It is found that the diffraction pattern decreases with the increase of the scattering angle and disappears at high scattering angles. In the low scattering angle region DD-ME2 and DD-PC1 densities give similar patterns. Overall, this analysis also confirms that the elastic scattering cross-section is well reproduced using the correct wave function together with the profile function used in this study.

3.3 Conclusions

In summary, we have discussed bulk properties like binding energy and charge radius for light mass nuclei using RHB (DD-ME2 and DD-PC1) formalism. Our theoretical results show a good agreement with the available experimental data. In general, the calculated value of total reaction cross-section σ_r using DD-ME2 densities are better than the result obtained by using DD-PC1 densities. We have shown that the calculated values of σ_r are in good agreement with the experimental data. σ_r decreases with the increase of the projectile energy E and σ_r is almost constant at high energy, as observed experimentally too. It has been also found that the total reaction cross-section increases with the increase of the projectile mass. The analysis of the differential scattering cross-section shows a clear diffraction pattern in which the magnitude of separation is large at a small scattering angle and the oscillation keeps on decreasing with an increase in scattering angles, as well as incident energy. It is pertinent to mention that in the present work, the nuclear deformation has not been considered explicitly even though it affects the reaction cross-section. Even for large deformation $|\beta_2|{\sim}0.2$, it amounts to a variation of about 2 % only [159]. Thus, we can conclude that the combined effect of deformation and rotation is significantly smaller than the effect of large neutron excess which is largely embedded in the density profile. Hence, employing reliable density distribution in conjunction with the Glauber model leads to a satisfactory description of the total reaction cross-section and elastic scattering differential cross-section over a wide energy range.

Chapter 4

Cluster decay half-lives in trans-tin and transition metal region[1]

4.1 Introduction

Cluster radioactivity was first predicted in 1980 by Sandulescu, Poenaru, and Greiner [24] on the basis of fragmentation theory, where cold reaction (fusion or fission) valleys are generated by the shell closure effects of one both the reaction partners [218]. In this new type of exotic radioactive decay, i.e., the cluster radioactivity process, the parent nuclei emit a particle heavier than the alpha particle and lighter than the lightest fission fragments [101, 219]. The first experimental signature of cluster radioactivity was observed via the spontaneous emission of ^{14}C cluster from the decay of ^{223}Ra by Rose and Jones [52]. Subsequently, cluster decay has been experimentally observed in different nuclei of the trans-lead region (Z=87-96), namely for the cluster decay of ^{14}C, ^{18,20}O, ^{23}F, ^{22,24,26}Ne, ^{28,30}Mg, and ^{32,34}Si [71, 91, 220]. In this region (Z=87-96) all cluster emissions have a doubly magic nucleus of ^{208}Pb (Z=82, N=126) or its neighboring nuclei as the daughter nuclei. In the recent past, two new islands of emission of clusters have been predicted by several theoretical models, first in the superheavy nuclei (SHN) region and second in the trans-tin region (Z=56-64) [221, 222, 223]. For the parent nuclei lying in the trans-tin region (Z=56-64), it has been predicted that daughter nuclei lie close to doubly magic nuclei ^{100}Sn (Z=50, N=50) [224, 225]. It is important to note that the

[1]The results discussed in this chapter have been published in *J. Phys. G: Nucl. Part. Phys.*, 49, 025101 (2021).

first experimental observation of cluster decay from the trans-tin region has been already confirmed by Oganessian *et al.* [56] at Dubna (Russia) and by Guglielmetti *et al.* [226] at GSI (Germany) in 1995. So far about 20 potential cluster emitters have been observed experimentally [227].

Cluster radioactivity is theoretically understood in a similar approach to the Gamow model of alpha decay based on the quantum tunneling effect. However, the description can be mainly classified into two types of approaches. The first one is known as the Preformed cluster model, it is assumed that the clusters made of several nucleons are performed in the parent nucleus before they could tunnel through the barrier created by the nuclear and Coulomb potentials [104, 105, 106]. The exponential dependence of the calculated tunneling probability thus calculated leads to a modified Geiger-Nutall law of cluster radioactivity of the particular cluster emission, relating half-lives for CR to the Q value of the reaction. However, in the second type of theoretical approach, namely the fission-based model [108], the parent nucleus is assumed to be deformed continuously and reach the saddle or scission shape to undergo cluster radioactivity [36, 94, 107]. In such type of fission model-based approach, Gamow's idea of quantum mechanical barrier penetration is still used, but without worrying about the cluster being or not being performed in the parent nucleus. Here the parent nucleus is assumed to undergo continuous dynamical changes from the initial one-nucleus system to the final separated multi-nucleus systems, as it penetrates the nuclear potential barrier and attains the saddle configuration, where both the masses and charges of the fission fragments are fixed. In this approach, the shape parametrization is chosen as fission-like, where the decaying system is considered as two intersecting spheres of different radii which are used to describe the decaying fragments. On the same lines, the Effective Liquid Drop Model (ELDM) developed by Goncalves and Duarte [162, 163, 164] is a successful model for calculating alpha decay, proton emission, and cluster radioactivity in a unified framework and has been used extensively for studying cluster radioactivity [228]. Microscopic calculations for the cluster radioactivity half-life predictions are thus model dependent as different microscopic/phenomenological nuclear models are used to calculate mass defect and the Q-value of the reaction with separate calculations for cluster emission probability. In addition, to reduce the model dependence and consider the Q value dependence, several analytic formulas have been introduced by fitting Q values and experimentally observed half-lives of cluster radioactivity processes. In 1993, Gupta *et al.* [30] first predicted the instability of 'stable' nuclei in the region $50 < Z < 82$ against exotic cluster decay using preformed cluster model. Based on analytic super asymmetric fission model [29] and preformed cluster model [31], half-life

for proton-rich nuclei (Z=56-64 and N=58-72) was calculated for cluster emissions ranging from ^{4}He to ^{28}Si. This region thus provided another very interesting CR case as daughter nuclei in the decay are found to doubly magic daughter nuclei ^{100}Sn (Z=50, N=50) or neighboring near-doubly magic nuclei. The calculated half-life for CR in this region is lower than the upper limit of measurement($T_{1/2} < 10^{30} s$). In recent years, the half-lives of cluster decay from ^{8}Be to ^{32}Si have been evaluated using different models for several nuclei in the different mass regions including the nuclei which are far from the β stability line either side [229, 230, 231, 232]. Very recently, Santhosh *et al.* [233, 234] have studied the cluster radioactivity of the trans-lead region by employing different models. In these studies, it has been shown that the cluster radioactivity of these nuclei is dependent on the models used. The CR nuclei in the transition metal region $72 \leqslant Z \leqslant 80$ exotic decay have not been confirmed experimentally yet. The confirmed cluster decay is found corresponding to the doubly magic daughter nuclei or its neighboring magic nuclei.
In this chapter, we have used the Effective Liquid Drop Model (ELDM) to determine the cluster decay half-lives, using mass excess data calculated from the relativistic mean-field model (NL3* parameter set) and test its accuracy and predicted ability. In the present work, we have calculated the binding energy per nucleon (B.E./A) of various isotopes of even-even parent nuclei (Xe, Ba, Ce, Nd, Hf, W, Os, Pt, and Hg), daughter nuclei, and emitted clusters (^{8}Be, ^{12}C, ^{16}O, ^{20}Ne and ^{24}Mg) using RMF (NL3* parameter set) model. The mass excess data (ΔM) for cluster decay is evaluated by making use of these binding energy per nucleon. This mass excess data (ΔM) has been used further, as input to obtain a Q value and determine the cluster decay half-lives with the ELDM. Further, to check the reliability, prediction ability, and model dependence of these calculations, we have compared our results with the available experimental results and other theoretical calculations including the ones that use the empirical formula Universal Decay Law (UDL) and the Scaling Law by Horoi *et al.*. Also, the Geiger-Nuttall plots of $Q^{(-1/2)}$ versus $log_{10}T_{1/2}$ for emission of ^{8}Be, ^{12}C, ^{16}O, ^{20}Ne, and ^{24}Mg clusters for various isotopes of parent nuclei have been analyzed.

4.2 Results and Discussions

In this chapter, we have studied the cluster decay half-lives ($log_{10}T_{1/2}$) from various isotopes of even-even parent nuclei (Xe, Ba, Ce, Nd, Hf, W, Os, Pt, and Hg) for the emission of alpha-like (^{8}Be, ^{12}C, ^{16}O, ^{20}Ne, and ^{24}Mg) clusters and half-lives of the non-alpha-like (^{22}Ne and ^{26}Mg) CR are also calculated for W and Nd isotopes. The mass defect and

Q values needed for cluster decay half-lives determination is calculated using the RMF model with NL3* parameter [111, 115]. Further, the calculation of cluster decay half-lives have been done using the Effective Liquid Drop Model (ELDM) [162, 163, 164]. In the ELDM, there are two inertial coefficients (Warner-Wheeler inertial coefficient and Effective inertial coefficient) used and two different modes (Varying Mass Asymmetry Shape (VMAS) and Constant Mass Asymmetry Shape (CMAS)) of cluster decay. We used a combination of the Varying mass Asymmetry Shape and Werner-Wheeler's inertia in the ELDM. It is to be noted here that all cluster decay half-lives calculations in ELDM have been performed here by using zero angular momenta. In the binding energy per nucleon calculation, we have used the oscillator shell N_F=N_B=20 for fermions and bosons.
At first, we calculate the binding energy per nucleon of various isotopes of parent nuclei, then find mass excess data, Q values, penetrability, decay constant, and clusters decay half-lives. We have determined the mass excess data (ΔM) by using the binding energy per nucleon in RMF (NL3* parameter set). The relation between binding energy per nucleon and mass excess data is given by

$$\text{Mass of the Nuclei} = ((\text{N}^*M_n + \text{Z}^*M_p)^*931.5 \text{ - A}^*\text{B.E./A})/931.5 \text{ u}$$
$$\Delta M = (\text{ Mass of the Nuclei - Mass No. of Nuclei})^*931.5 \text{ MeV}$$

Namely in the calculations of Q values and cluster decay half-lives, we use these mass excess data following the main purpose of the present study. To calculate the Q-value, we used mass excess data of RMF (NL3*) and finite-range-droplet model (FRDM). The following relation is given by,
^{8}Be :

$$Q_{Be}(N, Z) = \Delta M_p(N, Z) - \Delta M_d(N-4, Z-4) - \Delta M_e(4, 4) \tag{4.2.1}$$

^{12}C :

$$Q_C(N, Z) = \Delta M_p(N, Z) - \Delta M_d(N-6, Z-6) - \Delta M_e(6, 6) \tag{4.2.2}$$

^{16}O :

$$Q_O(N, Z) = \Delta M_p(N, Z) - \Delta M_d(N-8, Z-8) - \Delta M_e(8, 8) \tag{4.2.3}$$

^{20}Ne :

$$Q_{Ne}(N, Z) = \Delta M_p(N, Z) - \Delta M_d(N-10, Z-10) - \Delta M_e(10, 10) \tag{4.2.4}$$

^{24}Mg :

$$Q_{Mg}(N, Z) = \Delta M_p(N, Z) - \Delta M_d(N-12, Z-12) - \Delta M_e(12, 12) \tag{4.2.5}$$

Here $\Delta M_p(N, Z)$ is the mass excess of the parent nucleus in MeV, $\Delta M_d(N-4, Z-4)$, $\Delta M_d(N-6, Z-6)$, $\Delta M_d(N-8, Z-8)$, $\Delta M_d(N-10, Z-10)$ and $\Delta M_d(N-12, Z-12)$ are the mass excess of the daughter nuclei and $\Delta M_e(4,4)$, $\Delta M_e(6,6)$, $\Delta M_e(8,8)$, $\Delta M_e(10,10)$ and $\Delta M_e(12,12)$ are the mass excess of the clusters ^{8}Be, ^{12}C, ^{16}O, ^{20}Ne and ^{24}Mg, respectively. The FRDM mass excess data are taken from reference [235]. The positive Q value ($Q > 0$) for all possible combinations (parent and cluster) have been considered.

In this chapter, we have compared the prediction ability of different approaches used for

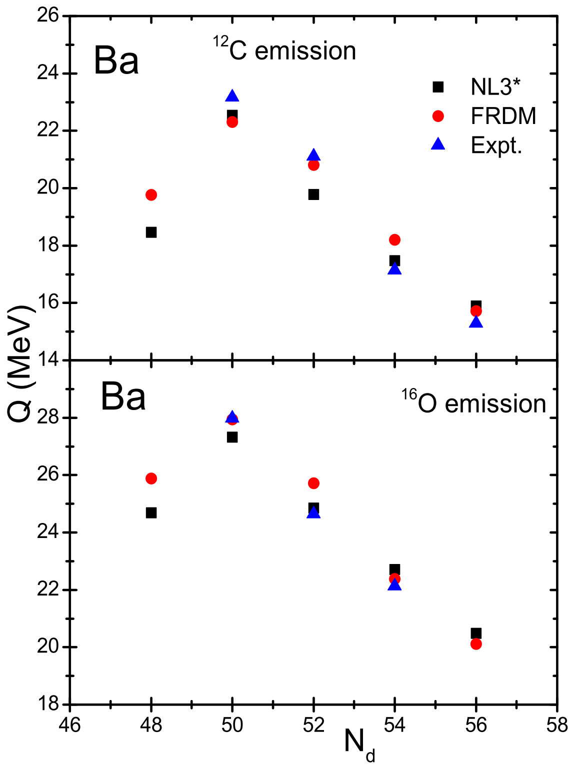

Figure 4.1: The Q values for the alpha-like clusters (^{12}C and ^{16}O) decay from Ba isotopes using RMF formalism with NL3* parameter set, compared with the FRDM and experimental data, wherever available.

cluster decay half-lives. For this, we have compared the results obtained by the ELDM model with the results obtained by the empirical formula, namely the UDL empirical formula and Scaling Law by Horoi *et al.*. Further, to compare the impact of the difference in Q value, we have also compared calculated half-lives using ELDM by two sets of Q-values obtained from RMF calculations, as well as from FRDM data.

Table 4.1: The Q-value, penetrability P, decay constant, and decay half-lives ($log_{10}T_{1/2}$ (s)) for the decay of alpha-like cluster (^{8}Be, ^{12}C, ^{16}O, and ^{20}Ne) from even-even parent nuclei in the trans-tin region.

Parent nuclei	**Daughter nuclei**	**Emitted cluster**	**Q (MeV)**			**Penetrability P**	**Decay constant $\lambda(s^{-1})$**	**$log_{10}T_{1/2}$ (s)**				
			NL3*	**FRDM**	**Expt.** [236]			**NL3***	**UDL**	**Horoi**	**FRDM**	**DNSM** [236]
^{106}Xe	^{98}Sn	^{8}Be	6.94	8.12		7.85×10^{-46}	1.69×10^{-25}	22.58	21.24	23.35	16.02	
^{108}Xe	^{100}Sn	^{8}Be	10.19	11.41		8.73×10^{-31}	2.76×10^{-10}	7.53	6.93	5.09	3.73	
^{110}Xe	^{102}Sn	^{8}Be	8.52	10.25		2.68×10^{-37}	7.08×10^{-17}	14.05	13.19	13.23	7.24	
^{112}Xe	^{104}Sn	^{8}Be	6.77	8.13		$1.01 \times 10-46$	2.13×10^{-26}	23.47	22.13	24.83	15.78	
^{114}Xe	^{106}Sn	^{8}Be	5.08	6.49		3.02×10^{-60}	4.78×10^{-40}	36.99	34.83	41.28	25.22	
^{108}Ba	^{100}Te	^{8}Be	6.98	8.24		3.92×10^{-48}	8.53×10^{-28}	24.88	23.49	25.66	17.73	
^{110}Ba	^{102}Te	^{8}Be	9.1	10.40		5.82×10^{-37}	1.65×10^{-16}	13.71	12.92	12.39	8.69	
^{112}Ba	^{104}Te	^{8}Be	7.97	9.22		3.36×10^{-42}	8.34×10^{-22}	18.95	17.92	18.82	13.1	
^{114}Ba	^{106}Te	^{8}Be	6.23	7.32		2.17×10^{-43}	4.15×10^{-53}	29.86	28.26	32.04	22.52	
^{116}Ba	^{108}Te	^{8}Be	4.38	5.81		1.10×10^{-52}	1.48×10^{-71}	48.31	45.47	53.97	33.31	
^{108}Xe	^{96}Cd	^{12}C	14.23	14.77		3.60×10^{-45}	1.42×10^{-24}	21.93	21.06	18.16	20.04	
^{110}Xe	^{98}Cd	^{12}C	16.59	17.18		1.51×10^{-37}	6.99×10^{-17}	14.28	13.70	9.28	12.68	
^{112}Xe	^{100}Cd	^{12}C	14.96	15.44		1.88×10^{-42}	7.85×10^{-22}	19.21	18.47	15.28	17.64	
^{114}Xe	^{102}Cd	^{12}C	12.51	12.95		9.00×10^{-52}	3.14×10^{-31}	28.55	27.44	26.43	26.6	
^{116}Xe	^{104}Cd	^{12}C	10.35	10.86		1.17×10^{-62}	3.37×10^{-42}	39.46	37.81	39.30	36.53	
^{110}Ba	^{98}Sn	^{12}C	18.46	19.77		3.37×10^{-35}	1.73×10^{-14}	11.95	11.45	6.15	8.86	
^{112}Ba	^{100}Sn	^{12}C	22.54	22.31	23.17	1.93×10^{-26}	1.21×10^{-05}	3.19	2.79	-4.19	3.61	0.44
^{114}Ba	^{102}Sn	^{12}C	19.78	20.81	21.11	6.83×10^{-32}	3.77×10^{-11}	8.64	8.22	2.51	6.42	4.08
^{116}Ba	^{104}Sn	^{12}C	17.48	18.2	17.15	1.96×10^{-37}	9.57×10^{-17}	14.18	13.70	9.27	12.28	16.20
^{118}Ba	^{106}Sn	^{12}C	15.89	15.72	15.29	5.52×10^{-42}	2.45×10^{-21}	18.73	18.14	14.78	19.29	22.56

(Continued on next page)

Table 4.1 – continued from previous page

Parent nuclei	Daughter nuclei	Emitted cluster	Q (MeV)			Penetrability P	Decay constant $\lambda(s^{-1})$	$log_{10}T_{1/2}$ (s)				
			NL3*	FRDM	Expt. [236]			NL3*	UDL	Horoi	FRDM	DNSM [236]
^{112}Ba	^{96}Cd	^{16}O	24.68	25.88		9.10×10^{-42}	6.12×10^{-21}	18.51	17.86	10.91	15.84	
^{114}Ba	^{98}Cd	^{16}O	27.32	27.94	27.98	5.38×10^{-36}	4.01×10^{-15}	12.74	12.17	4.52	11.53	5.80
^{116}Ba	^{100}Cd	^{16}O	24.85	25.71	24.65	3.99×10^{-41}	2.70×10^{-20}	17.87	17.28	10.56	15.95	15.40
^{118}Ba	^{102}Cd	^{16}O	22.71	22.38	22.13	2.72×10^{-46}	1.68×10^{-25}	23.08	22.38	16.59	23.95	22.41
^{120}Ba	^{104}Cd	^{16}O	20.48	20.11		1.19×10^{-52}	6.61×10^{-32}	29.4	28.59	23.93	30.58	
^{114}Ce	^{98}Sn	^{16}O	31.69	31.65		5.75×10^{-31}	4.96×10^{-10}	7.71	7.14	-1.46	7.79	
^{116}Ce	^{100}Sn	^{16}O	32.43	33.54		1.18×10^{-29}	1.04×10^{-08}	6.41	5.83	-2.79	4.72	
^{118}Ce	^{102}Sn	^{16}O	30.08	30.79	30.55	1.95×10^{-33}	1.60×10^{-12}	10.18	9.68	1.74	8.95	7.38
^{120}Ce	^{104}Sn	^{16}O	27.31	27.77		1.29×10^{-38}	9.61×10^{-18}	15.36	14.88	7.80	14.42	
^{122}Ce	^{106}Sn	^{16}O	25.11	25.12		2.23×10^{-43}	1.52×10^{-22}	20.13	19.61	13.35	20.12	
^{116}Ce	^{96}Cd	^{20}Ne	31.56	34.02		1.17×10^{-48}	9.97×10^{-28}	25.41	24.59	16.35	20.33	
^{118}Ce	^{98}Cd	^{20}Ne	33.09	34.83	34.64	2.78×10^{-45}	2.49×10^{-24}	22.03	21.27	12.96	18.63	13.04
^{120}Ce	^{100}Cd	^{20}Ne	30.31	32.19		2.81×10^{-51}	2.30×10^{-30}	28.05	27.23	19.57	23.76	
^{122}Ce	^{102}Cd	^{20}Ne	26.15	28.69		3.84×10^{-62}	2.72×10^{-41}	38.89	37.88	31.35	31.88	
^{124}Ce	^{104}Cd	^{20}Ne	23.91	25.84		2.97×10^{-69}	1.92×10^{-48}	46.01	44.78	39.06	39.71	
^{126}Ce	^{106}Cd	^{20}Ne	20.69	23.13		1.50×10^{-81}	8.40×10^{-61}	58.31	56.62	52.12	48.61	
^{118}Nd	^{98}Sn	^{20}Ne	36.53	39.03		2.62×10^{-41}	2.59×10^{-20}	18.06	18.29	9.41	14.71	
^{120}Nd	^{100}Sn	^{20}Ne	37.99	40.1		1.28×10^{-38}	1.31×10^{-17}	15.38	15.58	6.89	12.84	
^{122}Nd	^{102}Sn	^{20}Ne	34.17	37.54	37.58	1.96×10^{-45}	1.81×10^{-24}	22.18	22.58	14.37	16.92	13.30
^{124}Nd	^{104}Sn	^{20}Ne	31.67	34.5		1.53×10^{-50}	1.32×10^{-29}	27.29	27.81	20.14	22.45	
^{126}Nd	^{106}Sn	^{20}Ne	28.34	31.62		3.83×10^{-59}	2.94×10^{-38}	35.89	35.97	29.09	28.51	
^{128}Nd	^{108}Sn	^{20}Ne	25.18	28.76		1.98×10^{-66}	1.35×10^{-45}	43.18	45.12	39.08	35.51	

The results have been tabulated in table 4.1. The first column contains the parent nuclei, second and third columns contain the daughter nuclei and emitted clusters, respectively. The calculated Q-values using RMF in the present work along with FRDM, and experimental values [236] are listed in columns 4, 5, and 6, respectively. The penetrability and decay constants (λ) for the alpha-like cluster decays are given in columns 7 and 8 respectively. Columns 9-11 contain the cluster decay half-lives obtained using ELDM, UDL formula, and Horoi formula. Column 12 contains ELDM results with Q values obtained from FRDM data, and column 13 lists DNSM results [236] for the sake of comparison. From the results, one can see that ELDM and UDL results are quite similar but show a small difference in comparison to the results obtained by the Scaling Law of Horoi. This can be understood as the Horoi formula is the simple scaling law and the coefficient sets are estimated by fitting the experimental data with the parent charge number Z=87-96 only. Although small nuclear structure information is taken into account, their prediction power is not good. However, the UDL formula is derived from the α-like R-matrix theory, so its prediction accuracy is close to the microscopic results. The calculated Q values from RMF (NL3* parameter set) are also given in table 4.1 and are compared with FRDM values. A small discrepancy is observed which can be attributed to the microscopic origin of calculations of one set considering pairing strength and shell correction energy terms.

In table 4.2, we have presented the calculated Q values and cluster decay half-lives using RMF (NL3*), UDL, and the Scaling law of Horoi in the transition metal region. The experimental and FRDM data taken from reference [202, 235] respectively, are also given for comparison. It is evident from table 4.2 that the calculated Q values using RMF (NL3*) are slightly lower than the FRDM and experimental data because a small change in the values of a parameter of the NL3* and FRDM will affect the values of binding energy per nucleon. Also, we compare half-lives of RMF (NL3*), UDL, Horoi, FRDM, and UNIV reference [237]. The calculated half-lives using RMF (NL3*) and UDL values are almost the same but the results obtained by the Horoi formula are slightly lower. From Table 4.2 we can see that the calculated half-lives are larger than the FRDM and UNIV values. This disagreement can be understood due to the variation of Q values in RMF (NL3*), FRDM, and experimental data.

It can be seen from figure 4.1 that for the cluster decay of ^{12}C from $^{110-118}$Ba isotopes, the Q value has a maximum at doubly magic nuclei ^{100}Sn ($Z_d = 50, N_d = 50$). For the cluster decay of ^{16}O from $^{112-120}$Ba isotopes the Q value has a maximum for the formation of near doubly magic daughter nuclei ^{98}Cd ($Z_d = 48, N_d = 50$). The shell effect at $N_d = 50$ is very obvious and the shell effect at ^{100}Sn is most pronounced. Figure 4.2 shows

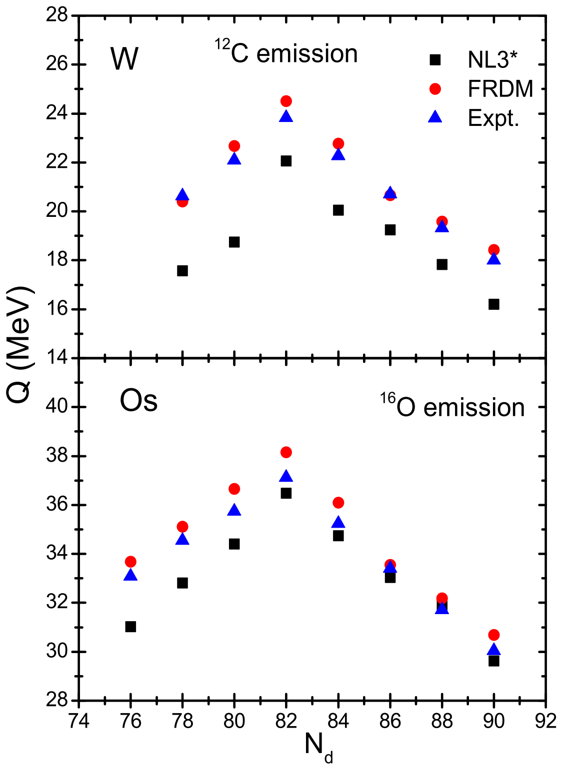

Figure 4.2: Same as figure 4.1, but for the clusters (^{12}C and ^{16}O) decay from W and Os isotopes, respectively.

the results for the Q values for the alpha-like clusters decay from W and Os isotopes of the transition metal region. It is observed that for the cluster decay of ^{12}C from $^{158-170}$W isotopes, the Q value has a maximum for daughter nuclei ^{150}Er ($Z_d = 68, N_d = 82$) and similarly ^{16}O decay from $^{160-174}$Os, the Q value has a maximum for daughter nuclei ^{150}Er ($Z_d = 68, N_d = 82$). The analyses of figures 4.1 and 4.2 clearly show that the calculated Q value indicates shell effects at $N_d = 50$, 82 and affects the half-lives. As the size of the α-like cluster increases, the Q value also increases.

The half-lives of the alpha-like clusters (^{12}C and ^{16}O) decay from various isotopes within the RMF(NL3*), UDL, Scaling Law by Horoi *et al.*, FRDM and DNS models as a function of the neutron number of a daughter (N_d) are plotted in figures 4.3 and 4.4. We can see from figure 4.3, where the plot for the cluster decay of ^{12}C from $^{108-116}$Xe and $^{110-118}$Ba isotopes is presented, that the minima of the cluster decay half-lives are found for the decay leading to near doubly magic daughter nuclei ^{98}Cd ($Z_d = 48, N_d = 50$) and doubly magic nuclei ^{100}Sn ($Z_d = 50, N_d = 50$), respectively.

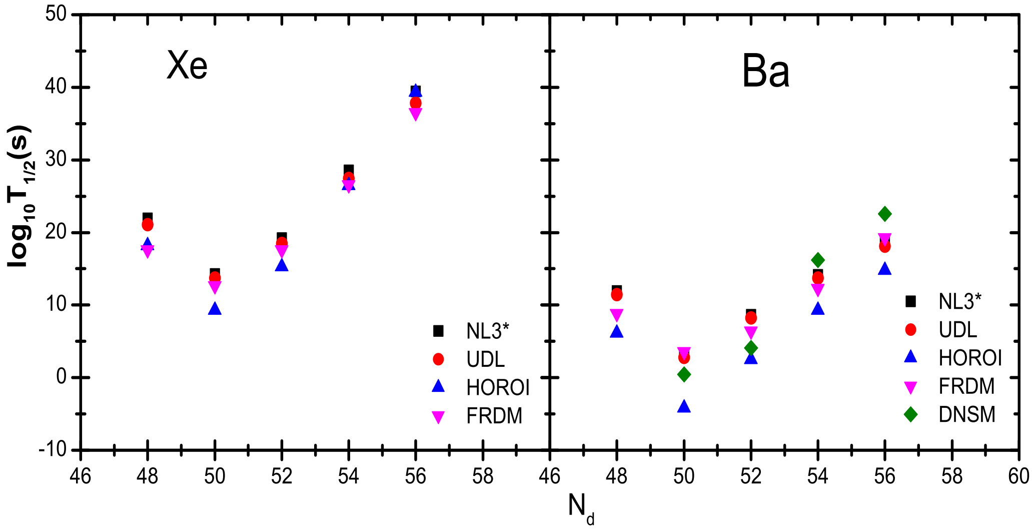

Figure 4.3: The computed $\log_{10}T_{1/2}$ (in s) values plotted against the neutron number of daughter nuclei (N_d) for the emission of ^{12}C from Xe and Ba isotopes. The DNSM data are taken from reference [236].

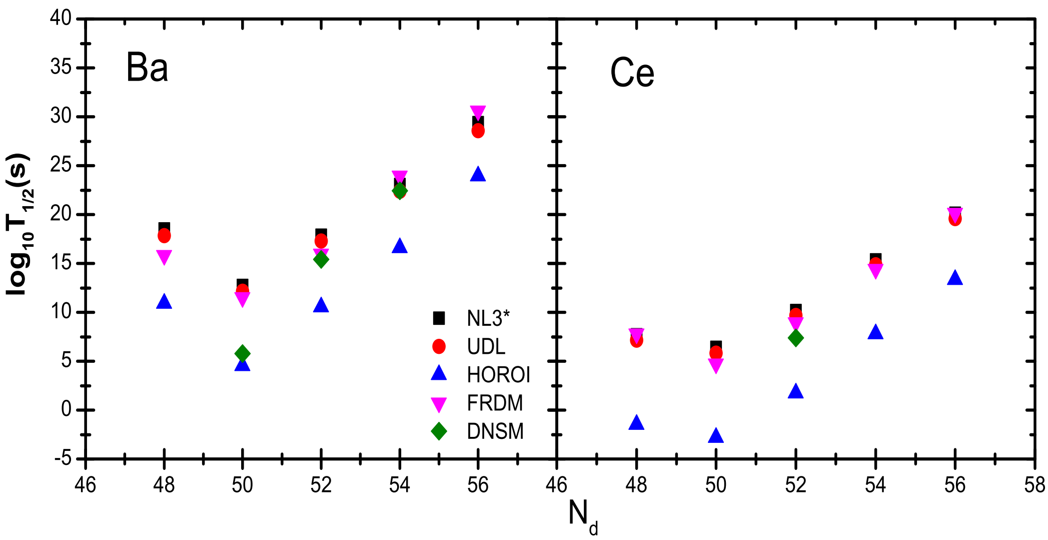

Figure 4.4: Same as for figure 4.3, but for the ^{16}O decay half-lives in the Ba and Ce isotopes. The DNSM data are taken from reference [236].

Table 4.2: The Q-value, penetrability P, decay constant ($\lambda(s^{-1})$) and decay half-lives ($log_{10}T_{1/2}$ (s)) for the decay of alpha-like cluster (^{8}Be, ^{12}C, ^{16}O, ^{20}Ne, and ^{24}Mg) from even-even parent nuclei in the transition metal region.

Parent nuclei	**Daughter nuclei**	**Emitted cluster**	**Q (MeV)**			**Penetrability P**	**Decay constant $\lambda(s^{-1})$**	**$log_{10}T_{1/2}$ (s)**				
			NL3*	**FRDM**	**Expt.** [202]			**NL3***	**UDL**	**Horoi**	**FRDM**	**UNIV** [237]
^{156}Hf	^{148}Er	^{8}Be	5.43	8.54	8.67	6.24×10^{-84}	1.05×10^{-63}	60.21	57.98	63.29	33.06	31.7
^{158}Hf	^{150}Er	^{8}Be	7.93	11.49	10.78	2.13×10^{-60}	5.24×10^{-40}	37.16	35.98	38.09	18.33	20.82
^{160}Hf	^{152}Er	^{8}Be	6.73	10.13	9.62	7.34×10^{-70}	1.53×10^{-49}	46.61	44.88	48.41	24.24	26.27
^{162}Hf	^{154}Er	^{8}Be	5.89	8.43	8.49	3.44×10^{-78}	6.30×10^{-58}	54.94	52.68	57.46	33.62	32.57
^{164}Hf	^{156}Er	^{8}Be	5.26	7.79	7.45	9.67×10^{-86}	1.58×10^{-65}	62.49	59.73	65.66	37.91	
^{166}Hf	^{158}Er	^{8}Be	4.56	6.97	6.50	6.87×10^{-96}	9.75×10^{-76}	72.64	69.18	76.63	44.31	
^{158}W	^{150}Yb	^{8}Be	6.07	9.84	10.001	1.75×10^{-79}	3.30×10^{-59}	56.24	53.94	57.91	27.89	26.46
^{160}W	^{152}Yb	^{8}Be	8.86	12.72	12.002	1.25×10^{-56}	3.43×10^{-36}	33.39	32.54	33.65	15.58	6.44
^{162}W	^{154}Yb	^{8}Be	8.05	11.51	10.990	2.03×10^{-61}	5.07×10^{-41}	38.17	37.45	39.34	20.06	21.72
^{164}W	^{156}Yb	^{8}Be	7.34	10.11	10.088	2.89×10^{-67}	6.58×10^{-47}	44.01	42.56	45.24	26.30	25.81
^{166}W	^{158}Yb	^{8}Be	7.04	9.29	9.180	1.90×10^{-69}	4.17×10^{-49}	46.19	44.78	47.82	30.54	30.56
^{168}W	^{160}Yb	^{8}Be	6.02	8.47	8.338	1.17×10^{-78}	2.19×10^{-58}	55.14	54.06	58.49	35.54	
^{160}Os	^{152}Hf	^{8}Be	6.28	10.39	10.42	5.01×10^{-80}	9.78×10^{-60}	56.77	54.56	57.89	28.16	
^{162}Os	^{154}Hf	^{8}Be	9.56	13.74	13.288	9.74×10^{-55}	2.89×10^{-34}	31.49	30.81	31.28	13.85	14.89
^{164}Os	^{156}Hf	^{8}Be	8.62	13.07	12.453	6.47×10^{-57}	1.73×10^{-36}	33.78	36.12	37.34	15.99	17.73
^{166}Os	^{158}Hf	^{8}Be	8.10	11.62	11.724	7.96×10^{-64}	2.01×10^{-43}	40.78	39.41	41.13	21.39	20.44
^{168}Os	^{160}Hf	^{8}Be	8.01	10.94	11.002	1.74×10^{-64}	4.32×10^{-44}	41.25	40.05	41.93	24.27	23.37
^{170}Os	^{162}Hf	^{8}Be	7.59	10.09	10.30	1.56×10^{-67}	3.68×10^{-47}	44.34	42.95	45.26	28.31	26.58
^{158}W	^{146}Er	^{12}C	17.58	20.41	20.627	1.84×10^{-59}	9.03×10^{-39}	36.21	35.97	33.28	26.63	25.09

(Continued on next page)

Table 4.2 – continued from previous page

Parent nuclei	Daughter nuclei	Emitted cluster	Q (MeV)			Penetrability	Decay	$log_{10}T_{1/2}$ (s)				
			NL3*	**FRDM**	**Expt.** [202]	**P**	**constant** $\lambda(s^{-1})$	**NL3***	**UDL**	**Horoi**	**FRDM**	**UNIV** [237]
^{160}W	^{148}Er	^{12}C	18.74	22.67	22.102	4.07×10^{-55}	2.13×10^{-34}	31.86	31.81	28.89	20.31	7.15
^{162}W	^{150}Er	^{12}C	22.07	24.51	23.830	5.33×10^{-45}	3.28×10^{-24}	21.75	21.98	18.39	15.85	16.8
^{164}W	^{152}Er	^{12}C	20.05	22.77	22.266	1.15×10^{-50}	6.43×10^{-30}	27.41	27.53	24.51	19.85	20.41
^{166}W	^{154}Er	^{12}C	19.25	20.67	20.716	4.07×10^{-53}	2.18×10^{-32}	29.86	29.92	27.20	25.46	24.44
^{168}W	^{156}Er	^{12}C	17.83	19.58	19.323	5.78×10^{-58}	2.87×10^{-37}	34.71	34.61	32.39	28.72	
^{170}W	^{158}Er	^{12}C	16.21	18.42	18.010	2.18×10^{-64}	9.86×10^{-44}	41.14	40.79	39.19	32.54	
^{160}Os	^{148}Yb	^{12}C	18.76	21.6	21.98	9.87×10^{-58}	5.17×10^{-37}	34.48	34.41	31.24	25.52	
^{162}Os	^{150}Yb	^{12}C	20.66	24.34	24.135	2.09×10^{-51}	1.20×10^{-30}	28.15	28.29	24.83	18.38	18.16
^{164}Os	^{152}Yb	^{12}C	23.02	26.49	25.848	9.81×10^{-45}	6.31×10^{-24}	21.48	21.80	18.02	13.61	14.44
^{166}Os	^{154}Yb	^{12}C	22.35	24.94	24.495	2.13×10^{-46}	1.32×10^{-25}	23.15	23.44	19.87	16.81	17.19
^{168}Os	^{156}Yb	^{12}C	21.74	23.23	23.271	5.98×10^{-48}	3.63×10^{-27}	24.69	24.97	21.62	20.17	19.88
^{170}Os	^{158}Yb	^{12}C	20.51	21.97	22.083	1.88×10^{-5}	1.07×10^{-30}	28.21	28.41	25.42	23.98	22.77
^{172}Os	^{160}Yb	^{12}C	18.39	20.86	20.932	1.83×10^{-58}	9.41×10^{-38}	35.21	35.18	32.79	27.07	
^{158}W	^{142}Dy	^{16}O	29.61	31.64	31.162	3.49×10^{-55}	2.81×10^{-34}	31.93	32.04	26.49	27.12	27.17
^{160}W	^{144}Dy	^{16}O	30.06	32.68	31.93	6.06×10^{-54}	4.96×10^{-33}	30.96	30.84	25.42	24.72	8.05
^{162}W	^{146}Dy	^{16}O	30.71	33.89	33.291	2.80×10^{-52}	2.34×10^{-31}	29.03	29.22	23.88	22.09	22.53
^{164}W	^{148}Dy	^{16}O	34.23	35.58	34.362	1.59×10^{-44}	1.48×10^{-23}	21.27	21.53	16.13	18.71	20.38
^{166}W	^{150}Dy	^{16}O	31.52	32.94	32.158	3.45×10^{-50}	2.96×10^{-29}	26.94	27.19	22.07	23.79	24.57
^{168}W	^{152}Dy	^{16}O	29.39	30.29	29.971	4.09×10^{-55}	3.28×10^{-34}	31.86	32.06	27.23	29.69	
^{170}W	^{154}Dy	^{16}O	27.04	28.73	27.842	2.25×10^{-61}	1.65×10^{-40}	38.12	38.22	33.67	33.48	
^{172}W	^{156}Dy	^{16}O	25.86	26.17	26.16	9.22×10^{-65}	6.50×10^{-44}	41.51	41.53	37.32	40.57	

(Continued on next page)

Table 4.2 – continued from previous page

Parent nuclei	Daughter nuclei	Emitted cluster	Q (MeV) NL3*	Q (MeV) FRDM	Q (MeV) Expt. [202]	Penetrability P	Decay constant $\lambda(s^{-1})$	$log_{10}T_{1/2}$ (s) NL3*	UDL	Horoi	FRDM	UNIV [237]
^{160}Os	^{144}Er	^{16}O	31.03	33.68	33.08	1.42×10^{-54}	2.67×10^{-27}	31.32	31.51	25.76	25.39	
^{162}Os	^{146}Er	^{16}O	32.81	35.12	34.556	2.22×10^{-50}	8.35×10^{-25}	27.11	27.39	21.71	22.34	22.58
^{164}Os	^{148}Er	^{16}O	34.41	36.65	35.743	6.74×10^{-47}	5.70×10^{-23}	23.64	23.95	18.37	19.31	20.32
^{166}Os	^{150}Er	^{16}O	36.48	38.15	37.131	9.73×10^{-43}	9.11×10^{-19}	19.49	19.81	14.35	16.53	17.8
^{168}Os	^{152}Er	^{16}O	34.75	36.1	35.244	6.17×10^{-46}	4.72×10^{-23}	22.68	23.03	17.74	20.08	20.93
^{170}Os	^{154}Er	^{16}O	33.04	33.55	33.415	2.35×10^{-49}	1.33×10^{-25}	26.01	26.45	21.31	25.03	24.32
^{172}Os	^{156}Er	^{16}O	31.91	32.18	31.712	8.78×10^{-52}	1.55×10^{-29}	28.54	28.87	23.91	27.91	
^{174}Os	^{158}Er	^{16}O	29.62	30.68	30.045	3.29×10^{-57}	1.83×10^{-33}	33.96	34.24	29.51	31.32	
^{166}Pt	^{150}Yb	^{16}O	36.89	38.92	38.583	1.65×10^{-44}	1.66×10^{-23}	21.26	21.67	15.98	17.68	17.67
^{168}Pt	^{152}Yb	^{16}O	38.96	41.08	40	9.80×10^{-41}	1.04×10^{-19}	17.48	17.83	12.26	14.02	15.33
^{170}Pt	^{154}Yb	^{16}O	37.79	39.33	38.364	1.21×10^{-42}	1.24×10^{-21}	19.39	19.78	14.36	16.73	17.78
^{172}Pt	^{156}Yb	^{16}O	36.73	37.40	36.898	1.78×10^{-44}	1.77×10^{-23}	21.22	21.64	16.36	19.98	20.14
^{174}Pt	^{158}Yb	^{16}O	35.34	36.16	35.428	4.61×10^{-47}	4.45×10^{-26}	23.82	24.26	19.12	22.19	22.68
^{176}Pt	^{160}Yb	^{16}O	33.64	34.59	33.96	1.73×10^{-50}	1.59×10^{-29}	27.24	27.69	22.71	26.23	
^{166}Pt	^{146}Er	^{20}Ne	40.02	46.44	46.572	2.51×10^{-63}	2.72×10^{-42}	40.02	40.18	33.02	27.26	26.1
^{168}Pt	^{148}Er	^{20}Ne	41.35	47.98	47.463	3.09×10^{-60}	3.46×10^{-39}	36.98	37.15	30.27	24.46	24.54
^{170}Pt	^{150}Er	^{20}Ne	45.28	49.28	48.568	2.61×10^{-52}	3.21×10^{-31}	29.06	29.25	22.87	22.18	22.7
^{172}Pt	^{152}Er	^{20}Ne	43.21	47.01	46.438	3.90×10^{-56}	4.57×10^{-35}	32.88	33.11	26.72	25.81	25.9
^{174}Pt	^{154}Er	^{20}Ne	40.31	44.48	44.328	4.40×10^{-62}	4.80×10^{-41}	38.83	39.06	32.58	30.25	29.35
^{176}Pt	^{156}Er	^{20}Ne	38.32	42.65	42.32	1.31×10^{-66}	1.35×10^{-45}	43.36	43.54	37.04	33.71	
^{178}Pt	^{158}Er	^{20}Ne	36.28	40.77	40.35	1.33×10^{-71}	1.31×10^{-50}	48.35	48.47	41.93	37.53	

(Continued on next page)

Table 4.2 – continued from previous page

Parent nuclei	**Daughter nuclei**	**Emitted cluster**	**Q (MeV)**			**Penetrability P**	**Decay constant** $\lambda(s^{-1})$	$log_{10}T_{1/2}$ **(s)**				
			NL3*	**FRDM**	**Expt.** [202]			**NL3***	**UDL**	**Horoi**	**FRDM**	**UNIV** [237]
^{170}Hg	^{150}Yb	^{20}Ne	44.18	50.86	50.95	1.18×10^{-57}	1.41×10^{-36}	34.41	34.68	27.78	22.65	
^{172}Hg	^{152}Yb	^{20}Ne	46.31	52.59	52.253	1.93×10^{-53}	2.42×10^{-32}	30.21	30.45	23.95	19.82	19.84
^{174}Hg	^{154}Yb	^{20}Ne	45.94	50.69	50.327	6.84×10^{-54}	8.52×10^{-33}	30.64	31.12	24.63	22.58	22.42
^{176}Hg	^{156}Yb	^{20}Ne	45.38	48.54	48.527	7.24×10^{-55}	8.91×10^{-34}	31.62	31.93	25.67	25.95	25.01
^{178}Hg	^{158}Yb	^{20}Ne	42.51	47.02	46.735	1.70×10^{-60}	1.96×10^{-39}	37.24	37.58	31.19	28.45	27.77
^{180}Hg	^{160}Yb	^{20}Ne	39.73	45.31	44.956	4.38×10^{-77}	4.71×10^{-56}	52.70	43.56	37.02	31.49	30.72
^{166}Pt	^{142}Dy	^{24}Mg	52.88	58.54	59.262	1.97×10^{-60}	2.81×10^{-39}	37.18	37.07	29.42	27.63	26.13
^{168}Pt	^{144}Dy	^{24}Mg	53.42	58.86	59.446	2.64×10^{-59}	3.82×10^{-38}	36.05	35.96	28.58	26.96	25.72
^{170}Pt	^{146}Dy	^{24}Mg	54.56	59.53	60.183	4.05×10^{-57}	5.98×10^{-36}	33.87	33.79	26.76	25.77	24.57
^{172}Pt	^{148}Dy	^{24}Mg	57.63	60.69	60.689	8.31×10^{-52}	1.29×10^{-30}	28.55	28.43	22.03	23.87	23.75
^{174}Pt	^{150}Dy	^{24}Mg	53.49	57.62	57.924	1.54×10^{-58}	2.23×10^{-37}	35.29	35.38	28.59	28.41	27.38
^{176}Pt	^{152}Dy	^{24}Mg	50.61	54.23	55.11	5.64×10^{-64}	7.73×10^{-43}	40.72	40.75	33.71	33.93	
^{178}Pt	^{154}Dy	^{24}Mg	48.64	51.95	52.33	8.27×10^{-68}	1.09×10^{-46}	44.56	44.60	37.43	37.94	
^{180}Pt	^{156}Dy	^{24}Mg	46.67	49.37	50.02	6.02×10^{-72}	7.61×10^{-51}	48.69	48.73	41.73	42.88	
^{170}Hg	^{146}Er	^{24}Mg	56.21	62.51	63.97	6.36×10^{-58}	9.68×10^{-37}	34.62	34.68	27.33	24.81	
^{172}Hg	^{148}Er	^{24}Mg	58.03	63.62	64.303	9.99×10^{-55}	1.56×10^{-33}	31.47	31.42	24.62	23.01	22.01
^{174}Hg	^{150}Er	^{24}Mg	60.76	64.77	65.118	3.08×10^{-50}	5.06×10^{-29}	26.99	26.87	20.63	21.24	20.87
^{176}Hg	^{152}Er	^{24}Mg	59.31	62.28	62.654	1.90×10^{-52}	3.05×10^{-31}	29.19	29.14	22.89	24.57	23.76
^{178}Hg	^{154}Er	^{24}Mg	55.97	59.47	60.222	1.13×10^{-57}	1.71×10^{-36}	34.42	34.47	27.92	28.65	26.85
^{180}Hg	^{156}Er	^{24}Mg	53.79	57.49	57.893	2.03×10^{-61}	2.95×10^{-40}	38.17	38.27	31.55	31.68	30.04
^{182}Hg	^{158}Er	^{24}Mg	51.43	55.3	55.66	8.21×10^{-66}	1.14×10^{-44}	42.56	42.69	35.75	35.27	

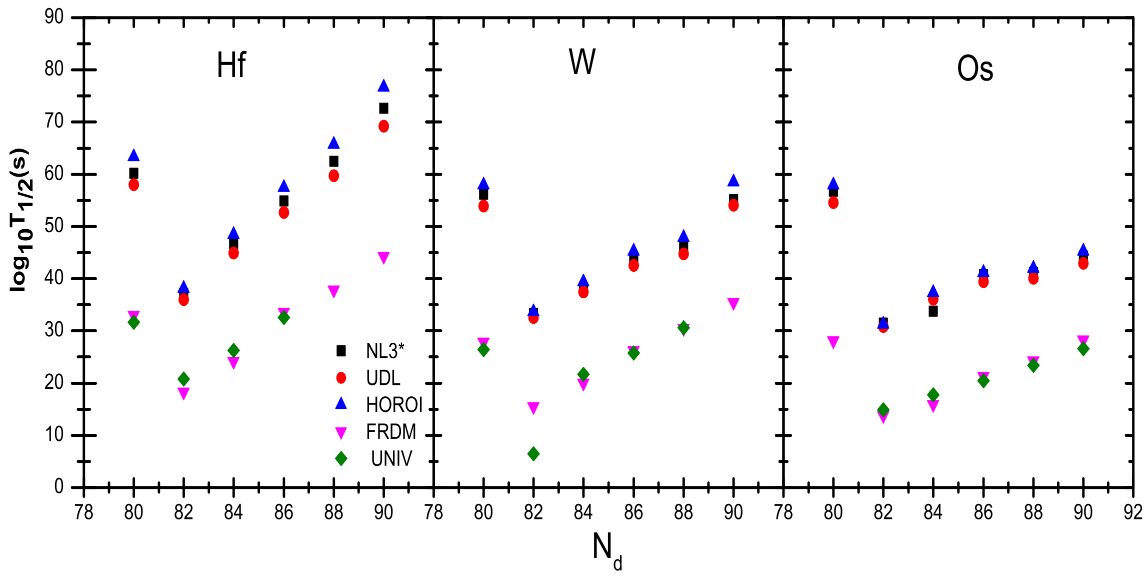

Figure 4.5: The $\log_{10}T_{1/2}$ (in s) values for ^{8}Be decay from various isotopes of the parent nuclei (Hf, W, and Os nuclei, respectively) plotted as a function of the neutron number of daughter nuclei (N$_d$). The UNIV data are taken from reference [237].

Figure 4.4 illustrates the cluster decay of ^{16}O from $^{112-120}$Ba and $^{114-122}$Ce isotopes. The minima of the cluster decay half-lives are found for the decay leading near doubly magic daughter nuclei ^{98}Cd ($Z_d = 48, N_d = 50$) and doubly magic nuclei ^{100}Sn ($Z_d = 50, N_d = 50$), respectively. It is clearly seen from figures 4.3 and 4.4 that the shell stabilizes at magic daughter nuclei ($N_d = 50$). We also compare these results with the results obtained from the dinuclear system model (DNMS) [236]. From Table 4.1 it is found that the difference is significant between our calculated half-lives and those with the DNSM, which is caused by the differences of our calculated Q-values and those of reference [236]. The CR half-lives are strongly dependent on the Q-values and the model chosen. The logarithm of half-life evaluated using RMF (NL3*) are compared with the experimental half-life [57] and reference [50] for ^{12}C cluster emitting from ^{114}Ba, and are given in Table 4.3. We see that the calculated RMF (NL3*) half-life is close to experimental data in comparison to the results of GLDM reference [50]. Therefore, the approach adopted in the present work (by calculating cluster decay half-lives using ELDM with RMF inputs) explains well for potential CR nuclei in trans-tin and transition metal regions.

The half-lives of the alpha-like clusters (^{8}Be, ^{12}C, and ^{16}O) decay of some isotopes (transition metal region) within the RMF(NL3*), UDL, and Scaling Law by Horoi *et al.*,

Table 4.3: Comparison between the experimental data of the ^{12}C radioactivity of ^{114}Ba isotope and the estimated ones by the NL3*, GLDM, FRDM and DNSM.

Parent nucleus	Daughter nucleus	cluster decay	Q (MeV) NL3*	Expt. [238]	FRDM [235]	Ref. [236]	$log_{10}T_{1/2}$ (s) NL3*	UDL	GLDM [50]	Expt. [57, 50]	FRDM	DNSM [236]
^{114}Ba	^{102}Sn	^{12}C	19.78	19.0	20.81	21.11	8.64	8.22	9.90	>4.10	6.42	4.08

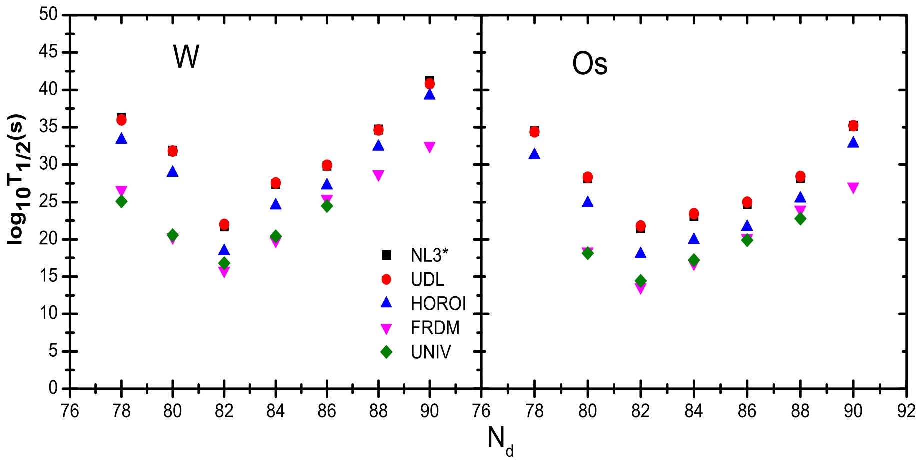

Figure 4.6: Same as for figure 4.5, but for the ^{12}C decay half-lives in the W and Os isotopes. The UNIV data are taken from reference [237].

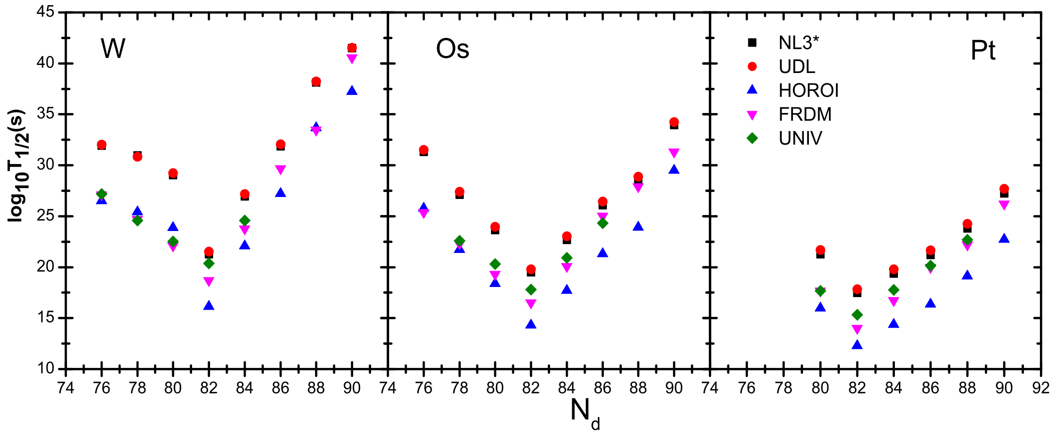

Figure 4.7: Same as for figure 4.5 and 4.6, but for the ^{16}O decay half-lives in the W, Os, and Pt isotopes. The UNIV data are taken from reference [237].

FRDM and UNIV [237] models as a function of the neutron number of a daughter (N_d) are plotted in figures 4.5-4.7. Figure 4.5 shows the plot for the cluster decay of ^{8}Be from $^{156-166}$Hf, $^{158-168}$W, and $^{160-170}$Os isotopes, respectively. The cluster decay half-lives are found to have minima for the decay leading to daughter nuclei ^{150}Er ($Z_d = 68, N_d = 82$), ^{152}Yb ($Z_d = 70, N_d = 82$), and ^{154}Hf ($Z_d = 72, N_d = 82$), which have magic neutron number $N_d = 82$. Figure 4.6 presents the cluster decay of ^{12}C from $^{158-170}$W and $^{160-172}$Os isotopes. The cluster decay half-lives are found to have a minimum value for the decay leading to magic daughter nuclei ^{150}Er ($Z_d = 68, N_d = 82$), ^{152}Yb ($Z_d = 70, N_d = 82$), respectively. Similarly, Figure 4.7 shows the cluster decay of ^{16}O from $^{158-172}$W, $^{160-174}$Os, and $^{166-176}$Pt isotopes. The minima of the cluster decay half-lives are found for the decay leading to magic daughter nuclei ^{148}Dy ($Z_d = 66, N_d = 82$), ^{150}Er ($Z_d = 68, N_d = 82$), ^{152}Yb ($Z_d = 70, N_d = 82$), respectively. The minimum value in the cluster decay half-lives corresponds to the higher barrier penetrability, which shows the doubly magic character (proton/neutron shell closure) of the daughter nuclei. In the present studies on trans-tin and transition metal region, it has been found that the decay half-lives have a minimum value for the decay leading to the doubly magic daughter nuclei ^{100}Sn ($Z_d = 50, N_d = 50$) or its neighboring daughter nuclei and magic daughter nuclei $N_d = 82$, respectively. Also, the decay half-lives show the minimum value for the magic neutron number of a daughter (N_d = 50, 82). These observations reveal the role of the strong shell effects in cluster radioactivity. We can see from figures 4.5-4.7 that the half-lives $log_{10}T_{1/2}$ shown versus neutron number of daughter nuclei N_d reveal the fact that the NL3*, UDL, Scaling Law by Horoi *et al.*, FRDM and UNIV exhibit almost similar trends in all plots, but the half-lives obtained using the Scaling Law by Horoi *et al.* reveal small deviations from NL3* and UDL values.

We also calculate the Q-values and half-lives of the alpha-like ($A_e = 4n, Z_e = N_e$, Z_e and N_e are the atomic number and neutron number of the emitted cluster, respectively) cluster radioactivity, as well as non-alpha-like ($A_e = 4n + 2, Z_e \neq N_e$) cluster radioactivity. The results are plotted in figures 4.8 and 4.9, respectively. The Q value of the ^{20,22}Ne decays for $^{160-174}$W isotopes obtained from RMF (NL3*) formalism are given in figure 4.8(a) for comparison. It is clear from figure 4.8(a) that the calculated Q value of ^{20}Ne decay is greater than those of the ^{22}Ne decays with shell effect at $N_d = 82$. We have repeated the same calculations for ^{24,26}Mg decays in $^{118-130}$Nd isotopes using the same formalism and the results are shown in figure 4.8(b). The Q-values of the ^{24}Mg decay are higher than those of the ^{26}Mg decay. In figure 4.9(a) we show the half-lives of the ^{20}Ne decay in W isotopes obtained from RMF (NL3*) formalism and empirical formulas (UDL and Scaling

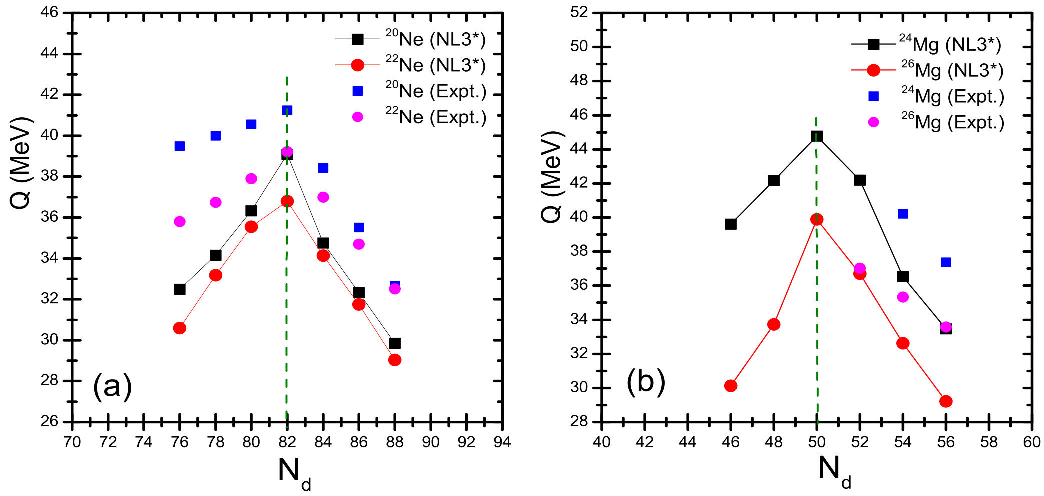

Figure 4.8: Comparison of Q value obtained from RMF (NL3*) calculations: (a) for ^{20,22}Ne emissions from W isotopes, (b) for ^{24,26}Mg emissions from Nd isotopes. The experimental data are taken from reference [202].

Law by Horoi *et al.*). For the same nucleus, the half-lives of the ^{22}Ne decay are shown in figure 4.9(b) for comparison. We would like to note that the half-lives of ^{22}Ne decay are greater than those of the ^{20}Ne decays. The minima of the cluster decay half-lives are found for the decay leading to magic daughter nuclei ^{146}Gd ($Z_d = 64, N_d = 82$). We have repeated the same calculations for ^{24,26}Mg decays in Nd isotopes using the same methods and the results are shown in figures 4.9(c) and (d). In this case, also the half-lives of the non-alpha-like cluster (^{26}Mg) decay is higher than those of the alpha-like cluster (^{24}Mg) decay. The minima of the cluster decay half-lives are found for the near doubly magic daughter nuclei ^{98}Cd ($Z_d = 48, N_d = 50$). Low Q values of the non-alpha-like cluster decays lead to larger half-lives. This results in the fact that non-alpha-like clusters decay are more complicated to observe than alpha-like $Z_e = N_e$.

In order to investigate the predictive power of our chosen model, we have calculated the standard deviation of half-live ($log_{10}T_{1/2}$) values for the RMF (NL3*) and have compared it with the calculated standard deviation of half-lives values of UDL and Scaling Law of Horoi. The standard deviation is given by

$$\sigma = \left[\frac{1}{n-1}\sum_{i=1}^{n}[log(T_{1/2}^{cal}) - log(T_{1/2}^{exp})]^2\right]^{1/2}. \qquad (4.2.6)$$

In the case of FRDM, we found that the standard deviation of the $log_{10}T_{1/2}$ is 5.32 for RMF (NL3*), 4.28 for UDL, and 6.62 for the scaling law of Horoi. For the case of DNSM,

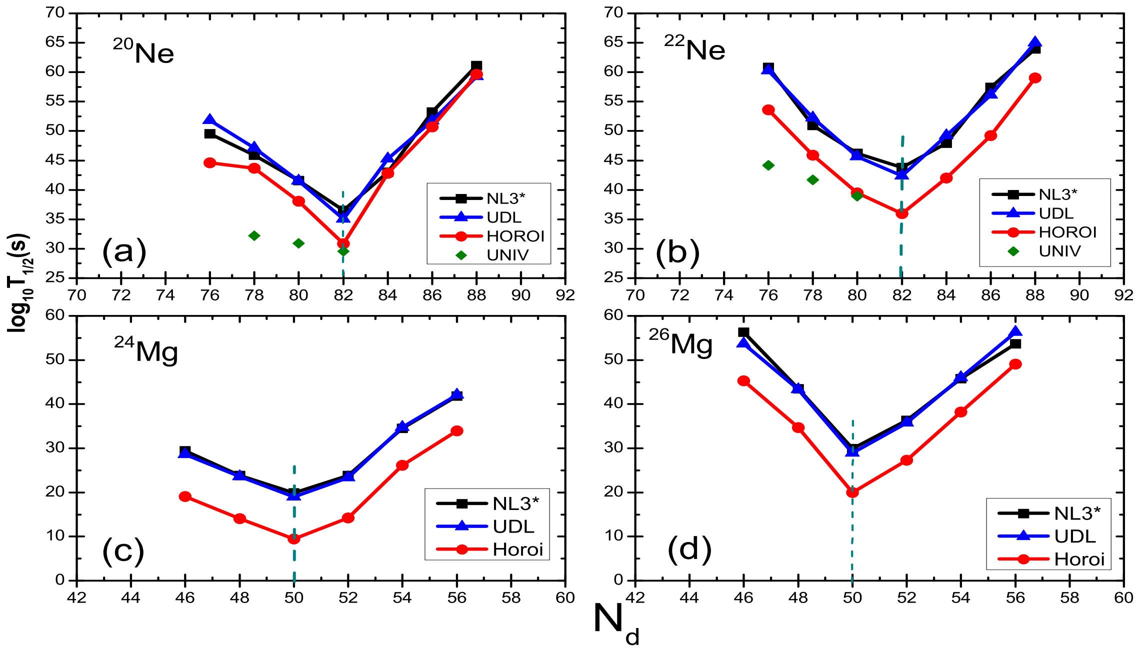

Figure 4.9: Comparison of half-lives obtained from RMF (NL3*) and empirical formula (UDL and Horoi) calculations: (a) for ^{20}Ne emission from W isotopes, (b) for ^{22}Ne emission from W isotopes, (c) for ^{24}Mg emission from Nd isotopes, and (d) for ^{26}Mg emission from Nd isotopes. The UNIV data are taken from reference [237].

we found that the standard deviation of the $log_{10}T_{1/2}$ is 5.46 for RMF (NL3*), 5.26 for UDL, and 4.99 for the scaling law of Horoi.

In 1911 Geiger and Nuttall experimentally confirmed the relation between the decay constant λ and the range R of alpha particles, which is the Geiger-Nuttall law [239, 240]. Figure 4.10 shows the Geiger-Nuttall plots for half-lives ($log_{10}T_{1/2}$) versus $Q^{-1/2}$ (Q in MeV) for the different clusters (^{8}Be, ^{12}C, ^{16}O, ^{20}Ne and ^{24}Mg) emitted from the parents $^{106-116}$Xe, $^{108-120}$Ba, $^{114-126}$Ce, $^{118-128}$Nd, $^{156-166}$Hf, $^{158-172}$W, $^{160-174}$Os, $^{166-180}$Pt, and $^{170-182}$Hg isotopes. A linear behavior in each case is clearly shown in figure 4.10. The Geiger-Nuttall law is written in the form:

$$log_{10}T_{1/2} = \frac{X}{\sqrt{Q}} + Y, \tag{4.2.7}$$

where X and Y are the slopes and intercepts of the straight lines, respectively. We would like to point out that the G-N law is for pure Coulomb potential. The calculated results plots reveal that the inclusion of surface potential and shell effect (through Q value) will not produce an extreme variation to the straight-line behavior. Each emitted alpha-like cluster has a distinct slope and intercept.

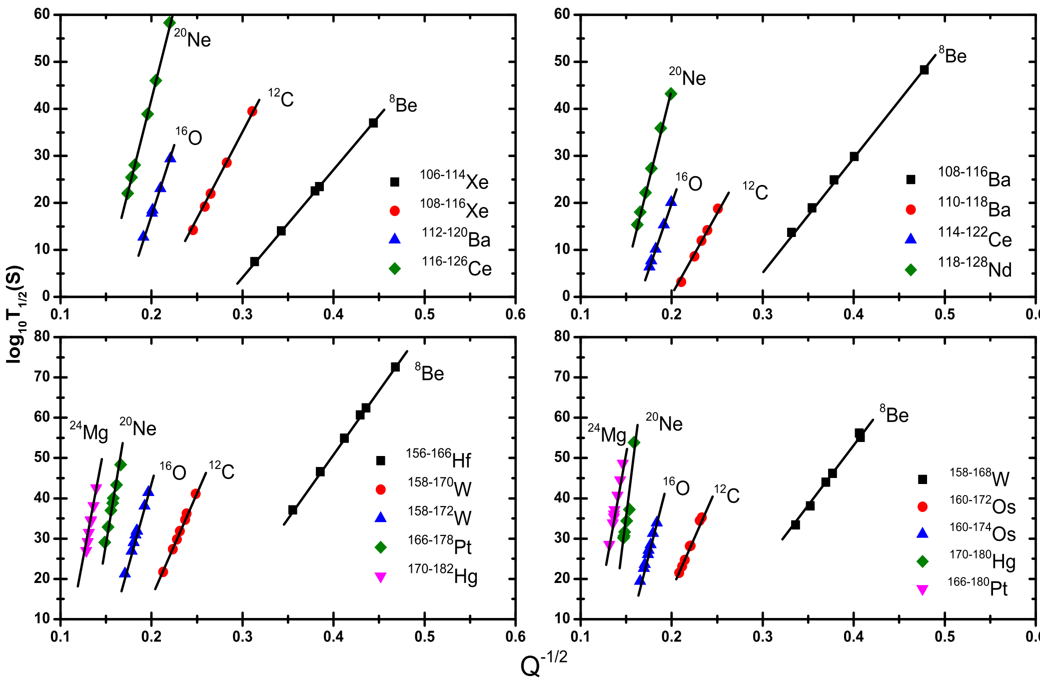

Figure 4.10: Geiger-Nuttall plots for $\log_{10}T_{1/2}$ (in s) versus $Q^{-1/2}(\mathrm{MeV}^{-1/2})$ for alpha-like clusters from different parent nuclei.

To examine the validity of the ELDM, we have shown the plot (Universal curve) between

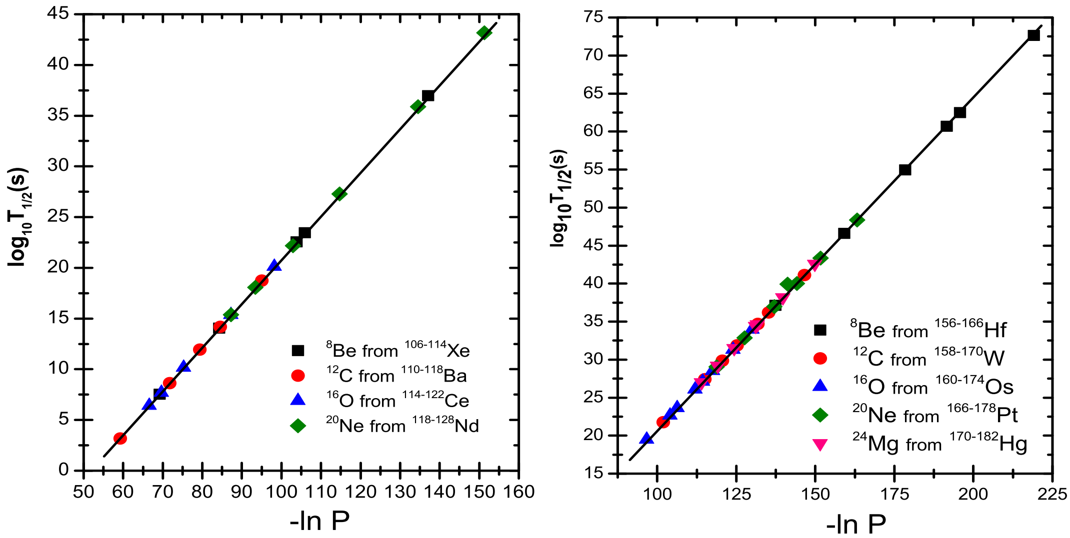

Figure 4.11: Universal curve for calculated $\log_{10}T_{1/2}$ (in s) versus negative logarithm of penetrability (-ln P) for alpha-like clusters (^{8}Be, ^{12}C, ^{16}O, ^{20}Ne and ^{24}Mg) from different parent nuclei.

logarithmic half-lives ($log_{10}T_{1/2}$) versus the negative logarithm of penetrability (-ln P). The universal curves for ^{8}Ba, ^{12}C, ^{16}O and ^{20}Ne from the parents $^{106-114}$Xe, $^{110-118}$Ba, $^{114-122}$Ce, and $^{118-128}$Nd and ^{8}Ba, ^{12}C, ^{16}O, ^{20}Ne and ^{24}Mg from the parents $^{156-166}$Hf, $^{158-170}$W, $^{160-174}$Os, $^{166-178}$Pt, and $^{170-182}$Hg are given in figure 4.11. Here, both the graphs are found to have linear behavior with nearly equal slopes of 0.457 and intercepts of -20.923, which exhibit that the assault frequency is almost a constant for all cluster's decay. This shows that the inclusion of surface potential does not produce a significant variation in the linear behavior of universal curves.

4.3 Conclusions

In summary, we have studied the Q values and cluster decay half-lives for even-even CR nuclei in the trans-tin region ($^{106-116}$Xe, $^{108-120}$Ba, $^{114-126}$Ce, and $^{118-128}$Nd) and transition metal region ($^{156-166}$Hf, $^{158-172}$W, $^{160-174}$Os, $^{166-180}$Pt, and $^{170-182}$Hg) using RMF model with NL3* parameter set and empirical formulas: UDL and Scaling Law by Horoi *et al.*. The ELDM of cluster decay has been used to calculate cluster decay half-lives.

The calculated Q value has a maximum for near doubly magic daughter nuclei ^{98}Cd, ^{102}Te and doubly magic daughter nuclei ^{100}Sn (Z = 50, N = 50) in the trans tin region and transition metal nuclei, the Q value has a maximum for neutron number of daughter nuclei N_d = 82, which is a magic number. The calculated Q value indicates the shell effects at N_d = 50, 82 and influences the half-lives. In the trans-tin region, the minima of the cluster decay half-lives are found for the decay leading to doubly magic daughter nuclei ^{100}Sn (Z = 50, N = 50) and near doubly magic daughter nuclei ^{102}Te, ^{98}Cd. The cluster decay half-lives are found to have a minimum value for the decay leading magic daughter nuclei ^{150}Er (Z = 68, N = 82), near doubly magic nuclei ^{152}Yb (Z = 70, N = 82), ^{154}Hf (Z = 72, N = 82), respectively, in transition metal region. The calculated half-lives of cluster decay using RMF(NL3*) are compared with the values of the empirical formula UDL and Scaling Law by Horoi *et al.*. It is found that our results obtained with ELDM in conjunction with RMF are close to the results obtained with the UDL formula. It can be seen that the prediction power of the Horoi formula is limited. It has been found that the UDL formula, derived from the α-like R-matrix theory, has better prediction ability giving comparable results with microscopic calculations. Also, results obtained in this work are in good agreement with experimental data as compared to the GLDM results [50]. Therefore, the ELDM in conjunction with relativistic model inputs is well-suited for explaining CR from trans-tin and transition metal regions. The decay constant (λ) for cluster decay will be maximum if the corresponding logarithmic half-life is minimum. It is found that the Q values of the ^{20}Ne and ^{24}Mg ($N_e = Z_e$) decays are larger than those of the ^{22}Ne and ^{26}Mg ($N_e \neq Z_e$) decays, but the half-lives of the non-alpha-like cluster (^{22}Ne and ^{26}Mg) decays are higher than those of the alpha-like cluster (^{20}Ne and ^{24}Mg) decays. Low Q values of the non-alpha-like cluster emissions lead to larger half-lives. The Geiger-Nuttal plots clearly show a linear behavior with different slopes and intercepts for various α-like clusters decay from various parent nuclei.

Chapter 5

Structure and decay modes study of Th, U, and Pu isotopes[1]

5.1 Introduction

The study of structural properties of heavy and super-heavy nuclei has become an interesting problem of nuclear physics with increasing access to the nuclei at extremes. Heavy nuclei are normally dynamically unstable. The energy is obtained by breaking the heavy nucleus into two components. However, few heavy nuclei decay by quantum-mechanical leakage through the potential barrier. The alpha decay, beta decay, and gamma decay of heavy nuclei are preceded by the synthesis of heavy nuclei which lie far from the stability line. The study of alpha decay is very informative and important, as it gives significant information about the shell and sub-shell structure of the parent nuclei.

Alpha decay was first described by Ernest Rutherford [241] and H. Geiger [242] at the beginning of the last century. Subsequently, the alpha decay phenomenon has been explained successfully as a quantum tunneling effect by G. Gamow [243] and by E. U. Condon and R. W. Gurney [244] in 1928. The half-lives of α-decay from various parent nuclei vary from 10^{-7} to 10^{18} s and α-decay emitted among 4 and 11 MeV of kinetic energies. The alpha decay half-lives of $^{218-219}$U isotopes have been experimentally measured by Leppanen et al. [245] in 2007. Sushil Kumar et al. [246] have studied the shell closure effects in heavy nuclei through cluster decay and have calculated half-lives for different cluster decay modes of ^{218}U isotope and also for ^{230,232,234,236}U isotopes using the

[1]The results discussed in this chapter have been published in *Nucl. Phys. A*, 1023, 122439 (2022).

preformed cluster model (PCM) model.

Cluster radioactivity is known as the spontaneous emission of a cluster whose mass lies at an intermediate position between alpha particles and the lightest fission fragments. It was first observed theoretically in 1980 by Sandulescu, Poenaru, and Greiner [24, 25]. After a few years, the spontaneous emission of a ^{14}C cluster from ^{223}Ra parent nuclei was experimentally confirmed by Rose and Jones from the University of Oxford [52]. The cluster decay half-lives of various parent nuclei vary from 10^{11} to 10^{30} s. A few years later the detection of ^{14}C from ^{223}Ra, many other decay modes, like ^{20}O, ^{23}F, ^{24,26}Ne, $^{28.30}$Mg and ^{32,34}Si, various radioactive nuclei like ^{221}Fr, $^{221-224,226}$Ra, ^{225}Ac, ^{228,230,232}Th, ^{231}Pa, $^{232-236}$U, ^{237}Np, ^{236,238,240}Pu and ^{241}Am were observed by several experimental groups around the world [69, 78, 93]. So far, ^{22}Ne, ^{24}Ne, ^{25}Ne, ^{26}Ne, ^{28}Mg, ^{29}Mg, and ^{30}Mg clusters decay from $^{230,232-236}$U isotopes have been experimentally confirmed [64]. The decay of heavier clusters have been experimentally observed in trans-lead region decaying into daughter nuclei are doubly magic or nearly doubly magic (i.e. ^{208}Pb (doubly closed-shell spherical nucleus with Z = 82, N = 126) or around neighboring nuclei) [52, 90, 91]. Even another island of CR was predicted in the trans-tin region decaying into the daughter nuclei close to the doubly magic nucleus ^{100}Sn [92]. The CR of the trans-lead region has been predicted since 1984.

Many theoretical models and approaches have been employed for the study of cluster radioactive phenomenon. In general, the description can be classified mainly into two types of models, 1) preformed cluster model and 2) fission-based model. In the PCM [247, 248, 249], it is assumed that the clusters made of various nucleons are performed in the parent nucleus before they could tunnel through the barrier created by the nuclear and Coulomb potentials [104, 105, 106]. In the fission-based model [108], the nucleus is assumed to be deformed continuously and reach the saddle or scission configuration to undergo cluster radioactivity [36, 94, 107]. In such type of fission model approach, Gamow's idea of quantum mechanical barrier penetration is still used, but without worrying about the cluster being or not being performed in the parent nucleus.

Goncalves and Duarte [162, 163, 164] introduced a model, the Effective Liquid Drop Model (ELDM) to study alpha decay, and cluster radioactivity in a unified framework and has been used for calculating half-life time [228] for the heavy and superheavy regions. In the ELDM model, the surface and Coulomb energies for the dinuclear shape were calculated analytically, thus obtaining the barrier penetrability factor for alpha decay and cluster emission. Microscopic calculations for the cluster radioactivity half-life predictions are thus model dependent as different microscopic/phenomenological nuclear models are used to calculate mass defect and the Q-value of the reaction with separate calculations for cluster emission probability. In addition, many empirical formulas have been introduced by fitting Q values and experimental half-lives of cluster radioactivity process, such as the UDL, Horoi, TM, and VS formulas.

In recent years, the CR half-lives from various clusters decay have been estimated within several models by inputting different kinds of Q-values [43, 46, 233, 250, 251]. These calculations provide useful content about the shell and/or sub-shell structure of the parent nuclei. In this work, we have used the ELDM with varying mass asymmetry (VMAS) shape and effective inertial coefficient to determine the alpha and cluster decay half-lives, using mass excess data calculated from a relativistic mean-field model (NL3* parameter set).

In this chapter, with the RMF model, we have calculated the bulk properties of Th, U, and Pu isotopes such as binding energy per nucleon (B.E./A), and root-mean-square (rms) radii with an NL3* parameter set. Next, we obtain the two-neutron separation energies (S_{2n}) and the differential variation of neutron separation energy (dS_{2n}) from the calculated B.E. of Th, U, and Pu isotopes. These calculations are associated with structural phenomena like closed shell and sub-shell structures. Along with this, the mass excess data (ΔM) for alpha and clusters decay are calculated by using the obtained binding energy per nucleon. This mass excess data (ΔM) has been used further as input to obtain a Q value and determine the alpha and cluster decay half-lives with the ELDM. Comparisons of our results with the available experimental results and the values obtained using the empirical formula Universal Decay Law (UDL), Viola-Seaborg (VS), TM and the Scaling Law by Horoi *et al.* are also made. In addition, the Geiger-Nuttall plots of $\sqrt{Q}$ versus $log_{10}T_{1/2}$ for emission of ^{8}Be, ^{12}C, ^{16}O, ^{20}Ne, and ^{24}Mg clusters for various isotopes of parent nuclei have been analyzed demonstrating their linear nature.

5.2 Results and Discussions

In this work, we have presented our calculated values of the ground state observables, namely, binding energy per nucleon (B.E./A), rms radii, two-neutron separation energy (S_{2n}), and differential variation of two-neutron separation energy (dS_{2n}) for even-even Th, U, and Pu isotopes obtained by using RMF model with NL3* parameter set. The NL3* parameter set has been widely used to evaluate different ground-state properties of the whole range of nuclei in the nuclear landscape. The calculated results are compared with FRDM and experimental data.

5.2.1 Binding energy per nucleon and rms radii

Using the well-known RMF model, we have examined the ground state properties of the considered isotopes namely the binding energy per nucleon (B.E./A), charge radii (R_{ch}), and rms radius (proton (r_p), and neutron (r_n)), with an NL3* parameter set. The theoretically evaluated results are compared with finite-range droplet model (FRDM) [235] data and available experimental results [202, 204], as given in Figs. 5.1, 5.2 and 5.3. In Fig. 5.1(a) the showed binding energy per nucleon (B.E./A) increases with the neutron number (N) increase, reaches the peak value at neutron number $N \sim 126$ ($A = 216$, $Z = 90$) for RMF (NL3*), FRDM, and experimental data, and it decreases towards a higher neutron number. This means that ^{216}Th is the most stable element from the B.E. per nucleon (B.E./A) plots. Similar results are also shown in Fig. 5.1 (b and c), the B.E./A increases with the neutron number (N) increase, reaches the maximum value at $N \sim 126$ [$A = 218$, $Z = 92$), and ($A = 220$, $Z = 94$)], after that it decreases with the higher neutron number (N). This means that ^{218}U and ^{220}Pu are also the most stable elements from the B.E. per nucleon (B.E./A) plots. Similar outcomes are also obtained from the experimental results [202] and FRDM values [235]. In order to analyze the predictive

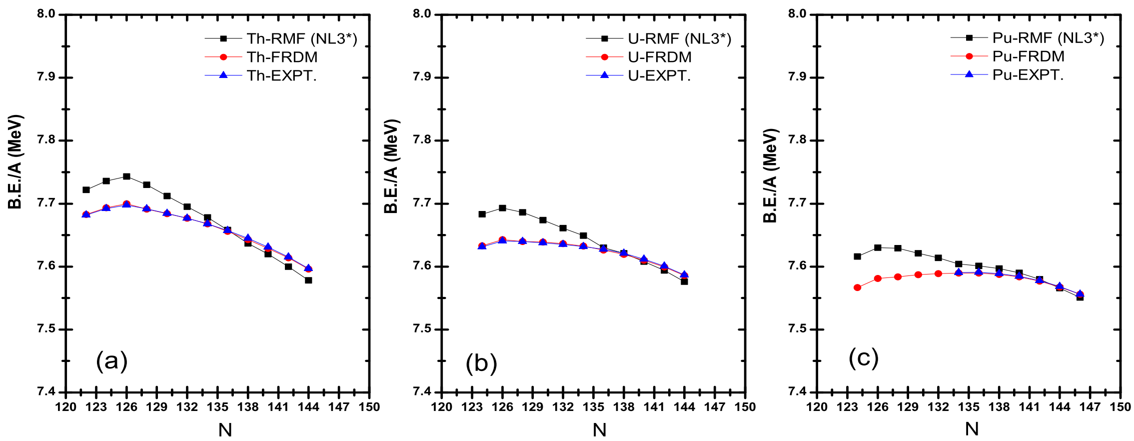

Figure 5.1: The binding energy per nucleon (B.E./A) calculated from RMF (NL3* parameter set) compared with the FRDM [235] and experimental values [202] for Th, U, and Pu isotopes.

power and accuracy of the selected RMF (NL3*) model, we have determined the mean deviation of binding energy per nucleon results for the NL3* parameter in comparison to the available experimental results of even-even Th, U, and Pu isotopes. The mean deviation ($\overline{\sigma}$) between any two different i^{th} observables Y_i, is written as

$$\overline{\sigma} = \frac{1}{n}\sum_{i=1}^{n} |Y_i^{exp.} - Y_i^{cal.}|. \tag{5.2.1}$$

The mean deviation for the calculated RMF values of B.E./A with respect to the experimental data is 0.015, 0.021, and 0.006 for Th, U, and Pu isotopes respectively. Also, the NL3* parameter values of the binding energy per nucleon slightly overestimate the experimental data for N = 122-136, N = 124-138, and N = 124-140 in Th, U, and Pu isotopes respectively but for the rest of the isotopes, the RMF results agree well with the experimental results [202] and FRDM values [235]. This also reveals that the nucleons are more bound for NL3* parameter set.

The rms charge radii (R_{ch}) for NL3* parameter are compared with the available experi-

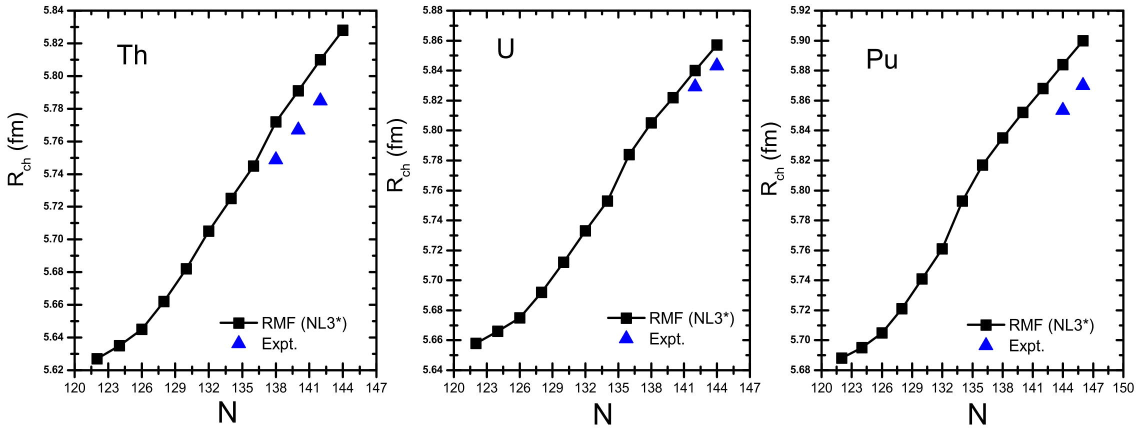

Figure 5.2: The charge radii (R_{ch}) of Th, U, and Pu isotopes for RMF (NL3*) formalism are compared with the available experimental data [204].

mental data [204] which are given in Fig. 5.2. From the Fig, we see that calculated results for NL3* overestimate slightly in comparison to the experimental data for all considered isotopes. The charge radii increase with the increasing neutron number N but with a small kink at N = 126, indicating the shell closure effect. A similar signature is also observed in Fig. 5.3, showing the rms radii of a neutron and proton ($R_{n,p}$) for the isotopic chains of even-even Th, U, and Pu nuclei obtained using the RMF formalism with NL3* parameter set. This confirms the observed shell enclosure at N = 126 for all the considered isotopes.

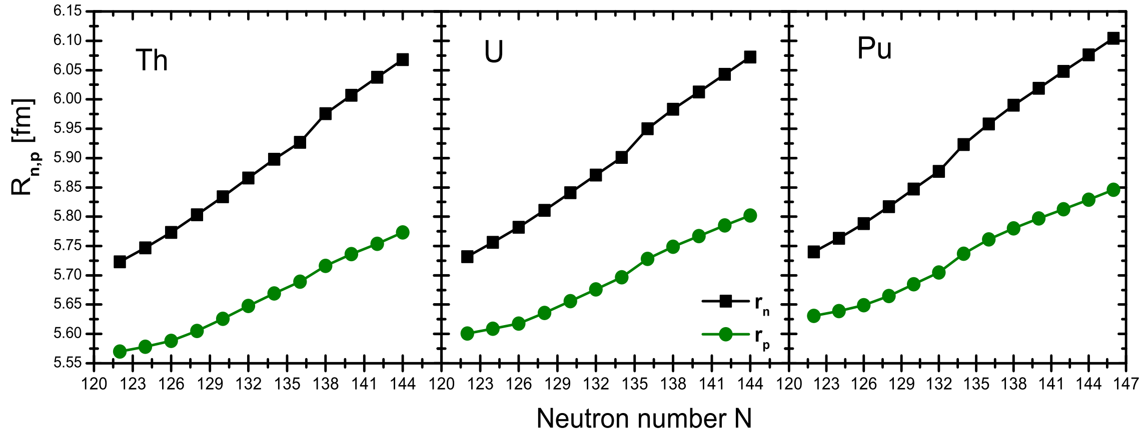

Figure 5.3: The neutron (r_n), and proton (r_p) radii of Th, U, and Pu isotopes calculated with the RMF (NL3*) formalism.

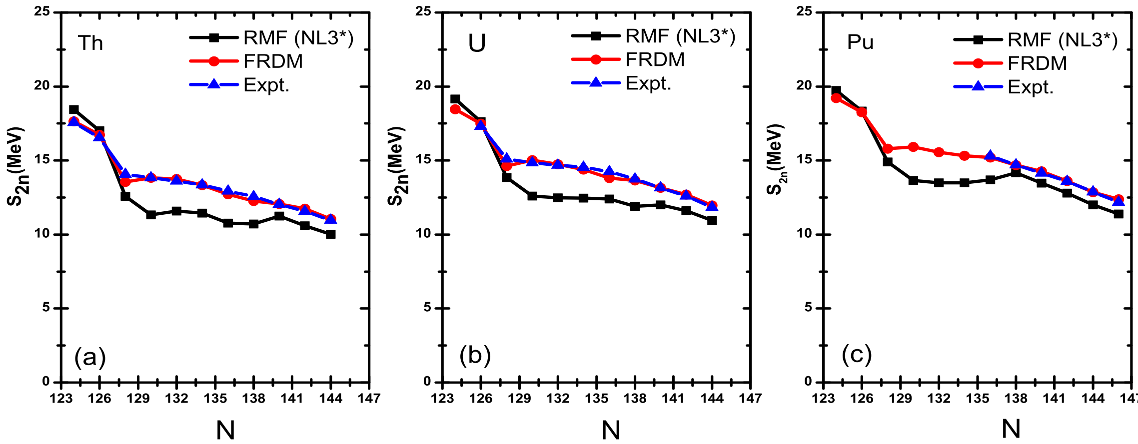

Figure 5.4: The two-neutron separation energy S_{2n} obtained from RMF (NL3* parameter set) for Th, U, and Pu isotopes compared with FRDM [235] and experimental results [202].

5.2.2 Two-neutron separation energy (S_{2n})

The two-neutron separation energy (S_{2n}) is a significant quantity in understanding the nuclear shell structure. In the present study, the $S_{2n}(N, Z)$ has been calculated from the binding energy (B.E.) by using RMF (NL3*) formalism, given by the following equation:

$$S_{2n}(N, Z) = B.E.(N, Z) - B.E.(N - 2, Z). \tag{5.2.2}$$

The S_{2n} values of parent nuclei for the chosen isotopes are compared with FRDM [235] and experimental data [202], as given in Fig. 5.4. From Fig. 5.4 (a, b, and c), it is distinctly shown that the S_{2n} results decrease with an increase in the neutron number (N) in considered isotopes except for a sharp fall seen at the neutron number $N = 126$ due to the effect of shell closure in the RMF (NL3*) model, as well as FRDM and experimental data. Here we found an unexpected change, possibly the reason for the existence of the shell/sub-shell closure. In Fig. 5.4 we see a possible major shell closure at neutron number $N = 126$ magic number.

5.2.3 Differential variation of two-neutron separation energy

The differential variation of the two-neutron separation energy (S_{2n}) with respect to the neutron number (N) i.e., $dS_{2n}(N, Z)$ is calculated using the relation

$$dS_{2n}(N,Z) = \frac{S_{2n}(Z,N+2) - S_{2n}(Z,N)}{2}. \tag{5.2.3}$$

We have theoretically calculated $dS_{2n}(N, Z)$ using Eq. (5.2.3) and then compared it with FRDM and experimental results $S_{2n}(N, Z)$. The theoretically calculated results of differential variation of the two-neutron separation energy (dS_{2n}) for even-even Th, U, and Pu isotopes plotted versus neutron number (N) is given in Fig. 5.5. In Fig. 5.5 (a, b, and c), for the isotopes of Th, U, and Pu nuclei, the value of dS_{2n} exhibits a sharp, large fall at neutron number $N = 126$ indicating the shell closure. In the dS_{2n} values, the sharp peak at N = 126 again confirms the shell/sub-shell of ^{216}Th, ^{218}U and ^{220}Pu. Also, the sharp decline appears in the same region ($N = 126$) as that of the S_{2n}.

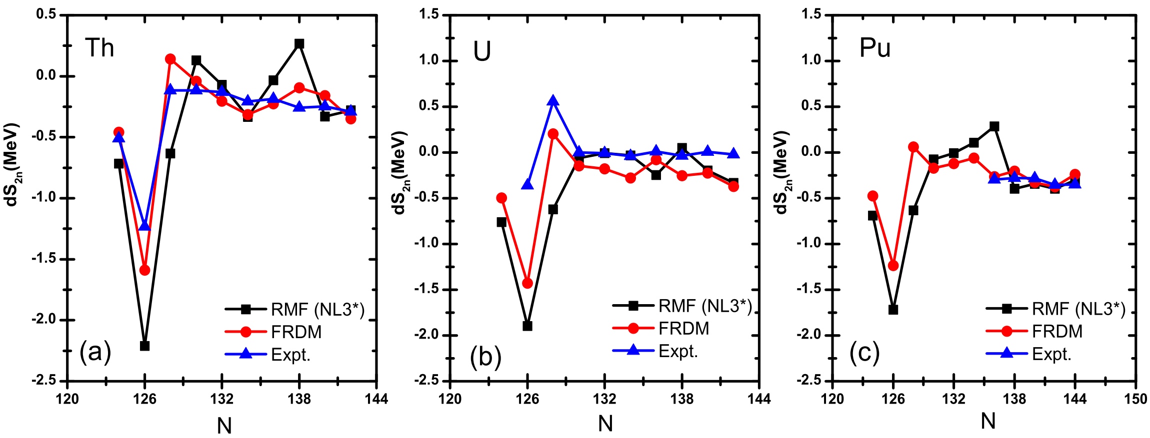

Figure 5.5: The calculated dS_{2n} obtained from RMF (NL3*) compared with FRDM [235] and experimental results [202] for Th, U, and Pu isotopes.

5.2.4 Alpha decay

We have investigated the Q_α and decay half-lives results for potential even-even isotopes of Th, U, and Pu nuclei. In this calculation of alpha-decay half-lives, we have used the ELDM model. In this model, we have chosen a combination of the varying mass asymmetry shape (VMAS) and effective inertial coefficient. It is essential to note here that in the ELDM model alpha decay half-lives estimation has been performed here by using zero angular momenta.

The theoretically calculated binding energy per nucleon (B.E./A) has been used to determine the Q_α-values, penetrability (P), decay constant (λ), and alpha decay half-lives of considered isotopes of parent nuclei. Firstly, using the B.E./A in RMF (NL3* parameter set), we have determined the mass excess data (ΔM). The relation between binding energy per nucleon and mass excess data is written as

$$\text{Mass of the Nuclei} = ((\text{N}^*M_n + \text{Z}^*M_p)^*931.5 - \text{A}^*\text{B.E./A})/931.5 \text{ u}$$
$$\Delta M = (\text{ Mass of the Nuclei - Mass No. of Nuclei})^*931.5 \text{ MeV}$$

We have further used these calculated mass excess data to estimate the Q_α-values using the following relation:

$$Q_\alpha(N,Z) = \Delta M_p(N,Z) - [\Delta M_d(N-2,Z-2) + \Delta M_e(2,2)]. \tag{5.2.4}$$

In Eq. (5.2.4) $\Delta M_p(N,Z)$ and $\Delta M_d(N-2,Z-2)$ are the mass excess of the parent and the daughter nuclei in MeV, respectively. $\Delta M_e(2,2)$ is the mass excess of the $^4_2$He nucleus. All possible cluster decays for the parent nuclei have been considered, for which Q-value ($Q > 0$) is found to be positive.

In Table 5.1 we have presented the theoretically calculated Q_α-values, penetrability (P), decay constant (λ), and the alpha decay half-lives for the selected even-even nuclei. We have tested the prediction power and accuracy of different models used for alpha decay half-lives investigation. For this, we have compared the values determined by the ELDM model with the results obtained by empirical formula, namely the UDL, VS, and Scaling Law by Horoi *et al.*. Further, to test the influence of the difference in the Q value, we have compared calculated alpha decay half-lives using ELDM using experimental mass defect data from Ref [202]. The results have been tabulated in Table 5.1. From Table 5.1 it is found that the alpha decay half-life has a minimum for the parent nucleus ^{218}Th as per the ELDM (NL3*), UDL, Horoi, and VS models. The experimental α-decay half-life also shows the minimum value of half-life at the ^{218}Th parent nucleus. The minimum half-life

Table 5.1: The Q_α value, penetrability, decay constant and the alpha decay half-lives for Th, U, and Pu isotopes.

Parent nuclei	**Daughter nuclei**	**Emitted cluster**	**Q-value** (MeV) [NL3*]	**Penetrability P**	**Decay constant** $\lambda(s^{-1})$	$log_{10}T_{1/2}$ **(s)** **ELDM** (NL3*)	**UDL**	**Horoi**	**VS**	Expt. [202] **Q-value** (MeV)	$log_{10}T_{1/2}$ **(s)**
^{214}Th	^{210}Ra	^{4}He	7.61	1.05E-22	3.67E-02	-0.54	-0.48	-0.69	-0.98	7.82	-1.06
^{216}Th	^{212}Ra	^{4}He	8.28	1.61E-20	6.12E+00	-2.73	-2.61	-2.81	-3.12	8.07	-1.58
^{218}Th	^{214}Ra	^{4}He	11.84	1.18E-12	6.44E+08	-10.59	-10.45	-10.74	-11.13	9.85	-6.93
^{220}Th	^{216}Ra	^{4}He	11.59	4.85E-13	2.58E+08	-10.21	-10.05	-10.31	-10.68	8.97	-5.12
^{222}Th	^{218}Ra	^{4}He	10.07	6.50E-16	3.01E+05	-7.33	-7.14	-7.31	-7.66	8.13	-2.56
^{224}Th	^{220}Ra	^{4}He	9.87	2.16E-16	1.18E+05	-6.92	-6.72	-6.86	-7.21	7.30	-1.02
^{226}Th	^{222}Ra	^{4}He	9.68	1.01E-16	4.51E+04	-6.53	-6.34	-6.45	-6.78	6.45	2.51
^{228}Th	^{224}Ra	^{4}He	8.96	1.81E-18	7.46E+02	-4.78	-4.61	-4.65	-4.98	5.52	7.29
^{216}U	^{212}Th	^{4}He	8.56	1.40E-20	5.47E-00	-2.67	-2.51	-2.84	-3.08	8.53	-2.35
^{218}U	^{214}Th	^{4}He	9.42	3.68E-18	1.59E+03	-5.08	-4.88	-5.19	-5.48	8.78	-3.28
^{220}U	^{216}Th	^{4}He	12.56	4.90E-12	2.83E+09	-11.21	-11.07	-11.37	-11.78	11.68	-9.45
^{222}U	^{218}Th	^{4}He	12.51	4.33E-12	2.49E+09	-11.16	-11.01	-11.28	-11.69	9.43	-6.14
^{224}U	^{220}Th	^{4}He	11.57	1.34E-13	7.14E+07	-9.65	-9.45	-9.69	-10.07	8.62	-3.07
^{226}U	^{222}Th	^{4}He	10.61	2.23E-15	1.09E+06	-7.87	-7.66	-7.85	-8.19	7.70	-0.73
^{228}U	^{224}Th	^{4}He	10.41	1.74E-16	1.03E+05	-7.42	-7.25	-7.41	-7.76	6.80	2.72
^{230}U	^{226}Th	^{4}He	8.87	2.18E-19	8.89E+01	-3.86	-3.67	-3.77	-4.04	5.99	6.21
^{232}U	^{228}Th	^{4}He	7.18	8.32E-25	2.74E-04	1.56	1.62	1.57	1.38	5.42	9.23
^{220}Pu	^{216}U	^{4}He	11.92	1.25E-13	6.82E+07	-9.39	-9.75	-9.91	-10.14		
^{222}Pu	^{218}U	^{4}He	14.65	1.11E-09	7.48E+11	-13.51	-13.83	-13.87	-14.33		
^{224}Pu	^{220}U	^{4}He	14.59	1.07E-09	7.19E+11	-13.49	-13.78	-13.81	-14.28		
^{226}Pu	^{222}U	^{4}He	13.85	1.29E-10	8.21E+10	-12.51	-12.77	-12.84	-13.24		
^{228}Pu	^{224}U	^{4}He	13.34	2.76E-11	1.69E+10	-11.81	-12.04	-12.12	-12.49	7.94	-1.08
^{230}Pu	^{226}U	^{4}He	11.43	2.51E-14	1.32E+07	-8.68	-8.88	-9.05	-9.24	7.17	2.49
^{232}Pu	^{228}U	^{4}He	8.13	2.69E-22	1.01E-01	-0.78	-0.96	-1.36	-1.11	6.71	4.89
^{234}Pu	^{230}U	^{4}He	7.76	1.78E-23	6.35E-03	0.36	0.21	-0.22	0.08	6.31	6.17
^{236}Pu	^{232}U	^{4}He	7.17	1.29E-25	4.24E-05	2.43	2.31	1.82	2.24	5.87	8.16

indicates the shell effect for the daughter nucleus ^{214}Ra ($A = 88$, N_d=126). Similarly in the case of U and Pu isotopes, the shell stabilization at the daughter nucleus ^{216}Th ($A = 90$, N_d=126) and ^{218}U ($A = 92$, N_d=126) having magic neutron number $N_d = 126$ is clearly observed. The calculated alpha decay half-lives using ELDM agree well with the half-lives obtained empirical formula UDL than that of the VS, and Scaling law of Horoi formula. It has been found that the UDL formula, derived from the α like-R matrix theory, has better prediction power giving comparable results with microscopic calculations. The Q_α

values are calculated using RMF (NL3*) and are also shown in Table 5.1 and compared with the experimental data. From Table 5.1, we find that the theoretically calculated Q_α values using RMF (NL3*) are slightly overestimated in comparison to the experimental data because the binding energy of the emitted alpha particle is slightly overestimated, and the corresponding mass excess data is underestimated for NL3* in comparison to the experimental data. The microscopic energy (shell correction energy), becomes crucial for the appropriate mass evaluation. The Q_α value and decay half-life, obtained from both the RMF calculation and experimental result, coincide well for the parent nucleus ^{216}U. We have calculated the standard deviation of alpha decay half-lives value for the ELDM (NL3*) and have compared it with the calculated standard deviation of half-lives value of the empirical formula UDL, VS, and Scaling Law of Horoi and experimental data. In the case of ELDM, we found that the standard deviation of the decay half-lives is 0.204 s for UDL, 0.497 s for VS, and 0.294 s for the scaling law of Horoi. For the case of experimental data, we found that the standard deviation of the $log_{10}T^{\alpha}_{1/2}$ is 6.58 s for ELDM (NL3*). The sensitivity of decay half-lives on Q_α can also be determined through the standard deviation in Q_α values which are found to be 2.757 MeV for RMF (NL3*). It is evident here to note that a small deviation in Q_α values are enough to change the alpha decay half-lives.

5.2.5 Cluster decay

We have also investigated the decay of different clusters such as ^{8}Be, ^{12}C, ^{16}O, ^{20}Ne, and ^{24}Mg in $^{218-234}$Th, $^{218-232}$U, and $^{224-238}$Pu isotopes. The Q-values are evaluated from mass excess data of RMF (NL3*) using the following relations:

^{8}Be :

$$Q_{Be}(N,Z) = \Delta M_p(N,Z) - [\Delta M_d(N-4,Z-4) + \Delta M_e(4,4)] \tag{5.2.5}$$

^{12}C :

$$Q_{C}(N,Z) = \Delta M_p(N,Z) - [\Delta M_d(N-6,Z-6) + \Delta M_e(6,6)] \tag{5.2.6}$$

^{16}O :

$$Q_{O}(N,Z) = \Delta M_p(N,Z) - [\Delta M_d(N-8,Z-8) + \Delta M_e(8,8)] \tag{5.2.7}$$

^{20}Ne :

$$Q_{Ne}(N,Z) = \Delta M_p(N,Z) - [\Delta M_d(N-10,Z-10) + \Delta M_e(10,10)] \tag{5.2.8}$$

^{24}Mg :

$$Q_{Mg}(N,Z) = \Delta M_p(N,Z) - [\Delta M_d(N-12,Z-12) + \Delta M_e(12,12)] \tag{5.2.9}$$

Here $\Delta M_p(N,Z)$ is the mass excess of the parent nucleus, $\Delta M_d(N-4,Z-4)$, $\Delta M_d(N-6,Z-6)$, $\Delta M_d(N-8,Z-8)$, $\Delta M_d(N-10,Z-10)$ and $\Delta M_d(N-12,Z-12)$ are the mass excess of the daughter nuclei and $\Delta M_e(4,4)$, $\Delta M_e(6,6)$, $\Delta M_e(8,8)$, $\Delta M_e(10,10)$ and $\Delta M_e(12,12)$ are the mass excess of the clusters ^{8}Be, ^{12}C, ^{16}O, ^{20}Ne and ^{24}Mg, respectively.

In this work, we have tested the prediction power and accuracy of different models used

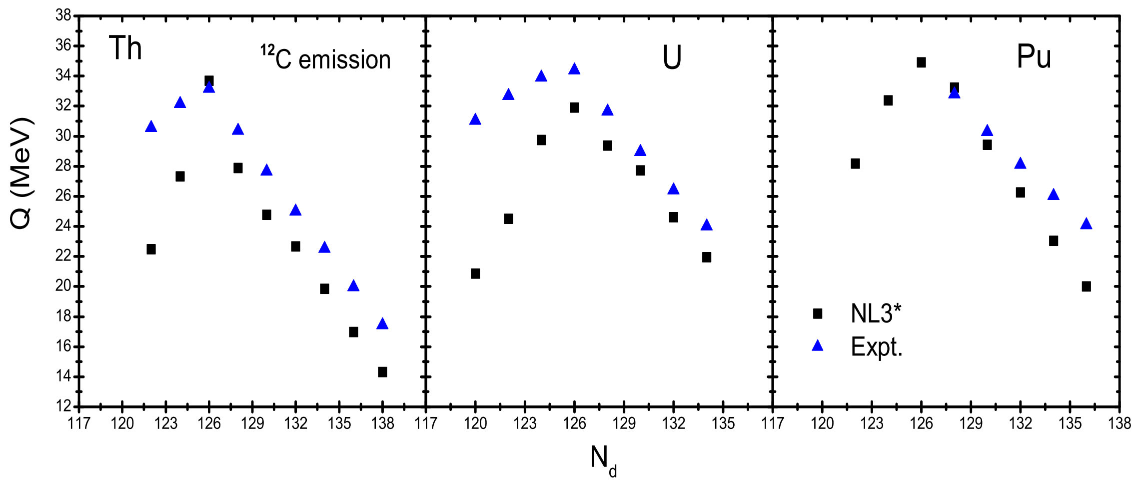

Figure 5.6: The Q-values for the ^{12}C decay from Th, U, and Pu isotopes using RMF formalism with NL3* parameter set, compared with the experimental data [203], wherever available.

for cluster decay half-lives calculation. The cluster decay half-lives have been calculated using ELDM and various empirical formulas: TM, Universal Decay Law (UDL), and Scaling Law by Horoi et al. The calculated Q-values and cluster decay half-lives ($log_{10}T_{1/2}$) are given in Table 5.2. The parent, daughter, and emitted cluster are listed in columns 1, 2, and 3 respectively. The theoretically calculated Q-value using RMF (NL3*) is listed in column 4. The penetrability and decay constant for the cluster decay are given in columns 5 and 6. Columns 7-10 contain the decay half-lives obtained using ELDM, UDL, Horoi, and TM models. The experimental Q-values and calculated half-lives using the UDL formula are listed in columns 11 and 12, respectively for the sake of comparison. From Table 5.2 it should be noticed that when ^{8}Be is decayed from $^{218-228}$Th isotopes, the cluster decay half-life has a minimum for the ^{220}Th nucleus for both theoretical and experimental Q-values. In the case of $^{218-230}$U and $^{222-234}$Pu isotopes, the cluster decay half-life has a minimum for ^{222}U and ^{224}Pu isotopes, which indicates possible shell and/or sub-shell closure at ^{214}Ra and ^{216}Th, daughters respectively. When cluster decay of ^{12}C from selected even-even isotopes, it is found from Table 5.2 that the half-life has a minimum for ^{222}Th, ^{224}U and ^{226}Pu parent nuclei, respectively. This indicates that the decay constant of ^{12}C is the maximum for ^{222}Th, ^{224}U, and ^{226}Pu isotopes. A similar observation is valid for the cluster decay of ^{16}O and ^{20}Ne from Th, U, and Pu isotopes. The minimum value of the logarithmic half-lives are found for ^{224}Th, ^{226}U and ^{228}Pu isotopes for the cluster decay of ^{16}O and ^{228}U, ^{230}Pu isotopes for the cluster decay of ^{20}Ne. In the case of the cluster decay of ^{24}Mg from Pu isotopes, the minimum value of the half-life is found for ^{232}Pu isotope with the ELDM (NL3*), UDL, TM, and Horoi formalism. However, the experimental value of half-life shows minima at the ^{228}Pu parent nucleus. This difference is perhaps because of the sensitivity of decay half-life to the angular momentum L [252] and Q-value [253]. For the cluster decay of ^{8}Be, ^{12}C, ^{16}O, ^{20}Ne and ^{24}Mg, logarithmic half-lives have minimum values for those decays which leads to the creation of daughter nuclei (i.e.,^{208}Pb, ^{210}Po, ^{212}Rn, ^{214}Ra, and ^{216}Th) having magic neutron number (N_d = 126). These observations reveal the role of shell closure in cluster radioactivity. From Table 5.2 it is found that the ELDM (NL3*) results matches nicely with the UDL results than that of TM, Horoi results. The decay half-life has a minimum value correspond-

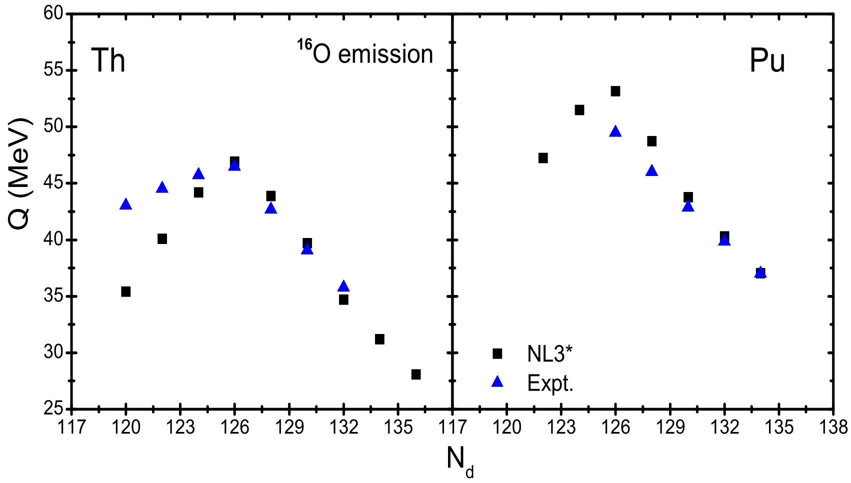

Figure 5.7: Same as figure 5.6, but for the ^{16}O decay from Th, and Pu isotopes, respectively.

ing to the maximum barrier penetrability and decay constant, which reveals the magic character of the daughter nuclei. The experimental Q values taken from reference [203] are also shown from a comparison in Table 5.2. It is evident from Table 5.2 that the calculated Q values using RMF (NL3*) are slightly underestimated than the experimental data because the binding energy of the emitted clusters is slightly underestimated and the corresponding mass excess data is overestimated for NL3* in comparison to the experimental data. Also, we can see that the calculated half-life results are higher than the experimental data. This disagreement can be understood due to the variation of Q values in the RMF (NL3*), and experimental data.

From Fig. 5.6 it is shown that ^{12}C decay from $^{218-234}$Th, $^{218-232}$U and $^{222-236}$Pu isotopes

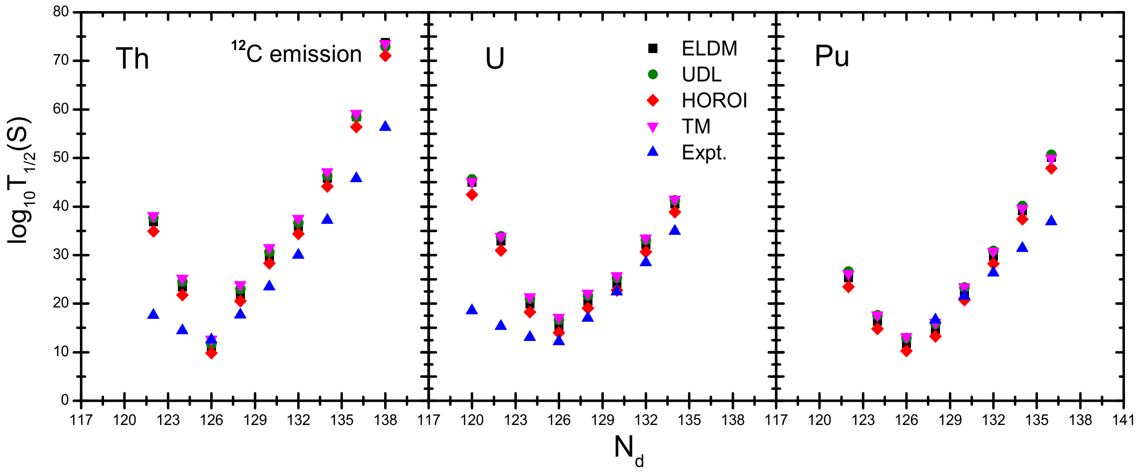

Figure 5.8: The computed $\log_{10}T_{1/2}$ (in s) values plotted against the neutron number of daughter nuclei (N_d) for the emission of ^{12}C from Th, U, and Pu isotopes.

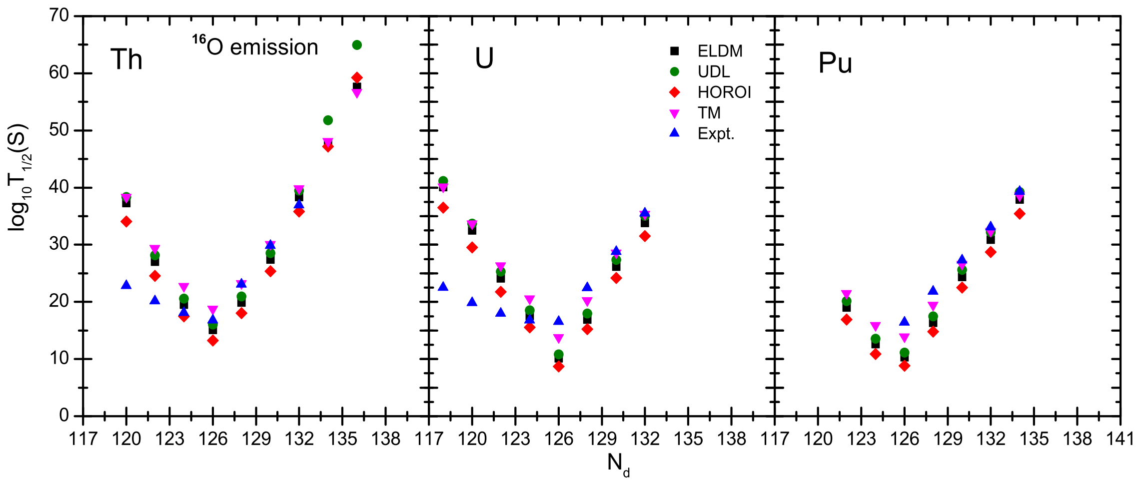

Figure 5.9: Same as figure 5.8, but for the ^{16}O decays half-lives in the Th, U, and Pu isotopes.

the Q-value has a maximum for the formation of daughter nuclei ^{210}Po ($Z_d = 84, N_d = 126$), ^{212}Rn ($Z_d = 86, N_d = 126$) and ^{214}Ra ($Z_d = 88, N_d = 126$), respectively. Similarly, for the cluster decay of ^{16}O, Q-value has a maximum for the formation of magic daughter nuclei (i.e., ^{208}Pb, and ^{212}Rn) having magic number ($N_d = 126$) shown in Fig. 5.7. These calculated results exhibit that the Q-value will be higher for those decay which leads to magic daughter nuclei ($N_d = 126$). In addition, the calculated Q-values reveal the shell effects at magic number $N_d = 126$ and influence the decay half-lives. As the size of cluster increases, the Q value also increases.

Figures 5.8 and 5.9 provide plots for the half-lives of the ^{12}C and ^{16}O decay from even-even Th, U and Pu isotopes within the ELDM, UDL, TM, and Scaling Law by Horoi *et al.* models using NL3* Q-values versus the neutron number of a daughter (N_d). In Fig. 5.8 the plot for the cluster decay of ^{12}C from $^{218-234}$Th, $^{218-232}$U and $^{222-236}$Pu isotopes, it can be seen that the minimum value of the cluster decay half-lives are obtained for the decay leading daughter nuclei ^{210}Po ($Z_d = 84, N_d = 126$), ^{212}Rn ($Z_d = 86, N_d = 126$) and ^{214}Ra ($Z_d = 88, N_d = 126$), respectively. The value of half-life, in the ELDM, UDL, TM, Horoi and Expt. data coincides well for the ^{222}Th, ^{224}U and ^{226}Pu parent nucleus, but towards large neutron number of a daughter (N_d) we do not have an agreement with the experimental data. Figure 5.9 illustrates the cluster decay of ^{16}O from $^{218-234}$Th, $^{218-232}$U and $^{224-236}$Pu isotopes. The minima of the cluster decay half-lives are obtained for the decay leading magic daughter nuclei ^{208}Pb ($Z_d = 82, N_d = 126$), ^{210}Po ($Z_d = 84, N_d = 126$), and ^{212}Rn ($Z_d = 86, N_d = 126$), respectively. In this study, it has been found that the cluster decay half-lives have a minimum for the decay leading to the doubly magic daughter nuclei ^{208}Pb ($Z_d = 82, N_d = 126$) or its neighbouring daughter nuclei. Also, these calculations confirm that the shell structure stabilizes at magic daughter nuclei ($N_d = 126$). The value of $log_{10}T_{1/2}$, in the RMF model, coincides well with the data for ^{208}Pb. The results presented in Figs. 5.8 and 5.9 confirm the fact that the four calculations ELDM, UDL, TM and Scaling law by Horoi and experimental results lead almost to similar trends of half-lives.

In order to find out the predictive strength of our selected theoretical model, we have determined the standard deviation of half-life values for the RMF (NL3*) and have compared it with the calculated standard deviation of half-lives values of UDL, TM, and Scaling Law of Horoi formula. The standard deviation is given by

$$\sigma = \left[\frac{1}{n-1}\sum_{i=1}^{n}[log(T_{1/2}^{cal}) - log(T_{1/2}^{exp})]^2\right]^{1/2}. \tag{5.2.10}$$

In the case of ELDM, we found that the standard deviation of the half-lives is 1.365 s for UDL, 2.231 s for TM, and 2.588 s for the scaling law of Horoi.

Table 5.2: Comparison of cluster decay half-lives for ^{8}Be, ^{12}C, ^{16}O, ^{20}Ne and ^{24}Mg decays for even-even Th, U, and Pu isotopes.

Parent nuclei	**Daughter nuclei**	**Emitted cluster**	**Q-value** (MeV) [NL3*]	**Penetrability P**	**Decay constant** $\lambda(s^{-1})$	$log_{10}T_{1/2}$ **(s) [NL3*]**				**Expt.[203]**	
						ELDM	**UDL**	**Horoi**	**TM**	**Q-value** (MeV)	$log_{10}T_{1/2}$**(s)** (UDL)
^{218}Th	^{210}Rn	^{8}Be	9.71	1.66E-67	5.02E-47	44.25	43.69	44.04	46.08	17.03	14.02
^{220}Th	^{212}Rn	^{8}Be	12.80	5.55E-51	2.21E-30	27.74	27.99	27.56	28.24	18.38	10.55
^{222}Th	^{214}Rn	^{8}Be	11.23	2.16E-58	7.56E-38	35.14	35.07	35.09	36.37	16.58	15.14
^{224}Th	^{216}Rn	^{8}Be	8.97	1.94E-72	5.41E-52	49.19	48.36	49.18	51.58	14.79	20.53
^{226}Th	^{218}Rn	^{8}Be	8.23	2.28E-78	5.83E-58	55.12	53.94	55.14	58.01	13.04	26.86
^{228}Th	^{220}Rn	^{8}Be	7.24	1.51E-87	3.39E-67	64.31	62.55	64.29	67.86	11.22	34.96
^{218}U	^{210}Ra	^{8}Be	6.22	1.13E-102	2.19E-82	79.42	76.72	78.08	82.43	16.52	16.96
^{220}U	^{212}Ra	^{8}Be	10.04	1.75E-67	5.45E-47	44.23	43.75	43.70	45.33	18.27	12.24
^{222}U	^{214}Ra	^{8}Be	13.53	1.19E-49	5.02E-29	26.4	26.79	26.03	26.27	19.26	9.84
^{224}U	^{216}Ra	^{8}Be	12.35	1.00E-54	3.85E-34	31.47	31.66	31.19	31.82	17.48	14.15
^{226}U	^{218}Ra	^{8}Be	10.47	1.38E-64	4.50E-44	41.33	41.03	41.06	42.44	15.73	19.09
^{228}U	^{220}Ra	^{8}Be	10.59	8.26E-64	2.72E-43	40.56	40.31	40.37	41.68	14.01	24.84
^{230}U	^{222}Ra	^{8}Be	7.75	4.03E-85	9.70E-65	61.87	60.38	61.43	64.34	12.35	31.51
^{222}Pu	^{214}Th	^{8}Be	13.04	1.49E-53	6.02E-33	30.31	30.58	29.65	29.86		
^{224}Pu	^{216}Th	^{8}Be	16.55	9.92E-41	5.11E-20	17.48	18.22	16.91	16.15		
^{226}Pu	^{218}Th	^{8}Be	15.55	7.50E-44	3.63E-23	20.6	21.26	20.13	19.60		
^{228}Pu	^{220}Th	^{8}Be	14.10	5.53E-49	2.42E-28	25.73	26.22	25.33	25.19	16.47	18.38
^{230}Pu	^{222}Th	^{8}Be	11.23	3.48E-62	1.22E-41	38.93	38.83	38.47	39.28	14.78	23.73
^{232}Pu	^{224}Th	^{8}Be	8.54	1.81E-80	4.82E-60	57.22	56.07	56.42	58.54	13.42	28.76
^{234}Pu	^{226}Th	^{8}Be	5.82	5.35E-111	9.69E-91	87.75	84.58	86.04	90.33	12.21	33.93
^{218}Th	^{206}Po	^{12}C	22.49	3.68E-60	2.31E-39	36.92	37.56	34.91	38.14	30.55	17.57
^{220}Th	^{208}Po	^{12}C	27.32	1.10E-46	8.42E-26	23.43	24.46	21.81	25.21	32.14	14.45
^{222}Th	^{210}Po	^{12}C	33.68	6.88E-34	6.48E-13	10.65	11.63	9.85	12.68	33.15	12.55

(Continued on next page)

Table 5.2 – continued from previous page

Parent nuclei	Daughter nuclei	Emitted cluster	Q-value (MeV) [NL3*]	Penetrability P	Decay constant $\lambda(s^{-1})$	$log_{10}T_{1/2}$ (s) [NL3*] ELDM	UDL	Horoi	TM	Expt.[203] Q-value (MeV)	$log_{10}T_{1/2}$(s) (UDL)
^{224}Th	^{212}Po	^{12}C	27.88	3.43E-45	2.68E-24	21.95	23.01	20.53	23.93	30.36	17.70
^{226}Th	^{214}Po	^{12}C	24.76	5.88E-53	4.07E-32	29.71	30.67	28.30	31.56	27.66	23.43
^{228}Th	^{216}Po	^{12}C	22.68	4.33E-59	2.74E-38	35.85	36.66	34.39	37.54	24.98	30.02
^{230}Th	^{218}Po	^{12}C	19.84	4.41E-69	2.45E-48	45.83	46.33	44.16	47.13	22.50	37.15
^{232}Th	^{220}Po	^{12}C	16.98	9.40E-82	4.46E-61	58.5	58.47	56.41	59.15	19.97	45.78
^{234}Th	^{222}Po	^{12}C	14.32	4.69E-97	1.87E-76	73.81	72.99	71.04	73.51	17.43	56.28
^{218}U	^{206}Rn	^{12}C	20.86	2.86E-68	1.67E-47	45.02	45.57	42.43	45.15	31.03	18.55
^{220}U	^{208}Rn	^{12}C	24.50	3.30E-56	2.26E-35	32.96	33.89	30.93	33.84	32.67	15.33
^{222}U	^{210}Rn	^{12}C	29.74	3.76E-43	3.13E-22	19.91	21.02	18.26	21.38	33.89	13.06
^{224}U	^{212}Rn	^{12}C	31.9	9.67E-39	8.62E-18	15.49	16.60	13.97	17.16	34.37	12.16
^{226}U	^{214}Rn	^{12}C	29.37	9.09E-44	7.46E-23	20.52	21.65	19.08	22.16	31.64	17.03
^{228}U	^{216}Rn	^{12}C	27.73	2.15E-47	1.67E-26	24.15	25.26	22.75	25.75	28.96	22.47
^{230}U	^{218}Rn	^{12}C	24.62	2.02E-55	1.39E-34	32.18	33.17	30.68	33.53	26.39	28.47
^{232}U	^{220}Rn	^{12}C	21.94	8.72E-64	5.35E-43	40.53	41.31	38.85	41.52	23.99	34.92
^{222}Pu	^{210}Ra	^{12}C	28.18	1.23E-48	9.68E-28	25.38	26.62	23.49	26.19		
^{224}Pu	^{212}Ra	^{12}C	32.38	1.20E-39	1.08E-18	16.41	17.57	14.77	17.64		
^{226}Pu	^{214}Ra	^{12}C	34.92	4.94E-35	4.82E-14	11.78	12.90	10.27	13.22		
^{228}Pu	^{216}Ra	^{12}C	33.28	6.75E-38	6.27E-17	14.64	15.82	13.23	16.11	32.79	16.63
^{230}Pu	^{218}Ra	^{12}C	29.44	2.21E-45	1.82E-24	22.13	23.34	20.72	23.42	30.28	21.53
^{232}Pu	^{220}Ra	^{12}C	26.25	5.01E-53	3.67E-32	29.78	30.90	28.26	30.78	28.09	26.34
^{234}Pu	^{222}Ra	^{12}C	23.03	1.96E-62	1.26E-41	39.18	40.09	37.38	39.69	26.03	31.42
^{236}Pu	^{224}Ra	^{12}C	20.02	2.11E-73	1.18E-52	50.15	50.69	47.90	49.95	24.07	36.85
^{218}Th	^{202}Pb	^{16}O	35.43	1.54E-60	1.49E-39	37.29	38.33	34.06	38.34	43.04	22.80

(Continued on next page)

Table 5.2 – continued from previous page

Parent nuclei	**Daughter nuclei**	**Emitted cluster**	**Q-value** (MeV) [NL3*]	**Penetrability P**	**Decay constant** $\lambda(s^{-1})$	$log_{10}T_{1/2}$ (s) [NL3*] **ELDM**	**UDL**	**Horoi**	**TM**	**Expt.[203]** **Q-value** (MeV)	$log_{10}T_{1/2}$(s) (UDL)
^{220}Th	^{204}Pb	^{16}O	40.11	2.51E-50	2.75E-29	27.07	28.17	24.55	29.39	44.51	20.17
^{222}Th	^{206}Pb	^{16}O	44.21	8.69E-43	1.05E-21	19.53	20.55	17.44	22.72	45.72	18.07
^{224}Th	^{208}Pb	^{16}O	46.94	2.35E-38	3.01E-17	15.11	16.02	13.26	18.79	46.48	16.76
^{226}Th	^{210}Pb	^{16}O	43.88	3.99E-43	4.77E-22	19.87	20.92	18.01	23.23	42.66	23.07
^{228}Th	^{212}Pb	^{16}O	39.71	1.15E-50	1.25E-29	27.42	28.56	25.37	30.11	39.05	29.87
^{230}Th	^{214}Pb	^{16}O	34.72	1.36E-61	1.29E-40	38.34	39.45	35.81	39.84	35.78	36.92
^{232}Th	^{216}Pb	^{16}O	31.21	5.68E-71	4.83E-50	47.72	51.75	47.21	48.11		
^{234}Th	^{218}Pb	^{16}O	28.07	7.35E-81	5.62E-60	57.61	64.94	59.23	56.71		
^{218}U	^{202}Po	^{16}O	35.41	2.40E-63	2.31E-42	40.09	41.18	36.46	40.16	44.58	22.52
^{220}U	^{204}Po	^{16}O	38.68	9.19E-56	9.69E-35	32.52	33.67	29.53	33.67	46.10	19.86
^{222}U	^{206}Po	^{16}O	42.91	2.22E-47	2.59E-26	24.13	25.27	21.75	26.38	47.21	17.98
^{224}U	^{208}Po	^{16}O	46.81	9.49E-41	1.21E-19	17.51	18.52	15.53	20.56	47.92	16.77
^{226}U	^{210}Po	^{16}O	51.85	2.15E-33	3.04E-12	10.12	10.81	8.69	13.81	48.01	16.53
^{228}U	^{212}Po	^{16}O	47.02	3.51E-40	4.50E-19	16.94	17.96	15.22	20.26	44.33	22.43
^{230}U	^{214}Po	^{16}O	41.56	2.03E-49	2.30E-28	26.17	27.37	24.18	28.59	40.82	28.79
^{232}U	^{216}Po	^{16}O	37.76	4.57E-57	4.70E-36	33.81	35.05	31.50	35.40	37.56	35.52
^{224}Pu	^{208}Rn	^{16}O	47.23	2.91E-42	3.75E-21	19.02	20.12	16.91	21.50		
^{226}Pu	^{210}Rn	^{16}O	51.51	7.05E-36	9.91E-15	12.63	13.53	10.91	15.92		
^{228}Pu	^{212}Rn	^{16}O	53.16	1.39E-33	2.02E-12	10.33	11.14	8.79	13.92	49.48	16.39
^{230}Pu	^{214}Rn	^{16}O	48.72	1.25E-39	1.66E-18	16.38	17.44	14.73	19.47	45.99	21.84
^{232}Pu	^{216}Rn	^{16}O	43.77	1.34E-47	1.60E-26	24.35	25.61	22.47	26.62	42.84	27.32
^{234}Pu	^{218}Rn	^{16}O	40.31	4.01E-54	4.40E-33	30.87	32.18	28.72	32.40	39.86	33.10
^{236}Pu	^{220}Rn	^{16}O	37.02	3.41E-61	3.44E-40	37.94	39.24	35.40	38.59	37.02	39.26

(Continued on next page)

Table 5.2 – continued from previous page

Parent nuclei	Daughter nuclei	Emitted cluster	Q-value (MeV) [NL3*]	Penetrability P	Decay constant $\lambda(s^{-1})$	$log_{10}T_{1/2}$ (s) [NL3*] ELDM	UDL	Horoi	TM	Expt.[203] Q-value (MeV)	$log_{10}T_{1/2}$(s) (UDL)
^{220}U	^{200}Pb	^{20}Ne	39.82	1.50E-85	1.62E-64	62.31	63.10	55.67	57.53	56.01	28.78
^{222}U	^{202}Pb	^{20}Ne	43.87	7.08E-75	8.42E-54	51.62	52.62	46.44	49.13	57.27	26.61
^{224}U	^{204}Pb	^{20}Ne	47.61	2.48E-66	3.21E-45	43.08	44.16	39.01	42.37	57.86	25.56
^{226}U	^{206}Pb	^{20}Ne	50.76	6.99E-60	9.63E-39	36.64	37.72	33.37	37.25	58.15	24.97
^{228}U	^{208}Pb	^{20}Ne	54.11	1.01E-53	1.49E-32	30.47	31.51	27.94	32.33	58.01	25.07
^{230}U	^{210}Pb	^{20}Ne	48.69	1.09E-63	1.44E-42	40.44	41.57	37.08	40.56	53.38	32.67
^{232}U	^{212}Pb	^{20}Ne	42.81	7.98E-77	9.26E-56	53.57	54.64	48.91	51.23	49.20	40.42
^{224}Pu	^{204}Po	^{20}Ne	49.42	9.74E-66	1.31E-44	42.49	43.65	38.29	41.39		
^{226}Pu	^{206}Po	^{20}Ne	52.70	2.83E-59	4.04E-38	36.02	37.16	32.69	36.21		
^{228}Pu	^{208}Po	^{20}Ne	56.08	3.06E-53	4.65E-32	29.99	31.05	27.42	31.43	60.60	23.88
^{230}Pu	^{210}Po	^{20}Ne	58.33	1.70E-49	2.69E-28	26.24	27.25	24.17	28.48	59.92	24.77
^{232}Pu	^{212}Po	^{20}Ne	51.08	6.69E-62	9.27E-41	38.65	39.85	35.47	38.65	55.77	31.34
^{234}Pu	^{214}Po	^{20}Ne	45.25	3.37E-74	4.14E-53	50.95	52.13	46.50	48.55	51.86	38.26
^{236}Pu	^{216}Po	^{20}Ne	40.87	2.97E-85	3.29E-64	62.01	63.03	56.31	57.34	48.16	45.56
^{238}Pu	^{218}Po	^{20}Ne	37.57	6.47E-95	6.59E-74	71.66	72.47	64.81	64.96	44.84	52.88
^{224}Pu	^{200}Pb	^{24}Mg	61.58	2.66E-69	4.44E-48	46.05	46.98	41.38	43.19		
^{226}Pu	^{202}Pb	^{24}Mg	64.68	1.23E-63	2.15E-42	40.39	41.28	36.68	39.02		
^{228}Pu	^{204}Pb	^{24}Mg	67.91	3.33E-58	6.13E-37	34.95	35.76	32.14	34.97	75.13	24.99
^{230}Pu	^{206}Pb	^{24}Mg	69.15	4.13E-56	7.73E-35	32.86	33.63	30.48	33.49	74.65	25.51
^{232}Pu	^{208}Pb	^{24}Mg	69.19	6.73E-56	1.26E-34	32.65	33.43	30.45	33.44	74.04	26.23
^{234}Pu	^{210}Pb	^{24}Mg	63.41	3.15E-65	5.42E-44	41.97	42.96	38.71	40.69	69.01	33.58
^{236}Pu	^{212}Pb	^{24}Mg	56.94	1.56E-77	2.40E-56	54.28	55.36	49.39	50.09	64.38	41.12
^{238}Pu	^{214}Pb	^{24}Mg	51.49	8.43E-90	1.18E-68	66.56	67.55	59.92	59.33	60.27	48.52

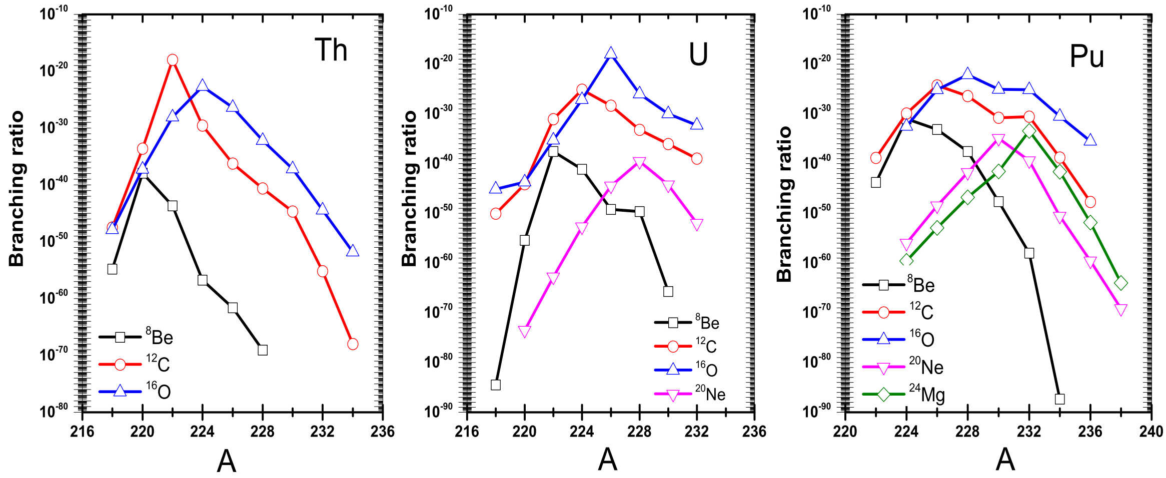

Figure 5.10: The branching ratio [Eq. (5.2.11)] versus mass number of parents Th, U, and Pu for different cluster decays.

To identify the effective decay mode for even-even isotopes of Th, U, and Pu, we have studied the branching ratios. The branching ratio (BR) of cluster decay with respect to alpha emission is defined as

$$BR = \frac{\lambda_{cluster}}{\lambda_{alpha}} = \frac{T_{1/2}^{alpha}}{T_{1/2}^{cluster}}, \tag{5.2.11}$$

where λ_{alpha} and $\lambda_{cluster}$ are the decay constants of alpha emission and cluster decay, respectively. The evaluated branching ratio of alpha emission with respect to cluster decay as a function of the mass number of parent nuclei are given in Fig. 5.10. The experimentally observed branching ratio relative to alpha-decay is $\geq 10^{-19}$. From Fig. 5.10 the branching ratio results predict that ^{12}C decay from ^{222}Th, and ^{16}O decay from ^{226}U are the compatible for measurement.

5.2.6 Geiger-Nuttall plot

In 1911 H. Geiger and J. Nuttal [240, 242] related the decay constant λ with the disintegration energy (Q) of different decay modes. In Fig. 5.11 we present the Geiger-Nuttal plots for half-lives ($log_{10}T_{1/2}$) versus $\sqrt{Q}$ (Q in MeV) for the different clusters (^{8}Be, ^{12}C, ^{16}O, ^{20}Ne and ^{24}Mg) emitted from the parents $^{218-234}$Th, $^{218-232}$U, and $^{224-238}$Pu isotopes. From Fig. 5.11 we can see that these plots reveal linear behavior in each case. The Geiger-Nuttal law is written in the form:

$$log_{10}T_{1/2} = \frac{X}{\sqrt{Q}} + Y, \tag{5.2.12}$$

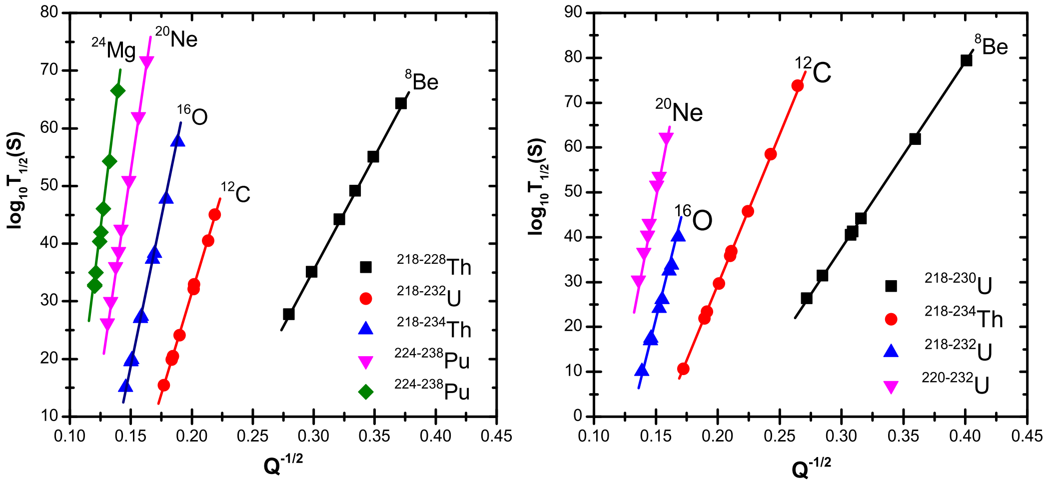

Figure 5.11: Geiger-Nuttall plots of $\log_{10}T_{1/2}$ (in s) versus $Q^{-1/2}$ for ^{8}Be, ^{12}C, ^{16}O, ^{20}Ne, and ^{24}Mg decay from different parent nuclei.

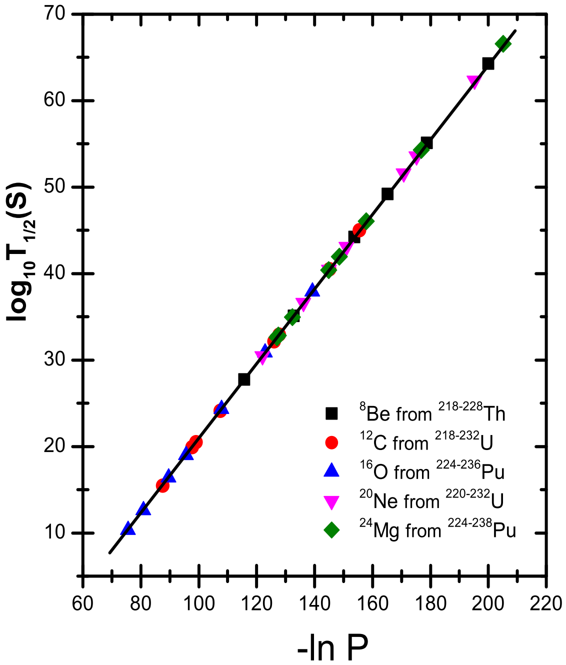

Figure 5.12: Geiger-Nuttall plots of $\log_{10}T_{1/2}$ (in s) versus -ln P for alpha-like clusters from different parent nuclei.

where X represents the slopes and Y are the intercepts of the straight lines. We would like to express that the G-N law is for ultimate Coulomb potential but our calculated results show that the inclusion of surface potential will not produce an extreme deviation

to the straight-line behavior. Each cluster decay has distinct slopes and intercepts. The linear nature of these plots shows the validity of the ELDM model.
The Universal curve between logarithmic half-lives ($log_{10}T_{1/2}$) versus the negative logarithm of penetrability (-ln P) is in favor of the validity of the chosen ELDM model. The plots for the emission of ^{8}Be, ^{12}C, ^{16}O, ^{20}Ne and ^{24}Mg clusters from $^{218-228}$Th, $^{218-232}$U, $^{224-236}$Pu, $^{220-232}$U and $^{224-238}$Pu isotopes are shown in Fig. 5.12. Here, we found that the plot is linear with the nearly same slope of $X = 0.439$ and intercept of $Y = -23.651$. The inclusion of surface potential does not produce a significant variation to the linear behavior of universal curves.

5.3 Conclusions

In summary, we have examined the bulk properties such as B.E./A and rms radii for even-even Th, U, and Pu isotopes using RMF (NL3*) formalism. From the B.E./A study of these isotopes, it is found that the ^{216}Th, ^{218}U, and ^{220}Pu are the most stable elements with $N = 126$. All values of charge radii increase with the neutron number N, although a minor decrement occurs at N = 126, which can be correlated with the shape transition. We have also calculated the two-neutron separation energies and differential from two-neutron separation energies of these isotopes, which confirm (Figs. 5.4 and 5.5) the possible major shell closure at $N = 126$ for these isotopes. In general, we can say that the theoretically obtained results are largely in good agreement with the FRDM [235] predictions and available experimental results [202].
Further, we have discussed the Q-values, alpha, and cluster decay half-lives for even-even $^{214-234}$Th, $^{216-232}$U, and $^{220-238}$Pu isotopes using the RMF model with NL3* parameter set. The alpha and cluster decay half-lives of these nuclei have been calculated using the ELDM model and various empirical formulas: UDL, VS, TM, Scaling Law by Horoi *et al.*. From Tables 5.1 and 5.2 it is observed that both theoretical and experimental Q-values have a maximum for doubly magic daughter nuclei ^{208}Pb (Z_d= 82, N_d = 126) and magic daughter nuclei ^{210}Po, ^{212}Rn, ^{214}Ra, ^{216}Th, ^{218}U (N_d=126, which is a magic number) for the chosen isotopes. The calculated Q-value reveals the shell effects at $N_d = 126$ and influences the half-lives. The alpha decay half-lives are found to have a minimum value for the decay leading magic daughter nuclei ^{214}Ra, ^{216}Th, ^{218}U in these isotopes denoting that the shell is stabilized. The cluster decay half-lives obtained for ^{8}Be, ^{12}C, ^{16}O, ^{20}Ne, and ^{24}Mg emissions from Th, U, and Pu isotopes indicate the shell is stabilized at the daughters ^{208}Pb, ^{210}Po, ^{212}Rn,^{214}Ra, ^{216}Th, and ^{218}U, with the small half-lives. The alpha

and cluster decay half-lives were compared with the corresponding ELDM values and with the results of the empirical formula UDL, VS, Scaling Law by Horoi *et al.* and TM. It is found that the ELDM results match nicely with the UDL results. It can be noticed that the prediction ability of VS, TM, and Horoi formula is limited. It has been found that the UDL formula, derived from the α like-R matrix theory, has better prediction power giving comparable results with microscopic calculations. Also, the results obtained in this work are in good agreement with experimental data. The penetrability (P) for a particular cluster decay will be maximum if the corresponding logarithmic half-life is minimum. The Geiger-Nuttal plots clearly show a linear behavior with different slopes and intercepts for different clusters decay from various parent nuclei. We conclude that the RMF (NL3*) formalism provides the coherent study of microscopic observables for all the considered isotopes.

Chapter 6

Study of Two-proton Emission Half-lives[1]

6.1 Introduction

An intriguing topic in nuclear research is to understand the exotic decay properties of unstable nuclei, with the development of a new generation of radioactive ion beam facilities and advanced detection technologies [254, 255, 256, 257, 258]. In recent years, the proton radioactivity as one of the exotic decay modes has attracted several researchers [256, 257, 258]. The two-proton ($2p$) radioactivity represents a simultaneous emission of two protons from the mother nucleus near the $2p$ drip-line [259]. The two-proton radioactivity phenomenon was first predicted in the 1960s by Zel'dovich [260] and Goldanskii [261, 262]. In 1965, Janecke [263] tried to investigate the possible nuclei for two-proton radioactivity and to find out their properties from the theoretical aspect. Galitsky and Cheltsov [264] presented the first opinion of two-proton radioactivity. Goldanskii [261] also gives the name of two-proton radioactivity. The spontaneous 2p radioactivity for even-even nuclei has been attributed to pairing correlations and virtual excitations to continuum state [257]. In this case, the one-proton decay process is energetically forbidden, whereas the two-proton decay is energetically allowed. The emission of two protons is a process that occurs by the Coulomb and centrifugal barriers. Only those nuclei that fulfill the condition for two-proton emission have a large Coulomb barrier. The Coulomb barrier is not high enough for the very light parent nuclei. During the $2p$ decay process,

[1]The results discussed in this chapter have been published in Acta Phys. Pol. B, 53, 10-A3 (2022).

the energy level of the $1p$ decaying channel is higher than that of $2p$ radioactivity. Two proton emission, known as true $2p$ radioactivity, is characterized by $Q_{2p} > 0$ and $Q_p < 0$ (where Q_{2p} and Q_p represent the released energy of two-proton and one-proton radioactivity, respectively) [256, 257, 258]. Another type called not true $2p$ radioactivity [265] ($Q_{2p} > 0$ and $Q_p > 0$), has been observed from very short-lived nuclear ground states, such as ^{6}Be [266], ^{12}O [267], and ^{16}Ne [268]. Protons are basically charged particles and, therefore, they are sensitive to the charge of other protons which construct a Coulomb barrier. This Coulomb barrier interrupts protons from immediately leaving the atomic nucleus even if they are unbound.

Several experimental studies have been carried out to identify possible nuclei of two-proton emitters. The probability of the two-proton decay width of ^{12}O and ^{16}Ne was introduced in 1978 by KeKelis *et al.* [268]. In 2002, the ground-state true two-proton radioactivity has been observed for the first time from $^{45}Fe \rightarrow^{43} Cr + p + p$ decay at the Grand Accelerateur National d'Ions Lourds (GANIL)(France) [269] and Gesellschaft fur Schwerionenforschung (GSI)(Germany) [259], respectively. The $2p$ decay process half-life in ^{45}Fe ranging between 3 ms and 8 ms was obtained by these research groups. The $2p$ radioactivity of ^{54}Zn was discovered at GANIL [270] in 2005 followed by the two-proton radioactivity of ^{48}Ni [271]. Mukha *et al.* studied the 2p decay of ^{19}Mg by understanding the decay products [272]. The decay of ^{19}Mg, short-lived $2p$ ground-state emitter, was studied at the Projectile-Fragment Separator (FRS) of GSI. A larger number of $^{19}Mg \rightarrow$ $^{17}Ne + p + p$ events were observed. Recently, Goigoux *et al.* [273] observed two-proton decay of ^{67}Kr in an experiment with the BigRIPS separator.

From the theoretical perspective, several approaches have been used for the study of the $2p$ radioactivity during the recent decades [274, 275, 276]. However, the description can be classified mainly into two kinds. The first one is known as simplified theoretical approaches, which include the direct decay model [264, 277, 278], the diproton model [279, 280, 281], and the simultaneous versus sequential decay model [282]. In the diproton model, the two emitted protons are correlated hardily and constituted a He-like cluster, including the effective liquid drop model (ELDM) [163, 164, 283], generalized liquid drop model (GLDM) [284], CPPM [285], Gamow-like model [182, 286], etc. However, in the three-body model [287, 288], the two protons and the nuclear core are distinct simultaneously, and the two protons are only suitable to the final correlation and decayed from the parent nucleus.

One of the very successful models for calculating two-proton decay half-lives is the Effective Liquid Drop Model (ELDM), which was introduced by Goncalves and Duarte

[228, 283] in 1993. In the ELDM model, the surface and Coulomb energies for the dinuclear appearance were investigated analytically, thus obtaining the Gamow's barrier penetrability factor for ^{2}He emission. Furthermore, empirical formulas have been introduced to find out $2p$ radioactivity by fitting the two-parameter and four-parameter which were proposed by Liu *et al.* [182] and Sreeja *et al.* [183], respectively. Within these empirical formulas, the experimental two-proton decay half-lives are reproduced with different accuracies.

In our present study with the RMF model, we have investigated the binding energy per nucleon (B.E./A) of Fe, Ni, Zn, Ge, Kr, and Zr isotopes with the NL3* parameter set. Next, we obtain the S_{2p} from the evaluated B.E. of these isotopes. We notice that the theoretically obtained results agree well with the FRDM [235] and available experimental results [203] for all the isotopes ranging from proton drip line to neutron drip line. Along with this, the mass excess data (ΔM) for 2p decay are calculated by using the obtained B.E./A from the RMF [115, 111], FRDM [235] and WS4 [289] models. The calculated mass excess results have been used further as input to find out a Q_{2p} value and investigate the two-proton decay half-lives by using an effective liquid drop model. Furthermore, comparisons of our investigated results with the available experimentally predicted result and with the results obtained using the empirical formula proposed by Sreeja *et al.* [183] and Liu *et al.* [182] are also made. In addition, we predict the half-lives of possible nuclei of the two-proton radioactivity in the range $30 \leq Z \leq 40$ with the released energy $Q_{2p} > 0$ and $Q_p < 0.2Q_{2p}$ obtained by RMF (NL3*) model. Comparisons of our results with the values obtained using the empirical formula of Sreeja and Liu are made too. Also, the Geiger-Nuttall plots of [$((\mathrm{Z}_d^{0.8} + l^{0.25})\ Q_{2p}^{-1/2})$] versus $log_{10}T_{1/2}$ for emission of ^{2}He for different isotopes of parent nuclei have been examined demonstrating their linear nature.

6.2 Results and discussions

The binding energy per nucleon (BE/A) is a fundamental and important nuclear property, which is necessary for understanding the stability of nuclei and studying the decay lifetime. In the present work, BE/A as a function of mass number (A) for selected isotopes of Fe, Ni, Zn, Ge, Kr, and Zr to study $2p$ radioactivity is calculated by using RMF formalism with NL3* parametrization. The results are shown in Fig. 6.1. To compare them qualitatively, we have also presented the FRDM [235] and experimental data [203] in Fig. 6.1. As one can see the results given in the panels of Fig. 6.1 are in excellent agreement with the experimental results for all the isotopes ranging from proton drip line to neutron drip line, qualitatively as well as quantitatively.

Further, to check the reliability and accuracy of these results, we have calculated two-

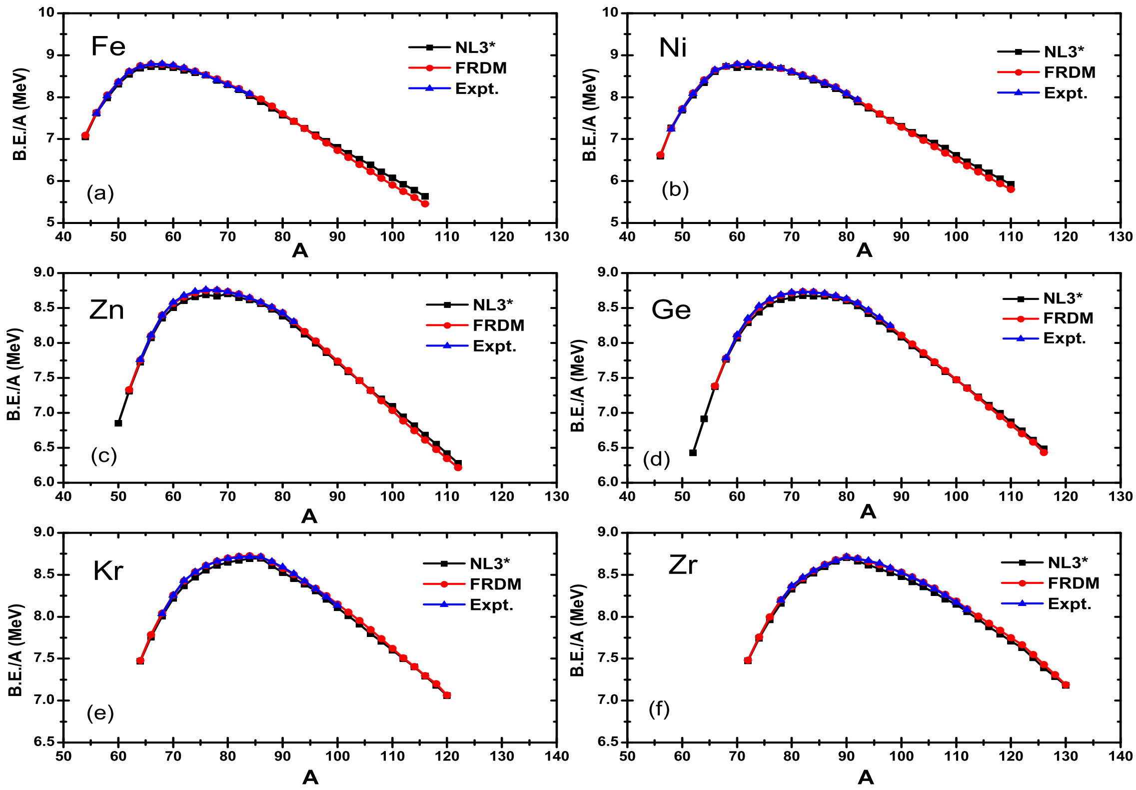

Figure 6.1: The total binding energy per nucleon for Fe, Ni, Zn, Ge, Kr, and Zr isotopes obtained with RMF (NL3*) and compared with the FRDM [235] and Expt. [203] results wherever available.

proton separation energy and compared it with the available experimental data. The two-proton separation energy (S_{2p}) is a considerable quantity in finding the structure and their effects on the nuclei and especially for making a reliable prediction of the two-proton emitters. In the present study, the $S_{2p}(N, Z)$ has been evaluated from the binding energy (B.E.) and is given in the form:

$$S_{2p}(Z, N) = B.E.(Z, N) - B.E.(Z - 2, N). \tag{6.2.1}$$

The B.E. (Z, N) and B.E. (Z-2, N) are calculated by using the RMF formalism with NL3* parameter. We would like to note that the results for S_{2p} are in good agreement with the FRDM predictions [235] as well as experimental [203] data. Also, we find that with the increase of mass number A toward the drip-line, the S_{2p} value gradually increases.

It is seen from Fig. 6.2 that the ^{45}Fe, ^{48}Ni, ^{54}Zn, ^{58}Ge, ^{59}Ge, ^{65}Kr, ^{67}Kr, ^{74}Zr and ^{75}Zr nuclei which have been found as ^{2}He emitters are placed beyond the proton drip line with negative separation energies of -0.981 MeV -1.819 MeV, -1.187 MeV, -1.75 MeV, -1.21 MeV, -3.21 MeV, -1.35 MeV, -2.071 MeV, and -0.975 MeV respectively. Such nuclei satisfying the condition $S_{2p} < 0$ may be the possible parent nuclei for simultaneous two-photon emission.

The theoretically calculated binding energies per nucleon of the considered isotopes

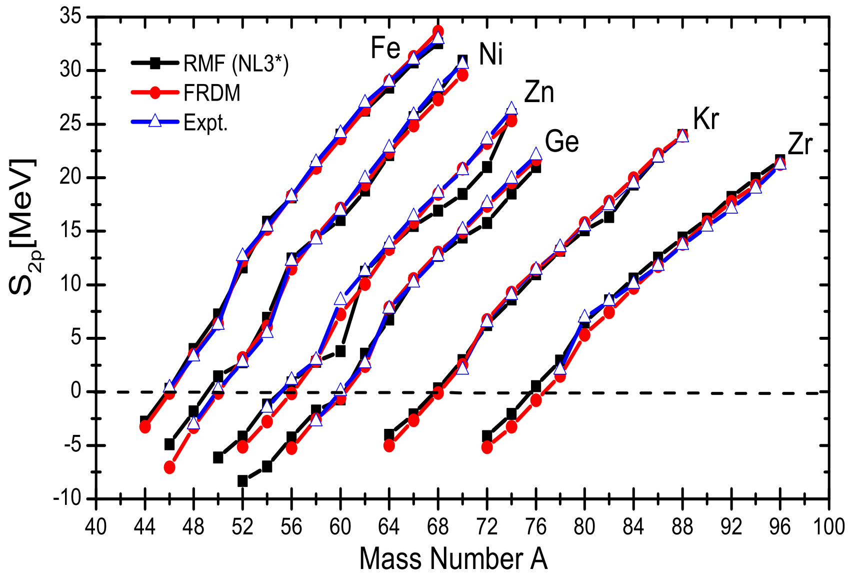

Figure 6.2: The two-proton separation energy for Fe, Ni, Zn, Ge, Kr, and Zr isotopes obtained with RMF (NL3*) and compared with the FRDM [235] and Expt. [203] results wherever available.

of parent nuclei in this work, using the RMF (NL3* parameter set) model, were used to determine the Q_{2p}-values, penetrability (P), and two-proton radioactivity half-lives. First, the mass excess data (ΔM) have been investigated by using the B.E./A in RMF (NL3*) formalism. The binding energy per nucleon is related to mass excess data in the following way written as

$$\text{Mass of the Nuclei} = ((\text{N}^*M_n + \text{Z}^*M_p)^*931.5 \text{ - A}^*\text{B.E./A})/931.5 \text{ u}$$
$$\Delta M = (\text{ Mass of the Nuclei - Mass No. of Nuclei})^*931.5 \text{ MeV}$$

We use these calculated mass excess data to estimate the Q_{2p}-values and two-proton decay half-lives by the expression

$$Q_{2p} = \Delta M_P - (\Delta M_{2p} + \Delta M_D). \tag{6.2.2}$$

In Eq. (6.2.2) ΔM_P notify the mass excess data for the parent nuclei in MeV and ΔM_{2p}, ΔM_D represents the mass excesses for the two-proton cluster and daughter nuclei, respectively. The $2p$-system or ^2He is an unbound system whose mass excess value is equal to twice the proton excess mass, i.e, $\Delta M_{2p} = 2 \times \Delta M_P = 2\times$ 7.289 MeV = 14.578 MeV. The

Table 6.1: Comparison between the experimental data of the $2p$ radioactivity of ^{45}Fe isotope and the estimated ones by the ELDM, GLDM [284], CPPM [285], Gamow-like [286], Skyrme parameter of SLy8 [290], Expt. [271], and two empirical formulas Sreeja [183] and Liu [182].

			$\log_{10}T_{1/2}$ (s)							
Decay case	$Q_{2p}^{expt.}$(MeV) [271]	l	ELDM	GLDM [284]	CPPM [285]	Gamow-like [286]	SLy8 [290]	Expt. [271]	Sreeja [183]	Liu [182]
$^{45}Fe \rightarrow {}^{43}Cr$	1.154	0	-2.43	-2.87	-2.71	-2.74	-2.88	-2.55	-1.80	-2.79

two-proton decay half-lives evaluated using ELDM are compared with the experimental half-life and GLDM, CPPM, Gamow-like, and Skyrme parameter of SLy8 models for $2p$ emitting from ^{45}Fe, and are given in Table 6.1. We see that the evaluated ELDM half-life is close to experimental data in comparison to the result of other models. Therefore, the approach adopted in the present work (by calculating $2p$ decay half-lives using ELDM with RMF inputs) explains well for two-proton radioactive nuclei.

We have tested the prediction power and accuracy of different theoretical approaches used for two-proton decay half-lives studies. For this task, the theoretically predicted results by the ELDM model has been compared with the results predicted by the empirical formulas of Liu and Sreeja, respectively. Further, to test the impact of the difference in Q_{2p} result, we have also compared theoretically obtained half-lives using ELDM by three sets of Q_{2p}-values obtained from the RMF model, WS4, as well as from FRDM prediction. The numerical results are listed in Table 6.2. A comparison with the experimental data is also presented. From Table 6.2, it should be noticed that the differences between the three kinds of Q_{2p} results are large. It is observed from the table Table 6.2 that the experimental Q_{2p} of ^{45}Fe, ^{48}Ni, and ^{54}Zn are reproduced better when using the RMF (NL3*) model as compared to the FRDM and WS4 models. This is because small changes in a force parameter of the NL3* and WS4, as well as FRDM, will affect the binding energy per nucleon results. The predicted accuracy is given by the RMF (NL3*) model for ^{54}Zn is the highest.

Then, the two-proton decay half-lives have been investigated using ELDM by inputting the three types of Q_{2p} values. Here, the angular momentum l is chosen to be zero. The corresponding decay half-lives are presented in columns 7th-11th of Table 6.2 together with their experimental values. We also investigate the half-lives by using empirical formulas: Liu and Sreeja by inputting RMF (NL3*) Q_{2p} values. From the comparison between the half-lives using ELDM (NL3*) and the half-lives calculated using Liu, and Sreeja formula, it is found that the ELDM and Liu values are almost identical but the results obtained with the Sreeja formula is slightly overestimated. As one can see from Table 6.2, the calculated decay half-lives results are larger than the FRDM predictions and WS4 values. Here, it is important to note that a very small difference in Q_{2p} results causes drastically change the two-proton decay half-lives.

To evaluate the predictive power and accuracy of our selected theoretical model, we

Table 6.2: The comparison of our theoretically calculated Q_{2p} using NL3*, FRDM [235], WS4 [289] model with the experimental data. $log_{10}T_{1/2}$ denotes the corresponding two-proton radioactivity half-lives within the ELDM by inputting the NL3*, FRDM, and WS4 model Q_{2p} values. The two-proton radioactivity half-lives also calculated using empirical formulas Liu [182] and Sreeja [183] by inputting Q_{2p} (NL3*) value.

Nuclei	Q_{2p} (MeV)				Penetrability	$\log_{10}T^{cal.}_{1/2}$ (s)					$\log_{10}T^{expt.}_{1/2}$ (s)
	NL3*	FRDM	WS4	Expt.	P	NL3*	Liu	Sreeja	FRDM	WS4	
^{45}Fe	1.63	1.89	2.06	1.210 [275]	2.395×10^{-16}	-6.90	-6.61	-5.46	-8.59	-9.43	-2.42 [275]
				1.100 [259]							-2.40 [259]
				1.140 [269]							-2.07 [269]
				1.154 [271]							-2.55 [271]
^{48}Ni	1.85	3.30	2.54	1.350 [271]	2.237×10^{-16}	-6.87	-6.59	-5.44	-12.64	-10.24	-2.08 [271]
				1.290 [291]							-2.52 [291]
				1.310 [292]							-2.52 [292]
^{54}Zn	1.18	2.77	1.98	1.280 [293]	7.140×10^{-23}	0.63	0.07	0.93	-10.01	-6.30	-2.76 [293]
				1.480 [270]							-2.43 [270]
^{67}Kr	1.25	1.33	3.06	1.690 [273]	1.708×10^{-27}	4.89	3.69	4.40	3.78	-7.89	-1.70 [273]

have estimated the standard deviation of two-proton decay half-life ($log_{10}T^{2p}_{1/2}$) predicted results with the RMF (NL3*) formalism and have compared it with the investigated standard deviation of half-lives result of the Liu and Sreeja formula. The standard deviation expression reads

$$\sigma = \left[\frac{1}{n} \sum_{i=1}^{n} [log(T_{1/2}^{exp}) - log(T_{1/2}^{cal})]^2 \right]^{1/2}. \tag{6.2.3}$$

In the case of experimental data, we obtained that the standard deviation of the $log_{10}T_{1/2}^{2p}$ is 4.98 for the RMF (NL3*), 7.61 for the FRDM, and 6.45 for the WS4. It is clearly seen that the σ = 4.98 for RMF (NL3*) has better predictive ability than FRDM, and WS4 models. In the case of RMF(NL3*), we obtained that the standard deviation of the $log_{10}T_{1/2}^{2p}$ is 0.693 for Liu and 1.06 for Sreeja, respectively.

Given the good agreement between the theoretically predicted outcomes with the ELDM using NL3* Q_{2p} values and the available experimental value, we use this theoretical ELDM (NL3*) approach to find out the decay half-lives of possible two-proton radioactive nuclei in the region of $30 \leq Z \leq 40$. An energy criterion was introduced by Olsen *et al.* [294], which reads $Q_{2p} > 0$ and $Q_p < 0.2Q_{2p}$, extracted from the NL3* model. In this work, an extended criterion is used on two-proton decay half-lives, $-12 \leq log_{10}T_{1/2}^{2p} \leq 2s$ [295]. The

Table 6.3: The comparison of calculated two-proton decay half-lives using ELDM, and two empirical formulas Liu [182] and Sreeja [183] by inputting the Q_{2p} (NL3*) values.

Nuclei	Q_{2p} (MeV)	l	Penetrability	$\log_{10}T_{1/2}$ (s)		
	NL3*		p	ELDM	Liu	Sreeja
$^{58}_{32}$Ge	1.75	0	4.006×10^{-20}	-3.12	-3.50	-2.48
$^{59}_{32}$Ge	1.55	0	3.645×10^{-21}	-2.08	-2.04	-1.07
$^{63}_{34}$Se	2.10	0	8.220×10^{-19}	-4.43	-4.39	-3.35
$^{65}_{36}$Kr	3.09	0	3.025×10^{-15}	-8.01	-7.42	-6.24
$^{70}_{38}$Sr	2.43	0	3.213×10^{-19}	-4.02	-3.92	-2.89
$^{74}_{40}$Zr	3.74	0	8.570×10^{-15}	-8.45	-7.54	-6.36
$^{75}_{40}$Zr	2.19	0	4.538×10^{-22}	-1.18	-1.63	-0.68

predicted half-lives are presented in Table 6.3. The first column contains the parent nuclei. The calculated Q_{2p}-value using the RMF is listed in column 2. The angular momentum and penetrability for ^{2}He decay are given in columns 3-4. For quantitative comparisons between the calculated two-proton decay half-lives using the ELDM, and empirical formula Liu, Sreeja results are listed in columns 5-7. The two-proton radioactivity can not be observed by the NL3* for the Z = 30 nuclides. Presently, a small number of experimentally discovered two-proton emitters are known, more discoveries on two-proton emitters are expected with the new generation of radioactive ion beam facilities. In addition, it can be seen from Table 6.3 that the light parent nuclei get shorter $log_{10}T_{1/2}^{2p}$ half-lives and the decay half-lives become higher for the heavy parent nuclei. For light nuclei, the Coulomb barrier among the daughter nucleus and two proton system is low. This is due to the smaller charge number so that more easily two protons can penetrate the Coulomb barrier. However, the Coulomb barrier becomes longer and longer with the increase of Z. As a result, the two proton decay half-life gets higher in the case of the heavy parent nuclei.

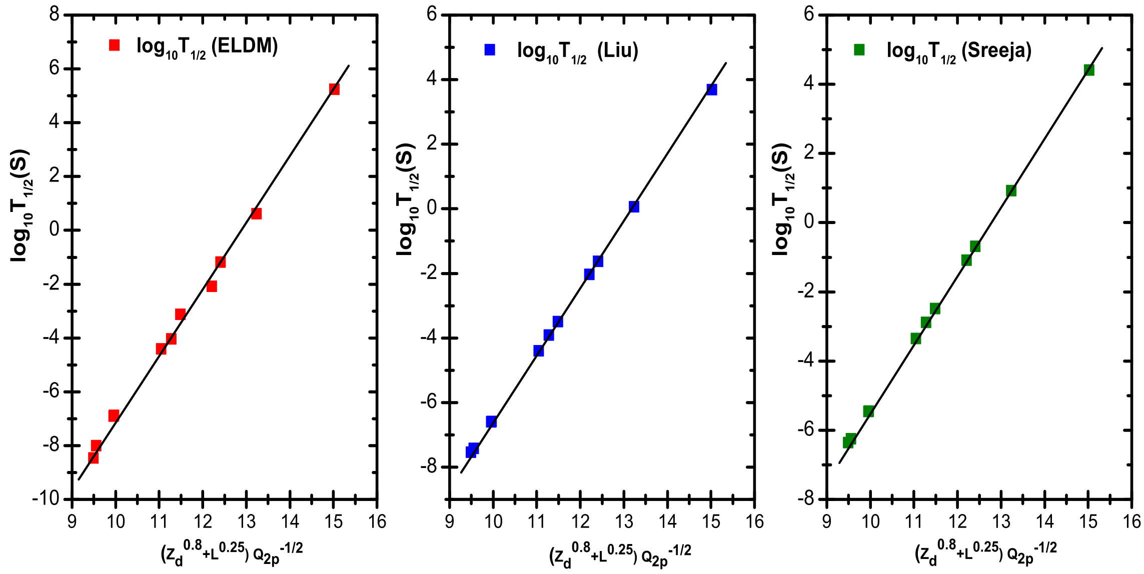

Figure 6.3: Geiger-Nuttall plots for $log_{10}T_{1/2}(s)$ versus $[(Z_d^{0.8} + l^{0.25})Q_{2p}^{-1/2}]$ for two-proton emitters from different parent nuclei.

In 1911 Geiger and Nuttal [240, 242] experimentally observed a standard relation between decay constant λ and the disintegration energy Q of several decay modes. The Geiger-Nuttal expression is written as

$$log_{10}T_{1/2} = \frac{X}{\sqrt{Q}} + Y, \tag{6.2.4}$$

Here, X and Y represent the slope and intercept of the straight line, respectively. Recently, based on the Geiger and Nuttal law, we put forward a two-parameter empirical formula for two-proton decay half-lives by considering the contribution of the daughter atomic number (Z_d) and angular momentum (l) on $T_{1/2}^{2p}$. It can be expressed as

$$log_{10}T_{1/2} = 2.032(Z_d^{0.8} + l^b)Q_{2p}^{-1/2} - 26.832. \quad (6.2.5)$$

To investigate the validity of the chosen ELDM approach, we have plotted the relation between the quantity $log_{10}T_{1/2}$ versus $[(\mathrm{Z}_d^{0.8} + l^{0.25})\mathrm{Q}_{2p}^{-1/2}]$. It is displayed in Fig. 6.3 for ^{2}He decay from different parent nuclei. Here, all the plots are found to have linear nature, which indicates that our theoretically predicted results are reliable. We hope our present predictions of ^{2}He decay of these isotopes could serve as a good basis in future theoretical as well as experimental investigations.

6.3 Conclusions

In summary, we have analyzed the B.E./A for Fe, Ni, Zn, Ge, Kr, and Zr isotopes using RMF (NL3*) formalism. There is an excellent agreement of B.E./A of our calculated RMF results with the FRDM prediction as well as experimental results for all the isotopes ranging from proton drip line to neutron drip line, qualitatively as well as quantitatively. The results obtained for the two-proton separation energies of these isotopes by the RMF (NL3*) are in good agreement with FRDM data, as well as with the experimental data.

Further, we have tested the prediction power and accuracy of different theoretical approaches used for two-proton decay half-lives investigation. The Q_{2p}-values of ^{45}Fe, ^{48}Ni, ^{54}Zn, and ^{67}Kr have been obtained from the RMF model, WS4, as well as from FRDM data. We found that the difference between the three kinds of Q_{2p} values are large. The experimental Q_{2p} of ^{45}Fe, ^{48}Ni, and ^{54}Zn are reproduced better by the results with the RMF (NL3*) model as compared to the FRDM and WS4 models. The accuracy of theoretical predictions depends highly on the reliability of these inputs, and hence the uncertainties of the investigated two-proton decay half-lives are rather large due to the Q_{2p} uncertainties. The investigated half-lives using the ELDM (NL3*) and Liu values are almost identical, but the results found by the Sreeja formula are slightly lower. In addition, we predict the half-lives of possible two-proton radioactive candidates in the region of $30 \leq Z \leq 40$. It may be provided a theoretical reference for future experiments.

Chapter 7

Summary and Conclusions

In the thesis, we have studied the nuclear reaction dynamics for light and medium mass nuclei and decay modes of various parent nuclei using the Relativistic mean-field model. We have used the well-known Glauber model for calculating the total reaction cross section (σ_r) and differential elastic scattering cross section ($\frac{d\sigma}{d\Omega}$). The nuclear density distributions of the projectile and the target nuclei required for the calculation of reaction cross-sections are obtained from the RHB model. For the study of alpha decay, cluster decay, and proton radioactivity of various potential radioactive nuclides by using the ELDM model. In the study of these different decay modes, the consideration of the nuclear shell closure and nuclear structure is an important aspect. In our studies, we have found that the alpha and cluster decay modes which are leading to the formation of daughter nuclei with neutron or proton numbers equal to magic numbers were having minimum half-lives. It clearly demonstrates the prominent role of the shell effect in cluster radioactivity.

In Chapter 1, we have presented a brief introduction of the subject along with the relevant work done by other researchers on the subject. The nuclear landscape along with other basic relevant terms for the study undertaken has been introduced in this chapter. A brief overview of the earlier theoretical and experimental study of cluster radioactivity in both trans-tin and trans-lead regions is provided. Motivation to take up present work has also been introduced.

In Chapter 2, we have given the details of the theoretical formalisms used in this thesis. We have presented the relativistic mean field (RMF) formalism with NL3* parameter, and the Relativistic Hartree Bogoliubov formalism with density-dependent meson exchange (DD-ME2), density-dependent point coupling (DD-PC1) in detail. The BCS pairing correlation for open-shell nuclei is included in this chapter. The details of the Glauber model, its description for investigating nuclear reaction cross-section, and the process of using the nuclear densities from this RMF formalism have been described. A detail of the effective liquid drop (ELDM) model is discussed in this chapter. The empirical formulas such as Universal Decay Law (UDL), Tavares-Medeiros (TM), Viola-Seaborg (VS), and Horoi formula, have been given for the sake of completeness in the discussion. The two-proton radioactivity half-lives are computed using the empirical formula Liu and Sreeja which is also discussed in this chapter.

In Chapter 3, we studied the binding energy and charge radius for light mass nuclei in the framework of RHB formalism with DD-ME2 and DD-PC1 parameter sets. The theoretically calculated results are found to be in good agreement with the available experimental data. In general, the comparative analysis of the total reaction cross section σ_r using DD-ME2 and DD-PC1 densities shows the superiority of DD-ME2 over DD-PC1. We have found that the calculated values of σ_r are in good agreement with the experimental data. It has been also found that the total reaction cross-section increases with the increase of the projectile mass. A study of the differential scattering cross-section with DD-ME2 and DD-PC1 densities shows that both calculated results are quite comparable to each other. However, at the higher angle region, the cross-sections deviate slightly from the experimental data, but the nature of the curve is similar. The oscillatory structure of the elastic scattering differential cross-section at a low scattering angle increases with the increase of incident projectile energy. Hence, employing reliable density distribution in conjunction with the Glauber model leads to a satisfactory description of the total reaction cross-section and elastic scattering differential cross-section over a wide energy range.

In Chapter 4, we have discussed the Q values and cluster decay half-lives for even-even CR nuclei in the trans-tin and transition metal region using the relativistic mean-field (RMF) model with NL3* parameter set. The Effective Liquid Drop Model of cluster decay has been used to calculate cluster decay half-lives. The half-lives are also computed using empirical formulas: UDL and Scaling Law by Horoi *et al.* The calculated Q value has a maximum for doubly magic daughter nuclei ^{100}Sn are its neighboring nuclei in the trans-tin region and transition metal nuclei, the Q value has a maximum for neutron number of daughter nuclei $N_d = 82$. The calculated Q value indicates the shell effects at $N_d = 50, 82$ and influences the half-lives. In the trans-tin region, the minima of the cluster decay half-lives are found for the decay which leads to doubly magic daughter nuclei ^{100}Sn or near doubly magic daughter nuclei. The minimum value of the cluster decay half-lives are found for the decay leading to magic daughter nuclei ^{150}Er, ^{152}Yb, ^{154}Hf, respectively, in the transition metal region. The half-lives of cluster decay calculated with ELDM in conjunction with RMF are close to the results obtained with the UDL formula. Also, ELDM results are in good agreement with experimental data as compared to the GLDM results [50]. Therefore, the ELDM in conjunction with relativistic model inputs is well suited for explaining CR from trans-tin and transition metal regions. Low Q values of the non-alpha-like cluster emissions lead to larger half-lives. The Geiger-Nuttal plots for various clusters decay from different parent nuclei show a linear behavior with different slopes and intercepts.

In Chapter 5, we have calculated the binding energy per nucleon (B.E./A), rms radii, two-neutron separation energies, and differential from two-neutron separation energies for even-even Th, U, and Pu isotopes using RMF (NL3*) formalism. From the B.E./A analysis of these isotopes, it is found that the ^{216}Th, ^{218}U, and ^{220}Pu are the most stable elements. The two-neutron separation energies and differential from two-neutron separation energies, show a sharp dip at $N = 126$, clearly showing major shell closure at $N = 126$. The theoretically obtained results by RMF (NL3*) are in good agreement with the FRDM predictions and available experimental results. Further, we have estimated the Q-values, alpha, and cluster decay half-lives for even-even $^{214-234}$Th, $^{216-232}$U, and $^{220-238}$Pu isotopes. The theoretical and experimental Q-values have a maximum for doubly magic daughter nuclei ^{208}Pb and its neighboring nuclei for the chosen isotopes. The calculated Q-value reveals the shell effects at $N_d = 126$ and influences the half-lives. The alpha decay half-lives are found to have a minimum value for the decay leading magic daughter nuclei ^{214}Ra, ^{216}Th, ^{218}U in these isotopes denote that the shell is stabilized. The cluster decay half-lives indicate the shell is stabilized at the daughters ^{208}Pb, ^{210}Po, ^{212}Rn, ^{214}Ra, ^{216}Th and ^{218}U, with the minimum half-lives. The results obtained by ELDM match nicely with the UDL results. Also, the results obtained in this work are in good agreement with experimental data. The Geiger-Nuttal plots clearly show a linear behavior with different slopes and intercepts for different clusters decay from various parent nuclei. We conclude that the RMF (NL3*) formalism provides the coherent study of microscopic observables for all the considered isotopes.

In Chapter 6, we have employed RMF (NL3*) formalism to calculate the B.E./A for Fe, Ni, Zn, Ge, Kr, and Zr isotopes for studying proton radioactivity. The calculated RMF results of B.E./A are found to be in excellent agreement with the experimental results as well as with FRDM predictions (where expt. data is not available) for all the isotopes ranging from proton drip line to neutron drip line, qualitatively as well as quantitatively.

The two-proton separation energies (S_{2n}) derived from the calculated B.E./A of these isotopes clearly show the evolution of shell structure near magic numbers.

Further, we have tested the prediction power and accuracy of different theoretical approaches used for the two-proton decay half-lives investigation. The Q_{2p}-values of ^{45}Fe, ^{48}Ni, ^{54}Zn, and ^{67}Kr have been obtained from the RMF model, WS4, as well as from FRDM data. From the analysis, we found that the difference between the three kinds of Q_{2p} values are quite large. The experimental Q_{2p} of ^{45}Fe, ^{48}Ni, and ^{54}Zn are reproduced better by the results with RMF (NL3*) model as compared to the FRDM and WS4 models. The accuracy of theoretical predictions depends highly on the reliability of these inputs, and hence the uncertainties of the investigated two-proton decay half-lives are rather large due to the Q_{2p} uncertainties. The half-lives results obtained using ELDM (NL3*) were compared with the values of the Liu and Sreeja formula and it is found that Liu values are almost identical, but the results obtained by the Sreeja formula are slightly less. In addition, we predict the half-lives of possible two-proton radioactive candidates in the region of $30 \leq Z \leq 40$. The calculated results can be taken as a prediction and theoretical reference for future experiments.

7.1 Future scope of the present work

In the present work, We have theoretically investigated the nuclear reaction dynamics of light and medium mass nuclei and nuclear decay modes using the Relativistic mean-field (RMF) model. We find that the RMF model provides a very successful tool to study the interesting nuclear properties across the nuclear landscape and for the nuclei lying near as well as far from the stability line. As a future extension to the present work, the following research objectives may be of much interest:
(i) The effect of deformation on the reaction dynamics calculation is of great interest.
(ii) To extend the reaction dynamics study through relativistic mean field formalism to the medium, heavy and super-heavy nuclei.
(iii) The deformed density of the relativistic mean field formalism be used directly in the calculations instead of converting it to its spherical equivalent.
(iv) The role of deformations of the parent, daughter, and emitted cluster on the half-life time of various parent nuclei both in trans-tin and trans-lead regions.
(v) Search of possible doubly magic nuclei heavier than ^{208}Pb nucleus in the superheavy region using the RMF model.
(vi) The role of neutron and proton magicity, and shell effects by studying the cluster

decay half-lives of different parent nuclei.
(vii) The study of the possibility of emission of heavy clusters from various parent nuclei both in the trans-tin and trans-lead regions.
(viii) To study and search for the new experimentally potential two-proton radioactivity candidates.
Overall continued experimental and theoretical efforts for the exotic nuclei are strongly encouraged to explore and develop our standing about the nuclear structure physics.

Bibliography

[1] E. Rutherford, "The scattering of α and β particles by matter and the structure of the atom", *Phil. Mag. Seri. 6,* **21**, pp. 669-688 (1911).

[2] J. Chadwick, "The Existence of a Neutron", *Proc. Roy. Soc. Lond. A* **136**, pp. 692-708 (1932).

[3] Hideki Yukawa, "On the Interaction of Elementary Particles I", *Proc. Phys. Math. Soc. Jap.* **17**, pp. 48-57 (1935).

[4] P.J. Karol, "Nucleus-nucleus reaction cross sections at high energies: Soft-spheres model", *Phys. Rev. C* **11**, pp. 1203-1209 (1975).

[5] G.F. Bertsch , H. Esbensen, and A. Sustich, "Coulomb versus nuclear breakup in ^{11}Li fragmentation", *Phys. Rev. C* **42**, pp. 758-761 (1990).

[6] Y. Ogawa, K. Yabana and Y. Suzuki, "Glauber model analysis of the fragmentation reaction cross sections of ^{11}Li", *Nucl. Phys. A* **543**, pp. 722-750 (1992).

[7] K. Yabana, Y. Ogawa, and Y. Suzuki, "Break-up effect on the elastic scattering and the optical potential of ^{11}Li", *Phys. Rev. C* **45**, pp. 2909-2918 (1992).

[8] B.K. Agrawal, S.K. Dhiman and R. Kumar, "Exploring the extended density-dependent Skyrme effective forces for normal and isospin-rich nuclei to neutron stars", *Phys. Rev. C* **73**, 034319 (2006).

[9] M. Dutra, O. Loureno, J.S. Sa Martins, A. Delfino, J.R. Stone, P.D. Stevenson, "Skyrme Interaction and Nuclear Matter Constraints", *Phys. Rev. C* **85**, 035201 (2012).

[10] S.K. Patra and C.R. Praharaj, "Relativistic mean field study of light medium nuclei away from beta stability", *Phys. Rev. C* **44**, pp. 2552-2565 (1991).

[11] B. Alex Brown, "New Skyrme interaction for normal and exotic nuclei", *Phys. Rev. C* **58**, pp. 220-231 (1998).

[12] M. Notani, H. Sakurai, N. Aoi, Y. Yanagisawa, A. Saito, N. Imai, T. Gomi, M. Miura, S. Michimasa, H. Iwasaki, N. Fukuda, M. Ishihara, T. Kubo, S. Kubono, H. Kumagai, S. M. Lukyanov, T. Motobayashi, T. K. Onishi, Yu E. Penionzhkevich, S. ShimouraT. Teranishi, K. Ue, V. Ugryumov, A. Yoshida, "New neutron-rich isotopes, ^{34}Ne, ^{37}Na and ^{43}Si, produced by fragmentation of a 64 A MeV ^{48}Ca beam", *Phys. Rev. C* **542**, pp. 49-54 (2002).

[13] Yu.Ts. Oganessian, V.K. Utyonkov, Yu.V. Lobanov, F.Sh. Abdullin, A.N. Polyakov, I.V. Shirokovsky, Yu.S. Tsyganov, G.G. Gulbekian, S.L. Bogomolov, B.N. Gikal, A.N. Mezentsev, S. Iliev, V.G. Subbotin, A.M. Sukhov, A.A. Voinov, G.V. Buklanov, K. Subotic, V.I. Zagrebaev, and M.G. Itkis, "Measurements of cross sections and decay properties of the isotopes of elements 112, 114, and 116 produced in the fusion reactions ^{233,238}U, ^{242}Pu, and ^{248}Cm + ^{48}Ca", *Phys. Rev. C* **70**, 064609 (2004).

[14] Yu.Ts. Oganessian, V.K. Utyonkov, Yu.V. Lobanov, F.Sh. Abdullin, A.N. Polyakov, I.V. Shirokovsky, Yu.S. Tsyganov, G.G. Gulbekian, S.L. Bogomolov, B.N. Gikal, A.N. Mezentsev, S. Iliev, V.G. Subbotin, A.M. Sukhov, A.A. Voinov, G.V. Buklanov, K. Subotic, V.I. Zagrebaev, and M.G. Itkis, "Publishers Note: Measurements of cross sections and decay properties of the isotopes of elements 112, 114, and 116 produced in the fusion reactions ^{233,238}U, ^{242}Pu, and ^{248}Cm + ^{48}Ca", *Phys. Rev. C* **71**, 029902(E) (2005)

[15] S.M. Lukyanov, Yu.E. Penionzhkevich, R. Astabatyan, S. Lobastov, Yu. Sobolev, D. Guillemaud-Mueller, G. Faivre, F. Ibrahim, A.C. Mueller, F. Pougheon, O. Perru, O. Sorlin, I. Matea, R. Anne, C. Cauvin, R. Hue, G. Georgiev, M. Lewitowicz, F.de Oliveira Santos, D. Verney, Z. Dlouhy, J. Mrazek, D. Baiborodin, F. Negoita, C. Borcea, A. Buta, I. Stefan and S. Grevy, "Experimental evidence for the particle stability of ^{34}Ne and ^{37}Na", *J. Phys. G: Nucl. Part. Phys.* **28**, pp. L41-L45 (2002).

[16] E. Margaret Burbidge, G.R. Burbidge, William A. Fowler, and F. Hoyle, "Synthesis of the Elements in Stars", *Rev. Mod. Phys* **29**, pp. 547-650 (1957).

[17] A.G.W. Cameron, "Nuclear Reactions in Stars and Nucleogenesis", *Publications of the Astronomical Society of the Pacific* **69**, pp. 201-222 (1957).

[18] R. Bass, "Nuclear Reaction with Heavy Ion: Texts and Monographs in Physics" (Springer-Verlag), Berlin (1980).

[19] R.J. Glauber, "Lectures in theoretical Physics", *(Interscience*, New York, 1959),Vol. 1, p. 315.

[20] Manoj Kumar Sharma, Pushendra P. Singh, Devendra P. Singh, Abhishek Yadav, Vijay Raj Sharma, Indu Bala, Rakesh Kumar, Unnati, B.P. Singh, and R. Prasad, "Systematic study of pre-equilibrium emission at low energies in ^{12}C and ^{16}O induced reactions", *Phys. Rev. C* **91**, 014603 (2015).

[21] S.T. Butler, "On Angular Distributions from (d, p) and (d, n) Nuclear Reactions", *Phys. Rev. American Phys. Society (APS)* **80**(6): pp 1095-1096, (1950).

[22] G.D. Alkhazov, S.L. Belostotsky, and A.A. Vorobyov, "Scattering of 1 Gev Protons on nuclei", *Phys. Rep.* **42**(c), pp 89-144, (1978).

[23] K.A. Petrzhak and G.N. Flerov, "Spontaneous fission of Uranium", *Zh. Eksp. Teor. Fiz.* **10**, pp. 1013-1017 (1940).

[24] A. Sandulescu, D.N. Poenaru, and W. Greiner, "New type of decay of heavy nuclei intermediate between fission and alpha decay", *Sov. J. Part. Nucl.* **11**, pp. 528-541 (1980).

[25] K.P. Santhosh and Indu Sukumaran, "Studies on cluster decay from trans-lead nuclei using different versions of nuclear potentials", *Eur. Phys. J. A* **53**, 136 (2017).

[26] D.N. Poenaru and W. Greiner, "Cluster Radioactivity", *Cluster in Nuclei, Lecture Notes in Physics, Springer, Berline, Heidelberg* **Vol 818**, pp.1-56 (2010).

[27] D.N. Poenaru, W. Greiner, M. Ivascu, and A. Sandulescu "Heavy cluster decay of trans-zirconium "stable" nuclides", *Phys. Rev. C* **32**, pp. 2198-2200, (1985).

[28] D.N. Poenaru, D. Schnabel, W. Greiner, D. Mazilu, and R. Gherghescu, "Nuclear Lifetimes for cluster radioactivities", *At. Data. Nucl. Data Tables* **48**, pp. 231-327, (1991).

[29] D.N. Poenaru, W. Greiner, and R. Gherghescu, "New island of cluster emitters", *Phys. Rev. C* **47**, pp. 2030-2037, (1993).

[30] Raj K. Gupta, Sarbjit Singh, Rajeev K. Puri, and Werner Scheid, "Instabilities against exotic cluster decays in "stable" nuclei with Z and N in the neighborhood of spherical and deformed closed shells", *Phys. Rev. C* **47**, pp. 561-566, (1993).

[31] Satish Kumar, and Raj K. Gupta, "Measurable decay modes of barium isotopes via exotic cluster emissions", *Phys. Rev. C* **49**, pp. 1922-1926, (1994).

[32] D.N. Poenaru, W. Greiner, and E. Hourani, "^{12}C emission from ^{114}Ba and nuclear properties", *Phys. Rev. C* **51**, pp. 594-600, (1995).

[33] Satish Kumar, J.S. Batra and Raj K. Gupta, "Cluster emissions with ^{132}Sn daughter from neutron-rich nuclei", *J. Phys. G: Nucl. Part. Phys.* **22**, pp. 215-219, (1996).

[34] Roberto Bonetti, Iosif Bulboaca, Florin Carstoiu, and Ovidiu Dumitrescu, "Hindrance factors in alpha and cluster radioactivity of ^{233}U", *Phys. Lett. B* **396**, pp. 15-20, (1997).

[35] K.P. Santhosh, and Antony Joseph, "Exotic decay in Ba isotopes via ^{12}C emission", *Pramana J. Phys.* **55**, pp. 375-382, (2000).

[36] K.P. Santhosh, R.K. Biju, Sabina Sahadevan, and Antony Joseph, "Exotic decay in proton-rich Nd isotopes", *Phys. Scr.* **77**, 065201, (2008).

[37] G. Shanmugam, G.M. Carmel Vigila Bai, and B. Kamalaharan, "Cluster radioactivities from an island of cluster emitters", *Phys. Rev. C* **51**, pp. 2616-2622, (1995).

[38] Satish Kumar, Dharam Bir, and Raj K. Gupta, "^{100}Sn-daughter α-nuclei cluster decays of some neutron-deficient Xe to Gd parents: Sn radioactivvity", *Phys. Rev. C* **51**, pp. 1762-1771, (1995).

[39] Sushil kumar, "Shell closure effects associated with tin daughter", *Proc. Int. Sym. Nucl. Phys.* **54**, pp. 204, (2009).

[40] M.S. Mehta, S.K. Patra, and Raj K. Gupta, "Magic numbers in neutron-rich nuclei using relativistic mean field model", *Proc. Int. Sym. Nucl. Phys.* **55**, pp. 204-205, (2010).

[41] G. Shiva Kumara Swamy, T.K. Umesh, "Half-lives of Cluster Decay of Neutron Rich Nuclei in Trans-Tin Region", *Int. J. Mod. Phys. E* **20**, pp. 2167-2175 (2011).

[42] K.P. Santhosh, "Cluster radioactivity leading to doubly magic ^{100}Sn and ^{132}Sn daughter", *Pramana J. Phys.* **76**, pp. 431-440, (2011).

[43] Zongqiang Sheng, Dongdong Ni, and Zhongzhou Ren, "Systematic calculations on cluster radioactivity half-lives", *J. Phys. G: Nucl. Part. Phys.* **38**, 055103, (2011).

[44] Sushil Kumar, "Decay studies of rare-earth nuclei to superheavy elements and the associated shell effects", *J. Phys.: Conf. Ser.* **282**, 012015, (2011).

[45] K.P. Santhosha, M.S. Unnikrishnan and B. Priyanka, "Role of neutron magicity in the cluster radioactivity", *Proc. DAE Symp. Nucl. Phys.* **57**, pp. 342-343 (2012).

[46] X.J. Bao, H.F. Zhang, B.S. Hu, G. Royer, and J.Q. Li, "Half-lives of cluster radioactivity with a generalized liquid-drop model", *J. Phys. G: Nucl. Part. Phys.* **39**, 095103, (2012).

[47] K.P. Santhosh, and R.K. Biju, "Stability of $^{248-254}$Cf isotopes against alpha and cluster radioactivity", *Annals of Physics* **334**, pp. 280-287 (2013).

[48] M. Ismail, A.Y. Ellithi, M.M. Selim, N. Abou-Samra, and O.A. Mohamedien, "Cluster decay half-lives and preformation probabilities", *Phys. Scr.* **95**, 7 (2017).

[49] Deepthy Maria Joseph, Nithu Ashok, and Antony Joseph, "A theoretical study of cluster radioactivity in platinum isotopes", *Eur. Phys. J. A* **54**, 8 (2018).

[50] Yonghao Gao, Jianpo cui, Yanzhao Wang and Jianzhong Gu, "Cluster radioactivity of neutron-deficient nuclei in trans-tin region", *Sci. Rep.* **10**, 9119 (2020).

[51] Joshua T. Majekodunmi, M. Bhuyan, D. Jain, K. Anwar, N. Abdullah, and Raj Kumar, "Cluster decay half-lives of $^{112-122}$Ba isotopes from the ground state and intrinsic excited state using the relativistic mean-field formalism within the preformed-cluster-decay model", *Phys. Rev. C* **105**, 044617, (2022).

[52] H.J. Rose and G.A. Jones, "^{208}Pb-daughter cluster radioactivity and the deformations and orientations of nuclei", *Nature (London)* **307**, pp. 245-247 (1984).

[53] D.V. Aleksandrov, A.F. Belyatskii, Yu.A. Glukhov, Nikol'skii, B. G.Novatskii, A. A. Ogloblin, and D.N. Stepanov, "Observation of the spontaneous emission of ^{14}C nuclei from ^{223}Ra", *JETP Lett.* **40**, pp 909-912, (1984).

[54] S. Gales, E. Hourani, M. Hussonnois, J.P. Schapira, L. Stab, and M. Vergnes, “Exotic Nuclear Decay of ^{223}Ra by Emission of ^{14}C Nuclei”, *Phys. Rev. Lett.* **53**, pp. 759-762, (1984).

[55] P.B. Price, J.D. Stevenson, S.W. Barwick, and H.L. Ravn, “Discovery of Radioactive Decay of ^{222}Ra and ^{224}Ra by ^{14}C Emission”, *Phys. Rev. Lett.* **54**, pp. 297-299, (1985).

[56] Yu.Ts. Oganessian, Yu.A. Lazarev, V.L. Mikheev, Yu.A. Muzychka, I.V. Shirokovsky, S.P. Tretyakova, V.K. Utyonkov, “Search for cluster decay of ^{114}Ba”, *Z. Phys. A* **349**, pp. 341-342, (1994).

[57] A. Guglielmetti, R. Bonetti, G. Poli, R. Collatz, Z. Hu, R. Kirchner, E. Roeckl, N. Gunn, P.B. Price, B.A. Weaver, A. Westphal, and J. Szerypo, “Nonobservation of ^{12}C cluster decay of ^{114}Ba”, *Phys. Rev. C* **56**, pp. R2912-2916(R) (1997).

[58] R. Bonetti, C. Chiesa, A. Guglielmetti, C. Migliorino, P. Monti, A.L. Pasinetti and H.L. Ravn, “Carbon radioactivity of ^{221}Fr and ^{221}Ra and the hindered decay of exotic odd-A emitters”, *Nucl. Phys. A* **576**, pp. 21-28, (1994).

[59] E. Hourani, M. Hussonnois, L. Stab, L. Brillard, S. Gales, J.P. Schapira, “Evidence for the radioactive Decay of ^{226}Ra by ^{14}C Emission”, *Phys. Rev. Lett.* **160**, pp. 375-379, (1985).

[60] M. Hussonnois, J.F. Le Du, L. Brillard, and G. Ardisson, “Possible cluster preformation in the ^{14}C decay of ^{223}Ra”, *Phys. Rev. C* **42**, R495(R), (1990).

[61] W. Kutschera, I. Ahmad, S.G. Armato, A.M. Friedman, J.E. Gindler, W. Henning, T. Ishii, M. Paul, and K.E. Rehm “Spontaneous ^{14}C emission from ^{223}Ra”, *Phys. Rev. C* **32**, pp 2036-2042, (1985).

[62] E. Hourani,L. Rosier, G. Berrier-Ronsin, A. Elayi, A.C. Mueller, G. Rappenecker, G. Rotbard, G. Renou, A. Liebe, L. Stab, and H.L. Ravn “Fine structure in ^{14}C emission from ^{223}Ra and ^{224}Ra”, *Phys. Rev. C* **44**, pp 1424-1434, (1991).

[63] E. Hourany, G. Berrier-Ronsin, A. Elayi, P. Hoffmann-Rothe, A.C. Mueller, L. Rosier, G. Rotbard, G. Renou, A. Liebe, D.N. Poenaru, and H.L. Ravn, “^{223}Ra nuclear spectroscopy in ^{14}C cluster radioactivity”, *Phys. Rev. C* **52**, pp 267-270, (1995).

[64] Roberto Bonetti and Alessandra Guglielmetti, "Cluster Radioactivity: An Overview After Twenty Years", *Rom. Rep. Phys.* **59**, pp. 301-310 (2007)

[65] R. Bonetti, C. Chiesa, A. Guglielmetti, C. Migliorino, A. Cesana, and M. Terrani, "Discovery of Oxygen radioactivity of atomic nuclei", *Nucl. Phys. A* **556**, pp 115-122, (1993).

[66] S.W. Barwick, P.B. Price, H.L. Ravn, E. Hourani, and M. Hussonnois, "Systematics of spontaneous emission of intermediate mass fragments from heavy nuclei", *Phys. Rev. C* **34**, pp 362-365, (1986).

[67] D. Weselka, P. Hille, and A. Chalupka, "Decay of ^{226}Ra by ^{14}C emission", *Phys. Rev. C* **41**, pp 778-781, (1990).

[68] R. Bonetti, C. Chiesa, A. Guglielmetti, R. Matheoud, C. Migliorino, A.L. Pasinetti, and H.L. Ravn, "Nuclear structure effects in the exotic decay of ^{225}Ac via ^{14}C emission", *Nucl. Phys. A* **562**, pp 32-40, (1993).

[69] P.B. Price, R. Bonetti, A. Guglielmetti, C. Chiesa, R. Matheoud, C. Migliorino, and K.J. Moody, "Emission of ^{23}F and ^{24}Ne in cluster radioactivity of ^{231}Pa", *Phys. Rev. C* **46**, pp 1939-1945, (1992).

[70] M. Hussonnois, J.F. Le Du, L. Brillard, J. Dalmasso, and G. Ardisson, "Search for a fine structure in the ^{14}C decay of ^{222}Ra", *Phys. Rev. C* **43**, pp 2599-2604, (1991).

[71] R. Bonetti, C. Carbonini, A. Guglielmetti, M. Hussonnois, D. Trubert and C.Le Naour, "Cluster decay of ^{230}U via Ne emission", *Nucl. Phys. A* **686**, pp. 64-70, (2001).

[72] Pan Qiangyan, Yang Weifan, Yuan Shuanggui, Li Zongwei, Ma Taotao, Luo Yixiao, Kong Dengming, Qiao Jimin, Luo Zihua, Zhang Mutian, and Wang Shuhong, "Search for heavy ion emission from the decay of ^{230}U", *Phys. Rev. C* **62**, 044612, (2000).

[73] S.P. Tretyakova, A. Sandulescu, V.L. Mikheev, D. Hasegan, I.A. Lebedev, Yu.S. Zamyatnin, Yu.S. Korotkin, and B.F. Myasoedov, "On the spontaneous emission of clusters by the ^{230}Th, ^{237}Np, and ^{241}Am nuclei", *JINR Dubna Rapid Commun.* **13**, pp. 34-40, (1985).

[74] R. Bonetti, C. Chiesa, A. Guglielmetti, R. Matheoud, G. Poli, V.L. Mikheev, and S.P. Tretyakova, "First observation of spontaneous fission and search for cluster decay of ^{232}Th", *Phys. Rev. C* **51**, pp. 2530-2533, (1995).

[75] A. Sandulescu, Yu.S. Zamyatnin, I.A. Lebedev, B.F. Myasoedov, S.P. Tretyakova, and D. Hasegan, "Ne emission by spontaneous decay of ^{231}Pa", *JINR Dubna Rapid Commun.* **15**, pp. 5-7, (1984).

[76] S.W. Barwick, P.B. Price, and J.D. Stevenson, "Radioactive decay of ^{232}U by ^{24}Ne emission", *Phys. Rev. C* **31**, pp. 1984-1986(R), (1984).

[77] R. Bonetti, E. Fioretto, C. Migliorino, A. Pasinetti, F. Barranco, E. Vigezzi, and R.A. Broglia, "Revising the chart of the nuclides by exotic decay", *Phys. Lett. B* **241**, pp. 179-183, (1990).

[78] R. Bonetti, C. Chiesa, A. Guglielmetti, C. Migliorino, A. Cesana, M. Terrani, and P.B. Price, "Neon radioactivity of uranium isotopes", *Phys. Rev. C* **44**, pp. 888-890, (1991).

[79] P.B. Price, K.J. Moody, E.K. Hulet, R. Bonetti, and C. Migliorino, "High-statistics study of cluster radioactivity from ^{233}U", *Phys. Rev. C* **43**, pp. 1781-1788, (1991).

[80] K.J. Moody, E.K. Hulet, Shicheng Wang, and P.B. Price, "Heavy-fragment radioactivity of ^{234}U", *Phys. Rev. C* **39**, pp. 2445-2447, (1989).

[81] S.P. Tretyakova, Yu.S. Zamyatnin, V.N. Kovantsev, Yu.S. Korotkin, V.L. Mikheev, and G.A. Timofeev, "Observation of nucleon clusters in the spontaneous decay of ^{234}U", *Z. Phys. A* **333**, pp. 349-353, (1989).

[82] S.P. Tret'yakova, V.L. Mikheev, V.A. Ponomarenko, A.N. Golovchenko, A.A. ogloblin, and V.A. Shigin, "Cluster decay of ^{236}U", *JEPT Lett.* **59**, pp. 394-397, (1994).

[83] K.J. Moody, E.K. Hulet, and P.B. Price, "Search for cluster radioactivity of ^{237}Np", *Phys. Rev. C* **45**, pp. 1392-1393, (1992).

[84] A.A. Ogloblin, N.I. Venikov, S.K. Lisin, S.V. Pirozhkov, V.A. Pchelin, Yu.F. Rodionov, V.M. Semochkin, V.A. Shabrov, I.K. Shvetsov, V.M. Shubko, S.P. Tretyakova, and V.L. Mikheev, "Detection of radioactive ^{236}Pu decay with emission of ^{28}Mg nuclei", *Phys. Lett. B* **235**, pp. 35-39, (1990).

[85] M. Hussonnois, J.F. Le Du, D. Trubert, R. Bonetti, A. Guglielmetti, T. Guzei, S.P. Tret'yakova, V.L. Mikheev, A.N. Golovchenko, A.N. Golovchenko, and V.A. Ponomarenko, "Cluster decay of ^{236}Pu and correlations of the probabilities of α decay, cluster decay, and spontaneous fission of heavy nuclei", *JEPT Lett.* **62**, pp. 701-705, (1995).

[86] Shicheng Wang, D. Snowden-lfft, P.B. Price, K.J. Moody, and E.K. Hulet, "Heavy fragment radioactivity of ^{238}Pu: Si and Mg emission", *Phys. Rev. C* **39**, 1647(R), (1989).

[87] S.W. Barwick, "Observation of novel radioactive decay by spontaneous emission of complex nuclei", *PhD Thesis University of California, Berkely* (1986).

[88] M. Paul, I. Ahmad, and W. Kutschera, "Search for ^{34}Si ions in ^{241}Am decay", *Phys. Rev. C* **34**, pp. 1980-1982, (1986).

[89] A.A. Ogloblin, R. Bonetti, V.A. Denisov, A. Guglielmetti, M.G. Itkis, C. Mazzocchi, V.L. Mikheev, Yu.Ts. Oganessian, G.A. Pik-Pichak, G.L. Poli, S.M. Pirozhkov, V.M. Semochkin, V.A. Shigin, I.K. Shvetsov, and S.P. Tretyakova, "Observation of cluster decay of ^{242}Cm", *Phys. Rev. C* **61**, 034301, (2000).

[90] D.N. Poenaru, in *ed.* D.N. Poenaru, Nuclear Decay Modes, Institute of Physics, Bristol, UK, **1996**.

[91] P. Buford Price, "Heavy-Particle Radioactivity (A> 4)", *Annu. Rev. Nucl. Part. Sci.* **39**, pp. 19-42 (1989).

[92] W. Greiner, M. Ivascu, D.N. Poenaru, and S. Sandulescu, in *Treatise on Heavy Ion Science,* edited by D.A. Bromley (Plenum, New York, 1989), Vol. 8, p. 641.

[93] S.S. Malik, S. Singh, R.K. Puri, S. Kumar and Raj K. Gupta , "Clustering phenomena in radioactive and stable nuclei and in heavy-ion collisions", *pramana - J Phys.* **32**, pp. 419-433 (1989).

[94] D.N. Poenaru, M. Ivascu, A. Sandulescu and W. Greiner, "Atomic nuclei decay modes by spontaneous emission of heavy ions", *Phys. Rev. C* **32**, 572 (1985).

[95] M.H. Johnson, and E. Teller "Classical Field Theory of Nuclear Forces", *Phys. Rev.* **98**, pp. 783-787, (1955).

[96] Hans-Peter Duerr, and Edward Teller "Interaction of Antiprotons with Nuclear Fields", *Phys. Rev.* **101**, pp. 494-495, (1996).

[97] J.D. Walecka, "A Theory of Highly condensed matter", *Ann. Phys.* **83**, pp. 491-529, (1974).

[98] Brain D Serot, and John Dirk Walecka, "The Relativistic Nuclear Many Body Problem", *Adv. Nucl. Phys.* **16**, pp. 1-327, (1986).

[99] R. Brockmann, "Relativistic Hartree-Fock description of nuclei", *Phys. Rev. C* **18**, pp. 1510-1524, (1978).

[100] R. Brockmann, W. Weise, "Relativistic single particle motion and spin-orbit coupling in nuclei and hypernuclei", *Nucl. Phys. A* **355**, pp. 365-382, (1981).

[101] Joachim Maruhn, and Walter Greiner, "Theory of fission-Mass Distributions Demonstrated for ^{226}Ra, ^{236}U, ^{258}Fm", *Phys. Rev. Lett.* **32**, pp. 548-551, (1974).

[102] Raj K. Gupta, Werner Scheid, and Walter Greiner, "Theory of Charge Dispersion in Nuclear Fission", *Phys. Rev. Lett.* **35**, pp. 353-356, (1975).

[103] A. Sandulescu, Raj K. Gupta, Werner Scheid and Walter Greiner, "Synthesis of new elements within the fragmentation theory: Application to Z=104 and 106 elements", *Phys. Lett. B* **60**, pp. 225-228, (1976).

[104] M. Warda, A. Zdeb, and L.M. Robledo, "Cluster radioactivity in superheavy nuclei", *Phys. Rev. C* **98**, 041602(R) (2018).

[105] A. Zdeb, M. Warda, and K. Pomorski, "Half-lives for alpha and cluster radioactivity within a Gamow-like model", *Phys. Rev. C* **87**, 024308 (2013).

[106] O.A.P. Tavares and E.L. Medeiros, "A simple description of cluster radioactivity", *Phys. Scr.* **86**, 015201 (2012).

[107] Y. -J. Shi, W.J. Swiatecki, "Estimates of Radioactive Decay by the Emission of Nuclei Heavier than α-Particles", *Nucl. Phys. A* **438**, pp. 450-460 (1985).

[108] D.N. Poenaru, Y. Nagame, R.A. Gherghescu and W. Greiner, "Systematics of cluster decay modes", *Phys. Rev. C* **65**, 054308 (2002).

[109] Y.K. Gambhir, P. Ring, and A. Thimet, "Relativistic Mean Field theory for finite nuclei", *Ann. Phys.* **198**, pp. 132-179, (1990).

[110] P. Ring, "Relativistic mean field theory in finite nuclei", *Prog. Part. Nucl. Phys.* **37**, pp. 193-263, (1996).

[111] J. Boguta, A.R. Bodmer, "Relativistic calculation of nuclear matter and the nuclear surface", *Nucl. Phys. A* **292**, pp. 413-428 (1977).

[112] L.I. Schiff, "Nonlinear Meson Theory of Nuclear Forces. I. Neutral Scalar Mesons with Point-Contact Repulsion", *Phys. Rev.* **84**, pp. 1-9, (1951).

[113] M. Rufa, P.G. Reinhard, J.A. Maruhn, W. Greiner, and M.R. Strayer, "Optimal parametrization for the relativistic mean-field model of the nucleus", *Phys. Rev. C* **38**, pp. 390-409, (1988).

[114] M.M. Sharma, M.A. Nagarajan, and P. Ring, "Rho meson coupling in the relativistic mean field theory and description of exotic nuclei", *Phys. Lett. B* **312**, pp. 377-381 (1993).

[115] W. Pannert, P. Ring, and J. Boguta, "Relativistic Mean-Field Theory and Nuclear Deformation", *Phys. Rev. Lett.* **59**, pp. 2420-2422 (1987).

[116] A. Shukla, Sven Aberg, and S.K. Patra, "Nuclear structure and reaction properties of even-even oxygen isotopes towards drip line", *J. Phys. G: Nucl. Part. Phys.* **38**, 095103 (2011).

[117] M. Del Estal, M. Centelles, X. Vinas, and S.K. Patra, "Effects of new nonlinear couplings in relativistic effective field theory", *Phys. Rev. C* **63**, 024314 (2001).

[118] T. Niksic, D. Vretenar, P. Ring, "Relativistic nuclear energy density functionals: Mean-field and beyond", *Prog. Part. Nucl. Phys.* **66**, pp. 519-548 (2011).

[119] S.K. Patra, Raj K. Gupta, B.K. Sharma, P.D. Stevenson and Walter Greiner, "Exotic clustering in heavy and superheavy nuclei within the relativistic and non-relativistic mean field formalisms", *J. Phys. G: Nucl. Part. Phys.* **34**, 2073 (2007).

[120] B.D. Serot and J.D. Walecka, "Recent Progress in Quantum Hadrodynamics", *Int. J. Mod. Phys. E* **6**, pp. 515-631 (1997).

[121] G.A. Lalazissis, S. Karatzikos, R. Fossion, D. Pena Arteaga, A.V. Afanasjev, P. Ring, "The effective force NL3 revisited", *Phys. Lett. B* **671**, pp. 36-41 (2009).

[122] S.K. Patra, "Effects of pairing correlation in light nuclei", *Phys. Rev. C* **48**, pp. 1449-1451 (1993).

[123] A. Shukla, B.K. Sharma, R. Chandra, P. Arumugam, and S.K. Patra, "Nuclear reaction studies of unstable nuclei using relativistic mean field formalisms in conjunction with the Glauber model", *Phys. Rev. C* **76**, 034601 (2007).

[124] T.R. Werner, J.A. Sheikh, W. Nazarewicz, M.R. Strayer, A.S. Umar, M. Misu, "Shape coexistence around ${}^{44}_{16}S_{28}$: the deformed N = 28 region", *Phys. Lett. B* **335**, pp. 259-265 (1994).

[125] T.R. Werner, J.A. Sheikh, M. Misu, W. Nazarewicz, J. Rikovska, K. Heeger, A.S. Umar, M.R. Strayer, "Ground-state properties of exotic Si, S, Ar and Ca isotopes", *Nucl. Phys. A* **597**, pp. 327-340 (1996).

[126] David G. Madland and J. Rayford Nix, "New model of the average neutron and proton pairing gaps", *Nucl. Phys. A* **476**, pp. 1-38, (1988).

[127] P. Moller and J.R. Nix, "Nuclear masses from a unified macroscopic-microscopic model", *At. Data Nucl. Data Tables* **39**, pp. 213-223 (1988)

[128] G.A. Lalazissis, D. Vretenar, P. Ring, M. Stoitsov, and L.M. Robledo, "Relativistic Hartree+Bogoliubov description of the deformed N=28 region", *Phys. Rev. C* **60**, 014310 (1999).

[129] A. Shukla, Sven Aberg, and Awanish Bajpeyi, "Systematic nuclear structure studies using relativistic mean field theory in mass region $A \sim 130$", *J. Phys. G: Nucl. Part. Phys.* **44**, 025104 (2017).

[130] G.A. Lalazissis, T. Niksic, D. Vretenar, and P. Ring, "New relativistic mean-field interaction with density-dependent meson-nucleon couplings", *Phys. Rev. C* **71**, 024312, (2005).

[131] T. Niksic, D. Vretenar, and P. Ring, "Relativistic nuclear energy density functionals: Adjusting parameters to binding energies", *Phys. Rev. C* **78**, 034318, (2008).

[132] S. Typel and H.H. Wolter, "Relativistic mean field calculations with density-dependent meson-nucleon coupling", *Nucl. Phys. A* **656**, pp. 331-364 (1999).

[133] T. Niksic, D. Vretenar, P. Finelli, and P. Ring, "Relativistic Hartree-Bogoliubov model with density-dependent meson-nucleon couplings", *Phys. Rev. C* **66**, 024306, (2002).

[134] F. Hofmann, C.M. Keil, and H. Lenske, "Density dependent hadron field theory for asymmetric nuclear matter and exotic nuclei", *Phys. Rev. C* **64**, 034314 (2001).

[135] F.de Jong and H. Lenske, "Asymmetric nuclear matter in the relativistic Brueckner-Hartree-Fock approach", *Phys. Rev. C* **57**, pp. 3099-3107 (1998).

[136] Yuan Tian, Z.Y. Ma, and P. Ring, "A finite range pairing force for density functional theory in superfluid nuclei", *Phys. Lett. B* **676**, pp. 44-50 (2009).

[137] R.J. Glauber, "Cross Sections in Deuterium at High Energies", *Phys. Rev.* **100**, pp. 242-248 (1955).

[138] R.N. Panda, M. Panigrahi, Mahesh K. Sharma, and S.K. Patra, "Evidence of a Proton Halo in ^{23}Al: A Mean Field Analysis", *Phys. of Atom. Nucl.* **81**, pp. 417-428 (2018).

[139] B. Abu-Ibrahim, K. Fujimura, and Y. Suzuki, "Evidence of a Proton Halo in 23Al: A Mean Field Analysis", *Nucl. Phys. A* **657**, pp. 391-428 (1999).

[140] J. Chauvin, D. Lubrun, A. Lounis, and M. Buenerd, "Low and intermediate energy nucleus-nucleus elastic scattering and the optical limit of Glauber theory", *Phys. Rev. C* **28**, pp. 1970-1974 (1983).

[141] M. Buenerd, A. Lounis, J. Chauvin, D. Lebrun, P. Martin, G. Duhamel, J.C. Gondrand, and P.De Saintignon, "Elastic and inelastic scattering of carbon ions at intermediate energies", *Nucl. Phys. A* **424**, pp. 313-428 (1984).

[142] P. Shukla, "Glauber model and the heavy ion reaction cross section", *Phys. Rev. C* **67**, 054607 (2003).

[143] A. Bhagwat and Y.K. Gambhir, "Microscopic description of recently measured reaction cross sections of neutron-rich nuclei in the vicinity of the N = 20 and N = 28 closed shells", *Phys. Rev. C* **77**, 027602 (2008).

[144] S.K. Charagi, "Nucleus-nucleus reaction cross section at low energies: Modified Glauber model", *Phys. Rev. C* **48**, pp. 452-454 (1993).

[145] S.K. Charagi and S.K. Gupta, “Coulomb-modified Glauber model description of heavy-ion reaction cross sections”, *Phys. Rev. C* **41**, pp. 1610-1618 (1990).

[146] S.K. Charagi and S.K. Gupta, “Nucleus-nucleus elastic scattering at intermediate energies: Glauber model approach”, *Phys. Rev. C* **56**, pp. 1171-1174 (1997).

[147] A. Bhagwat and Y.K. Gambhir, “Recently measured reaction cross sections with low energy fp-shell nuclei as projectiles: Microscopic description”, *Phys. Rev. C* **73**, 054601 (2006).

[148] T. Zheng, T. Yamaguchi, A. Ozawa, M. Chiba, R. Kanungo, T. Kato, K. Katori, K. Morimoto, T. Ohnishi, T. Suda, I. Tanihata, Y. Yamaguchi, A. Yoshida, K. Yoshida, H. Toki, and N. Nakajima, “Study of halo structure of ^{16}C from reaction cross section measurement”, *Nucl. Phys. A* **709**, pp. 103-118 (2002).

[149] H.L. Bradt and B. Peters, “The Heavy Nuclei of the Primary Cosmic Radiation”, *Phys. Rev.* **77**, pp. 54-75 (1950).

[150] S. Kox, A. Gamp, R. Cherkaoui, A.J. Cole, N. Longequeue, J. Menet, C. Perrin and J.B. Viano, “Direct measurements of heavy-ion total reaction cross sections at 30 and 83 MeV/nucleon”, *Nucl. Phys. A* **420**, pp. 162-172 (1984).

[151] S. Kox, A. Gamp, C. Perrin, J. Arvieux, R. Bertholet, J.F. Bruandet, M. Buenerd, Y.El Masri, N. Longequeue, and F. Merchez, “Transparency effects in heavy-ion collisions over the energy range 100-300 MeV/nucleon”, *Phys. Lett. B* **159**, pp. 15-18 (1985).

[152] S. Kox, A. Gamp, C. Perrin, J. Arvieux, R. Bertholet, J.F. Bruandet, M. Buenerd, R. Cherkaoui, A.J. Cole, Y.El-Masri, N. Longequeue, J. Menet, F. Merchez, and J.B. Viano, “Trends of total reaction cross sections for heavy ion collisions in the intermediate energy range”, *Phys. Rev. C* **35**, pp. 1678-1691 (1987).

[153] Geant4 Physics Reference Manual.

[154] W.Q. Shen, B. Wang, J. Feng, W.L. Zhan, Y.T. Zhu, and E.P. Feng, “Total reaction cross section for heavy-ion collisions and its relation to the neutron excess degree of freedom”, *Nucl. Phys. A* **491**, pp. 130-146 (1989).

[155] L.W. Townsend and J.W. Wilson, Comment on "Trends of total reaction cross sections for heavy ion collisions in the intermediate energy range", *Phys. Rev. C* **37**, pp. 892-893 (1988).

[156] L. Sihver, M. Lantz, and A. Kohama, "Improved parametrization of the transparency parameter in Kox and Shen models of total reaction cross sections", *Phys. Rev. C* **89**, 067602 (2014).

[157] R.K. Tripathi, F.A. Cucinotta, and J.W. Wilson, "Accurate universal parameterization of absorption cross sections III-light systems", *Nucl. Instrum. Methods* **155**, pp. 349-356 (1999).

[158] L. Sihver, C.H. Tsao, R. Silberberg, T. Kanai, and A.F. Barghouty, "Total reaction and partial cross section calculations in proton-nucleus (Z_i < 26) and nucleus-nucleus reactions (Zp and Z_i < 26)", *Phys. Rev. C* **47**, pp. 1225-1236 (1993).

[159] Kei Iida, Akihisa Kohama, and Kazuhiro Oyamatsu, "Formula for Proton-Nucleus Reaction Cross Section at Intermediate Energies and Its Application", *J. Phys. Soc. Jpn.* **76**, 044201 (2007).

[160] H.P. Wellisch and D. Axen, "Total reaction cross section calculations in proton-nucleus scattering", *Phys. Rev. C* **54**, pp. 1329-1332 (1996).

[161] R.K. Tripathi, Francis A. Cucinotta, and John W. Wilson, "Accurate universal parameterization of absorption cross sections", *Nucl. Instr. and Meth.* **117**, pp. 347-349 (1996).

[162] M. Gonalves and S.B. Duarte, "Effective liquid drop description for the exotic decay of nuclei", *Phys. Rev. C* **48**, pp. 2409-2414 (1993).

[163] M. Gongalves, , S.B. Duarte, E. Garcia and O. Rodriguez, "PRESCOLD: Calculation of the half-life for alpha decay, cluster radioactivity and cold fission processes", *Comput. Phys. Commun.* **107**, pp. 246-252 (1997).

[164] S.B. Duarte, O. Rodrguez, O.A.P. Tavares, M. Gonalves, F. Garca, and F. Guzmn, "Cold fission description with constant and varying mass asymmetries", *Phys. Rev. C* **57**, pp. 2516-2522 (1998).

[165] M. Gaudin, "Energie coulombienne du solide uniformement charge limite par deux spheres secantes", *J. Phys. France* **35**, pp. 885-894 (1974).

[166] Y.-J. Shi, W.J. Swiatecki, "Estimates of the Influence of Nuclear Deformations and Shell Effects on the Lifetimes of Exotic Radioactivities", *Nucl. Phys. A* **464**, pp. 205-222 (1987).

[167] K.P. Santhosh, R.K. Biju, Sabina Sahadevan, "Semi-empirical formula for spontaneous fission half life time", *Nucl. Phys. A* **832**, pp. 220-232 (2009).

[168] G. Royer, "Alpha emission and spontaneous fission through quasi-molecular shapes", *J. Phys. G: Nucl. Part. Phys.* **26**, pp. 1149-1170 (2000).

[169] D.N. Poenaru, R. A. Gherghescu, and W. Greiner, "Single universal curve for cluster radioactivities and alpha decay", *Phys. Rev. C* **83**, pp. 014601 (2011).

[170] M. Balasubramaniam, S. Kumarasamy, N. Arunachalam, and Raj K. Gupta, "New semiempirical formula for exotic cluster decay", *Phys. Rev. C* **70**, 017301 (2004).

[171] Dongdong Ni, Zhongzhou Ren, Tiekuang Dong, and Chang Xu, "Unified formula of half-lives for alpha decay and cluster radioactivity", *Phys. Rev. C* **78**, 044310 (2008).

[172] Zhongzhou Ren, Chang Xu, and Zaijun Wang, "New perspective on complex cluster radioactivity of heavy nuclei", *Phys. Rev. C* **70**, 034304 (2004).

[173] C. Qi, F.R. Xu, R.J. Liotta, R. Wyss, M.Y. Zhang, C. Asawatangtrakuldee, and D. Hu, "Microscopic mechanism of charged-particle radioactivity and generalization of the Geiger-Nuttall law", *Phys. Rev. C* **80**, 044326 (2009).

[174] C. Qi, F.R. Xu, R.J. Liotta, and R. Wyss, "Universal Decay Law in Charged-Particle Emission and Exotic Cluster Radioactivity", *Phys. Rev. Lett.* **103**, 072501 (2009).

[175] Mihai Horoi, B.Alex Brown, Aurel Sandulescu, "Scaling Law in Cluster Decay", *arXiv:nucl-th/9403008* Nuclear Theory, (1994).

[176] Mihai Horoi, "Scaling behaviour in cluster decay", *J. Phys. G: Nucl. Part. Phys.* **30**, pp. 945-955 (2004).

[177] V.E. Viola Jr, G.T. Seaborg, "Nuclear systematics of the heavy elements-II Lifetimes for alpha, beta and spontaneous fission decay", *J. Inorg. Nucl. Chem.* **28**, pp. 741-761 (1966)

[178] A. Sobiczewski, Z. Patyk, and S. Cwiok, "Deformed superheavy nuclei", *Phys. Lett. B* **224**, pp. 1-4 (1989)

[179] Rashmirekha Swain, S.K. Patra and B.B. Sahu, "Nuclear structure and decay modes of Ra isotopes within an axially deformed relativistic mean field model", *Chin. Phys. C* **42**, 084102 (2018)

[180] O.A.P. Tavares, E.L. Medeiros, "A calculation method to estimate partial half-lives for exotic radioactivities", *Eur. Phys. J. A* **49** (6), pp. 1-4 (2013)

[181] A.M. Lane and R.G. Thomas, "R-Matrix Theory of Nuclear Reactions", *Rev. Mod. Phys.* **30**, pp. 257-353 (1958).

[182] Hong-Ming Liu, You-Tian Zou, Xiao Pan, Jiu-Long Chen, Biao He, and Xiao-Hua Li, "New Geiger-Nuttall law for two-proton radioactivity", *Chin. Phys. C* **45**, 024108 (2021).

[183] I. Sreeja and M. Balasubramaniam, "An empirical formula for the half-lives of exotic two-proton emission", *Eur. Phys. J. A* **55**, pp. 33 (2019).

[184] Isao Tanihata, "Neutron halo nuclei", *J. Phys. G: Nucl. Part. Phys.* **22**, pp. 157-198, (1996).

[185] P. Arumugam, B.K. Sharma, P.K. Sahu, S.K. Patra, T. Sil, M. Centelles and X. Vinas, "Versatility of field theory motivated nuclear effective Lagrangian approach", *Phys. Lett. B* **601**, pp. 51-55 (2004).

[186] P.G. Hansen and B. Jonson, "The Neutron Halo of Extremely Neutron-Rich Nuclei", *Eur. phys. Lett.* **4**, pp. 409-414, (1987).

[187] A. Ozawa, T. Suzuki, and I. Tanihata, "Nuclear size and related topics", *Nucl. Phys. A* **693**, pp. 32-62, (2001).

[188] Xiang-Xiang Sun, Jie Zhao, and Shan-Gui Zhou, "Shrunk halo and quenched shell gap at N = 16 in ^{22}C Inversion of sd states and deformation effects", *Phys. Lett. B* **785**, pp. 530-535, (2018).

[189] A.J. Miller, K. Minamisono, A. Klose, D. Garand, C. Kujawa, J.D. Lantis, Y. Liu, B. Maa, P.F. Mantica, W. Nazarewicz, W. Nrtershuser, S.V. Pineda, P.-G. Reinhard, D.M. Rossi, F. Sommer, C. Sumithrarachchi, A. Teigelhfer and J. Watkins, "Proton

superfluidity and charge radii in proton-rich calcium isotopes", *Nature Phys.* **15**, pp. 432-436, (2019).

[190] V. Morcelle, R. Lichtenthler, R. Linares, M.C. Morais, V. Guimares, A. Lpine-Szily, P.R.S. Gomes, J. Lubian, D.R. Mendes Junior, P.N.De Faria, A. Barioni, L.R. Gasques, J.M.B. Shorto, K.C.C. Pires, J.C. Zamora, R.P. Condori, V. Scarduelli, J.J. Kolata, H. Amro, F.D. Becchetti, H. Jiang, E.F. Aguilera, D. Lizcano, E. Martinez-Quiroz, and H. Garcia, "Elastic scattering and total reaction cross section for the ^{7}Be+^{27}Al system at near-barrier energies", *Phys. Rev. C* **89**, 044611 (2014).

[191] I. Tanihata, T. Kobayashi, T. Suzuki, K. Yoshida, S. Shimoura, K. Sugimoto, K. Matsuta, T. Minamisono, W. Christie, D. Olson, H. Wieman, "Determination of the density distribution and the correlation of halo neutrons in ^{11}Li", *Phys. Lett. B* **287**, pp. 307-311, (1992).

[192] Y. Togano, T. Nakamura, Y. Kondo, J.A. Tostevin, A.T. Saito, J. Gibelin, N.A. Orr, N.L. Achouri, T. Aumann, H. Baba, F. Delaunay, P. Doornenbal, N. Fukuda, J.W. Hwang, N. Inabe, T. Isobe, D. Kameda, D. Kanno, S. Kim, N. Kobayashi, T. Kobayashi, T. Kubo, S. Leblond, J. Lee, F.M. Marqus, R. Minakata, T. Motobayashi, D. Murai, T. Murakami, K. Muto, T. Nakashima, N. Nakatsuka, A. Navin, S. Nishi, S. Ogoshi, H. Otsu, H. Sato, Y. Satou, Y. Shimizu, H. Suzuki, K. Takahashi, H. Takeda, S. Takeuchi, R. Tanaka, A.G. Tuff, M. Vandebrouck, K. Yoneda, "Interaction cross section study of the two-neutron halo nucleus ^{22}C", *Phys. Lett. B* **761**, pp. 412-418, (2016).

[193] K. Tanaka, T. Yamaguchi, T. Suzuki, T. Ohtsubo, M. Fukuda, D. Nishimura, M. Takechi, K. Ogata, A. Ozawa, T. Izumikawa, T. Aiba, N. Aoi, H. Baba, Y. Hashizume, K. Inafuku, N. Iwasa, K. Kobayashi, M. Komuro, Y. Kondo, T. Kubo, M. Kurokawa, T. Matsuyama, S. Michimasa, T. Motobayashi, T. Nakabayashi, S. Nakajima, T. Nakamura, H. Sakurai, R. Shinoda, M. Shinohara, H. Suzuki, E. Takeshita, S. Takeuchi, Y. Togano, K. Yamada, T. Yasuno, and M. Yoshitake, "Observation of a Large Reaction Cross Section in the Drip-Line Nucleus ^{22}C", *Phys. Rev. Lett.* **104**, 062701 (2010).

[194] W. Horiuchi, Y. Suzuki, B. Abu-Ibrahim, and A. Kohama, "Systematic analysis of reaction cross sections of carbon isotopes", *Phys. Rev. C* **75**, 044607 (2007).

[195] A. Ozawa, T. Kobayashi, T. Suzuki, K. Yoshida, and I. Tanihata, "New Magic Number, N = 16, near the Neutron Drip Line", *Phys. Rev. Lett.* **84**, 5493 (2000).

[196] A.N. Antonov, M.K. Gaidarov, D.N. Kadrev, P.E. Hodgson, and E. Moya de Guerra, "Charge Density Distributions and Related From Factors in Neutron-Rich Light Exotic Nuclei", *Int. J. Mod. Phys. E* **13**, pp. 759-772 (2004).

[197] A.N. Antonov, D.N. Kadrev, M.K. Gaidarov, E.Moya de Guerra, P. Sarriguren, J.M. Udias, V.K. Lukyanov, E.V. Zemlyanaya, and G.Z. Krumova, "Charge and matter distributions and form factors of light, medium, and heavy neutron-rich nuclei", *Phys. Rev. C* **72**, 044307 (2005).

[198] K. Varga, S.C Pieper, Y. Suzuki, and R.B. Wiringa, "Monte Carlo integration in Glauber model analysis of reactions of halo nuclei", *Phys. Rev. C* **66**, 034611 (2002).

[199] B. Abu-Ibrahim, Y. Ogawa, Y. Suzuki, and I. Tanihata, "Cross section calculations in Glauber model: I. Core plus one-nucleon case", *Comput. Phys. Commun.* **151**, pp. 369-386 (2003).

[200] A. Bhagwat and Y.K. Gambhir, "Microscopic investigations of mass and charge changing cross sections", *Phys. Rev. C* **69**, 014315 (2004).

[201] B.K. Sharma, S.K. Patra, Raj K. Gupta, A. Shukla, P. Arumugam, P.D. Stevenson, and Walter Greiner, "Reaction cross-sections for light nuclei on ^{12}C using relativistic mean field formalism", *J. Phys. G: Nucl. Part. Phys.* **32**, 2089 (2006).

[202] National Nuclear Data Center (NNDC) in Brookhaven National Laboratory, http://www.nndc.bnl.gov/nndc/nudat2/.

[203] G. Audi, A.H. Wapstra, and C. Thibault, "The Ame2003 atomic mass evaluation: (II). Tables, graphs and references", *Nucl. Phys. A* **729**, pp. 337-676 (2003).

[204] I. Angeli and K.P. Marinova, "Table of experimental nuclear ground state charge radii: An update", *Atomic Data and Nuclear Data Tables* **99**, pp. 69-95 (2013).

[205] G. Hagen, A. Ekstrm, C. Forssn, G.R. Jansen, W. Nazarewicz, T. Papenbrock, K.A. Wendt, S. Bacca, N. Barnea, B. Carlsson, C. Drischler, K. Hebeler, M. Hjorth-Jensen, M. Miorelli, G. Orlandini, A. Schwenk, and J. Simonis, "Neutron and weak-charge distributions of the ^{48}Ca nucleus", *Nature Phys.* **12**, pp. 186-190 (2016).

[206] X. Roca-Maza, M. Centelles, F. Salvat, and X. Vinas, "Theoretical study of elastic electron scattering off stable and exotic nuclei", *Phys. Rev. C* **78**, 044332 (2008)

[207] J.Y. Hostachy, M. Buenerd, J. Chauvin, D. Lebrun, and Ph. Martin, J.C. Lugol, L. Papineau, P. Roussel, N. Alamanos, J. Arvieux, and C. Cerruti "Elastic and inelastic scattering of ^{12}C ions at intermediate energies", *Nucl. Phys. A* **490**, pp. 441-470 (1988).

[208] M. Fukuda, T. Ichihara, N. Inabe, T. Kubo, H. Kumagai, T. Nakagawa, Y. Yano, I. Tanihata, M. Adachi, K. Asahi, M. Kouguchi, M. Ishihara, H. Sagawa and S. Shimoura, "Neutron halo in ^{11}Be studied via reaction cross sections", *Phys. Lett. B* **268**, pp. 339-344 (1991).

[209] M. Takechia, T. Ohtsubob, T. Kubokic, M. Fukudad, D. Nishimurad, T. Suzukic, T. Yamaguchic, A. Ozawae, T. Moriguchie, T. Sumikamaf, H. Geisselg, N. Aoia, N. Fukudaa, I. Hachiumacs, N. Inabea, Y. Ishibashie, Y. Itohe, D. Kamedaa, K. Kusakaa, M. Lantza, M. Miharad, Y. Miyashitaf, S. Momotah, K. Namihirac, H. Ohishie, Y. Ohkumab, T. Ohnishia, M. Ohtakea, K. Ogawae, Y. Shimbarab, T. Sudaa, S. Suzukib, H. Takedaa, K. Tanakaa, R. Watanabeb, M. Winklerg, Y. Yanagisawaa, Y. Yasudae, K. Yoshinagaf, A. Yoshidaa, K. Yoshidaa, and T. Kubo, "Measurements of nuclear radii for neutron-rich Ne isotopes $^{28-32}Ne$", *Nucl. Phys. A* **834**, pp. 412c-415c (2010).

[210] T. Nagahisa and W. Horiuchi, "Examination of the ^{22}C radius determination with interaction cross sections", *Phys. Rev. C* **97**, 054614 (2018).

[211] R.M. DeVries and J.C. Peng, "Nucleus-nucleus total reaction cross sections", *Phys. Rev. C* **22**, pp. 1055-1064 (1980).

[212] W. Horiuchi, S. Hatakeyama, S. Ebata and Y. Suzuki, "Extracting nuclear sizes of medium to heavy nuclei from total reaction cross sections", *Phys. Rev. C* **93**, 044611 (2016).

[213] T. Eliyakut-Roshko, R.H. McCamis, W.T.H. van Oers, R.F. Carlson, and A.J. Cox, "Measurements of proton total reaction cross sections for ^{58}Ni and ^{60}Ni including nonrelativistic and relativistic data analyses", *Phys. Rev. C* **51**, pp. 1295-1302 (1995).

[214] A. Auce, A. Ingemarsson, R. Johansson, M. Lantz, G. Tibell, R.F. Carlson, M.J. Shachno, A.A. Cowley, G.C. Hillhouse, N.M. Jacobs, J.A. Stander, J.J. van Zyl, S.V. Fortsch, J.J. Lawrie, F.D. Smit, and G.F. Steyn "Reaction cross sections for protons on ^{12}C, ^{40}Ca, ^{90}Zr, and ^{208}Pb at energies between 80-MeV and 180-MeV", *Nucl. Phys. A* **653**, pp. 341-354 (1999).

[215] V. Lapoux, N. Alamanos, F. Auger, V. Fkou-Youmbi, A. Gillibert, F. Marie, S. Ottini-Hustache, J-L. Sida, D.T. Khoa, Y. Blumenfeld, F. Marchal, J-A. Scarpaci, T. Suomijrvi, J.H. Kelley, J.-M. Casandjian, M. Chartier, M.D. Cortina-Gil, M. Mac Cormick, W. Mittig, F. de Oliveira Santos, A.N. Ostrowski, P. Roussel-Chomaz, K.W. Kemper, N. Orr, and J.S. Winfield, "Coupling effects in the elastic scattering of ^{6}He on ^{12}C", *Phys. Rev. C* **66**, 034608 (2002).

[216] J.S. Al-Khalili, M.D. Cortina-Gil, P. Roussel-Chomaz, N. Alamanos, J. Barrette, W. Mittig, F. Auger, Y. Blumenfeld, J.M. Casandjian, M. Chartier, V. Fekou-Youmbi, B. Fernandezc, N. Frascariae, A. GillibertC, H. Laurente, A. Lepine-Szily, N.A. Orr, V. Pascalon, J.A. Scarpaci, J.L. Sida, T. Suomijarvie, "Elastic scattering of ^{6}He and its analysis within a four-body eikonal model", *Phys. Lett. B* **378**, pp. 45-49 (1996).

[217] V.K. Lukyanov, D.N. Kadrev, E.V. Zemlyanaya, A.N. Antonov, K.V. Lukyanov and M.K. Gaidarov, "^{6}He + ^{12}C elastic scattering using a microscopic optical potential", *Phys. Rev. C* **82**, 024604 (2010).

[218] R.K. Gupta and W. Greiner, "Cluster Radioactivity", *Int. J. Mod. Phys.* **3**, pp. 335-433 (1994).

[219] Sham K. Arun, Raj K. Gupta, BirBikram Singh, Shefali Kanwar, and Manoj K. Sharma, "^{208}Pb-daughter cluster radioactivity and the deformations and orientations of nuclei", *Phys. Rev. C* **79**, 064616 (2009).

[220] E. Hourani, M. Gussonnois and D.N. Poenaru, " Radioactivities by light fragment (C, Ne, Mg) emission", *Ann. Phys. Paris* **14**, pp. 311-345 (1989).

[221] K.P. Santhosh and R.K. Biju, "Alpha decay, cluster decay and spontaneous fission in $^{294-326}$122 isotopes", *J. Phys. G: Nucl. Part. Phys.* **36**, 015107 (2008).

[222] D.N. Poenaru, R.A. Gherghescu and Walter Greiner, "Heavy-Particle Radioactivity of Superheavy Nuclei", *Phys. Rev. Lett.* **107**, 062503 (2011).

[223] D.N. Poenaru, R.A. Gherghescu and Walter Greiner, "Nuclear inertia and the decay modes of superheavy nuclei", *J. Phys. G: Nucl. Part. Phys.* **40**, 105105 (2013).

[224] K. Manimaran and M. Balasubramaniam, "Cluster Radioactivity in Trans-Tin region using semiempirical formula", *Int. J. Mod. Phys. E* **18**, pp. 1509-1520 (2009).

[225] G. Sawhney, K. Sharma, M.K. Sharma, and R.K. Gupta (Nuclear Structure, 2016) *EPJ Web of Conferences, vol.* **117** 04013

[226] A. Guglielmetti, R. Bonetti, G. Poli, P.B. Price, A.J. Westphal, Z. Janas, H. Keller, R. Kirchner, O. Klepper, A. Piechaczek, E. Roeckl, K. Schmidt, A. Plochocki, J. Szerypo, and B. Blank, "Identification of the new isotope ^{114}Ba and search for its α and cluster radioactivity", *Phys. Rev. C* **52**, pp. 740-743 (1995).

[227] R. Bonetti, and A. Guglielmetti 1999 *Heavy elements and related new phenomena* vol. II ed by W. Greiner, and R.K. Gupta (World Scientific, Singapore) p. 643

[228] S.B. Duarte, O.A.P. Tavares, F. Guzman, A. Dimarco, F. Garcia, and O. Rodriguez, "Half-Lives for Proton emission, Alpha Decay, Cluster Radioactivity, and Cold fission processes calculated in a unified theoretical framework", *At. Data and Nucl. Data Tables* **80**, pp. 235-299 (2002).

[229] Nithu Ashok, Deepthy Maria Joseph and Antony Joseph, "Cluster decay in Osmium isotopes using Hartree-Fock-Bogoliubov theory", *Mod. Phys. Lett. A* **31**, 1650045 (2016).

[230] Deepthy Maria Josepha, Nithu Ashok, and Antony Joseph, "A theoretical study of cluster radioactivity in platinum isotopes", *Eur. Phys. J. A* **58**, pp. 8 (2018).

[231] Nithu Ashok, Antony Joseph, "Alpha and cluster decay half-lives in Tungsten isotopes: A microscopic analysis", *Nucl. Phys. A* **977**, pp. 101-111 (2018).

[232] K.P. Santhosha and B. Priyanka, "The role of doubly magic ^{208}Pb and its neighbour nuclei in cluster radioactivity", *Eur. Phys. J. A* **49**, pp. 66 (2013).

[233] K.P. Santhosh, B. Priyanka, M.S. Unnikrishnan, "Cluster decay half-lives of trans-lead nuclei within the Coulomb and proximity potential model", *Nucl. Phys. A* **889**, pp. 29-50 (2012).

[234] K.P. Santhosh and Tinu Ann Jose, "Half-lives of cluster radioactivity using the modified generalized liquid drop model with a new preformation factor", *Phys. Rev. C* **99**, 064604 (2019).

[235] P. Moller, A.J. Sierk, T. Ichikawa and H. Sagawa, "Nuclear ground-state masses and deformations: FRDM (2012)", *At. Data and Nucl. Data Tables* **109**, pp. 1-204 (2016).

[236] S.N. Kuklin, G.G. Adamian, and N.V. Antonenko, "Spectroscopic factors and cluster decay half-lives of heavy nuclei", *Phys. Rev. C* **71**, 014301 (2005).

[237] K.E. Abd El Mageed, L.I. Abou Salem, K.A. Gado, and Asmaa G. Shalaby, "Cluster Decay Half-Lives of 5d Transition Metal Nuclei Using the Coulomb and Proximity Potential Model", *Chin. J. Phys.* **53**, 120304 (2015).

[238] C. Mazzocchi, Z. Janas, L. Batist, V. Belleguic, J. Dring, M. Gierlik, M. Kapica, R. Kirchner, G.A. Lalazissis, H. Mahmud, E. Roeckl, P. Ring, K. Schmidt, P.J. Woods, J. Zylicz, "Alpha decay of ^{114}Ba", *Phys. Lett. B* **532**, pp. 29-36 (2002).

[239] H. Geiger and J.M. Nuttall, "XL. The ranges of the α-particles from uranium", *Philos. Mag. Series 6*, **23:135**, pp. 439-445 (1912).

[240] H. Geiger, "Reichweitemessungen an α-strahlen", *Z. Phys.* **8**, pp. 45-47 (1922).

[241] E. Rutherford, "VIII. Uranium Radiation and the Electrical conduction Produced by it", *Philos. Mag. Series 5*, **47**, pp. 109-163 (1899).

[242] H. Geiger and J.M. Nuttall, "The ranges of the Alpha particles from various radioactive substances and a relation between range and period of transformation", *Philos. Mag.* **22**, pp. 613-621 (1911).

[243] G. Gamow, "Zur Quantentheorie des Atomkernes", *Z. Phys.* **51**, pp. 204-212 (1928).

[244] Ronald W. Gurney and Edw. U. Condon, "Wave Mechanics and Radioactive Disintegration", *Nature* **122**, pp. 439 (1928).

[245] A.P. Leppanen, J. Uusitalo, M. Leino, S. Eeckhaudt, T. Grahn, P.T. Greenlees, P. Jones, R. Julin, S. Juutinen, H. Kettunen, P. Kuusiniemi, P. Nieminen, J. Pakarinen, P. Rahkila, C. Scholey, and G. Sletten, "α decay studies of the nuclides ^{218}U and ^{219}U", *Phys. Rev. C* **75**, 054307 (2007).

[246] Sushil Kumar, Ramna Rani and Rajesh Kumar , "Shell closure effects studied via cluster decay in heavy nuclei", *J. Phys. G: Nucl. Part. Phys.* **36**, 015110 (2009).

[247] S. Landowne and C.H. Dasso, "Novel aspects of the carbon-decay mode of radium", *Phys. Rev. C* **33**, pp. 387-389(R) (1986)

[248] R. Blendowske, T. Fliessbach, H. Walliser, "Microscopic calculation of the ^{14}C decay of Ra nuclei", *Nucl. Phys. A* **464**, pp. 75-89 (1987)

[249] Satish Kumar and Raj K. Gupta, "Neck formation and deformation effects in a preformed cluster model of exotic cluster decays", *Phys. Rev. C* **55**, pp. 218-226 (1997)

[250] Ajeet Singh, A. Shukla and M.K. Gaidarov, "Cluster decay half-lives in trans-tin and transition metal region using RMF theory", *J. Phys. G: Nucl. Part. Phys.* **49**, 025101 (2022)

[251] O.A.P. Tavares, L.A.M. Roberto and E.L. Medeiros, "Radioactive decay by the emission of heavy nuclear fragments", *Phys. Scr.* **76**, pp. 375-384 (2007)

[252] Bidhubhusan Sahu, S.K. Agarwalla, and S.K. Patra, "Half-lives of proton emitters using relativistic mean field theory", *Phys. Rev. C* **84**, 054604 (2011)

[253] R.D. Page, L. Bianco, I.G. Darby, J. Uusitalo, D.T. Joss, T. Grahn, R.-D. Herzberg, J. Pakarinen, J. Thomson, S. Eeckhaudt, P.T. Greenlees, P. M. Jones, R. Julin, S. Juutinen, S. Ketelhut, M. Leino, A.-P. Lepp anen, M. Nyman, P. Rahkila, J. Sar en, C. Scholey, A. Steer, M.B. G omez Hornillos, J.S. Al-Khalili, A.J. Cannon, P.D. Stevenson, S. Ert urk, B. Gall, B. Hadinia, M. Venhart, and J. Simpson "Two-proton radioactivity", *Phys. Rev. C* **75**, 061302(R) (2007)

[254] Yanzhao Wang, Yonghao Gao, Jianpo Cu and Jianzhong Gu, "Nuclear properties of Z = 114 isotopes and shell structure of ^{298}114", *Commun. Theor. Phys.* **72**, 025303 (2020)

[255] Chen Qiu and Xian-Rong Zhou, "Effect of Tensor Force on the Halo Structure of ^{29}Ne and ^{31}Ne", *Commun. Theor. Phys.* **61**, pp. 101-105 (2014)

[256] B. Blank and M. Ploszajczak, "Two-proton radioactivity", *Rep. Prog. Phys.* **71**, 046301 (2008)

[257] Bertram Blank and Marek Poszajczak, "Nuclear structure at the proton drip line: Advances with nuclear decay studies", *Prog. Part. Nucl. Phys.* **60**, pp. 403-619 (2008)

[258] M. Pfutzner, M. Karny, L.V. Grigorenko, and K. Riisager, "Radioactive decays at limits of nuclear stability", *Rev. Mod. Phys.* **84**, pp. 567-619 (2012)

[259] M. Pftzner, E. Badura, C. Bingham, B. Blank, M. Chartier, H. Geissel, J. Giovinazzo, L.V. Grigorenko, R. Grzywacz, M. Hellstrm, Z. Janas, J. Kurcewicz, A.S. Lalleman, C. Mazzocchi, I. Mukha, G. Mnzenberg, C. Plettner, E. Roeckl, K.P. Rykaczewski, K. Schmidt, R.S. Simon, M. Stanoiu and J.-C. Thomas, "First evidence for the two-proton decay of ^{45}Fe", *Eur. Phys. J. A* **14**, pp. 279-285 (2002)

[260] Ya.B. Zel'dovich, "The Existence of New Isotopes of Light Nuclei and the Equation of State of Neutrons", *Sov. Phys. JETP* **11**, pp. 812-818 (1960)

[261] V.I. Goldansky, "On neutron-deficient isotopes of light nuclei and the phenomena of proton and two-proton radioactivity", *Nucl. Phys.* **19**, pp. 482-495 (1960)

[262] V.I. Goldansky, "Two-proton radioactivity", *Nucl. Phys.* **27**, pp. 648-664 (1961)

[263] J. Janecke, "The emission of protons from light neutron-deficient nuclei", *Nucl. Phys.* **61**, pp. 326-341 (1965)

[264] V.M. Galitsky, and V.F. Cheltsov, "Two-proton radioactivity theory", *Nucl. Phys.* **56**, pp. 86-96 (1964)

[265] You-Tian Zou, Xiao Pan, Xiao-Hua Li, Hong-Ming, Xi-Jun Wu, and Biao He, "Systematic study of two-proton radioactivity with a screened electrostatic barrier", *Chin. Phys. C* **45**, pp. 104102 (2021)

[266] Ward Whaling, "Magnetic Analysis of the $Li^6(He^3,t)Be^6$ Reaction", *Phys. Rev.* **150**, pp. 836-838 (1966)

[267] R.A. Kryger, A. Azhari, M. Hellstrom, J.H. Kelley, T. Kubo, R. Pfaff, E. Ramakrishnan, B.M. Sherril, M. Thoennessen, S. Yokoyama, R.J. Charity, J. Dempsey, A. Kirov, N. Robertson, D.G. Sarantites, L.G. Sobotka, and J.A. Winger, "Two-proton emission from the Ground State of ^{12}O", *Phys. Rev. Lett.* **74**, pp. 860-863 (1995)

[268] G.J. KeKelis, M.S. Zisman, D.K. Scott, R. Jahn, D.J. Vieira, Joseph Cerny, and F. Ajzenberg-Selove, "Masses of the unbound nuclei ^{16}Ne, ^{15}F, and ^{12}O", *Phys. Rev. C* **17**, pp. 1229-1238 (1978).

[269] J. Giovinazzo, B. Blank, M. Chartier, S. Czajkowski, A. Fleury, M.J. Lopez Jimenez, M.S. Pravikoff, and J.-C Thomas, "Two-Proton Radioactivity of ^{45}Fe", *Phys. Rev. Lett.* **89**, 102501 (2002)

[270] B. Blank, A. Bey, G. Canchel, C. Dossat, A. Fleury, J. Giovinazzo, I. Matea, N. Adimi, F. De Oliveira, I. Stefan, G. Georgiev, S. Grevy, J.C. Thomas, C. Borcea, D. Cortina, M. Caamano, M. Stanoiu, F. Aksouh, B.A. Brown, F.C. Barker, and W.A. Richter, "First Observation of ^{54}Zn and its Decay by Two-Proton Emission", *Phys. Rev. Lett.* **94**, 232501 (2005)

[271] C. Dossat, A. Bey, B. Blank, G. Canchel, A. Fleury, J. Giovinazzo, I. Matea, F. De Oliveira Santos, G. Georgiev, S. Grevy, I. Stefan , J. C. Thomas, N. Adimi, C. Borcea, D. Cortina Gil, M. Caamano, M. Stanoiu, F. Aksouh, B.A. Brown, and L.V. Grigorenko, "Two-proton radioactivity studies with ^{45}Fe and ^{48}Ni", *Phys. Rev. C* **72**, 054315 (2005).

[272] I. Mukha, K. Summerer, L. Acosta, M.A.G. Alvarez, E. Casarejos, A. Chatillon, D. Cortina-Gil, J. Espino, A. Fomichev, J. E. Garca-Ramos, H. Geissel, J. Gomez-Camacho, L. Grigorenko, J. Hoffmann, O. Kiselev, A. Korsheninnikov, N. Kurz, Yu. Litvinov, I. Martel, C. Nociforo, W. Ott, M. Pfutzner, C. Rodrguez-Tajes, E. Roeckl, M. Stanoiu, H. Weick, and P. J. Woods, "Observation of Two-Proton Radioactivity of ^{19}Mg by Tracking the Decay Products", *Phys. Rev. Lett.* **99**, 182501 (2007).

[273] T. Goigoux, P. Ascher, B. Blank, M. Gerbaux, J. Giovinazzo, S. Grvy, T. Kurtukian Nieto, C. Magron, P. Doornenbal, G.G. Kiss, S. Nishimura, P.-A. Sderstrm, V.H. Phong, J. Wu, D.S. Ahn, N. Fukuda, N. Inabe, T. Kubo, S. Kubono, H. Sakurai, Y. Shimizu, T. Sumikama, H. Suzuki, H. Takeda, J. Agramunt, A. Algora, V. Guadilla, A. Montaner-Piza, A. I. Morales, S.E.A. Orrigo, B. Rubio, Y. Fujita, M. Tanaka, W. Gelletly, P. Aguilera, F. Molina, F. Diel, D. Lubos, G. de Angelis, D. Napoli, C. Borcea, A. Boso, R.B. Cakirli, E. Ganioglu, J. Chiba, D. Nishimura, H. Oikawa, Y. Takei, S. Yagi, K. Wimmer, G. de France, S. Go, and B.A. Brown, "Two-Proton Radioactivity of ^{67}Kr", *Phys. Rev. Lett.* **117**, 162501 (2016).

[274] J. Giovinazzo, "The two-proton radioactivity in the $A \sim 50$ mass region", *J. Phys. G: Nucl. Part. Phys.* **31**, pp. S1509-S1515 (2005).

[275] L. Audirac, P. Ascher, B. Blank, C. Borcea, B.A. Brown, G. Canchel, C.E. Demonchy, F. de Oliveira Santos, C. Dossat, J. Giovinazzo, S. Grevy, L. Hay, J. Huikari, S. Leblanc, I. Matea, J.-L Pedroza, L. Perrot, J. Pibernat, L. Serani, C. Stodel, and J.-C Thomas, "Direct and β-delayed multi-proton emission from atomic nuclei with a time projection chamber: the cases of ^{43}Cr, ^{45}Fe, and ^{51}Ni", *Eur. Phys. J. A* **48**, 179 (2012).

[276] B.J. Cole, "Stability of proton-rich nuclei in the upper sd shell and lower pf shell", *Phys. Rev. C* **54**, pp. 1240-1248 (1996).

[277] L.V. Grigorenko and M.V. Zhukov, "Two-proton radioactivity and three-body decay. IV. Connection to quasiclassical formulation", *Phys. Rev. C* **76**, 014009 (2007).

[278] E. Olsen, M. Pfutzner, N. Birge, M. Brown, W. Nazarewicz, and A. Perhac, "Landscape of Two-Proton Radioactivity", *Phys. Rev. Lett.* **111**, 139903 (2013).

[279] F.C. Barker, "^{12}O ground-state decay by ^{2}He emission", *Phys. Rev. C* **63**, 047303 (2001).

[280] B. Alex Brown, "Diproton decay of nuclei on the proton drip line", *Phys. Rev. C* **43**, pp. R1513-R1517 (1991).

[281] W. Nazarewicz, J. Dobaczewski, T.R. Werner, J.A. Maruhn, P.-G. Reinhard, K. Rutz, C.R. Chinn, A.S. Umar, and M.R. Strayer, "Structure of proton drip-line nuclei around doubly magic ^{48}Ni", *Phys. Rev. C* **53**, pp. 740-751 (1996).

[282] R. Alvarez-Rodrguez, H.O.U. Fynbo, and A.S. Jensen, "Distinction between Sequential and Direct Three-Body Decays", *Phys. Rev. Lett.* **100**, 192501 (2008).

[283] M. Gonalves, N. Teruya, O.A.P. Tavares, S.B. Duarte, "Two-proton emission half-lives in the effective liquid drop model", *Phys. Lett. B* **774**, pp. 14-19 (2017).

[284] J.P. Cui, Y.H. Gao, Y.Z. Wang, and J.Z. Gu, "Two-proton radioactivity within a generalized liquid drop model", *Phys. Rev. C* **101**, 014301 (2020).

[285] De-Xing Zhu, Hong-Ming Liu, Yang-Yang Xu, You-Tian Zou, Xi-Jun, Peng-Cheng Chu, and Xiao-Hua Li, "Two-proton radioactivity within Coulomb and proximity potential model", *Chin. Phys. C* **46**, 044106 (2022).

[286] Hong-Ming Liu, Xiao Pan, You-Tian Zou, Jiu-Long Chin, Jun-Hao Cheng, Biao He, and Xiao-Hua Li, "Systematic study of Two-proton radioactivity half-lives within a Gamow-like model", *Chin. Phys. C* **45**, 044110 (2021).

[287] L.V. Grigorenko, R.C. Johnson, I.G. Mukha, I.J. Thompson, and M.V. Zhukov, "Theory of Two-Proton Radioactivity with Application to ^{19}Mg and ^{48}Ni", *Phys. Rev. Lett.* **85**, pp. 22-25 (2000).

[288] L.V. Grigorenko, R.C. Johnson, I.G. Mukha, I.J. Thompson, and M.V. Zhukov, "Two-proton radioactivity and three-body decay: General problems and theoretical approach", *Phys. Rev. C* **64**, 054002 (2001).

[289] Ning Wang, Min Liu, Xizhen Wu, Jie Meng, "Surface diffuseness correction in global mass formula", *Phys. Lett. B* **734**, pp. 215-219 (2014).

[290] Xiao Pan, You-Tian Zou, Hong-Ming Liu, Biao He, Xiao-Hua Li, Xi-Jun Wu, and Zhen Zhang, "Systematic study of Two-proton radioactivity half-lives using two-potential and Skyrme-Hartree-Fock approaches", *Chin. Phys. C* **45**, 124104 (2021).

[291] M. Pomorski, M. Pftzner, W. Dominik, R. Grzywacz, A. Stolz, T. Baumann, J.S. Berryman, H. Czyrkowski, R. Dbrowski, A. Fijakowska, T. Ginter, J. Johnson, G. Kamiski, N. Larson, S.N. Liddick, M. Madurga, C. Mazzocchi, S. Mianowski, K. Miernik, D. Miller, S. Paulauskas, J. Pereira, K.P. Rykaczewski, and S. Suchyta, "Proton spectroscopy of ^{48}Ni, ^{46}Fe, and ^{44}Cr", *Phys. Rev. C* **90**, 014311 (2014).

[292] Meng Wang, G. Audi, F.G. Kondev, W.J. Huang, S. Naimi, and Xing Xu, "The Ame2016 atomic mass evaluation", *Chin. Phys. C* **41**, 030003 (2017).

[293] P. Ascher, L. Audirac, N. Adimi, B. Blank, C. Borcea, B.A. Brown, I. Companis, F. Delalee, C.E. Demonchy, F. de Oliveira Santos, J. Giovinazzo, S. Grvy, L.V. Grigorenko, T. Kurtukian-Nieto, S. Leblanc, J-L Pedroza, L. Perrot, J. Pibernat, L. Serani, P.C. Srivastava, and J-C. Thomas, "Direct Observation of Two Protons in the Decay of ^{54}Zn", *Phys. Rev. Lett.* **107**, 102502 (2011).

[294] E. Olsen, M. Pfutzner, N. Birge, M. Brown, W. Nazarewicz, and A. Perhac, "Landscape of Two-Proton Radioactivity", *Phys. Rev. Lett.* **110**, 222501 (2013).

[295] Yanzhao Wang, Jianpo Cui, Yonghao Gao and Jianzhong Gu, "Two-proton radioactivity of exotic nuclei beyond proton drip-line", *Commun. Theor. Phys.* **73**, 075301 (2021).

List of Publications

Published:

1. **Ajeet Singh**, A. Shukla, and M.K. Gaidarov, "Cluster decay half-lives in trans-tin and transition metal region using RMF theory", *J. Phys. G: Nucl. Part. Phys.*, **49**, 025101 (2021).

2. **Ajeet Singh**, and A. Shukla, "Cluster Radioactivity Study of Transition Metal region using RMF theory", *Bulgarian Journal of Physics*, **48**, pp. 505-513 (2021).

3. **Ajeet Singh**, A. Shukla, and M.K. Gaidarov, "A combined Glauber model plus Relativistic Hartree Bogoliubov theory analysis of nuclear reactions with light and medium mass nuclei", *Pramana - J. Phys.*, **96**, 8 (2022).

4. **Ajeet Singh**, A. Shukla, and M.K. Gaidarov, "Structure and decay modes study of Th, U, and Pu isotopes using Relativistic mean-field model", *Nuclear Physics A*, **1023**, 122439 (2022).

5. **Ajeet Singh**, A. Shukla, V. Kumar, and M.K. Gaidarov, "Study of Two-proton Emission Half-lives using Relativistic mean-field model", *Acta Phys. Pol. B*, **53**, 10-A3 (2022).

Book Chapters:

1. Awanish Bajpeyi, **Ajeet Singh** and A. Shukla "Correlation of nuclear structure observables with the nuclear reaction measurable for astrophysical p-process", *In Book Nuclear Structure Physics.*

2. Akhilesh Yadav, **Ajeet Singh** and A. Shukla "Nuclear Energy and Conventional Clean Fuel", *In Book Status and Future Challenges for Non-conventional Energy*

Sources Volume I.

Conferences/Symposium:

1. **Ajeet Singh**, A. Shukla and Akhilesh Yadav "Nuclear Reaction Studies of Carbon isotopes in conjunction with RMF theory and Glauber model", *Proceedings of the DAE Symp. on Nucl. Phys.,* Vol. **63**, pp. 534-535 (2018), BARC, Mumbai, India.

2. **Ajeet Singh**, and A. Shukla "Nuclear Reaction Studies of unstable nuclei using RMF theory in conjunction with the Glauber model", *Proceedings of the DAE Symp. on Nucl. Phys.,* Vol. **64**, pp. 471-472 (2019), Lucknow, Uttar Pradesh, India.